

Autonomous photonic biosensor

Alexander Drayton

Doctor of Philosophy

University of York

Physics

June 2021

Abstract

Early diagnosis and targeted disease treatment are essential elements of healthcare provision. Current systems often revolve around symptomatic diagnosis and laboratory testing when needed. These systems often result in semi-blind treatment or long wait times. Point-of-care biosensors that can quantify specific biomarkers have an important role to play in this context as they bridge the gap of quick and specific testing in healthcare provision.

Photonic biosensors have been demonstrated as a laboratory diagnostic tool with well-established advantages, achieving low limits of detections for protein biomarkers. Several issues remain before they can be translated into commonly used point-of-care instruments. Ideally, integrated photonic biosensors should be inexpensive, sensitive and easy to use. However, many existing photonic biosensors require complex readout equipment, such as external spectrometers, or precise and bulky optical coupling.

Presented in this thesis is the development of a low-cost photonic biosensing instrument. The modality used is that of a chirped one-dimensional guided mode resonance sensor. When used in conjunction with a monochromatic source, detection can be accomplished simply by a camera in a compact microscope-style configuration.

A study into the performance of low-cost components was conducted to understand the sources of noise. With the understanding gained from this study the instrument was able to achieve a bulk refractive index sensitivity of $3.1 \pm 0.6 \times 10^{-5}$ Refractive Index Units. This limit of detection is comparable to other laboratory based modalities and so the device was tested with C-Reactive Protein and Immunoglobulin G assays as example proteins. The best performance achieved was detection of 1 ng/mL for C-Reactive Protein, well below the clinically relevant range. The limits of detection achieved using low-cost components indicates that photonic biosensors are well suited to clinical situations and have the potential to play a significant role in the development of diagnostics in the future for healthcare.

Contents

List of Figures.....	9
List of Tables.....	13
Acknowledgments.....	14
Author's Declaration.....	16
1. Introduction.....	23
1.1. Thesis scope.....	23
1.2. Figures of merit for sensing.....	25
1.2.i. Limit of detection.....	25
1.2.ii. Q-factor and sensitivity.....	26
1.2.iii. Evanescent tail sensing.....	27
1.3. Comparison between GMR sensors and other sensing modalities.....	28
1.3.i. GMR - a historical perspective.....	28
1.3.ii. Surface plasmon resonance.....	29
1.3.iii. Nanohole arrays.....	30
1.3.iv. Microrings.....	31
1.3.v. Bimodal waveguide.....	31
1.3.vi. Comparison summary.....	33
1.4. Economic considerations.....	34
1.4.i. The valley of death and technological lock-in.....	34
1.4.ii. Point-of-care testing.....	35
2. Theory.....	37
2.1. Describing light.....	37
2.1.i. Maxwell's equations.....	37
2.2. Periodic structures.....	40
2.2.i. General periodic structures.....	40
2.2.ii. Guided mode resonance.....	41
2.2.iii. Polarisation and resonance properties.....	44
2.2.iv. Grating parameters.....	45
2.2.v. Effect of incidence angle.....	47

2.3.	Chirped guided mode resonance.....	48
2.3.i.	Spectral-spatial equivalence	48
3.	Methods.....	51
3.1.	General fabrication steps.....	51
3.1.i.	Choice of materials.....	51
3.1.ii.	Sample preparation: dicing and cleaning	52
3.1.iii.	Spin coating.....	54
3.1.iv.	Electron-beam lithography.....	54
3.1.v.	Sample development and reactive ion etching	57
3.1.vi.	Sample finishing.....	58
3.2.	Chirped GMR design	59
3.2.i.	Continuous polygon design	59
3.2.ii.	Moving to lower wavelengths: effect on resolution.....	60
3.2.iii.	Final structure outcome	62
3.3.	Additive manufacturing: 3D printing methods.....	64
3.3.i.	Parallels with lithography and resolution limits.....	65
3.3.ii.	CAD part design and model preparation.....	66
3.3.iii.	Part printing and finishing	67
4.	Device prototyping and development	69
4.1.	Discrete setup and issues.....	69
4.2.	Instrument design considerations.....	70
4.2.i.	Optical path and components	70
4.2.ii.	Light and manipulation	71
4.2.iii.	Design aspects in confined space.....	72
4.2.iv.	Achieving collimation and alignment procedure.....	73
4.3.	Microfluidic cartridge.....	74
4.3.i.	PDMS vs 3D printed channels	75
4.3.ii.	Sensor chip sealing and mounting.....	76
4.3.iii.	Part compatibility with chemical solutions.....	76
5.	Laboratory to point-of-care.....	78
5.1.	Point-of-care context.....	78

5.2.	Low-Q vs. high-Q resonant systems.....	79
5.2.i.	Lower Q modalities - using guided mode resonance	82
5.2.ii.	Camera choice.....	83
5.2.iii.	Visual Q and apparent sensitivity.....	86
5.2.iv.	Fano tracking for time measurements	87
5.2.v.	Scalability and nano-imprint lithography	89
5.2.vi.	Visual clarity: using RCLEDs.....	91
5.3.	Analysis of system performance.....	93
5.3.i.	Parameters entering the performance comparison.....	93
5.3.ii.	Nature of the model	95
5.3.iii.	Impact of source and resonance linewidth on performance	99
5.3.iv.	Experimental performance.....	100
5.4.	Contrast enhancement using polarisation.....	106
5.5.	Comparison with other modalities.....	108
5.6.	Discussion and conclusions.....	110
6.	Biological measurements	112
6.1.	Relevance of biological assays	112
6.1.i.	Functionalisation protocol.....	113
6.1.ii.	Diffusion boundary layer impact on assays.....	116
6.2.	Assay viability and parameter considerations.....	117
6.2.i.	QCM-D as an assay development tool.....	117
6.2.ii.	CRP and IgG assay testing.....	118
6.2.iii.	Probing the diffusion boundary layer	122
6.3.	Fluidic delivery of samples	125
6.3.i.	PDMS channel fabrication.....	125
6.3.ii.	PDMS implementation	127
6.3.iii.	Fluidic pumping and sample Injection.....	127
6.3.iv.	Fluidic integration using printed channels.....	129
6.3.v.	Summary	135
6.4.	Antibody functionalisation.....	135
6.4.i.	Comparison of fluidic parameters.....	136

6.4.ii. Functionalisation variation	139
6.5. Biological measurements on the integrated device.....	139
6.5.i. Performance of protein assay	140
6.5.ii. Protein assay troubleshooting.....	141
6.5.iii. Channel placement effect on surface chemistry.....	143
6.5.iv. Further factors – operating wavelength and source.....	144
6.6. Comparison with other handheld devices.....	144
6.7. Multiplexing capabilities.....	146
7. Outlook.....	148
7.1. Measuring success and potential improvements	148
7.1.i. Potential improvements	148
7.2. Economic considerations for commercialisation.....	149
7.2.i. Manufacturing techniques.....	149
7.2.ii. Component cost.....	151
7.3. Preliminary work for further development.....	152
7.3.i. Interferometry in an autonomous device.....	152
7.3.ii. Integrated fluidics for clinical samples.....	154
7.3.iii. Antibiotic susceptibility assay.....	156
7.3.iv. Dopamine-based surface chemistry.....	157
8. Conclusion.....	160
Bibliography	162

List of Figures

Figure 1: Basic operation of a guided mode resonance sensor.....	24
Figure 2: Operation principle of a surface plasmon resonant sensor.....	29
Figure 3: Operation principle of microring resonator sensor.....	31
Figure 4: Operation principle of a bimodal waveguide sensor.....	32
Figure 5: A representation of the valley of death for technology.....	35
Figure 6: Flow diagram of traditional compared to point-of-care diagnostics.....	36
Figure 7: Diffraction orders occurring from a basic periodic grating.....	40
Figure 8: Reflectivity plot of thickness vs wavelength for a grating structure.....	42
Figure 9: Light interaction with a periodic structure with period near- λ	43
Figure 10: Spectra for TE and TM polarised light incident on a grating structure...	45
Figure 11: Reflectivity response against wavelength for period, filling fraction, thickness and cover index.....	46
Figure 12: Reflectivity response against incident angle.....	47
Figure 13: Four ways of chirping a GMR.....	49
Figure 14: Image of a period chirped GMR and a hyperspectral image of the wavelength response across the same GMR.....	50
Figure 15: S4 simulations and Fresnel reflection corrected measurement of Fabry- Perot response of silicon nitride and amorphous silicon.....	52
Figure 16: Key steps of sample patterning using electron beam lithography.....	53
Figure 17: Proximity effect illustration.....	55
Figure 18: SEM micrographs of a 150 nm structure with increased spacing and plot of the actual size against the feature spacing.....	56
Figure 19: Schematic of the reactive ion etcher used to etch samples.....	58
Figure 20: Images of two Chirped GMR designs for continuous polygon design....	60
Figure 21: Illustration the staircase effect in EBL.....	61
Figure 22: Two fabricated chirped GMRs with different filling fraction exhibiting the effect of staircasing.....	62
Figure 23: Images of a chirped GMR with an optimised design.....	62
Figure 24: RCWA simulation of the reflectance of a 1D GMR.....	63
Figure 25: Schematic of an Inverted Stereolithography 3D printer.....	65
Figure 26: Schematic of the Sparrow criterion for polymerisation threshold.....	66
Figure 27: Examples for printing different types of structures.....	67
Figure 28: A rendering of the setup that is used to measure Guided Mode Resonance samples.....	69
Figure 29: A schematic and image of the discrete setup that was a proof of concept of miniaturisation.....	70

Figure 30: Schematics and image of the printed housing and components of the compact instrument.....	71
Figure 31: RCLED mounted in a printed cartridge.	72
Figure 32: A Cross section view of the lens track system.	73
Figure 33: Images of the tools and results of collimation in the instrument.....	74
Figure 34: Optical micrograph of a chirped GMR sensor chip placed across two PDMS channels.	75
Figure 35: A rendering of the printed fluidic cartridge top and base with the glass chip and orange tape gasket.	76
Figure 36: Mass change of 3D printed material using Formlabs® black and clear resins reporting both mass change and visual changes.	77
Figure 37: Wavelength and intensity variation of a low-cost Fabry Perot laser diode and comparison of current sources.	80
Figure 38: Wavelength and intensity variation of a Vertical-cavity surface-emitting laser.	81
Figure 39: Example spectra of a resonant cavity LED with and without filter.....	82
Figure 40: Readout noise of example CMOS and CCD sensors.....	84
Figure 41: The interplay of 3 major factors for a chirped GMR sensor.....	86
Figure 42: Example image of a chirped GMR with a selected region of interest used for fitting.....	88
Figure 43: A graphic illustrating how the resonance is tracked by fitting the Fano resonance curve over time.....	88
Figure 44: Image of a chirped GMR sensor produced by electron beam lithography and nanoimprint lithography.....	89
Figure 45: SEM micrograph of the edge face of a Chirped GMR produced via Electron beam lithography and Nanoimprint lithography.....	90
Figure 46: Chirped GMR sensors illuminated by a laser diode and a halogen source filtered via a monochromator.....	91
Figure 47: Chirped GMR sensors illuminated by a halogen source filtered via a monochromator and an RCLED with a 1 nm and 3 nm linewidth filter.....	92
Figure 48: Comparison of the 3σ of a) 1 nm filtered RCLED and b) 3 nm filtered RCLED with fixed cover index of 1.3333.....	93
Figure 49: Histogram of pixel intensities across an image when illuminated by a coherent source both with and without the use of a diffuser disk de-speckler.	94
Figure 50: Steps used to apply noise to an S4 simulation to generate a predicted noise for the various components of the instrument.....	96
Figure 51: A plot showing the data from a Monte Carlo simulation of noise added to a simulated GMR Spectrum compared to experimental values.	97

Figure 52: Plot of measured resonance linewidth for different source linewidths and limit of detection as a function of resonance Q value convolved with a 1 nm linewidth source.....	99
Figure 53: Illustration of the implementation of a reference channel.....	100
Figure 54: Bulk refractive index measurements.	101
Figure 55: Data used to calculate the 3σ values of the instrument.....	103
Figure 56: Schematic diagrams of the laboratory setup that was the basis for miniaturisation and a schematic of my instrument.....	104
Figure 57: 3σ noise for the laboratory setup using a halogen light source and monochromator and the instrument using a 1 nm filtered RCLED.....	105
Figure 58: Modified setup used to implement cross-polarisation as a noise reduction technique.	106
Figure 59: Images of a GMR resonance using a single polariser compared to using the polarisation contrast enhancement method.....	107
Figure 60: Comparison of the 3σ of a Chirped GMR with and without contrast enhancement.....	107
Figure 61: A chirped GMR resonance using a coherent source exhibiting speckle compared to a resonance of the GMR sensor with cross-polarisation applied.....	108
Figure 62: Structures of IgG1 protein structure and CRP protein structure.....	112
Figure 63: The functionalisation process for protein assays.....	113
Figure 64: The (3-mercaptopropyl) trimethoxysilane (MPTES) and maleimide-PEG6-succinimidyl ester (PEG) molecules used for surface functionalisation.	114
Figure 65: Functionalisation steps and the chemical structures that bind to the surface.	115
Figure 66: Graphic illustration of the diffusion boundary layer.....	116
Figure 67: Schematic of a QCM-D sensor and the expected response of the resonant frequency from binding and unbinding.	117
Figure 68: QCM-D resonant frequency data of 4 IgG assay.....	119
Figure 69: QCM-D data comparing IgG and CRP Assays.	120
Figure 70: Three separate control measurements of the IgG assay using different parameters.....	121
Figure 71: QCMD data of an IgG assay done at different flow rates.....	122
Figure 72: Binding events of 10 $\mu\text{g}/\text{mL}$ IgG at different flow rates and a plot of parameter k from the fits against flow rate.....	123
Figure 73: Schematic of the 3D printed mould for PDMS channels with silicon and SU8 masters.....	126
Figure 74: Clamp that holds the PDMS channels and GMR sensor together.....	127
Figure 75: Schematic diagram with syringe pumping and a sample loop.	128

Figure 76: Laminar flow concept for delivering different samples to adjacent GMR sensors.	129
Figure 77: Computer aided designs and images of printed fluidic circuit elements for fluidic delivery.	130
Figure 78: COMSOL simulations of 3D printed laminar flow channels.....	132
Figure 79: Images of printed fluidics sealed with tape and epoxy and images of operation.	133
Figure 80: A 3 channel laminar flow schematic and images of 3 fluid operation...	134
Figure 81: Example antibody binding data for anti-IgG and anti-CRP measured on a GMR.	136
Figure 82: Average shifts observed on GMR sensors for a variety of flow rates and concentrations compared for anti-CRP and anti-IgG.	137
Figure 83: Plot of the antibody shifts for each parameter combination.....	138
Figure 84: A plot of antibody shift against casein blocking shift on a chirped GMR sensor.	139
Figure 85: Measurement of a low concentration CRP assay.....	140
Figure 86: Resonance shifts observed upon antigen binding for a variety of configurations.	141
Figure 87: Shift analysed across the width of the GMR in a channel.	143
Figure 88: Example measurement using three channels. Green highlighted areas show where PDMS is in contact with sensor surface.	146
Figure 89: Economics of scale of the three manufacturing techniques.....	150
Figure 90: Wavelength and Phase response for a grating structure.	152
Figure 91: Schematic of the double slit interference method employed for compact phase interferometry.	153
Figure 92: Filtered whole blood using the Vivid™ Plasma Separation Membrane and capillary channels showing travel of whole and dilute blood.....	154
Figure 93: Rendering of a capillary flow cartridge and an assembled cartridge with blood filtering and plasma flow to the GMR sensor.	155
Figure 94: Resonance shift plot for a beta lactam drug assay.	157
Figure 95: I IgG protein assay using poly-dopamine surface chemistry.	158

List of Tables

Table 1: Comparison of different photonic sensing modalities..	33
Table 2: Comparison between PDMS and 3D printing for the fabrication of microfluidic channels.....	75
Table 3: Noise contributions expressed as normalised standard deviations of the main elements to system performance.....	95
Table 4: Summary of some Photonics modalities used for low-cost approaches to biosensing.....	109
Table 5: Association and dissociation constants for antibody-antigen binding for CRP and IgG.....	116
Table 6: Parameters used in COMSOL fluidic simulation.....	131
Table 7: Values of antibody and antigen shifts pertaining to the data in Figure 85.	142
Table 8: Summary of Photonic modalities used for low-cost approaches to biosensing with refractive index LOD and protein assay LOD.....	145

Acknowledgments

I would like to take a moment to express my gratitude to all those that have supported me over the nearly four years of working towards this thesis. I am extremely proud to have accomplished this and it would not have happened without them.

First I would like to thank my supervisor, Professor Thomas Krauss, for championing me throughout my project and providing countless opportunities for growth, both personally and scientifically. My deepest gratitude especially for the support in developing my writing style, without which this thesis would be only a shadow of what is presented here. It has been a privilege to be a part of his research group and I could not have imagined the amazing journey or destination when I started my PhD.

I would also like to thank Dr Steve Johnson (Department of Electronic Engineering) and Dr Christopher Reardon for their advice and guidance throughout my project. Your input has helped shape my understanding and has a huge part to play in the chosen direction.

I would like to thank the many members of the Photonics and Bio-Inspired Technologies research groups in York, both present and past who have had some impact on my project. In particular I would like to thank Callum Silver for his friendship and the support he provided in a multitude of ways; Dr Casper Kunstmann-Olsen, Dr Matt Simmons, George Duffett and Kalum Thurgood-Parkes for the D&D sessions that got me through writing; Rhys Ashton, Josh Male, Dr Lisa Miller, Dr Steve Thorpe, Dr Yue Wang, Isabel Barth, Dr Giampaolo Pitruzzello, Dr Kezheng Li, Dr Donato Conteduca, Manuel Deckart, Shrishty Bakshi, Dr Jose Juan-Colás, Dr Ben Coulson, Dr Ahmed Kenaan and Dr Lewis Reeves thank you for your discussions and contributions, no matter how small, these have moulded me and this work. I have sorely missed the coffee breaks, group meals and pub trips so I hope we get opportunity in the future.

Finally I would like to thank those who are outside the research group for their support that they may not realise has been extremely important to me: Jake Lucas, Elliot Rowe, Simon Parker and Sam Mealand for their timeless friendship, prayer and support. Also, those from York Baptist Church, but especially Tom Dunning, Dr Joe Bennett, Andy Herbert, Sarah Herbert and the Earswick house group. I would also like to thank my parents for their support in proof reading and always believing in me.

Finally I would like to thank my wife Hannah, to whom this thesis is dedicated, for suffering all the lows this thesis has brought. You have helped carry me through the tough times and I could not have achieved this high without you!

Author's Declaration

I, Alexander Drayton, declare that this thesis entitled, "Autonomous photonic biosensor", and the work presented in it are my own. I confirm that:

- This work was done wholly or mainly while in candidature for a research degree at this University.
- Where I have consulted the published work of others, this is always clearly attributed.
- Where I have quoted from the work of others, the source is always given. With the exception of such quotations, this thesis is entirely my own work.
- I have acknowledged all main sources of help.
- Where the thesis is based on work done by myself jointly with others, I have made clear exactly what was done by others, collaborators are named and attributed, and what I have contributed myself.

What follows is a list with details of publications that were published in the course of the work undertaken for this thesis, had contributions therein (1-3) as well as past publications (4), conferences attended (and pending), as well as summer school attendances.

Publications:

1. A. Drayton, I. Barth, and T. F. Krauss, 'Guided mode resonances and photonic crystals for biosensing and imaging', in *Semiconductors and Semimetals 100, Photonic Crystal Metasurface Optoelectronics*, 2019, pp. 115-148.
2. A. Drayton, K. Li, M. Simmons, C. Reardon, and T. F. Krauss, 'Performance limitations of resonant refractive index sensors with low-cost components', *Opt. Express*, vol. 28, no. 22, p. 32239, 2020.
3. K. Li, R. Gupta, A. Drayton, I. Barth, D. Conteduca, C. Reardon, K. Dholakia, and T. F. Krauss, 'Extended Kalman Filtering Projection Method to Reduce the 3σ Noise Value of Optical Biosensors', *ACS Sensors*, vol. 5, no. 11, pp. 3474-3482, 2020.
4. A. Drayton, J. Zehner, J. Timmis, V. Patel, G. Vallejo-Fernandez, and K. O'Grady, 'A comparative measurement technique of nanoparticle heating for magnetic hyperthermia applications', *J. Phys. D. Appl. Phys.*, vol. 50, no. 49, 2017.

Conferences:

1. Drayton, A., Reardon, C., Krauss, T.F., Autonomous Photonic Biosensor based on Guided Mode Resonance. Oral presentation at CLEO Europe 2019, Munich, June 2019.
2. Drayton, A., Simmons. M., Silver, C., Miller, L., Johnson, S., Krauss, T.F., Simple Photonic Biosensor for the detection of Antibiotic Resistance. Poster presentation at Sensors in Medicine 2019, London, September 2019.
3. Drayton, A., Simmons. M., Silver, C., Miller, L., Johnson, S., Krauss, T.F., Low-Cost and Portable Photonic Immuno-sensor based on Guided Mode Resonance. Flash talk and poster presentation at MicroTAS 2020, Virtual, October 2020.
4. Drayton, A., Reardon, C., Krauss, T.F., Low-Cost and Portable Photonic Immuno-sensor based on Guided Mode Resonance. Oral presentation (Invited) at 31st Anniversary World Congress on Biosensors 2020, Postponed to July 2021.

Summer Schools:

1. 10th Advanced Study Course on Optical Chemical Sensors – ASCOS 2017 – Třešť (Czech Republic) – July 2017.
2. Physics of Life Summer School 2018: New Approaches to Biomolecular Structure, Dynamics and Function – Durham University – July 2018.
3. Innovation and Entrepreneurship in Photonics summer school - University of St. Andrews – June 2018.

To Hannah Elizabeth Drayton

“Even though I walk through the valley of the shadow of death, I will fear no evil...”

1. Introduction

As of 2020, the world has changed profoundly. The COVID-19 pandemic has had wide reaching implications, from people's approach towards disease transmission to the general public's understanding of healthcare. Furthermore, the pandemic has accelerated research in some areas, such as vaccines, due to a huge funding push [1] resulting in the fastest vaccine approval in history. Questions have also been raised as to whether our current systems and technology are as good as they can be [2]. While institutional and societal changes will take years or decades to come to fruition, the pandemic has created a space for new healthcare innovation, especially rapid testing.

Despite the perceived slow pace of healthcare decision making, there have been significant developments in diagnostics. As one example of biosensing development, DNA sequencing first emerged in the 1970s but has developed into the chip based ion-torrent system that was released in the 2010s [3]. To put this in context, the Babbage Difference Engine - often considered the start of computer development, was invented in the 1830s. It could be said then that biosensing has come further in 40 years than computers have in a decade. While this is the case, it is not a wholly fair comparison as a lot of the development in the biosensing field has benefited from advances in integrated circuit development.

One area that has benefited greatly from the development of computer technology is photonics, which often uses similar fabrication techniques (cf. chapter 3) and has parallels in the underlying principles (cf. chapter 2). A recent report has shown that the global Biophotonics market was worth \$31.6 billion in 2015 and is estimated to grow to \$63.1 billion by 2022. [4]. The clear implication is that such devices are not only desirable but they will solve many problems we currently face in diagnostics.

1.1. Thesis scope

The approach of this work was to take a sensor proven successful in a laboratory environment and, by using low-cost components, create an instrument that drives the technology towards commercialisation. Components and fabrication techniques were considered carefully in order to create a device suitable for a healthcare setting. Achieving this goal mostly relies on the hallmark of the photonic device, the chirped guided mode resonance (GMR), used as the active sensing component. The basic principle of operation of GMR is illustrated in Figure 1. While achieving the goal of

generating a highly sensitive device for label free detection is desirable, this is not the full picture and should not be the sole focus. The GMR modality chosen is compared to other photonic sensors to give a perspective on its merits and shortcomings. Furthermore, the broader picture of how this device may fit into a healthcare setting will be considered as well as some hurdles that may be encountered in development, to pre-empt or avoid them.

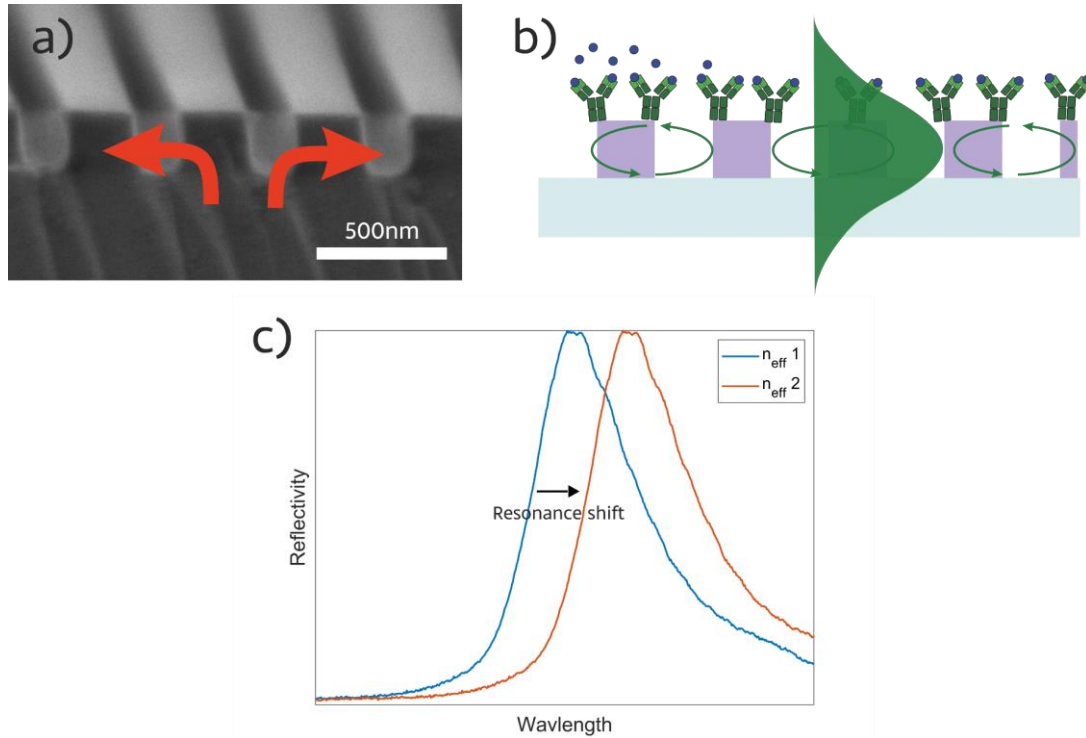


Figure 1: a) Light coupling into a GMR. b) Waveguide mode with evanescent tail probing protein binding. c) Measured response of wavelength shift due to change in the photonic modes effective index, $\lambda_{res} = n_{eff}a$ where a is the period of the structure.

An in-depth look at the theory behind the GMR modality is provided in chapter 2. The corresponding fabrication process for the sensor is presented in chapter 3. This chapter also presents the technologies needed to manufacture the housing, using additive manufacturing as a rapid low-cost approach. The device development and final configuration is outlined in chapter 4 to give context to the two main results chapters.

As economic considerations were a key part of the development of this device a study was undertaken into the noise of the instrument when using low-cost components (cf. chapter 5). Light source and camera noise were the main aspects considered, although the effect of pixel size and resonance linewidth has also been studied. Once again, the key aim is not to achieve the highest performing technology, as such, my results were compared to those of other low-cost photonic biosensors. The perspectives gained from these studies informed not only the choice of configuration moving forward, but also added context to the decisions made.

With a biosensor configuration identified and optimised, an exploration into its use as an immunosensor is presented in chapter 6. First the functionalisation process is detailed, describing how capture molecules are bound to the sensor surface. Immunoglobulin G and C-Reactive protein assays were used due to their clinical relevance and availability. Initial exploration into the assay was conducted on a commercial quartz crystal microbalance system before being tested on the GMR instrument developed in this work. The results are once again discussed in comparison to other photonic biosensors.

The work contained within this thesis had many engineering challenges which has highlighted several aspects of technology development often ignored in the literature. The originality of this work comes from the requirements resulting from the self-imposed constraints of creating a low-cost and compact device. These constraints have delivered a device that is commercially viable in a point-of-care setting and therefore, the outlook of this thesis is mainly focused on how to propel this work into future commercialisation.

1.2. Figures of merit for sensing

1.2.i. Limit of detection

When discussing the performance of photonic biosensors, it is important to have a way to compare the variety of modalities presented in the literature. We use a figure of merit (FOM) that is applicable across the field. A FOM is important as it allows us to compare different implementations and also to benchmark improvements, for example in chapter 5. The FOM often employed for photonic sensors is the limit of detection (LOD). LOD is the smallest measurable value which, in photonics, is often expressed in terms of refractive index shift e.g. $\Delta n = 10^{-5}$. Refractive index is used due to its intrinsic link with how photonic biosensors work (cf. chapter 2). The LOD [5] is defined as:

$$LOD = LOB + 3\sigma$$

Here, the limit of blank (*LOB*) is the sensor measurement when there is no analyte present, essentially, a baseline for the sensor's measurement. For this reason, the LOD is often just approximated to three times the standard deviation (3σ), simply put, the LOD is three times higher than the noise of the system [6].

Measuring the LOD in this way is highly convenient, however, it is hard to translate this number into a biological LOD. Generally, the biological LOD is measured directly

through the smallest concentration that can be seen above the noise. Consideration must therefore be given to; electronic, biochemical and photonic factors when discussing the performance range of a sensor. The first two factors discussed here are also dealt with in later chapters (electronic factors - chapter 5 and biochemical factors - chapter 6) and the photonic considerations are touched upon in section 1.2.ii and chapter 2.

Electronic factors: Essentially describing noise, the electronic factors arise from a multitude of sources in a system. The light source will not be perfectly stable in intensity or wavelength noise. Detectors will also suffer noise from the discretisation of the data and the thermal noise that is generated in operation. Most noise sources can be mitigated using either post processing techniques, such as algorithms, or by experimental improvements such as temperature stabilising the source or changing the integration time. Such control measures could lead one to assume that optical sensing is limited by photon shot noise, in practice however, other sources of noise will prevent this limit being reached. This is especially true when considering cheaper sensors like the one considered in this work.

Biochemical factors: Using biochemistry provides the highest source of variability in the LOD. This arises from multiple sources such as difference in the capture molecule that will bind to a target, like a protein in blood e.g. is it naturally derived or synthetic? Is there a difference in affinity? How the capture molecule is bound to the surface also matters e.g. does its conformation change affect the availability of binding sites? The analyte also matters, e.g. is it a buffer or a clinical matrix such as plasma, which can affect the amount of non-specific binding; the surface density, fluidic delivery, pH and temperature. There are a multitude of factors to consider even before trying to compare different molecules of similar size. For this reason, most biological LODs should be as directly comparable as possible. However, this is often not possible and it should be expected that even if two modalities have similar photonic limits of detection the reported biological LODs could vary by several orders of magnitude.

1.2.ii. Q-factor and sensitivity

Beyond the LOD, the Q-factor and the Sensitivity are other essential figures of merit that are essential for assessing the performance of a resonant photonic biosensor. I discuss these and their relationship next.

Q-Factor: The photonic modalities of relevance to this thesis employ some form of resonance. The resonance has an inherent property called the quality factor or Q-factor which is related to the energy stored in the resonator. The Q-factor for photonic

systems is typically defined as the ratio of the resonance's central wavelength to its full width at half maximum:

$$Q = \frac{\lambda_0}{\Delta\lambda}$$

This very simple and convenient formula relates the 1/e decay time of a resonance to its spectral half-width and assumes a Lorentzian oscillator. The Lorentzian line shape is equivalent to a Fano line shape which has no asymmetry [7] (cf. chapter 2). Generally speaking, the higher the Q-factor of a sensor, the better its performance, as a sharper resonance is easier to track. Therefore, the smallest detectable wavelength shift is directly proportional to the Q-factor [6].

Sensitivity: Bulk sensitivity is the property that expresses the shift of the resonance in terms of wavelength shift ($\Delta\lambda$) which is a function of the change of the external refractive index (Δn) [8];

$$S = \frac{\Delta\lambda}{\Delta n}$$

The units of sensitivity are nm/RIU, with RIU being refractive index unit, a dimensionless quantity. Since Q-factor and bulk sensitivity are both related to the sensor performance it seems clear that the product of both is a good starting point for the desired figure of merit used in comparison. Thus, this metric is typically used to compare the different configurations as discussed in section 1.3.

1.2.iii. *Evanescent tail sensing*

The bulk sensitivity of a system is only a proxy for its performance due to the nature of the evanescent tail used in photonic sensing. The evanescent tail describes the overlap of the resonance mode with the analyte that forms the upper cladding of the waveguide. The tail of the electric field can be described in terms of the effective index of the mode (n_{eff}) and the index for the cover material (n_{cover}) [8,9]:

$$E(z) = E_0 e^{-zp} \quad p = \frac{2\pi}{\lambda} \sqrt{(n_{eff}^2 - n_{cover}^2)}$$

Here the decay constant (p) and electric field ($E(z)$) are in the z direction as this is above the structure, transverse to the propagation direction of the mode, with E_0 being the initial and maximum field intensity. It is clear to see that the decay length is related to the contrast between the indices of the cover and the resonance mode. Since the sensitivity of the system is directly related to the overlap of the field with the analyte [10], a disconnect emerges between bulk sensitivity and biological sensitivity.

Typically, photonic systems such as the GMR and the surface plasmon resonance (SPR) have evanescent tails of a few hundred nanometres [8]. In contrast, common proteins such as IgG are only 10-15 nm in their longest dimension [11]. This means that target analytes will not fully overlap with the evanescent tail in the same way as a bulk solution will. These factors, in addition to the biochemical factors previously discussed, make a FOM that is applicable across all biosensors and all analytes difficult to define. It is therefore important to consider the LODs in terms of the FOM relating to Q-factor and bulk sensitivity ($S \times Q$) as well as considering the surface sensitivity for specific target analytes.

1.3. Comparison between GMR sensors and other sensing modalities

1.3.i. GMR - a historical perspective

The guided mode resonance phenomenon has roots in the Woods anomalies described in 1902 [12], where Wood observed that there were drops in intensity from incident light diffracted from ruled gratings. Five years later it was explained by Rayleigh that the anomaly occurred when the light is scattered at 90° to the grating surface [13]. Later in the 1990s Magnusson developed the discovery further by creating a grating using highly refractive material to support a guided mode for the light that is coupled tangentially to the surface [14]. Thus was born the term "Guided Mode Resonance (GMR)". A more in-depth look at GMRs is detailed in chapter 2. The key feature of GMRs are their wavelength specific reflection and the ability to couple into them at normal incidence.

Since 1990 there has been much development in the use of GMRs for applications such as transmission bandpass filters [15] and, more pertinent to our discussion, for biosensing [8,16-18]. There are some clear advantages to using GMR such as the ease of light in-coupling. This however is often traded off against lower Q-factor compared to other sensor modalities, so it is very instructive to tension the GMR against competing approaches. The most obvious of the competitors are; the widely considered "gold standard" of label-free biosensing, namely SPR commercialised by Biacore (now GE®), the Microring Resonator, commercialized by Genalyte®, and the Bimodal Waveguide Interferometric biosensor, pioneered by Lechuga's group at ICN2, Barcelona.

1.3.ii. Surface plasmon resonance

Surface plasmon resonance (SPR) biosensors were developed in the 1980's as one of the first embodiments of optical biosensors [19]. Like GMR, they use out-of-plane excitation, which makes it relatively easy to couple to. The mode that is used for transduction is a surface plasmon mode, however, which is based on a surface charge oscillation at a metal-dielectric interface. The surface plasmon can be understood as a travelling wave and as such, it is excited by k-vector matching at the interface; the incident light is directed through a prism or a high-index hemisphere, and by adjusting the angle, its propagation constant can be adjusted to match that of the plasmon mode, illustrated in Figure 2a. When the k-vectors do not match, the light from the prism does not couple into the plasmon and the light is reflected. When the angle varies and they do match, the light does couple and the plasmon is excited. Since the plasmon is a lossy mode, a lot of the light is dissipated before it couples back, so a characteristic dip is observed in reflection (Figure 2b). It is the travelling wave nature of the surface plasmon that gives it its exquisite sensitivity, because the smallest changes in effective index of the plasmon mode will lead to a resonance shift [20]. As a result, sensitivities of several 1000 nm/RIU have been reported [21].

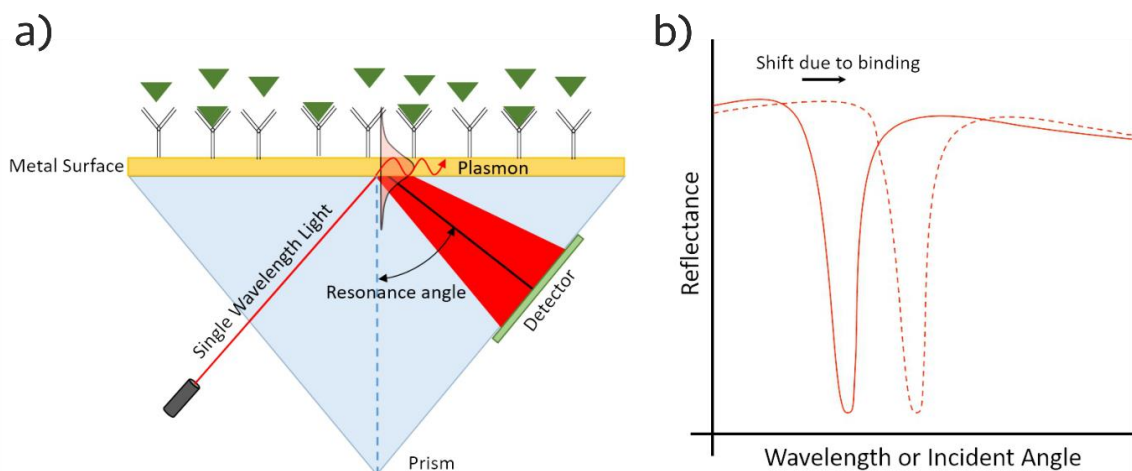


Figure 2: a) Operation principle of a surface plasmon resonant sensor and b) observation of the characteristic dip in reflectance spectrum upon coupling. Reprinted with permission from [8] © Elsevier.

Because of the lossy nature of the plasmon mode, SPR systems have very low Q-factors, i.e. of the order of $Q = 10-20$ which is the lowest of the sensing modalities I explore here. The low Q-factor is offset by the high sensitivity, previously mentioned, so the overall figure of merit $S \times Q \approx 10^4 - 10^5$ nm/RIU which is comparable to most bio-sensing platforms including the GMR. As a result, the typical implementation of SPR, such as in Biacore's SPR system, exhibits a limit of detection in the ng/mL range [22,23], making it useful for immunoassays, while it is not the most sensitive of all available biosensors.

1.3.iii. Nanohole arrays

Plasmonic nanohole arrays represent a hybrid between SPR and GMR, because they merge plasmon modes with periodic arrays. Nanohole arrays first came to the fore upon the observation of extraordinary optical transmission (EOT). EOT describes the phenomenon whereby light is observed to transmit through an array of sub-wavelength holes with a transmission that is much higher than expected from geometry alone. EOT is typically explained as a three-step process whereby light first couples to the surface plasmon at the metal interface, the plasmon then propagates through the holes and couples back to a free-space mode on the other side [24]. The conversion to plasmons explains how light can transmit through tiny holes that are well below any classical cut-off [25,26], which is why the effect is termed "extraordinary" optical transmission.

The recognition that nanohole arrays can be used for sensing came later with key demonstrations by Altug *et al.* who explored the resonance characteristics and relevant sensing applications [27]. The resonances they studied usually exhibit Q-factors of the order of $Q \approx 100$ when working with liquids [28] and sensitivities of up to 650 nm/RIU which yields a FOM of $S \times Q \approx 10^4$ - 10^5 nm/RIU, which is comparable albeit slightly higher than SPR and GMR structures. As a result, nanoholes have exhibited impressive detection limits down to 500 pg/mL for the real-time molecular binding of IgG and 145 pg/mL for VEGF [29].

These values demonstrate the strength of the nanohole array method as it combines the benefits of GMR with its ease of coupling with the sensitivity of SPR. The only downside is that the transmission is relatively low ($T \approx 10$ -20%) which results in weak signals. Since plasmonic nanoholes only work in transmission, it also means that the collection optics interferes with the fluidic access, i.e. detection electronics and fluidics are on the same side of the device. As stated previously, the fact that GMR and SPR can operate in reflection means that the optics and the electronics can be placed on one side of the device and the fluidics on the other, which is much more elegant for practical implementations.

As a counterpart to the plasmonic nanoholes is an array of nanoholes in dielectric material by Conteduca *et al.* [30]. This dielectric configuration operates as a 2D GMR and so can perform in reflection which is advantageous compared to the plasmonic variety. The work presented by Conteduca *et al.* demonstrated a $Q = 450$ and a bulk sensitivity of 140 nm/RIU yielding a FOM comparable to other implementations of GMR of $S \times Q = 6.3 \times 10^4$. While this FOM is in the region of other sensors the performance is seen more acutely with the demonstrated LOD of 1 pg/mL for IgG [30].

1.3.iv. Microrings

Microrings are guided-mode devices where light propagates in the form of a whispering gallery mode which is resonant when an integer number of wavelengths fit into the circumference of the ring. The mode is strongly confined to the waveguide (Figure 3) and is a proper long-lived guided mode (unlike the leaky mode of the GMR or the very lossy mode of the SPR), so very high Q-factors can be achieved. In fact, Q-factors into the $Q \approx 10^8$ - 10^9 have been achieved with microdisk resonators [31] but these are not typically used for sensing as the Q-factors are impractically high; as explored by Hu *et al.* [32], Q-factors above 10^5 are not useful in this context because the wavelength noise of typical lasers then limits the accuracy of determining the resonance. In terms of sensitivity, microrings tend to be worse than the other modalities, because the same strong confinement to the waveguide that is needed for the high Q-factor tends to limit the overlap of the mode with the analyte, such that sensitivities of $S \approx 50$ - 80 nm/RIU are typically being achieved [33,34]. Nevertheless, due to the high Q-factor, the overall figure of merit tends to be quite high, i.e. $S \times Q \approx 10^5$ - 10^6 nm/RIU, which is higher than the other modalities explored so far.

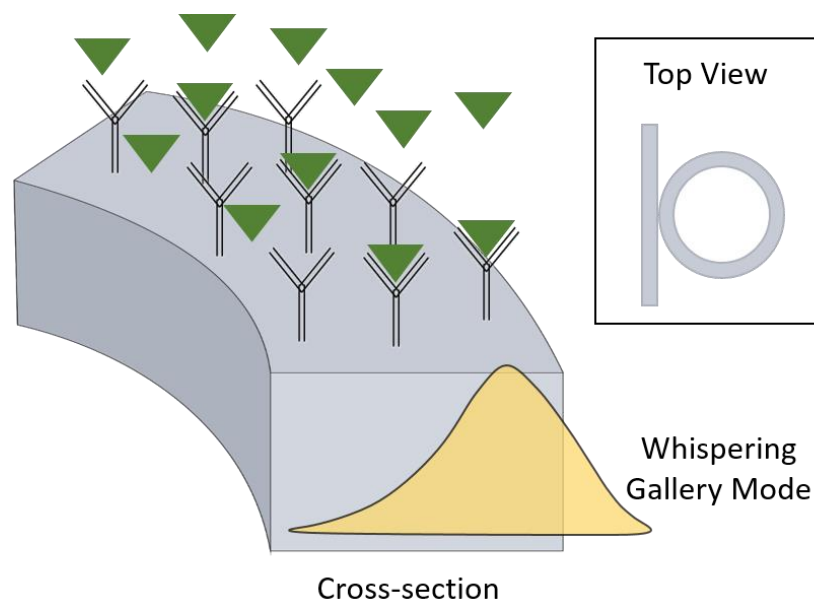


Figure 3: Operation principle of microring resonator sensor with the top view also showing the access waveguide. Reprinted with permission from [8] © Elsevier.

1.3.v. Bimodal waveguide

Bimodal waveguides represent the class of interferometric waveguide sensors. Bimodal waveguides obtain the sensing information by interfering two modes that co-exist in the same waveguide. The advantage of this approach is the “common-path” nature of the interferometer, which ensures high stability due to the fact that the signal and the reference experience exactly the same external influences. This feature is in contrast

to the more commonly employed Mach-Zehnder geometry whereby the signal and the reference experience different paths, so any noise source that is specific to one path does not occur on the other so cannot be normalized out.

The principle of the bimodal interferometer is sketched in Figure 4. The device starts with a single mode input. The waveguide thickness is then changed at the mode splitter which serves to excite the first order mode. The two modes then propagate with different propagation constants and have a different overlap with the analyte, so they experience a different phase delay on interaction. At the output, the two modes are made to interfere and the interference pattern represents a direct measure for the relative phase change between the two modes [35]. Bi-modal waveguides are an elegant solution because they are less complex than conventional interferometers and they have demonstrated detection limits of 2.5×10^{-7} RIU [36]. Bi-modal waveguides have thus achieved a limit of detection of 10 pg/mL of human growth hormone (hGH) [37]. A brief note, while this could be compared to the 1 pg/mL result of the nanohole arrays, hGH is $\sim 6 \times$ smaller in terms of mass than IgG which makes a direct comparison difficult. Nevertheless, this performance is an impressive feat.

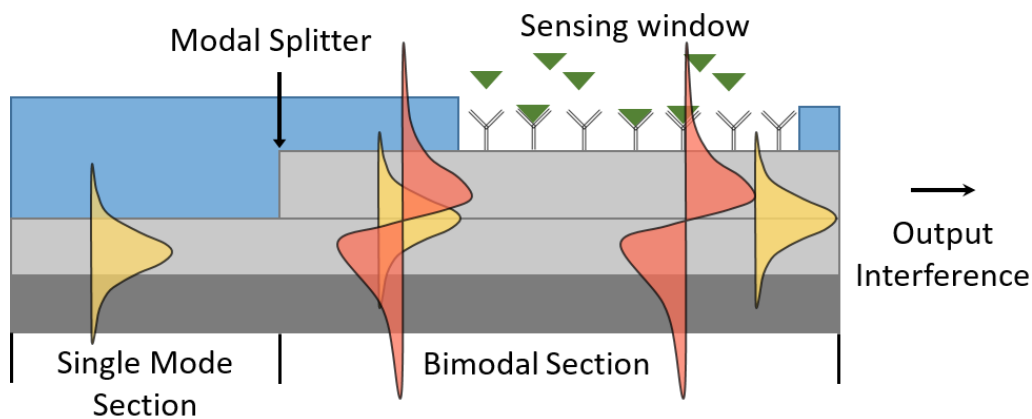


Figure 4: Operation principle of a bimodal waveguide sensor. Reprinted with permission from [8] © Elsevier.

1.3.vi. Comparison summary

The various forms of optical biosensor all have benefits and drawbacks, each taking advantage of the modal properties of light. By considering the various modalities, it becomes clear that a higher Q value tends to dominate the $S \times Q$ figure of merit, however due to biological considerations, this does not always lead to a low LOD in terms of bio-particle detection. A high Q tends also to reduce the sensitivity, although this reduction is small compared to the gain in Q-factor.

Table 1: Comparison of different sensing modalities. The relative similarity in performance is quite striking, although the microring and bimodal waveguide clearly have the advantage.

Structure	Analyte	Q-factor	Bulk Sensitivity (nm/RIU)	FOM $S \times Q$ (nm/RIU)	LOD
SPR (Biacore) [22]	CEA antigen	~20	~10 ³	~2x10 ⁴	3 ng mL ⁻¹
GMR [38]	Different Solutions	~85	510	4.3x10 ⁴	-
GMR [39]	Streptavidin	~150	88	1.3x10 ⁴	1 ng mL ⁻¹
Micro Rings [40,41] ^a	MCP-1	2x10 ⁴	65 [33] ^b	1.3x10 ⁶	0.5 pg mL ⁻¹
Bi-modal Waveguide [36]	HCL Solutions	-	6x10 ² πrad/RIU	-	2.5x10 ⁻⁷ RIU
Bi-modal Waveguide [37]	hGH	-	6x10 ² πrad/RIU ^c	-	10 pg mL ⁻¹
Nanobeam Cavity [42]	CEA antigen	1x10 ⁴	~70	~7x10 ⁵	0.1 pg mL ⁻¹
Plasmonic nanohole Array [29]	IgG	<100	700	~7x10 ⁴	145 pg mL ⁻¹
Dilectric nanohole Array (2D GMR) [30]	IgG	450	140	6.3x10 ⁴	1 pg mL ⁻¹

^a Multiple references used as specific details on Genalyte Maverick™ systems are difficult to find.

^b Sensitivity used as approximate to determine the FOM.

^c Assumed to be the same as other work(s) from the same research group due to the same structure being used.

1.4. Economic considerations

In the literature, photonic biosensors are often compared only in terms of raw performance. Considerations of the cost of implementation is rarely mentioned or only considered once a technology is ready to spin out. While it is clear that research institutions like universities encourage spin out companies due to the utilisation of intellectual property, there is a disparity between research output and technology reaching the market.

Here I will briefly cover some concepts that are worth considering in device development.

1.4.i. The valley of death and technological lock-in

In 2013 the UK government released a report aimed to highlight the issues of translating technology from research to industry, i.e. bridging the valley of death [43]. The valley of death pertains to the lack of resources either from research funding or industry to develop technology. This gap is illustrated in Figure 5. One reported issue is that researchers do not consider or do not understand needs that are only relevant to industry and commercialisation [44]. While such understanding will clearly have an impact on the ability to translate technology the main issue is the lack of capital needed to fund translation, which was also identified in the 2013 report [43]. While there is some small resource overlap which supplies the trickle of technology from academia to the market, there are clearly issues on both sides. Industry is not willing to take risks on technology that is only reported to work in a handful of publications, in contrast academia loses interest when trying to develop technology as the perceived novelty decreases.

Beyond the barrier of funding is the issue of technological lock-in [45]. Technological lock-in describes the fact that the market tends towards a standard technological solution and so generates hurdles for innovations that deviate from this standard. Many new technologies do have clear advantages but struggle to compete with the maturity of current technology. One way around this is to create a loss leader where the product makes a loss until the economies of scale arise but this requires heavy initial investment and a willing company. A solution is to find a niche market where either the advantages outweigh the cost or there is an unmet need for the current attributes of the technology [46].

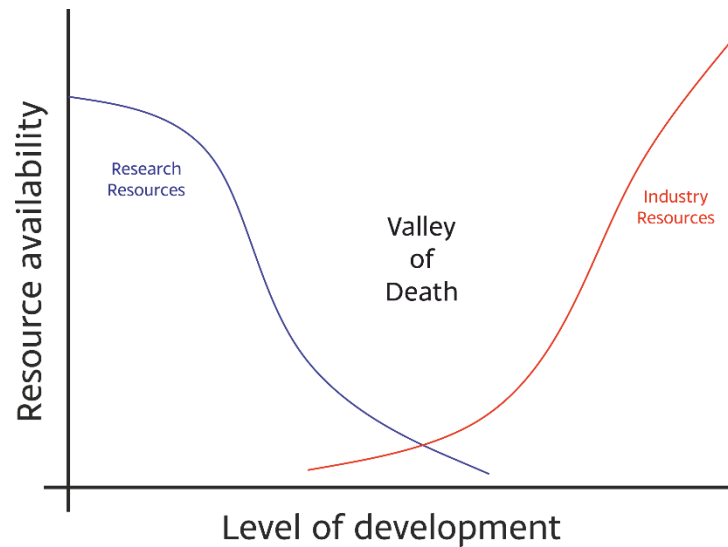


Figure 5: A representation of the valley of death where there is a lack of resources available to develop technology.

A final approach, utilised in this work, is to exploit already available technology. For example, using off-the-shelf components or established manufacturing processes that already exist as a foundation for development. The advantage of this approach is that it is applicable to both industry and research, although it may lead to a lack of perceived novelty in academia. There is some funding from sources such as the Knowledge Transfer Partnership and Innovate UK which aim to address the gap between industry and academia thereby aiding in bridging the valley of death.

1.4.ii. Point-of-care testing

For biosensors and medical diagnostic technology, there are several other considerations needed before market entry [47]. Some hurdles to overcome are regulatory approval processes and the need to go beyond incremental technological improvements. For example, if a new test is invented that is 10% (being more than just a marginal improvement) more accurate than current tests but costs the same, it is unlikely to break ground in replacing the old technology. A better approach is to invent a new technology that can do something that was not possible before. For example, one can design technology to be used at the point-of-care (POC), e.g. the patient's bedside or in GP surgeries and pharmacies, which provides results that could previously only be obtained in a laboratory, thereby significantly reducing the time to result. For POC testing to be implemented, it therefore needs to be low-cost and rapid, but also as highly performing as the laboratory test it aims to replace. Figure 6 presents a simplified flow chart of how a health service like the NHS currently operates and how POC testing may simplify the timeline. An excellent example is continuous glucose sensors for diabetics. This has eliminated the need for very involved and time

consuming laboratory testing. The use of glucose sensors has surged in recent years as approaches like this improve health outcomes and lift pressure off resources within the healthcare system [48].

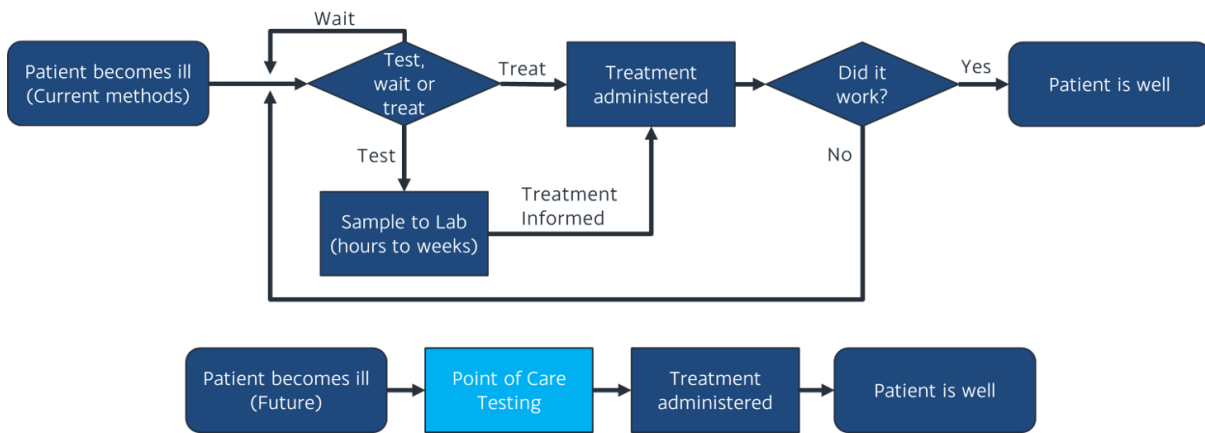


Figure 6: Flow diagram of traditional compared to point-of-care diagnostics.

Despite the perceived advantages of such diagnostic devices, there are several boundaries to health services like the NHS moving towards new approaches which have been laid out by the British In-vitro Diagnostics association [49]. These include, but are not limited to, the structure of health system funding and a lack of understanding of the benefits and implications of point-of-care diagnostics [50]. Despite the inertia of health systems to take up technology there is some adoption, albeit slowly, and so POC should be considered as an approach for developing new devices. By considering a point-of-care approach and the barriers described in Section 1.4.i, new technology can be realised and thereby increase technological innovation in healthcare [47].

Having now considered the motivations for my project and the key aspects involved in technology development, I will now discuss some theoretical background. This background will focus on the operation and underlying physics of the GMR modality.

2.Theory

Electromagnetic radiation is a fundamental part of the universe, with the cosmic background radiation indicating that it played an integral role in its development. The study of light has always been a key component of science, from the early practices of modern optics in ancient Greece all the way to Einstein's theory of relativity. Photonics, as a field, looks beyond utilising light as it is, such as using a telescope to observe the night sky, and aims to move towards controlling the flow of light in new and wonderful ways. A particular type of nanostructure termed "photonic crystal" is especially good at manipulating light. Photonic crystals are analogous to the crystal lattices of solid-state physics. Solid-state photonic crystal lattices have a similar effect on photons as solid state lattices have on electrons. In a photonic crystal, the electrons are replaced by electromagnetic waves and the atoms by modulation of the dielectric material on a wavelength-scale. Atomic lattices are described by the Schrödinger equation and photonic crystals are described by Maxwell's equations. The two theoretical frameworks are, in fact, quite similar and it can be observed that a photonic crystal can produce effects such as band gaps [51]. A simple embodiment of a structure that utilises a 'stop band' is a dielectric mirror which is made up of alternating high and low refractive index materials. By tuning the thickness of the layers to match the phase of the propagating light, constructive and destructive interference can be achieved, so the transmission or reflection can be tailored. Structures for controlling light have a wide variety of applications, for example the use of a dielectric stack in Fabry-Perot filters, vertical-cavity surface-emitting lasers (VCSELs) and more. The structures of most interest for this work are periodic one-dimensional gratings.

2.1. Describing light

2.1.i. Maxwell's equations

Light, when considered as a propagating plane wave, consists of an oscillating electric (E) and magnetic (B) field. Both the electric and magnetic components are in phase and are perpendicular to each other and also to the direction of travel. The direction of travel for the wave is described by the wave vector k .

The full description of the propagation of light is contained in Maxwell's equations [52]:

$$\begin{aligned}\nabla \cdot B &= 0 & \nabla \times E &= -\frac{\delta B}{\delta t} \\ \nabla \cdot E &= \frac{\rho}{\epsilon_0} & \nabla \times B &= \mu_0 J - \mu_0 \epsilon_0 \frac{\delta E}{\delta t}\end{aligned}$$

where ρ and J are the charge and current densities, μ_0 and ϵ_0 are the permeability and permittivity of vacuum, respectively. A full treatment is laid out by Joannopoulos *et al.* [51]. For the description of light propagation in a dielectric structure, we typically make the following assumptions to simplify the treatment [51] as follows:

- There are no sources of light in the structure and it is free from charges or currents, so $\rho = 0$ and $J = 0$.
- The field strengths are small enough such that we can neglect non-linear effects that arise from the constitutive relationships of D (displacement field) to E and H (magnetic induction field) to B . ($D_r = \epsilon_0 \epsilon_r E_r$ and $H_r = \mu_0 \mu_r B_r$)
- The materials are macroscopic and isotropic.
- The permeability of all materials is assumed to be μ_0 , i.e. $\mu_r = 1$ (they are non-magnetic).
- As the wavelength ranges considered are small, the material dispersion (i.e. frequency dependence of ϵ_r) is discounted.
- In the wavelength ranges considered, the materials are taken to be fully transparent as absorption is sufficiently small (i.e. the relative permittivity is purely real and positive).

With these assumptions the equations above reduce to the following:

$$\begin{aligned}\nabla \cdot B &= 0 & \nabla \times E &= -\frac{\delta B}{\delta t} \\ \nabla \cdot E &= 0 & \nabla \times B &= -\mu_0 \epsilon_0 \frac{\delta E}{\delta t}\end{aligned}$$

The two curl equations are of key interest; they present as a coupled first order pair of differential equations, which can be decoupled by taking the curl of both sides and substituting accordingly, arriving at [53]:

$$\nabla^2 E = \mu_0 \epsilon_0 \frac{\delta^2 E}{\delta t^2} \quad \nabla^2 B = \mu_0 \epsilon_0 \frac{\delta^2 B}{\delta t^2}$$

These equations now describe the propagation of a wave. Assuming that the wave propagates in a vacuum ($\epsilon_r = 1$ and $\mu_r = 1$), the speed of propagation of the wave is given by:

$$c = \frac{1}{\sqrt{\mu_0 \epsilon_0}}$$

which we know as approximately $3 \times 10^8 \text{ ms}^{-1}$. As we are concerned with the speed of light in a material, the relative permittivity and permeability needs to be accounted for. This can be achieved by using the refractive index as a scaling factor:

$$n = \sqrt{\frac{\mu \epsilon}{\mu_0 \epsilon_0}}$$

Using this expression, the speed of light in a material is now given as c/n ; as already mentioned, the materials considered here have a $\mu_r \approx 1$, which leads to $n = \sqrt{\epsilon_r}$.

If we take the second order differentials and only look at the electric field (because this is the only field we can manipulate) and consider the electric field in one direction only, we can write the decoupled equations as follows:

$$\frac{\delta^2 E_y}{\delta x^2} = \mu_0 \epsilon_0 \frac{\delta^2 E_y}{\delta t^2}$$

A straightforward solution to this equation is harmonic,

$$E_y = E_0 e^{i(kx - \omega t)}$$

which describes a wave propagating with a velocity $c = k\omega = f\lambda$. Expressed more generally, the electric and magnetic fields can be written as follows:

$$E(r, t) = E(r) e^{-i\omega t} \quad B(r, t) = B(r) e^{-i\omega t}$$

These equations now give a way to represent the 'modes' we see in a structure with a spatial profile (e.g. $E(r)$ multiplied by the complex angular frequency). Here the spatial profile depends on the distribution of the permittivity in the material or structure. By combining Maxwell's equations under the assumptions stated previously, a master equation can be produced [51]:

$$\nabla \times \left(\frac{1}{\epsilon_r} \nabla \times B(r) \right) = \left(\frac{\omega}{c} \right)^2 B(r)$$

where this equation can be treated as an eigenvalue function for which the spatial profiles ($B(r)$) are operated on by $\left(\nabla \times \left[\frac{1}{\epsilon_r} \nabla \times \right] \right)$ [51]. The modes or eigenvalues of the

system $\left(\left[\frac{\omega}{c}\right]^2\right)$ described in this way are determined by the frequencies, often denoted as angular frequency (ω). The master equation is in the form of the magnetic field because of the convenience of its form, however the electric field can be recovered as both the electric and magnetic fields are linked [51].

2.2. Periodic structures

2.2.i. General periodic structures

When dealing with structures of periodic refractive index, we can make use of Bloch's theorem, which describes the modes as propagating waves operated on by a function $u_k(r)$ (by definition, u_k has the same periodicity in k-space as the structure) [54]. This gives us an equation of the form:

$$E_k(r) = u_k(r)e^{i(k \cdot r)}$$

If we modulate epsilon, and thus u_k , in terms of a grating vector $G = 2\pi/a$ with period a , the description of the modes takes the form,

$$E_k(r) = \sum_{m=-\infty}^{\infty} E_m e^{i(k+mG) \cdot r} \quad \text{where } m \text{ is an integer}$$

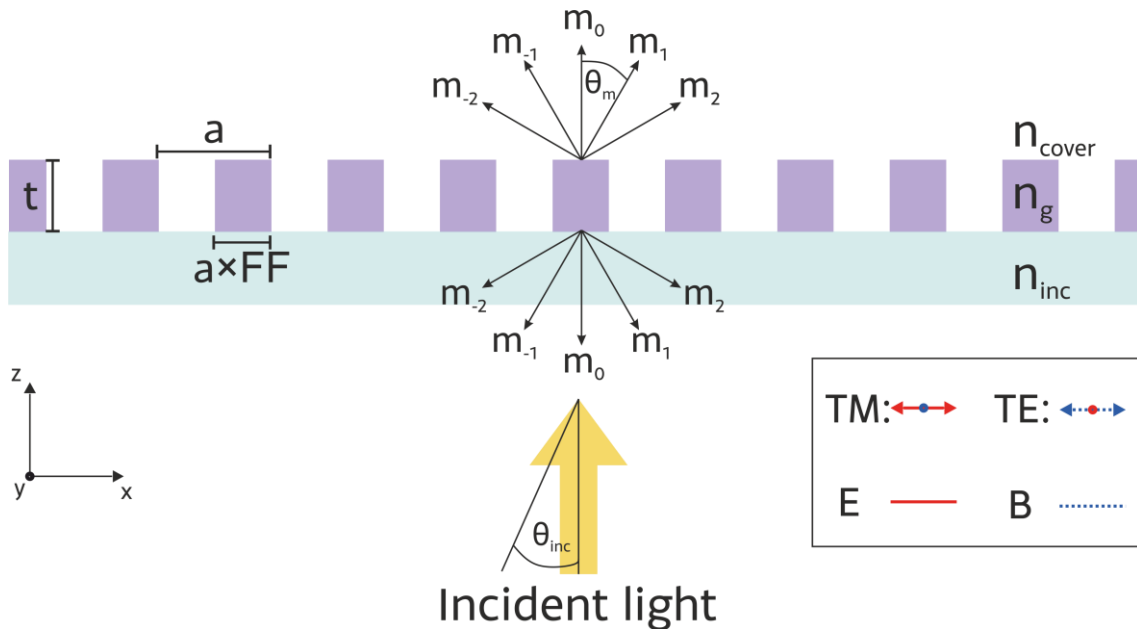


Figure 7: Diffraction orders occurring from a basic periodic grating of refractive index n_g with polarisation notation used in this work. TE is when the electric field is parallel to the grating lines, while TM has the magnetic field parallel to the grating lines. The grating parameter's period a , thickness t and filling fraction FF are labelled.

This describes the conditions for the diffraction orders that the incident wave splits into when incident on a periodic structure. The response of a plane wave diffracted by a periodic structure is illustrated in Figure 7.

The wave vector k describes the propagation of the wave and due to the boundary conditions imposed by the field and the conservation of momentum, we can treat the grating vector as a phase matching condition for the periodicity (here only given in the x-direction).

$$k_{x,m} = k_{x,inc} - mG \quad \text{where } m \text{ is an integer}$$

Here, m denotes the diffraction orders, which are described by integer multiples of the grating vector $G = 2\pi/a$. By further substituting $k_{x,inc} = n_{inc} \frac{2\pi}{\lambda_0} \sin(\theta_{inc})$ and $k_{x,m} = n_{eff} \frac{2\pi}{\lambda_0} \sin(\theta_m)$, we arrive at the familiar grating equation.

$$n_{eff} \sin(\theta_m) = n_{inc} \sin(\theta_{inc}) - \frac{m\lambda_0}{a}$$

$$\sin(\theta_m) = \frac{n_{inc}}{n_{eff}} \sin(\theta_{inc}) - \frac{m\lambda_0}{n_{eff}a}$$

θ_m is the diffraction angle of the m^{th} order mode and θ_{inc} is the incident angle and λ_0 is the wavelength of the resonance. In the same way that the speed of light is affected by the refractive index of the material, the wavelength of the diffracted modes is described by $\frac{\lambda_0}{n_{eff}}$. In this context n_{eff} is the electric field weighted average of the refractive index 'seen' by the mode in the grating. As seen in section 2.2.iv, tuning the parameters of the grating equation gives us a way to utilise our grating in interesting ways and to tune the wavelength of this mode.

2.2.ii. Guided mode resonance

When considering the types of structures used in this work, a useful tool has been the "S4" software. The S4 tool box is an implementation of the rigorous coupled wave analysis (RCWA) method by Moharam and Gaylord [55] which has been compiled by researchers at Stanford [56]. I have employed S4 to study relevant parameters and to design my structures. All photonic structures described in this thesis were simulated using the S4 toolbox.

Depending on the size of the structure relative to the wavelength of light, we observe different regimes. Figure 8 plots the reflectivity of a 1D periodic structure made of silicon nitride (Si_3N_4 $n = 2$) at normal incidence for varying thickness and wavelength. Both axes are normalised to the grating period and we see three distinct responses

which are marked out. Also present in Figure 8 are schematics providing a representation of how the light responds to the grating structure. Each schematic describes a different regime, depending on the ratio between the incident wavelength and the grating period (λ_0/a).

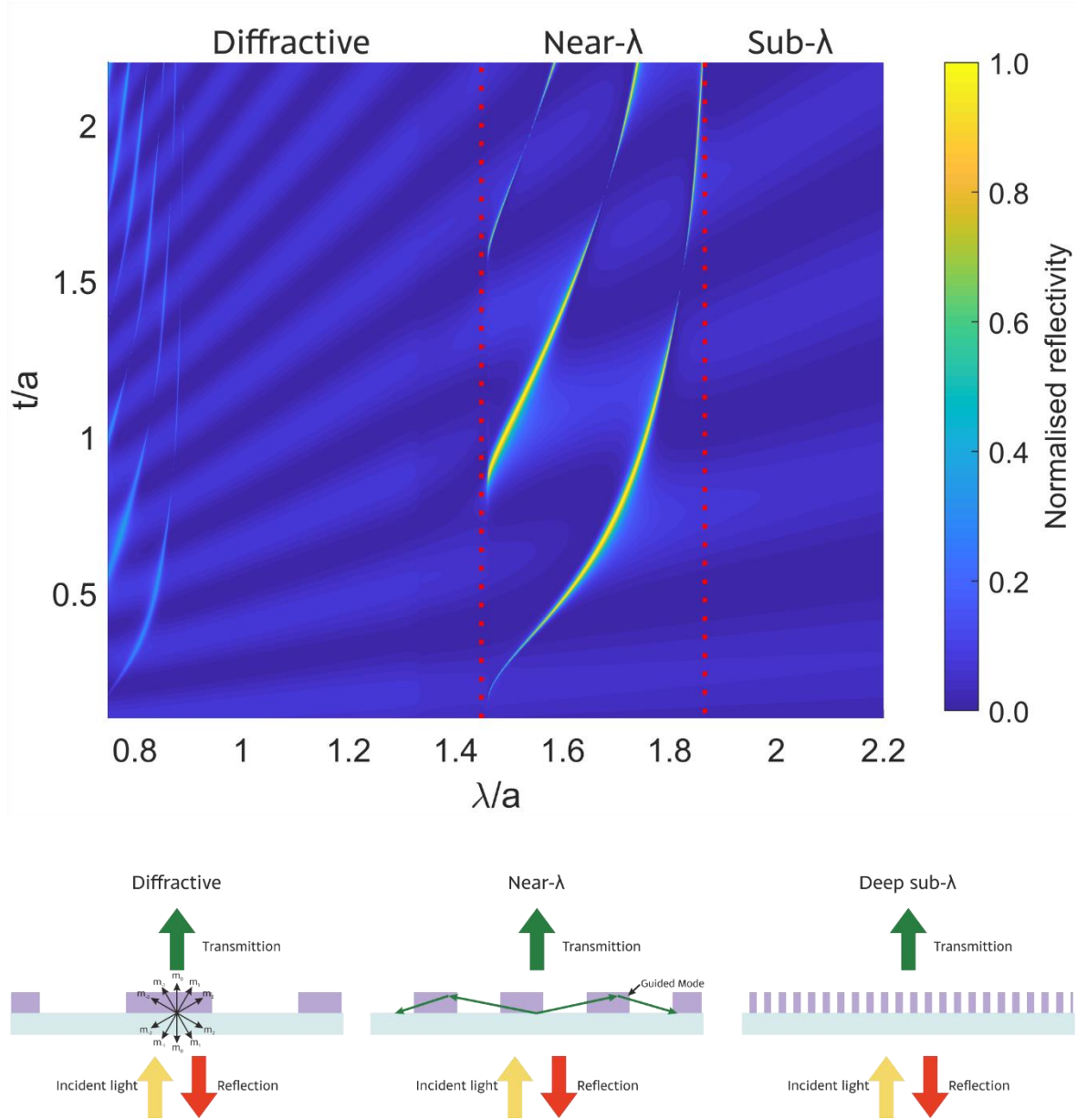


Figure 8: Reflectivity response of thickness vs wavelength for a grating structure with parameters $a = 439 \text{ nm}$, $n_{inc} = 1.45$, $n_g = 2$, $n_{cover} = 1.33$ and $FF = 0.7$ illuminated by TM polarised light. The schematics illustrate the interactions with incident light for the different regimes of the plot.

The three regimes are as follows:

Diffractive ($\frac{\lambda_0}{a} \lesssim 1.4$): The grating is purely diffractive and generates modes at different angles, seen as the faint lines at 0.8, bounded by the constraints of the grating equation. The Fabry-Perot response of the thin film is seen to modulate the response.

Near- λ ($1.4 \lesssim \frac{\lambda_0}{a} \lesssim 1.8$): For the near wavelength regime, it can be seen that there are modes of high intensity. These are the guided mode resonances, which occur for the special case when the final term in the grating equation is unity, i.e. $\frac{\lambda_0}{n_{eff}a} = 1$. It is important to note that the n_{eff} is the key factor in satisfying the grating equation. Consider light incident normal to the grating ($\theta_{inc} = 0$) in this special situation. The grating equation then becomes:

$$\sin \theta_m = m$$

In this form, the solutions are limited to two modes, one of which is transmitted ($\theta_m = 0^\circ$ when $m = 0$) and the other diffracted into the grating layer ($\theta_m = 90^\circ$ when $m = \pm 1$). The mode that is coupled into the grating layer is guided by the high n_{eff} index layer [57].

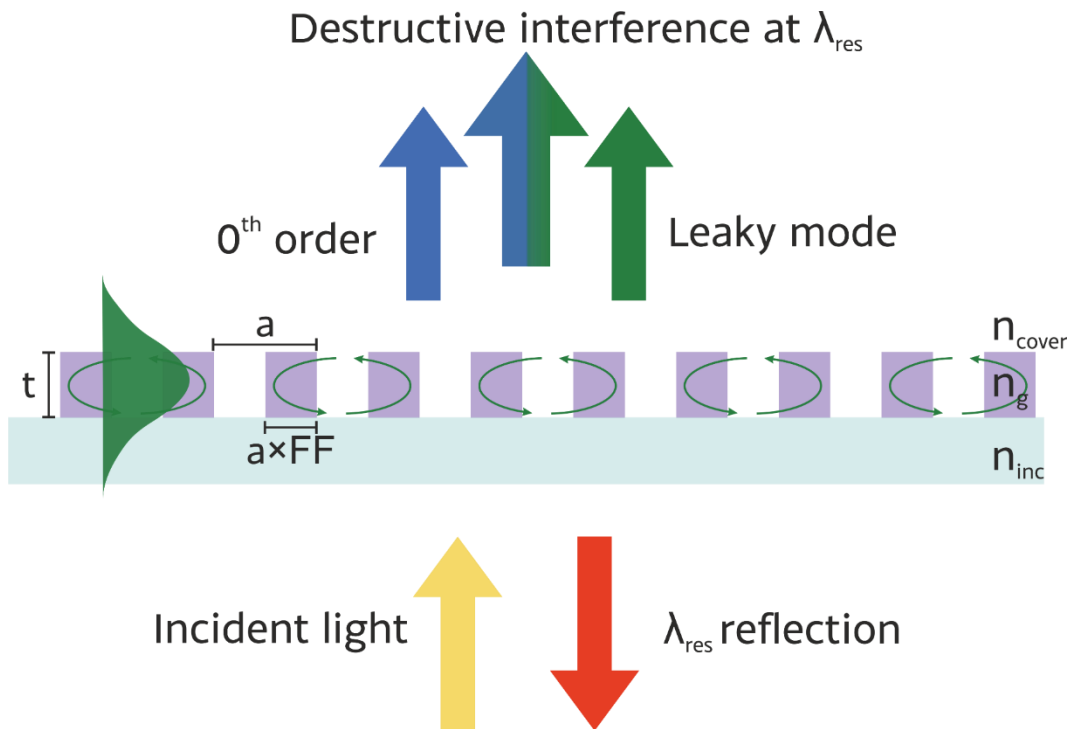


Figure 9: Light interaction with a periodic structure with period near- λ with light coupling into a guided mode in the grating layer and leaking out to produce a high reflection resonance.

Despite the mode being guided, the periodic nature of the grating layer causes scattering at each interface, which causes the mode to lose energy, hence the reason for referring to it as a quasi-guided or leaky mode. The leaked energy then interferes with the zero-order transmission and by fine-tuning the parameters, the phases of the quasi-guided and transmitted mode can destructively interfere. Due to this destructive interference, the energy of the reflected mode can achieve unity reflectivity at the resonant wavelength. A pictorial representation of this description is shown in

Figure 9, showing the leaky guided mode in green, with a representation of the evanescent tail discussed in section 1.2.iii that is utilised for sensing. It is this phenomenon which is called the Guided Mode Resonance (GMR) [14, 16,58–60].

Sub- λ ($1.8 \lesssim \frac{\lambda_0}{a}$): The final region to mention from Figure 8 is when the grating period is sufficiently small compared to the wavelength that the light does not ‘see’ the grating. In this case, light simply behaves as if it was incident on a thin film with refractive index n_{eff} between the cover index and the substrate index. The response of the light at each interface is described by the Fresnel equations regarding reflection and transmission.

2.2.iii. Polarisation and resonance properties

The resonance seen when the grating period approaches the wavelength of the waveguide mode is described by the Fano-function. The Fano-resonance line shape asymmetry is described as arising from the interference of the discrete resonance states with broadband states [7]. In practice, this means that the resonance is asymmetric due to the interference between the broad Fabry-Perot response of the thin film and the grating resonance. The equation that describes a Fano resonance is as follows:

$$f(x) = a \frac{(bc + [x - d])^2}{c^2 + (x - d)^2} + e$$

where a is the amplitude, b is the asymmetry factor of the resonance, c is half the linewidth, d is the resonance position and e is an offset coefficient.

The resonance in the structure has different properties depending on the polarisation of the incident light. We typically define the Transverse Magnetic (TM) mode as the mode that has the magnetic field oscillations aligned parallel to the grating lines (perpendicular to grating vector) and the Transverse Electric (TE) mode as the mode with electric field oscillations parallel to the grating lines (perpendicular to grating vector). This notation of TE and TM modes is equivalent to that used in Figure 7.

The first difference between TE and TM can be seen in the spectra and field plots of Figure 10 where the electric field is used to gain information of how the light sits in the structure [10]. The TM has a significantly higher Q-factor than the TE, which arises from the asymmetry (around $x = 0$) in the electric field profile. While the field intensities of the TM lobes are equal in terms of absolute intensity, the mirror symmetry of the lobes on each side of the grating ridges are of opposite sign. Therefore, the scattered components are equal and opposite, so cancel each other out,

leading to a higher Q-factor of the mode [61]. Conversely, the TE mode has a symmetric field profile (around $x = 0$) and so is more easily radiated away from the structure, hence possesses a broader resonance.

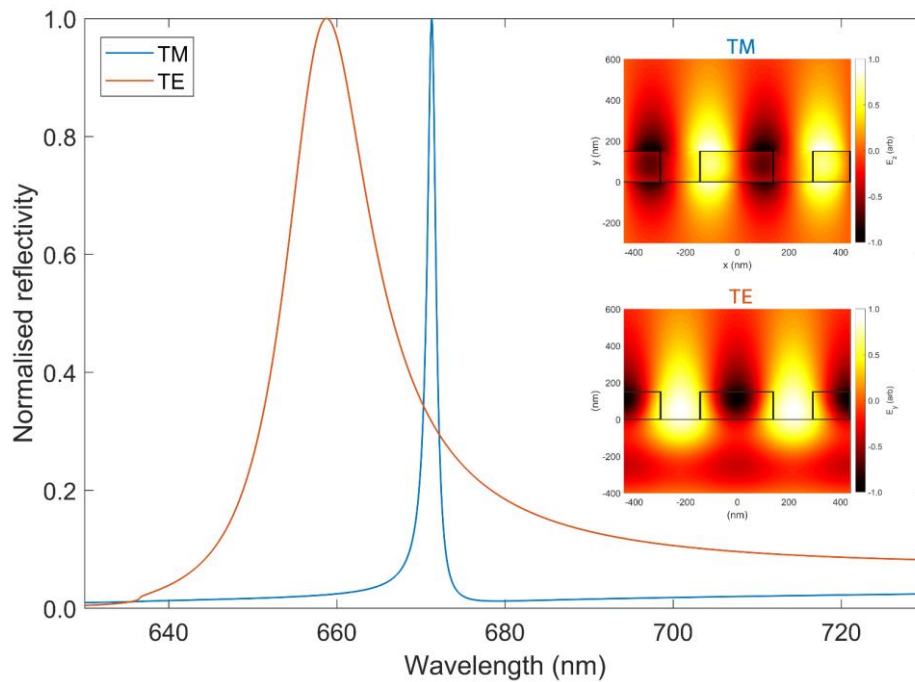


Figure 10: Spectra for both TE and TM polarised light incident on a structure where $a = 439$ nm, $t = 150$ nm, $n_{inc} = 1.45$, $n_g = 2$, $n_{cover} = 1.33$ and $FF = 0.7$. The inserts present S4 simulations of the electric field profile of the mode in the structure for each polarisation.

The second difference is the mode profile. For the TE mode, the predominant field intensity is in the grooves of the structure, while the TM mode has a stronger modal field on the surface. This leads to TM being more surface sensitive which is beneficial for the sensing application. As such, further sections focus on the TM mode due to its benefits regarding peak tracking (cf. chapter 5) and surface sensitivity (cf. section 1.2.iii).

2.2.iv. Grating parameters

When considering the guided mode resonance created by such a 1D grating, it is useful to consider how the different parameters of the structure affect the phase matching of the leaky and 0th order modes. Figure 11 presents a sweep across multiple parameters for TM polarisation. The design is a Si_3N_4 grating on a glass substrate ($t = 15$ nm, $a = 440$ nm, $FF = 0.7$) covered in H_2O . Individually, each of these parameters were swept against wavelength and plotted in terms of reflectivity, as these are all in the near- λ region of Figure 8.

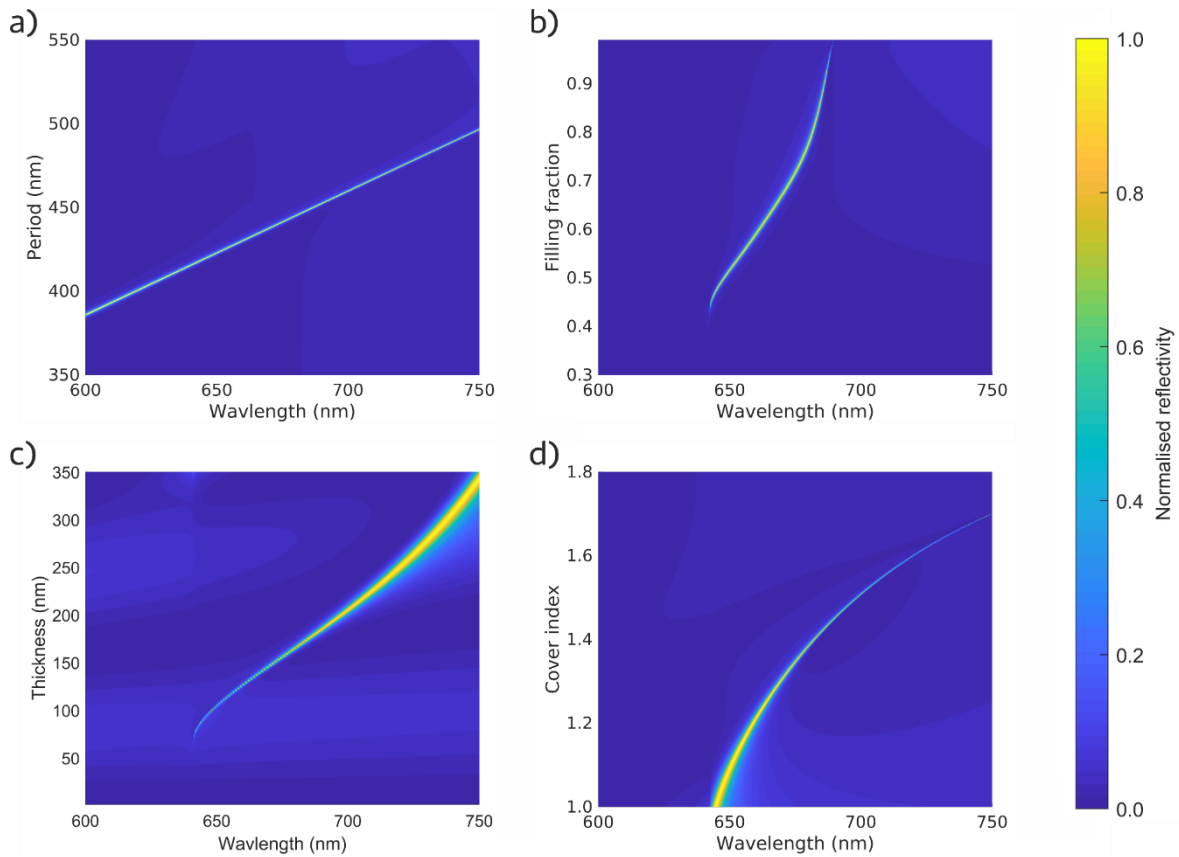


Figure 11: Reflectivity response against wavelength, for a) period a , b) filling fraction FF , c) thickness t , d) cover index n_{cover} . The baseline parameters are: $a = 439$ nm, $t = 150$ nm, $n_{inc} = 1.45$, $n_g = 2$, $n_{cover} = 1.33$ and $FF = 0.7$ illuminated by TM polarised light.

Period (Figure 11a): The relationship of period to wavelength is linear and therefore has the simplest relationship which makes sense if we consider the scalability of Maxwell's equations. When considering changing a structure to resonate at a new wavelength the first parameter to change should be the period as it is the easiest to predict.

Filling fraction and Thickness (Figure 11b and c): Both of these parameters follow the same trend of increasing the resonance wavelength as they increase. This is a result of the effective index of the mode increasing as the proportion of high index material increases in the waveguide layer. The filling fraction has an upper value, defined by the grating structure becoming a slab waveguide, and a lower value, limited by the effective index n_{eff} needed to support a GMR. The thickness has a similar lower limit but no upper limit. As thickness increases, the GMR will support multiple resonances as the waveguide becomes multimodal. This can be seen in Figure 8, as the structure grows in thickness value there are multiple wavelengths exhibiting high reflectivity.

Cover Index (Figure 11d): As the refractive index of the cover medium increases, the mode moves further into the cover, as the contrast of the waveguide layer and cover decreases. The eventual result is that the mode is not supported and will fully leak into the cover. This situation is analogous to an asymmetric waveguide with light not fully confined on all sides [57]. The resonance shape will vary with cover index as indicated by the narrowing of the reflectivity line in Figure 11d. For biological assays, the refractive index change is small enough that the resonance shift will appear linear and the change of resonance linewidth is of no concern.

2.2.v. Effect of incidence angle

One final parameter to consider is the angle of incidence. While I use normal incidence and have endeavoured to collimate the incoming light, in reality, the use of extended sources such as LEDs leads to a range of input angles. Accordingly, Figure 12 presents the resonance wavelength plotted against incident angle. The structure has the same parameters as those previously. I note that as the angle increases, the resonance wavelength also increases. As the incoming k vector moves off-normal while being imparted with the same momentum by the structure, the resonance condition is fulfilled for a longer wavelength.

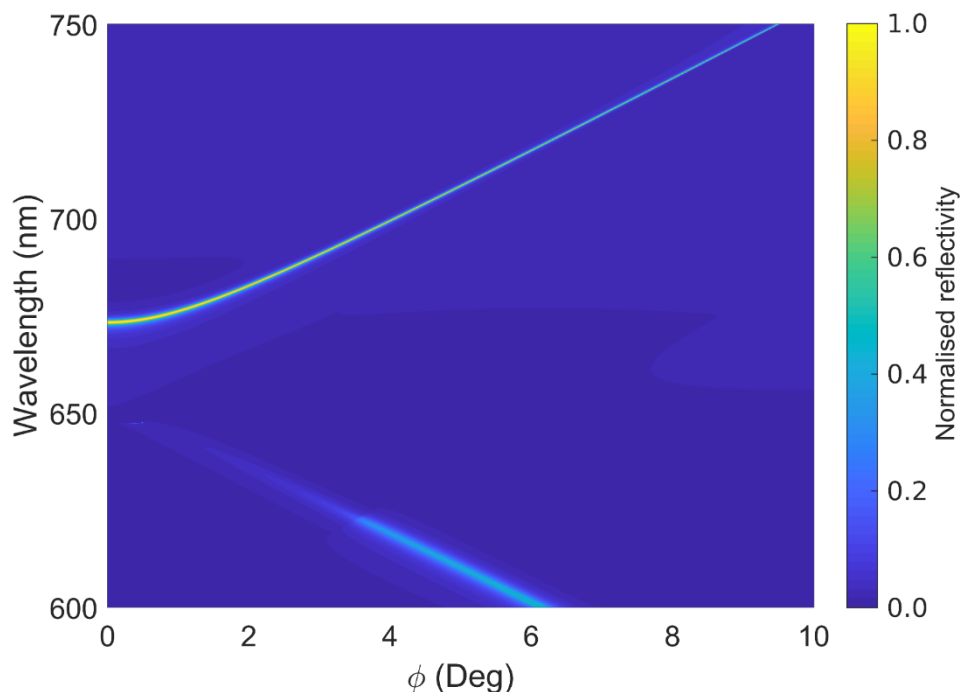


Figure 12: Reflectivity response against incident angle. Structure parameters were: $a = 439 \text{ nm}$, $n_{inc} = 1.45$, $n_g = 2$, $n_{cover} = 1.33$ and $FF = 0.7$ illuminated by TM polarised light.

When considering this angle-dependent response in terms of sub-optimal collimation, we can understand a range of input angles as the superposition of multiple resonance

conditions. On the other hand, as long as the angles are small ($<1^\circ$) the resonance wavelength does not change markedly. For example, assuming the numerical aperture of the collimating lens (0.725 for 12 mm focal length lenses cf. chapter 4) is greater than that of the source (~ 0.5 for LED used cf. chapter 4) the beam divergence after collimation can be approximated by the following relationship [62]:

$$\theta_{div} = \frac{D_s}{f_{col}}$$

where θ_{div} is the divergence angle in radians, D_s is the source diameter and f_{col} is the focal length of the collimating lens. The LED used in this work has an emission aperture of 80 μm and the collimating lens has a focal length of 12 mm which yields a divergence of 0.0067 Radians or 0.38° . As this is well below 1° the effect of the extended source should be negligible.

2.3. Chirped guided mode resonance

A fundamental part of my research has been working with chirped GMRs, a geometry first realised by Triggs *et al.* [63]. The chirp is used to translate the spectral response into a spatial response, which allows for a simple readout of the spectrum with a camera.

2.3.i. Spectral-spatial equivalence

Spectral-spatial equivalence is the process of mapping the spectral response of a GMR into the spatial domain as opposed to using a spectrometer readout. By considering Figure 11, I note that several parameters can be changed to implement a chirped response. All of these effectively vary n_{eff} along one dimension, hence each part of the grating exhibits a different resonant wavelength. If we then illuminate the structure with a monochromatic source, only the areas where the wavelength of the source matches the resonance of the source will reflect the signal back. As the cover index then changes, e.g. due to protein binding, the resonance condition for the entire structure will shift and thus will the position at which the resonance occurs, allowing detection to be accomplished with simply a camera.

While there are multiple ways to chirp the n_{eff} of the grating as shown in Figure 13, some of these are more straightforward to implement than others. For example, thickness and refractive index changes are rather difficult to produce reliably in practice. Therefore, the most straightforward approaches are the ones that can use

standard lithographic processes, such as fill-factor or period. Originally, Triggs *et al.* [63] varied the fill-factor by adjusting the exposure dose. Instead, I determined to use period chirping via a fanned structure as shown in Figure 13b).

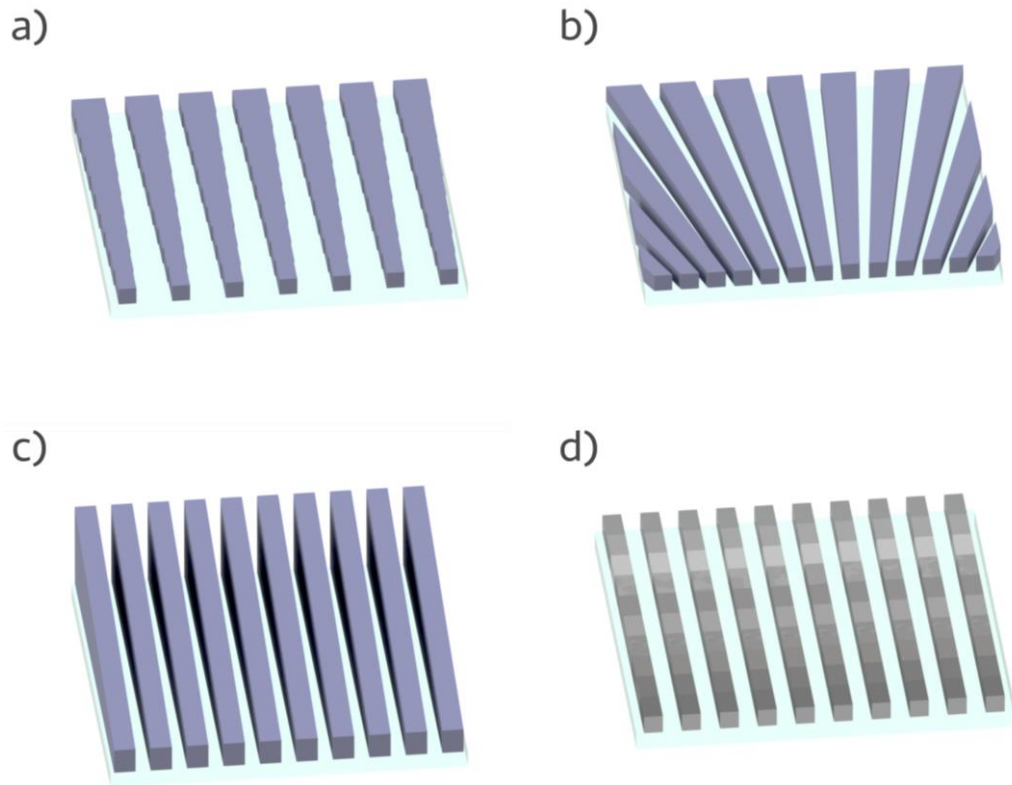


Figure 13: Four ways of chirping a GMR by varying a parameter to change the effective index across the grating through a) filling fraction, b) period, c) thickness and d) refractive index.

Period chirping has the advantage of controlling the spatial mapping in the design rather than lithographically which aids in fabrication consistency, An example setup used to measure such a chirped GMR is presented in chapter 4 with an example resonant image shown here in Figure 14a. By imaging the same structure with multiple monochromatic sources (i.e. by using a halogen and a monochromator) a composite image can be generated showing the resonance wavelength as a function of position (Figure 14b). Such images are called hyperspectral images.

Having now described how the GMR modality operates, the next chapter will discuss the methods used to fabricate the GMR sensors and compare the resulting structure with simulations. The discussion of the methods employed then leads into how the instrument is constructed to measure the fabricated structures and which components would be best employed. Several of the challenges faced are linked to the operation of a GMR such as its angular dependence as well as how the light source and resonance

linewidths interact. With this in mind the aspects discussed here are pivotal to the decisions made later in the optimisation of the instrument.

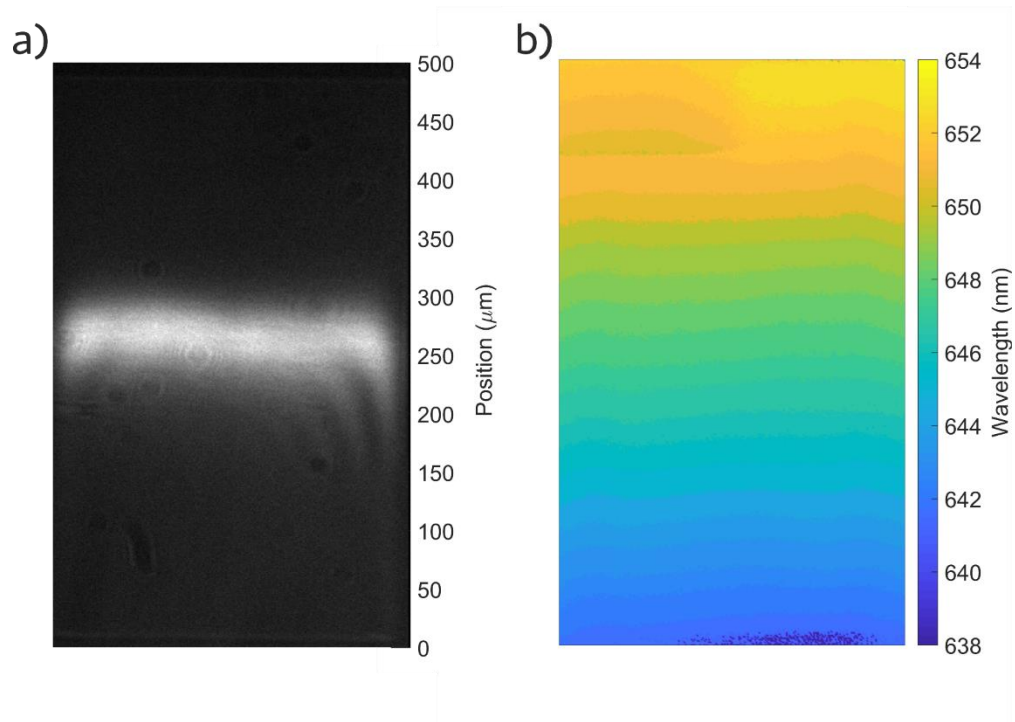


Figure 14: a) Image of a period chirped GMR illuminated by 647.5 nm wavelength light. b) a hyperspectral image of the wavelength response across the same GMR.

3. Methods

My research builds on two fabrication methods which together form the backbone of what I have achieved. The first is the fabrication of the GMR sensor itself; the other is the fabrication of the housing of the readout unit for the sensor. Both work together to create a complete instrument and both have had their challenges. The sensor fabrication has remained relatively constant throughout my research. The recipe used for fabricating GMRs in our group was first developed in 2013 and underpins the initial development of the chirped GMR concept [63]. The lithographic fabrication of the sensors was conducted in our ISO 6 class cleanroom, which the group operates in the Nanocentre at the University of York.

The main changes to the sensor fabrication I implemented relate to standardisation and reproducibility, as well as to changing to shorter wavelength operation. Standardisation and reproducibility were desired to show consistency as this is a crucial aspect for commercialisation. With commercialisation in mind, additive manufacturing ("3D Printing") was chosen for developing the device housing. The benefits of additive manufacturing are its ability to quickly prototype complex and bespoke parts at relatively low-cost. However while additive manufacturing allows for quick prototyping, it is not a scalable process. For the purposes of my research, this is not an issue, as the resolution is comparable to that achievable by injection moulding [64,65], which is commonly used in mass manufacturing.

Previously the group worked predominantly at near-infrared wavelengths around 850 nm. While this move to shorter wavelengths did not have any conceptual implications, as all the design rules scale, it did have some impact on the lithography techniques I used. Moving to 650 nm operation also allowed me to change to a resonant cavity LED lightsource, which offers several advantages as discussed in section 5.2.

3.1. General fabrication steps

3.1.i. *Choice of materials*

Silicon Nitride (Si_3N_4) is the primary material used by our group [59, 63,66] for making various biosensor chips. The material has several advantageous properties: it is sufficiently robust to be used in a point-of-care device, it is chemically inert [67,68] and biocompatible [69,70]. Silicon nitride's optical properties are also desirable given its high refractive index, which is approximately $n = 2.0$ at 650 nm [71]. It is also fully

transparent throughout the visible region. An alternative to silicon nitride is amorphous silicon, developed by other members of our group, which is produced using sputtering techniques. Its main advantage is its higher refractive index, approximately $n = 2.4 - 2.7$ in the visible and near-infrared [72]. However, the amorphous silicon has a slightly higher absorption at the 650 nm operational wavelength, which limits its utility. Additionally, the material was relatively new to the group and could not be deposited with the same reproducibility, hence I focussed on silicon nitride throughout this work. The Fabry-Perot response of each material shown in Figure 15 shows the higher index of amorphous silicon via its higher reflectivity at the peak wavelength. It is clear, however, that for de-ionised water (DI water), which has a similar refractive index as most biological material and buffers presented through this work, the reflectivity is near the minimum for 650 nm operation, which is advantageous for achieving high-Q-resonances. Naturally, the thickness can be adjusted to shift the minimum to the desired wavelength more accurately. Measurements in air are provided for comparison.

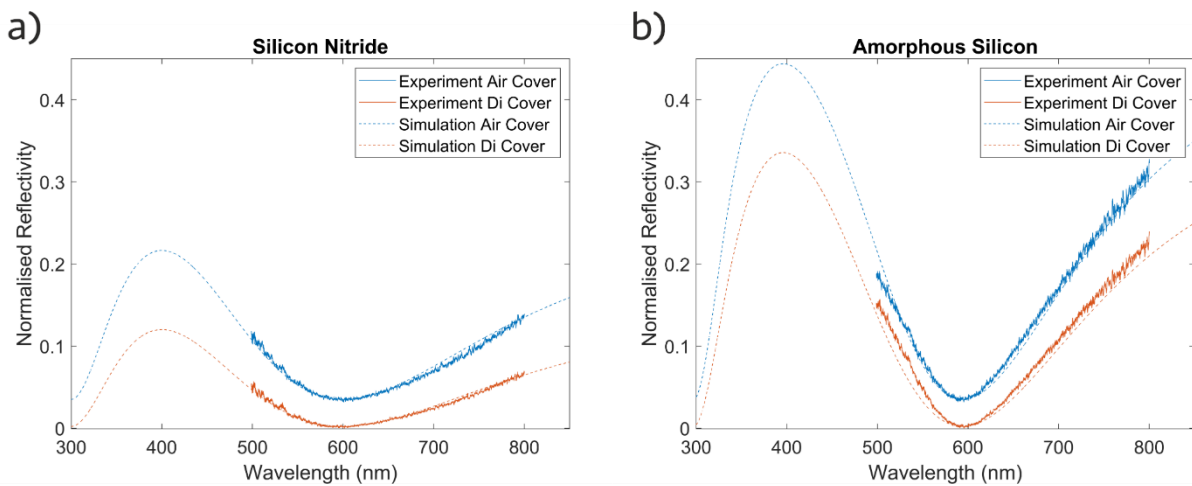


Figure 15: S4 simulations and Fresnel reflection corrected measurement of Fabry-Perot response. a) 150 nm thick layer of silicon nitride of refractive index $n = 2.0$. b) Approximately 110 nm thick layer of amorphous silicon of refractive index $n \approx 2.7$.

The silicon nitride purchased was from Silison (UK) which is deposited by PECVD (plasma-enhanced chemical vapour deposition). The silicon nitride is deposited onto 100 mm diameter, 525 μm thick borosilicate glass wafer and the silicon nitride layer is 150 nm thick.

3.1.ii. Sample preparation: dicing and cleaning

All of the steps laid out in sections 3.1.ii - 3.1.vi are presented in Figure 16 to show the general process flow post sample dicing. The steps laid out below were conducted in

a laminar flow hood where possible within the clean room providing an ISO 5 environment.

The wafers were diced into $15 \times 15 \text{ mm}^2$ squares using our Disco DAD320 dicing saw. While the size is somewhat arbitrary, it is relatively large compared to the $<1 \text{ mm}^2$ sensor size, mainly for handling and for the ability to apply a uniform resist coating.

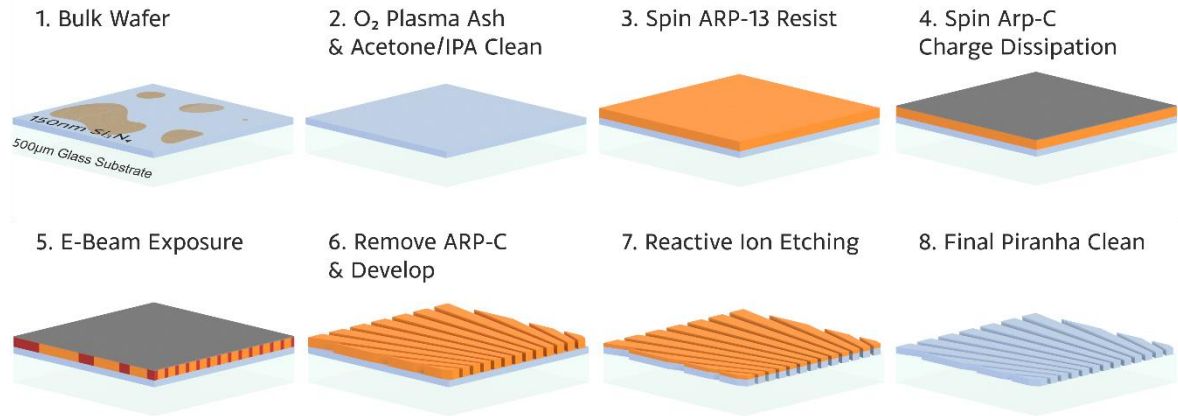


Figure 16: Key steps involved in patterning a silicon nitride sample using electron beam lithography described in sections 3.1.ii - 3.1.vi.

The samples are cleaned in a two-step process. The first step is to ash the sample in an oxygen plasma, which oxidises any unwanted material (e.g. organic material), on the silicon nitride surface. The asher used is a Hennikker plasma HTP-200 which produces a low-pressure plasma at kHz frequencies, and the plasma it produces is oxygen (O_2) plasma at 0.4 mbar. The power is set to 100% (200 W) for cleaning and the oxygen flow rate was set to 5 SCCM. The plasma oxidises any organic material on the wafer surface, however it does not create much physical bombardment, so the silicon nitride is untouched. The by-products are CO_2 and H_2O which are volatile and pumped away, however there can be a residue left on the surface of the wafer, which is why the second cleaning step is required. The ashing process has the added benefit of making the silicon nitride surface more hydrophilic and so the resist wets the surface better, leading to a superior spin.

The second part is an acetone wash, where the ashed sample is placed in an ultrasonic bath for 5 minutes. The acetone is a sufficiently strong solvent to remove any residue that remains on the sample surface. As there are no structures on the sample at this point, the ultrasonic bath can be used at full power. The ultrasonic bath aids in the removal of substances on the surface as it agitates any residue or dust particles. The sample is then removed from the acetone and placed in isopropyl alcohol (propan-2-ol or IPA) and placed back in the ultrasonic bath for a further 3 minutes. The IPA is used to wash off the acetone, as despite acetone having a higher vapor pressure at room

temperature and thus evaporating more quickly, it can leave a residue. Finally, the samples are blown dry with nitrogen.

3.1.iii. Spin coating

The fabrication process uses a lithographic resist and a charge dissipation layer.

Lithographic resist: We use AR-P 6200.13 (ARP-13) [73] from ALLRESIST GmbH as the primary electron-beam lithography resist. This resist is positive (explained more in 3.1.iv) designed for high contrast for the production of integrated circuits. Samples are spun at 5000 rpm for 60 s, then baked at 180 °C for 5 minutes. These steps produce a thickness \approx 350 nm which is thicker than our intended etch depth of 150 nm because the resist erodes significantly during the dry etch process; we tend to use a minimum ratio of 1.5 of resist thickness vs. etch depth.

Charge Dissipation Layer: A charge dissipation layer is needed as the glass substrate is not conductive and the charge from the electron-beam lithography would build up on the surface and deflect the incident electrons. The dissipation layer is a spinnable resist, AR-PC 5091.02 (ARP-C) [74], also from ALLRESIST GmbH. ARP-C is preferable to a metal charge dissipation layer as it is water soluble which makes it easier to remove post-exposure. The sample is spun at 2000 rpm for 60 s and baked at 90 °C for 2 minutes.

3.1.iv. Electron-beam lithography.

Electron beam lithography (E-Beam Lithography) is a powerful tool that can reach higher resolutions than optical lithography (usually using wavelengths in the UV) techniques [75]. By exposing a resist to a beam of electrons, the energy imparted causes a change in the chemical properties of the resist. In the process used for my work, the electrons break down the polymer layer, which can then be washed away by a developer leaving the unexposed resist untouched. A resist that is washed away when exposed is called a positive resist.

The E-Beam Lithography system produces the pattern by steering the beam across the sample. The electrons are focused using electric or magnetic fields. The fields used are analogous to optical lenses in a traditional microscope, with a condenser and objective lens, producing a fine beam. Scanning coils then steer the beam to write the desired structures. The exposable area is limited, called the writefield, which in our case is 500 μm x 500 μm in size. The interferometrically controlled stage works in conjunction with the writefield to produce larger patterns by stitching multiple writefields together.

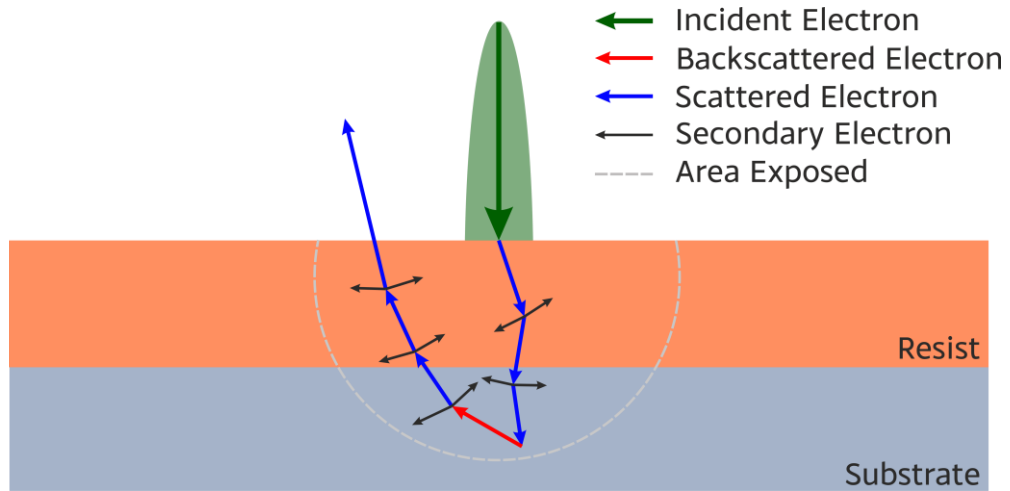


Figure 17: A schematic of electrons interacting with a resist on a substrate to illustrate the proximity effect.

Wave-particle duality allows us to exploit the wave properties of the electrons. Since the wavelength of electrons can be very small when accelerated by a high voltage, they can achieve much smaller wavelengths than photons in the visible or UV. The wavelength is given by the de Broglie relationship.

$$\lambda = \frac{hc}{pc}$$

$$pc = \sqrt{2 \times KE \times m_0 c^2}$$

where $hc = 1239.84 \text{ eV}\cdot\text{nm}$ and pc is expressed in electron volts. For our 50 kV system, we have a de Broglie wavelength of $\lambda \approx 5 \text{ pm}$. Usually, in an optical microscope, the resolution limit is of the same order of magnitude as the wavelength of light, assuming large numerical aperture lenses. The smallest resolvable distance is determined by the Rayleigh criterion [76]:

$$R = \frac{0.61 \times \lambda}{NA}$$

However, electron beam systems, such as those utilised for EBL or electron microscopy, generally have very low numerical apertures because the electron lenses have strong distortion effects that, unlike lenses in light optics, are very difficult to compensate for. The electron source also produces electrons that vary widely from the beam axis, making beam collimation difficult. To combat these effects, small apertures (10's of μm) and long focal lengths are used, which leads to a very small numerical aperture of typically $NA \approx 0.01$ and a minimum spot size of $\approx 1 \text{ nm}$, two orders of magnitude greater than the wavelength of the electrons used.

Despite the spot size of the electron beam being ≈ 1 nm, the smallest feature size that can be written is larger than that and is limited by the proximity effect [77–79], which depends on the acceleration voltage. The high acceleration voltage used to produce the short wavelength ensures that the electrons travel through the resist, rather than just exposing the top. The electrons travel fully through the resist and are backscattered from the substrate. The backscattered electrons and the secondary electrons they produce then interact with the resist as illustrated in Figure 17. The interaction volume of this process is what defines the minimum feature size of ≈ 10 nm.

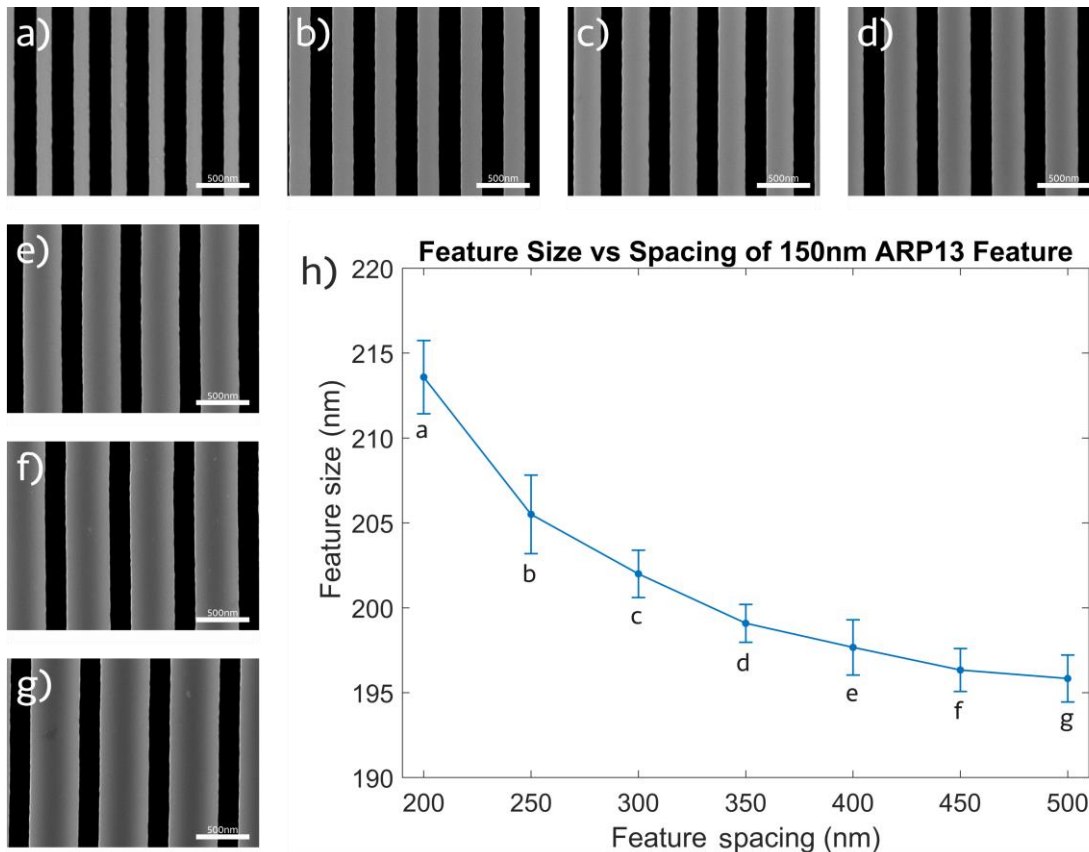


Figure 18: a-g) SEM micrographs of a 150 nm structure (black areas) with increased spacing, using a positive resist starting at 200 nm in steps of 50 nm. h) Plot of the actual size of 150 nm structures against the feature spacing.

The same proximity effect can also lead to the merging of features or a loss of definition. When fabricating a 1D GMR, the only relevant proximity effect is that the filling fraction of the structure may change, which can be compensated for in the design. The effect of this and general proximity dosing can be seen in Figure 18. Here, a pattern of 150 nm width is written and the spacing is increased in 50 nm steps to measure how the pattern size changes. As this is done using ARP-13, which is a positive resist, the patterned feature is the trench of the final structure. It is worth noting that from Figure 18h, the structure size appears to level off to a minimum of around 195 nm. This minimum size is given by the parameters of the exposure, development and

etch parameters and can be optimised. However, for my research, I am less concerned with matching experiment and simulation perfectly; instead, it is more important for me to generate a structure that can be repeated and that resonates at the correct wavelength.

Our electron beam lithography system is a Raith GmbH Voyager system, which has an electrostatic column used for steering the electrons. I typically used the low current mode with a 30 μm aperture and a focal length of 20 mm. This gave a current ≈ 130 pA and produces a typical exposure dose of 145 $\mu\text{C}/\text{cm}^2$, which was controlled by the dwell time, i.e. how long the shutter was open for. I typically used the smallest step size of the system, i.e. 0.5 nm. Using the parameters discussed above, the usual write time of a single 300 $\mu\text{m} \times 500 \mu\text{m}$ chirped GMR is approximately 9 minutes.

3.1.v. Sample development and reactive ion etching

Once exposed, the sample is developed, using Xylene at room temperature for 2 minutes, followed by washing in IPA and blow-drying with nitrogen.

The pattern is then transferred into the substrate using Reactive Ion Etching (RIE), also called dry etching. RIE is a plasma-based process where the sample is placed on a stage which is the driven electrode of a capacitor configuration with the process gas being fed in at low (\approx mBar) pressure. The system is driven at 13.56 MHz at a power of 10-100 W, which is sufficient to ionise the process gas. The ionisation of the gas provides free electrons which, being small, move with the electric field more easily than the heavier ions, which creates a negative DC bias on the stage and creates the net effect of accelerating the positively charged ions in the plasma towards the stage. The process is illustrated in Figure 19.

Dry etching is a balance between chemical and physical processes. The chemical process relies on reactive species that reach the sample by diffusion, so produce an isotropic etch. The physical etching process, in contrast, is driven by ionised particles accelerated by the Rf field, so they remove material through impact, which is highly directional and produces an anisotropic etch profile [80]. The physical process on its own is relatively slow and may produce roughness. By controlling the AC power and pressure, the two etch mechanisms can be balanced to produce both a high etch rate and smooth sidewalls [81].

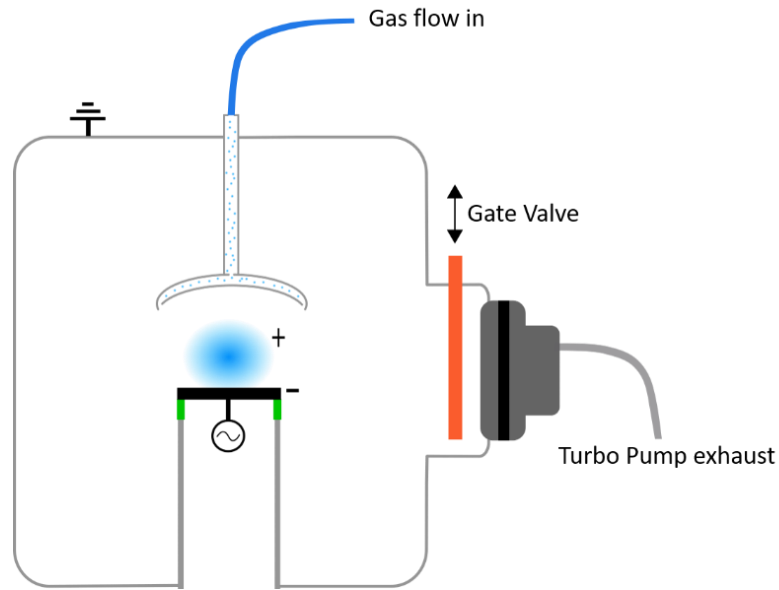


Figure 19: Schematic of the reactive ion etcher used to etch samples. The inflow gas is ionised by an alternating voltage applied to the stage. The stage develops a negative charge compared to the positively charged plasma, accelerating the positive ions towards the sample.

For the etching of silicon nitride, our group has developed a process using a mixture of CHF_3 at 58 SCCM and O_2 at 2 SCCM (29:1). The CHF_3 is the source of the F^+ ions that chemically etch the silicon nitride [82]. The small amount of O_2 is used to react with the remaining hydrocarbons and hydrofluorocarbons preventing recombination, which keeps the etchant molecule concentration high [83]. The pressure is kept at 0.18 mbar by using a gate valve between the main chamber and the turbo pump. The measured DC voltage is kept at -355 V (achieved with a power of approximately 45 W). The DC voltage is the important parameter as it drives the physical process while the gas flow/pressure controls the chemical process. All of these parameters combined lead to an etch rate of $\approx 21\text{-}22$ nm per minute. I typically used 7 minutes and 15 seconds for the 150 nm thick silicon nitride layer. The etch rate of the ARP13 is similar to that of silicon nitride which explains the use of a resist that is thicker than the desired etch depth.

The yield of the process is approximately 80-90% with the most common cause of error being drift in the e-beam system (between samples without realignment in the same exposure). When fabricated in a foundry setting, it is expected that yield would be higher as the pattern transfer is not as variable in nano-imprint lithography between samples compared with e-beam lithography (without constant re alignment).

3.1.vi. Sample finishing

As a final step, samples are cleaned by removing the remainder of the resist using 1165 Microposit Remove[®] and sonication for 15 minutes. The power of the sonic bath is

reduced to 50% to avoid damaging the etched nanostructures. Next, the sample is cleaned using the same steps that were used post-ashing, i.e. 5 minutes in acetone followed by 3 minutes in IPA, both sonicated at 50% power. The sample is then blow-dried with nitrogen.

To ensure that the sample is fully clean, it is chemically washed in a solution colloquially known as piranha [84]. Piranha is a reagent made by mixing sulfuric acid, H_2SO_4 (50% w/v in H_2O) with hydrogen peroxide H_2O_2 (32.5% w/v in H_2O) in a ratio of 3:1. As the H_2O_2 is a strong oxidising agent, it can be reduced by H_2SO_4 which generates a significant amount of heat when mixed [85]. As chemical reaction rates depend on temperature, the beaker containing the piranha solution is placed in a cold water bath in order to control the temperature and thereby the reaction rate. The water bath acts as a thermal mass which cools and slows the reaction of the two components. At first, there is a rapid dehydration process from the H_2SO_4 which carbonises the organic contaminants on the sample surface. Then, the reaction of H_2SO_4 and H_2O_2 creates atomic oxygen, which is highly reactive and will attack even stable carbon-based compounds that may be left from the dehydration. As a result, piranha removes the organic residues from the surface as well as hydroxylating the surface, in a similar fashion to the asher, making it highly hydrophilic and preparing it well for the functionalisation steps that are due to follow. The sample is finally rinsed in de-ionised water to remove any remnant of the piranha solution. To ensure that there are no smudges left from the de-ionised water, the final steps are to sonicate at 50% power in acetone for 5 minutes and IPA for 3 minutes.

3.2. Chirped GMR design

3.2.i. *Continuous polygon design*

When first envisaged and fabricated by Triggs *et al.* [63] the chirp was produced by stacking multiple gratings of the same period next to each other and varying the dose factor, which is the time a sample area is exposed to the electron beam. While varying the dose, thus the filling factor, affords finer steps compared with the period, I decided to vary the period. The main motivation for this is that changing the period produces a more linear response on the resonant wavelength, as discussed in section 2.2.iv, compared to the filling factor, which is only linear over specific short ranges. In terms of the fabrication, dose changes are more difficult to control and suffer wider

variations, so using a constant dose for the entire structure simplifies the current dosage. However, it does make the design aspect more complicated.

To solve this issue, a continuous polygon design was first implemented in our group by Dr Li and Dr Reardon. They developed a Matlab script that would generate trapezoidal polygons which were arranged to generate the pattern as shown in Figure 20. By sweeping the grating lines out at an angle, the period could be changed continuously and then the structure could be cut out to give the final design. I built on this script and edited the code to change it to sweep out in both directions. This design minimised the angle of the last polygon, thus keeping the resonance line as straight as possible.

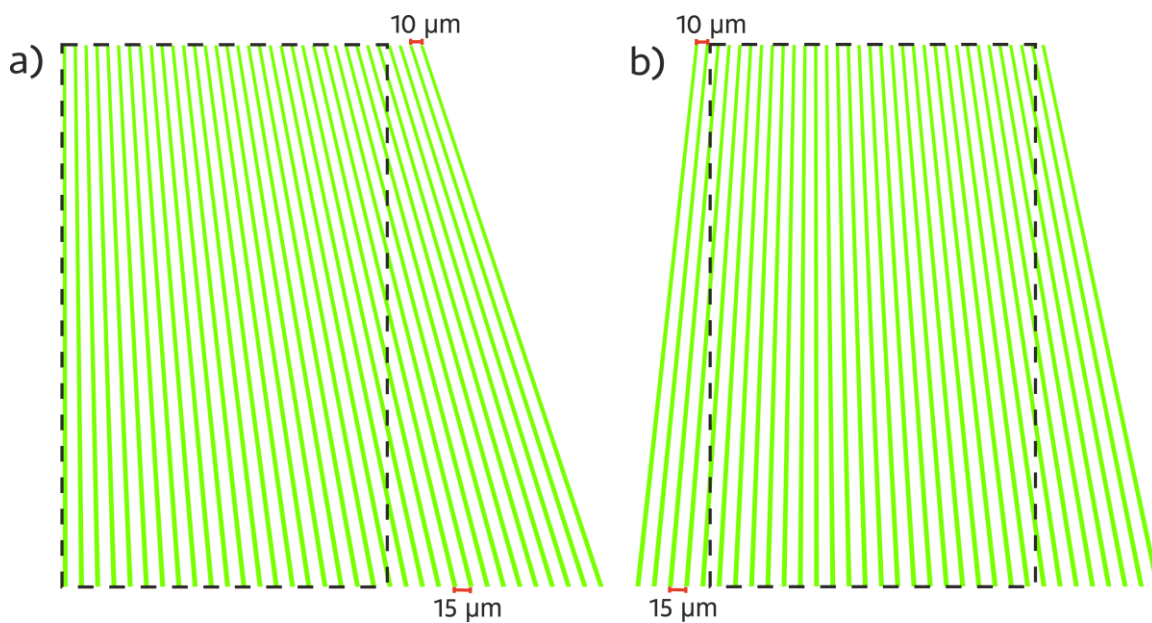


Figure 20: Images of two chirped GMR designs, both designed with a 70% fill factor. The period range is $10\ \mu\text{m}$ to $15\ \mu\text{m}$ to better show the difference visually compared to the usual range in the 100s of nm. The dashed boxes show the zone cut out for the final size of the GMR sensor of $300\ \mu\text{m} \times 500\ \mu\text{m}$.

3.2.ii. Moving to lower wavelengths: effect on resolution

One of the wonders of Maxwell's equations is that they are scale-invariant, so a photonic crystal designed for one wavelength can be tuned to work at a different wavelength by scaling the dimensions accordingly [63]. This invariance makes it very easy to move from the 850 nm originally used by Triggs *et al.* [63] to a lower wavelength such as the 650 nm targeted here. However, there are more factors involved than simply the physics of the resonance. There are also the practicalities of fabrication, which are linked to the resolution and the pixelation of the electron beam lithography system. The crux of the issue in moving from 850 nm to 650 nm is that the structures become smaller, so the pixels of the EBL system become relatively larger. This effect

is illustrated in Figure 21, where one structure that makes up a chirped GMR is shown both straight and tilted to represent the staircase effect that occurs when designing a continuous chirp.

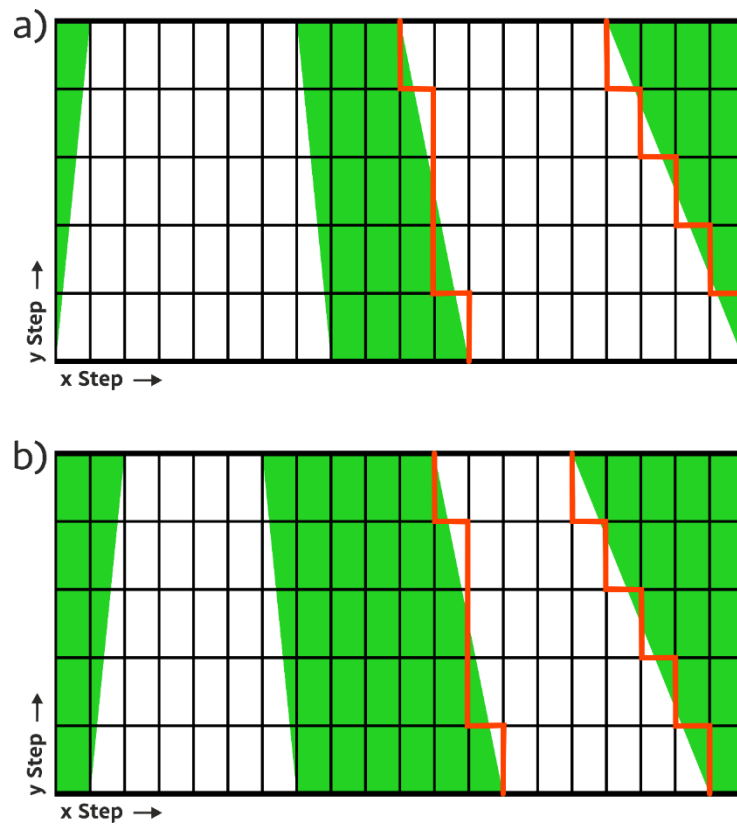


Figure 21: Example of features exposed in EBL exaggerated for clarity to highlight the staircase effect a) A larger fill factor structure with a smaller feature size (in green) to expose. b) A smaller fill factor structure with larger feature size (in green) to expose. The resulting staircase distortion in b) is a larger proportion of the exposed area due to the smaller feature size.

The comparison shown in Figure 21 illustrates how the edges of the higher and lower filling fractions both sweep through similar resolution changes in terms of pixels. However, the exaggerated case highlights that for a smaller feature written (green structures Figure 21) in, the staircasing effect impacts on a larger portion of the feature. The effect of this staircasing is demonstrated in Figure 22a, where the structure with the higher filling fraction has discontinuities and splits from the centre line where both halves sweep out from. This is an inherent issue of the ratio between the pixel size of the system and the feature size; the easiest solution is to increase the feature size, or, in other words, decrease the fill-factor of the grating. Figure 22b shows that moving to a larger written feature removes these resolution issues and smoothes the resonance by moving from a smallest feature of 86.2 nm to 129.3 nm.

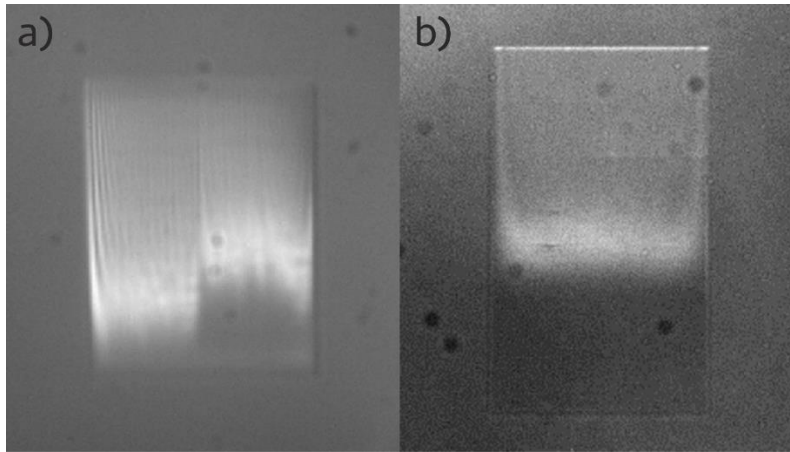


Figure 22: Two fabricated chirped GMRs. a) Grating covering period range between 439 nm and 431 nm with a fill factor of 80% and 400 μm width. The effect of staircasing is apparent from the uneven resonance line in both halves of the grating which arise from the stair casing sweeping in different directions. b) Grating with a period range between 431 nm and 441 nm and a fill factor 70% and 300 μm width showing a much more uniform resonance.

3.2.iii. Final structure outcome

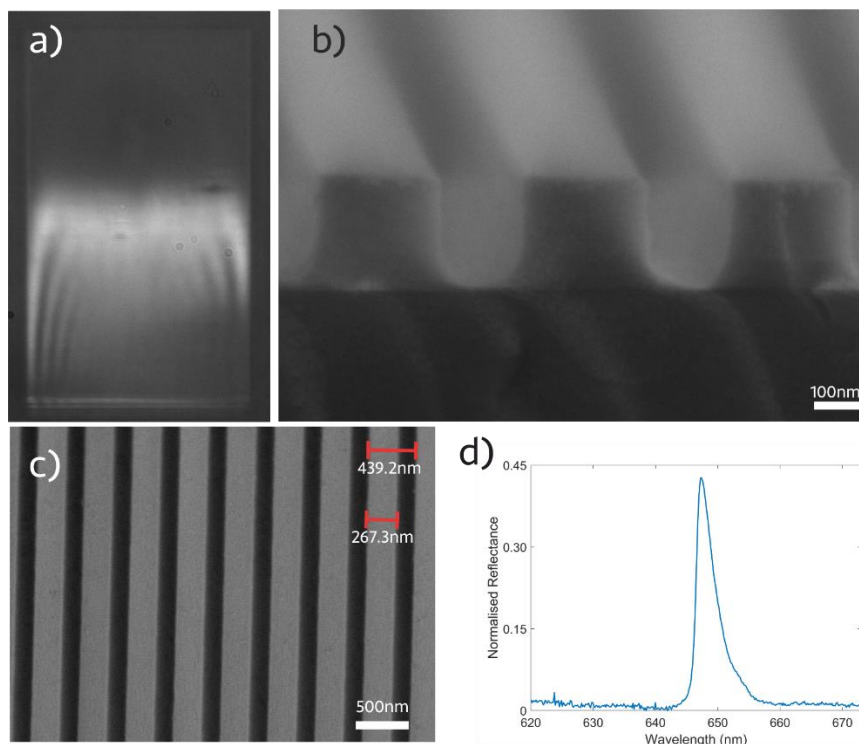


Figure 23: Images of a chirped GMR sensor of period 433 nm to 443 nm at a designed 70% filling fraction imaged in different ways. a) Resonance image obtained with an illumination wavelength of 647.1 nm. b) SEM micrograph of the grating facet. c) SEM micrograph of the grating, top view. d) Resonance measured with a spectrometer for a period of 440 nm, normalised to a mirror.

Figure 23 shows an example structure fabricated using the processes described in section 3.1. The structure was designed as a period chirp from 433 nm to 443 nm with

a filling fraction of the high-index material of 70%. Using a $145 \mu\text{C}/\text{cm}^2$ base dose and following dry etching, the actual filling fraction is $\approx 60\%$ as shown by the SEM micrograph of Figure 23c. The reason for the lower fill-factor is the exposure dose discussed in 3.1.iv. Figure 23d shows the resonance of a non-chirped GMR that has a $Q\text{-factor} = 190 \pm 8$ normalised to a high-quality mirror with a linewidth of $3.4 \pm 0.1 \text{ nm}$ and operating at 650 nm , here the errors are from the discretisation of the data points used to obtain the linewidth. A useful exercise is to compare the results of Figure 23 to simulated results. Figure 24 presents the reflectance spectra (Figure 24a) and the z component of the electric field for the TM mode (Figure 24a). It is interesting to note that even when using the actual feature dimensions taken from Figure 22c, there are differences between experiment and simulation.

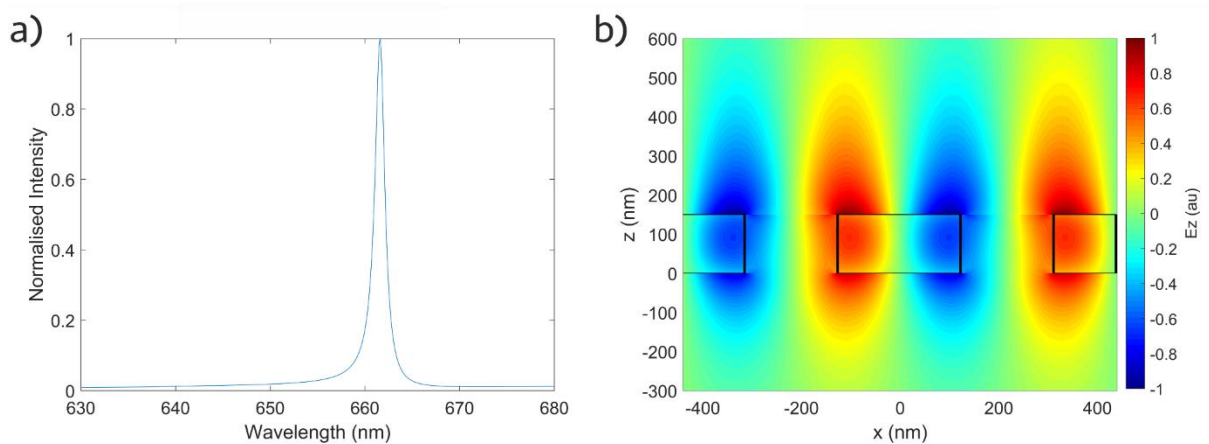


Figure 24: a) RCWA simulation of the reflectance of a 1D GMR with period 440 nm and filling fraction 0.6 . b) Field plot at the maximum of the resonance for the structure in a) at 661 nm .

Q-factor: The simulation exhibits a Q of 508 , $2.7\times$ higher than the experimental value. The difference is mostly due to the perfection of the simulation compared to the actual fabricated structure. One example is the side walls will not be atomically smooth. Another consideration is the features at the corners of the field in Figure 24b which will represent unstable scattering, reducing mode confinement.

Wavelength: Experimentally the resonance wavelength was measured as 647 nm while the simulation resonance is at 661 nm . The main reason the measured parameters do not match the simulation is that the SEM measurement is not accurate; depending on the contrast settings, the sizes can easily vary by a few nm . The rounding of the grating structures base from the dose gradient will also have an effect on n_{eff} shifting the wavelength.

Amplitude: In Figure 24b the field sits at the corners of the grating structure. The overlap seen will exhibit as a discontinuity in the real structures phase matching

condition reducing reflectivity. Furthermore the rounding at the structure base will create different scattering at the interfaces to what the simulation predicts.

3.3. Additive manufacturing: 3D printing methods

The housing of the biosensor instrument was produced by 3D printing, i.e. an additive manufacturing technique realised on a FormLabs FORM 3 SLA printer [86]. Using 3D printing allowed the ability to produce the housing on a much shorter timescale than having it made in the mechanical workshop using classical subtractive methods. 3D printing can be realised by a number of techniques:

a) Material jetting, which is similar to two-dimensional ink jet printing. Each layer is 'printed on top of each other' in a powder bed using binder chemicals [87]. Material jetting is a relatively new technology and so is more expensive and less developed while producing similar results to SLA printing.

b) Powder fusion, where metal powder is heated and so fused together [87] produces metal parts that are typically used as prototyping tools for use in moving machinery or other heavy duty parts that would be expensive to prototype through subtractive manufacturing due to complex geometry.

c) Fuse Deposition Modelling (FDM) which works by heating and extruding material and depositing it layer by layer to build up a structure [86]. FDM is limited by the size of the extrusion nozzle and material so while it is great for larger parts it struggles with fine detail.

d) We decided to use Stereolithography (SLA) which utilises laser polymerisation. SLA was chosen as its resolution is higher than that of FDM methods [88-90], while still being similarly low-cost in terms of equipment and materials. SLA uses a container of a liquid resin, which is exposed to light from a UV laser that cross-links the resin and polymerises it into a solid structure, as shown in Figure 25. The laser is scanned across the field of view to create the structure. Another reason for choosing the SLA modality is that the facilities for part-finishing, which include washing to remove un-polymerised material followed by curing, were already available.

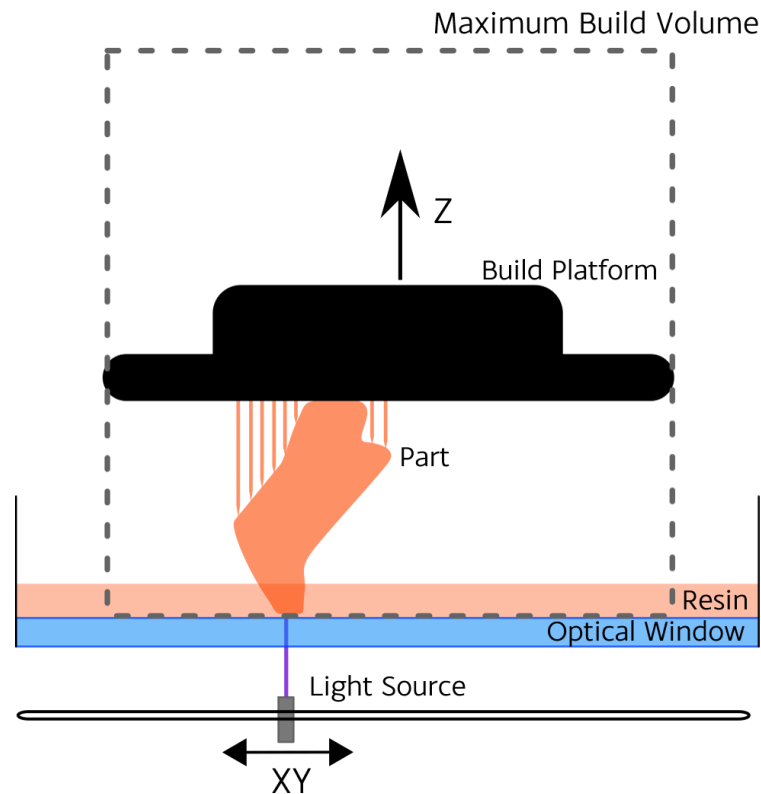


Figure 25: Schematic of an Inverted Stereolithography 3D printer with the structure rising out of the resin tank, so the structure is built upside down.

3.3.i. Parallels with lithography and resolution limits

SLA printing has many parallels with the lithographic techniques described in section 3.1 as it is a form of optical lithography, with the resin being analogous to a negative resist. The resins are made of urethane dimethacrylate (55-75%), methacrylate monomer (15-25%) and a UV activated photoinitiator (<0.9%). The FORM 3 uses a 250 mW 405 nm wavelength laser to cross-link the monomers and create a polymer plastic. The specific resins used are Formlabs' black (RS-F2-GPBK-04), white (RS-F2-GPWH-04) and clear (RS-F2-GPCL-04) resins. Predominantly the black resin was used due to its opacity at visible wavelengths. However since the conclusion of this work Formlabs has released medical grade plastics (FLBMAM01 and FLBMCL01) suited to the use in diagnostic devices.

The resolution limit of the 3D printer arises from a combination of the laser spot size, the polymerisation threshold dose, the build platform resolution, and UV light scattering and absorption of non-active compounds. The resolution follows the Sparrow criterion, which is based on the summation of the intensity curves [64,65]; Figure 26a shows a single Gaussian spot and the energy threshold for polymerisation. Figure 26b shows two features being written closely together, where due to the summation of intensity, they combine into one feature. As reaching this threshold only

depends on the total energy deposited into the resin, the two features can be exposed at separate times and still fuse. The FORM 3 has a spot full width half maximum of 85 μm , which is much greater than the wavelength of light, so the Rayleigh limit does not need to be considered. In practise, the FORM 3 has a minimum resolution of 100-300 μm , depending on the colour of the resin and the shape of the specific feature.

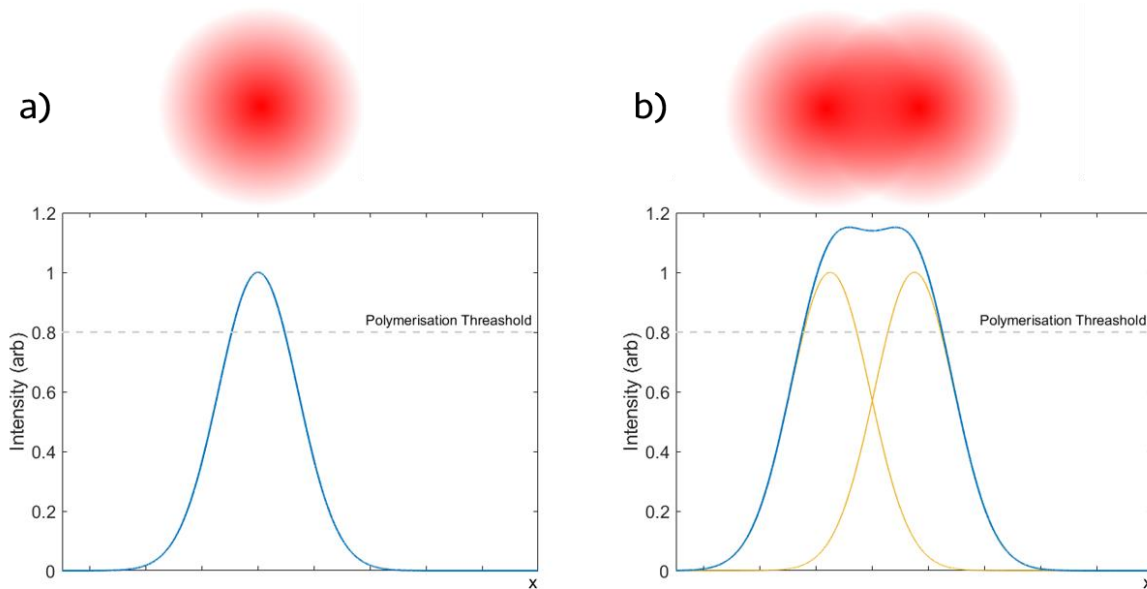


Figure 26: Schematic of energy thresholds with SLA printing polymerisation processes. a) shows a single feature and only the area above the threshold line is fully polymerised. b) shows how two features will combine based on the Sparrow criterion because the combined intensity is above the polymerisation threshold.

Please note that the spatial resolution is limited by different mechanisms; in xy, the resolution is determined by the laser spot and Sparrow criterion discussed above, while in the z-direction, the resolution is controlled by the stage movement and can be set to 25 μm , 50 μm and 100 μm . Naturally, the smaller the step size, the longer the printing time. I also note that the achievable resolution of the FORM 3 is comparable to that of injection moulding used in mass manufacturing [64,65], which is relevant for scaling up the technology in the future.

3.3.ii. CAD part design and model preparation

In order to design the housing and all relevant parts, I used Autodesk Inventor, which is an industry standard in CAD and manufacturing and is free to use for academic institutes. Autodesk has the capability of creating three-dimensional objects in a sketch-and-extrude format and can also be used to create assemblies from multiple parts to test how well they fit together before printing.

The peculiarity of the printing process (i.e. writing proceeds upside down) requires placing supports underneath the item to be printed. Figure 27a shows a high detail model with dimensions of 30.37 mm × 32.57 mm × 40.41 mm with relevant support structures in place and Figure 27b an example of the instrument housing base with dimensions of 83.49 mm × 83.49 mm × 40.00 mm. The housing is designed to be printed directly on the build platform.

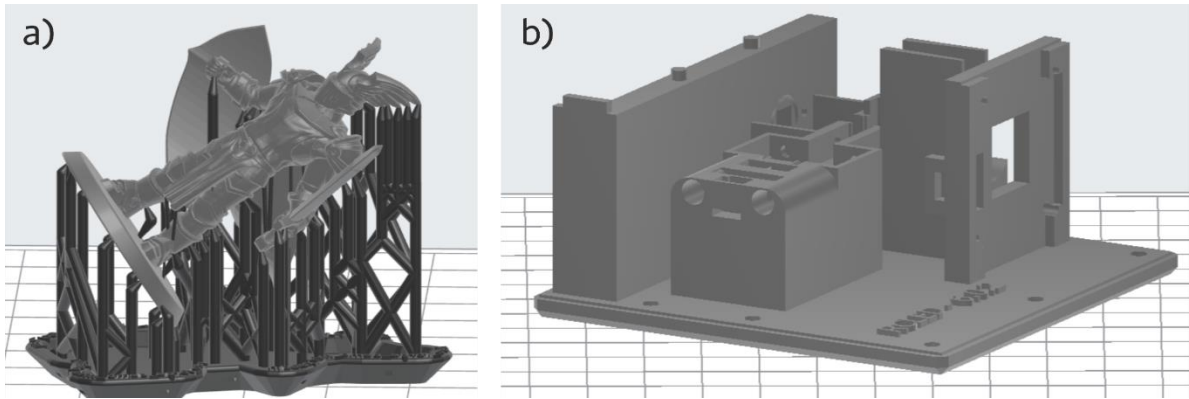


Figure 27: Examples for printing different types of structures. a) A fine detail model requiring many support structures. b) Example of the instrument housing designed to be printed directly on the build platform with no supports.

When printing small overhangs, they need to be supported or the detail would be lost. Figure 27a shows an extreme example of this. Conversely, Figure 27b shows the instrument housing designed to be printed without supports. The largest issue is to ensure that any vertical structure will have sufficient mechanical strength during the print, which is why I chose to make vertical parts at least 1 mm thick and minimised aspect ratios. Any critical overhanging structures were designed to be as small as possible and circular so they would keep to their designed shape. Vertical square openings were only used where the final shape was not tolerance-critical and so they are often larger than required with joins on multiple sides to avoid misprinting. Smaller areas were designed with drain holes to allow resin to drain out. Any overhangs that could not be joined on multiple sides were removed and printed separately and attached post-print. As the base of the model in Figure 27b is placed directly on the build platform, a chamfer is added to aid in removal without damaging the part or the build platform. Printing on the build platform is also less accurate for the first few layers, so the base is thickened to accommodate this.

3.3.iii. Part printing and finishing

Once the part is printed, there are multiple steps to finish it; the wash, cure and finishing steps, with the wash step being performed first. The wash step consists of two rough rinses in baths of IPA to remove any bulk volumes of uncured resins. Then

a more comprehensive wash is conducted in the Form Wash from Formlabs, again using IPA where the part is submerged and a large stir bar agitates the IPA to ensure all the uncured resin is removed. The final wash step is typically performed for a minimum of 30 minutes, but in case there are many small gaps or extrusions, this time is increased. The part is then checked for uncured resin and this is then cleared either manually or by spraying with IPA and then repeating the final wash step. Once the part is washed, it is blown dry with compressed air. As the next step, the part is cured in the Formlabs Form Cure, which flood-illuminates the part with UV light at 60 °C for 1 hour. The curing step is done to ensure the resin is fully cross-linked. The cross linking slightly shrinks the part and so this must be considered when designing parts with tight tolerances. The curing has the benefit of improving tensile strength at the cost of flexibility. Any uncured resin left after the wash step would also be cured in this step, which is clearly undesirable. Any changes to the topography due to support structures that would affect the performance of the final printed parts was removed by filing with jewellers' files or sanding.

4. Device prototyping and development

The laboratory-based setup that is generally used to measure GMR samples in the research group is shown in the rendered graphic of Figure 28. This setup, or slight variants, have been used for a variety of studies [30, 59,91-93]. The setup takes up the majority of an optical bench; the goal of my project was to miniaturise this setup into a portable instrument.

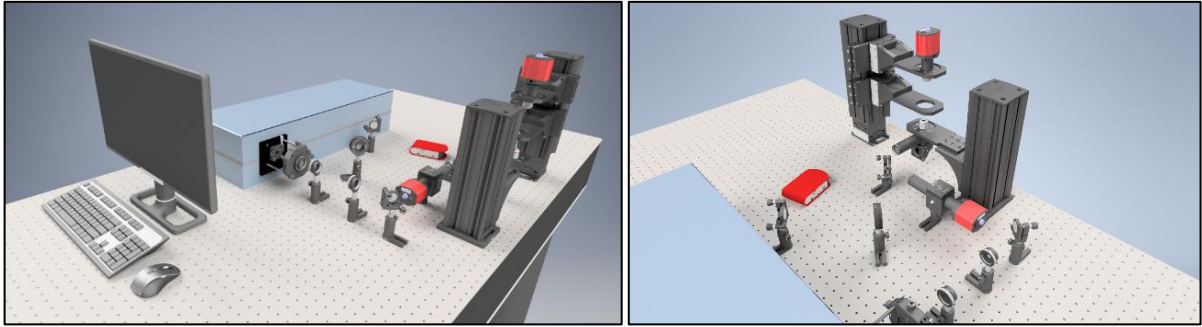


Figure 28: A rendering, from two viewing angles, of the setup that is used to measure Guided Mode Resonance samples. The setup consists of a broadband monochromated source that is collimated by a microscope objective that also images the sample.

4.1. Discrete setup and issues

To produce an initial proof of concept, I designed a setup that utilised all of the smaller optical elements intended for the instrument on discrete mounts shown in Figure 29. The mounts were all Thorlabs® components; the initial lenses were of 10 mm focal length, with a beam splitter cube and an 850 nm laser. As the instrument uses the chirped GMR modality, it only requires a fixed wavelength source, thus removing one of the largest components of the setup of Figure 28, i.e. the monochromator. While this discrete setup provided the first proof-of-concept of minimising a large laboratory setup into a compact arrangement, it was not an ideal solution. The main drawback was that the discrete mounts for the optical elements were bulky and did not allow for the manoeuvrability that was originally envisaged. A setup using 25 mm lenses was constructed, shown in Figure 29, which showed that miniaturisation was possible but used larger lenses than were intended for the instrument. I therefore decided to move to 3D printing prototyping, as it allowed for a quick turnaround time and gave much more flexibility.

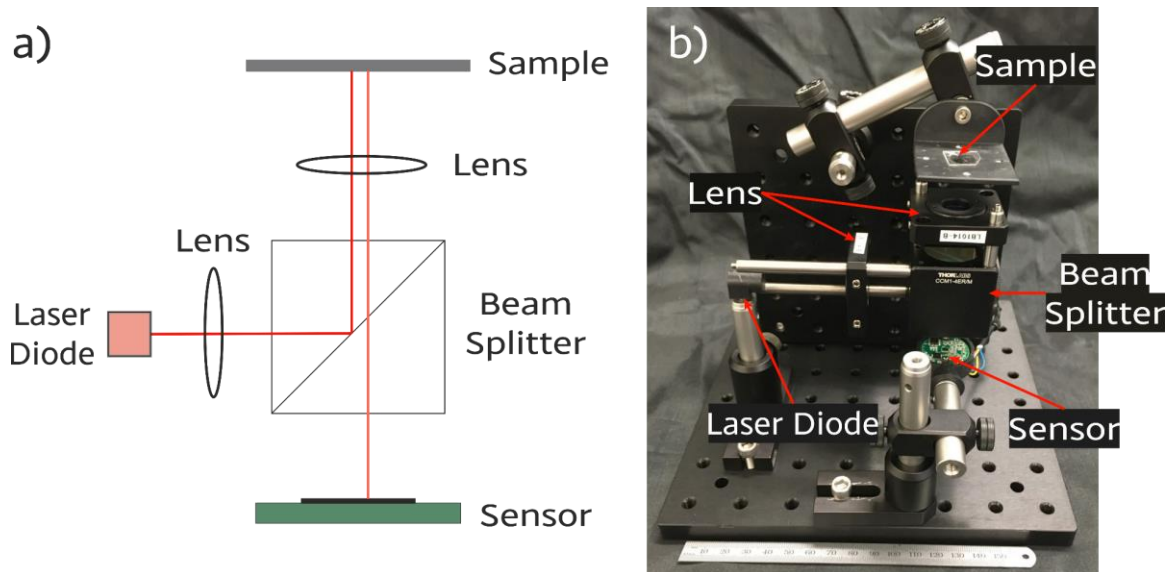


Figure 29: a) A schematic of the discrete setup that was a proof of concept of the miniaturisation of the setup shown in Figure 28. b) An image of the second discrete setup that used 25 mm focal length lenses following the schematic of a).

4.2. Instrument design considerations

The key aspects of the 3D printed design are described below.

4.2.i. Optical path and components

The optical path was designed as a cut-out so that the walls of the instrument formed a rigid backbone for supporting the optical components. This is presented in Figure 30a with the final instrument shown in Figure 30b. A 5 mm minimum spacing was chosen both for reasons of manufacturability (the resin used in the 3D printing process needs space for draining) and because the smallest optical components were a 5 mm beamsplitter cube and the 6 mm imaging lens housed in mounts presented in Figure 30c.

The camera was a DMM 72BUC02-ML from The Imaging Source GmbH [94], which has an Aptina MT9P031 CMOS sensor. Shown in Figure 30d the sensor was easily integrated as the camera chip is already mounted on a printed circuit board and has USB connectivity. The circuit boards have pre-drilled holes in precise locations for mounting the board to whatever framework the specific application demands. This arrangement made it easy to mount the camera to the instrument and align the sensor to the central part of the beam path.

The other key component is the beam splitter cube, which is a 5 mm non-polarising beam splitter. I chose a pressure fit mount for the beam splitter which grips the four corners of the component. For polarisation control (cf. chapter 5), I chose a film polariser (“Polaroid”) that was very cost-effective as it could be cut to size and mounted in a circular mount. The custom mount then had an extrusion which is used to rotate it to the correct polarisation angle.

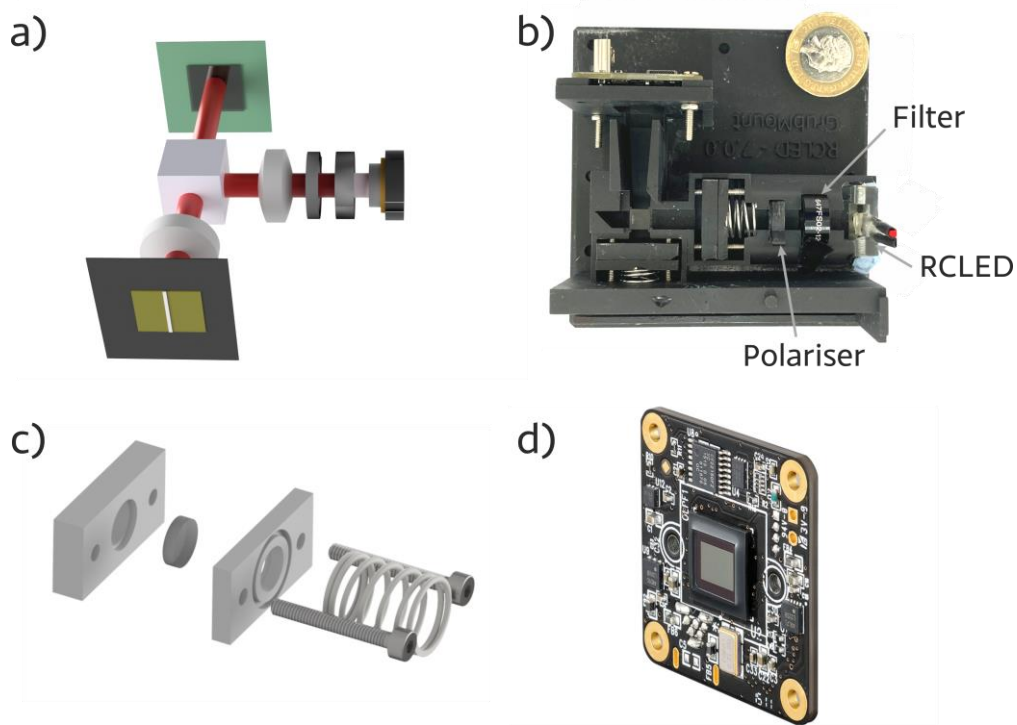


Figure 30: a) Schematic of the beam path layout. b) an image of the printed housing with light source optics labelled. c) a rendering of the components used in the lens housing. d) an image of the camera used in the instrument DMM 72BUC02-ML - The Imaging Source GmbH. Reprinted with permission from The Imaging Source GmbH [94]

4.2.ii. Light and manipulation

The light source I chose was a resonant cavity LED (RCLED), Firecomms Ltd. (FB00AKAR), which has a quoted numerical aperture of ~ 0.5 . The RCLED was housed in a cartridge by three M2 set screws that allowed for precise positioning. The cartridge with an RCLED mounted inside is shown in Figure 31; it pressure-fits into the main device body, which together with the three set screws allowed alignment with respect to the centre of the beam path.

The lenses are held in printed mounts that have extrusions - these allow them to be placed into the beam path. The design of the extrusions was made simpler by the CAD files provided by Thorlabs as the curvature could be matched precisely. These mounts are then mounted between an M2 bolt with a nut applying pressure to one side of the

mount and a spring to the other side, which allows for fine-alignment, both in angle and in position, by using a 16 mm long screw. The lenses had a range of movement of almost a centimetre, giving ample room for manoeuvre.

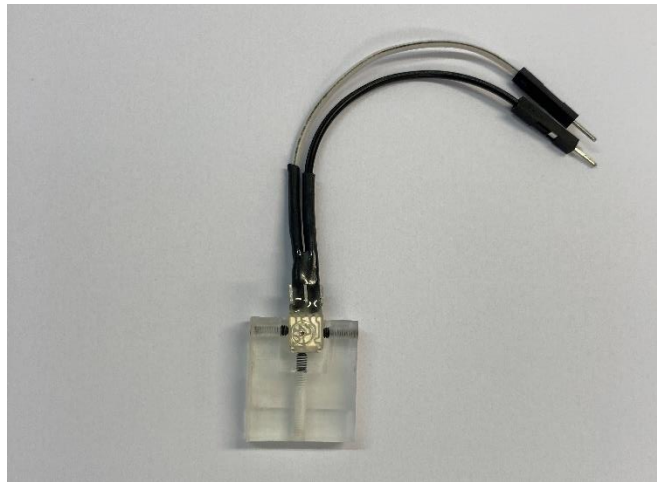


Figure 31: RCLED mounted in a printed cartridge and held in place with 3 grub screws.

The imaging lens I chose had a diameter of 6 mm and a focal length of 10 mm. This short focal length allowed for a magnification of 2:1 in a confined space, the low magnification making the system tolerant to positional inaccuracies. The collimating lens has a 9 mm diameter with a focal length of 12 mm. This small increase in focal length, compared to the imaging lens, was chosen in order to increase the tolerance for collimating light. The larger diameter was chosen to ensure that the collimating lens had a larger numerical aperture than the imaging lens. This ensured that the back-aperture of the imaging lens is fully filled and the field of view fully illuminated.

4.2.iii. Design aspects in confined space

As described in chapter 3 the tolerances of the 3D printing process have an impact on the positioning of the optical elements. The mechanical strength of the 3D printed parts is thickness-dependent, so components such as the springs and screws used for mounting need sufficient material around them to take the strain of the pressure and tension. While the instrument housing can in general be designed with sufficient material to ensure the required strength, there are some delicate areas: the mounting of the imaging lens, which sits at the edge of the housing, needs to accommodate the cartridge with the GMR sensor chip. The cartridge mount also needs to be strong to allow repeated insertion and it needs to be accurately placed in the imaging plane. Unlike a laboratory setup that has several degrees of freedom for active adjustment, the alignment here is entirely passive. Taking all of these considerations into account, the base of the sample section was designed to be 5 mm thick to give sufficient

strength to all the mounts. Nevertheless, the spring and adjustment screws ended up being very close together, with only a small bridge of material (highlighted in red in Figure 32) separating them. Since the surrounding elements have ample material around them, the system had sufficient strength and this minor overlap did not cause any issues.

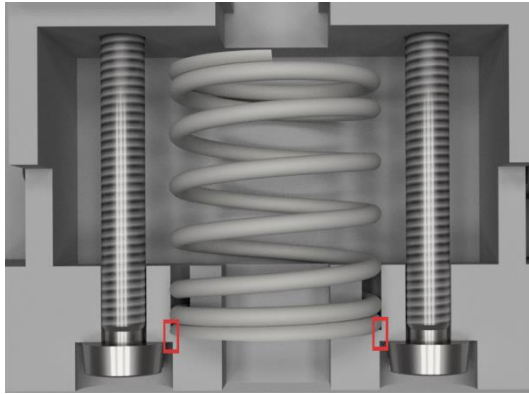


Figure 32: A cross-section view of the lens track system spring and bolts with the thinnest print part marked.

4.2.iv. Achieving collimation and alignment procedure

When compared with an experimental setup such as that shown in Figure 28, the integrated instrument offers a lot less fine tuning. One area where this is an issue is the collimation of light, which is required to excite the guided mode resonance with a clean resonance. There are several factors working against the perfect collimation of light, such as the extended nature of the RCLLED light source and the small beam path, which precludes techniques such as Köhler illumination. Nevertheless, I was able to achieve collimation of sufficient quality as described below.

Generating collimated light is relatively straightforward in principle, as it simply requires generating a planar wave front which propagates as a parallel beam. One way to achieve this is to use a large distance from a source, such as the sun, which at a sufficiently large distance can be considered to generate plane waves. Since this approach is rather impractical, one can simply place a point source in the focal plane of a lens.

As described above, two lenses were used to provide the two points of movement. One to allow focusing of the imaging lenses and then the second lens to move the image of the source to the back focal plane of the imaging lens. The alignment of the imaging lenses was simply checked using the camera. To check the collimation of the light source through both lenses a collimation tool was used. The tool, or collimation tube, was constructed of lens tubes holding a ground glass diffuser one focal length away

from a lens (Figure 33a and b). The glass diffuser acts as a screen to image a focused spot (or image of the light source) as can be seen in Figure 33c and d with an image of a distance source visible in Figure 33c and imaging the monochromator slits of a setup in Figure 33d. The tube not only aided in collimation of the source but also highlighted any undesired angular components, exhibited when the spot is not central (Figure 33e). An image of the result from the collimated RCLED is shown in Figure 33f.

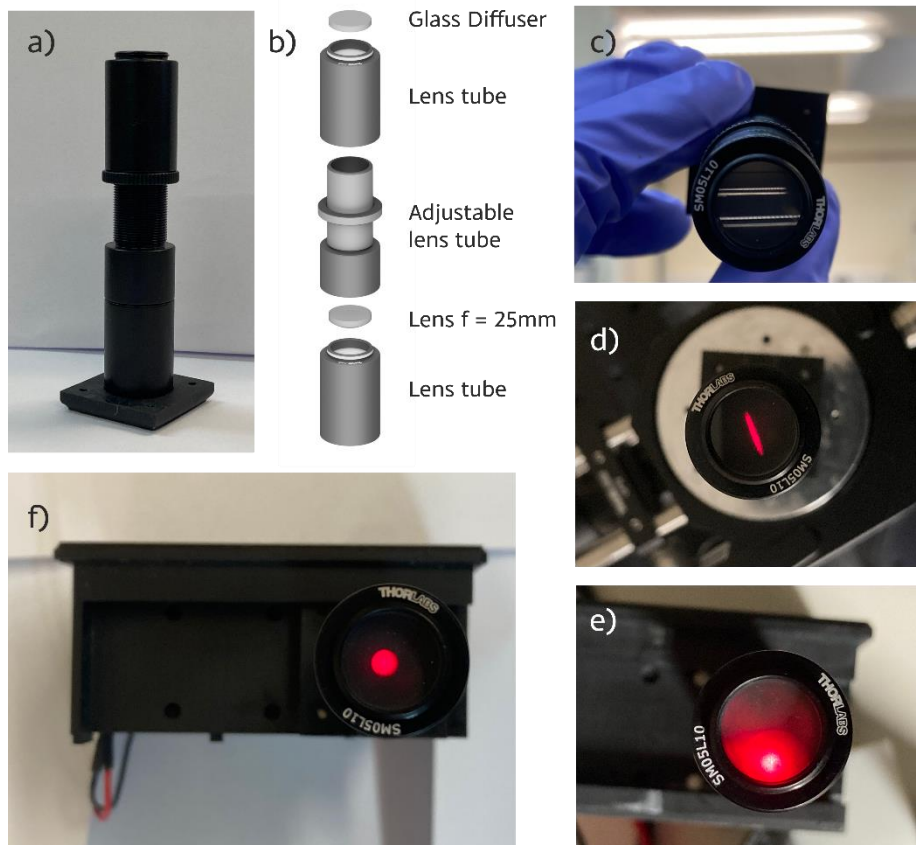


Figure 33: a) Elements used to collimate the light source of the instrument. b) Detail and c) image of a distant source focused on the glass diffuser. d) Image of source from a monochromated halogen source. e) Off-axis and poorly collimated RCLED source. f) Well-collimated image of the source.

4.3. Microfluidic cartridge

Handling the fluidic analyte is important for delivering the target proteins to the sensor chip. Generally, PDMS is used for fluidics in research environments [95–98] and while PDMS is very versatile, I decided to use 3D printed cartridges for compatibility with the 3D printed housing; this method was also chosen with a view towards transfer to a scalable manufacturing process in the future. PDMS may be a common occurrence in

a research environment but in commercial settings it is rarely utilised as other materials are preferable [99].

4.3.i. PDMS vs 3D printed channels

Given its versatility, initial fluidic circuits were realised in PDMS in order to establish the most favourable geometry (Figure 34) before transferring the design to 3D printing.

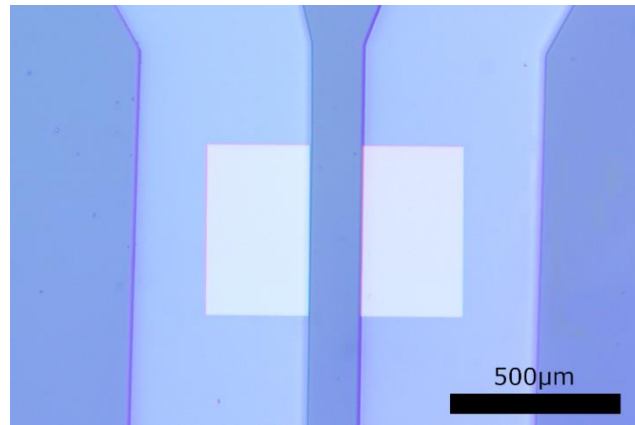


Figure 34: Optical micrograph of a chirped GMR sensor chip placed across two PDMS channels. One channel is used as the measurement channel and the other is used as a reference.

Table 2: Comparison between PDMS and 3D printing for the fabrication of microfluidic channels

	PDMS channels	3D printed Cartridges
Mounting	O ₂ Bonding/Clamping	Adhesive bonding/Clamping
Channel size limiting factors	Mould spin thickness and lithography resolution (10's µm)	Gasket thickness and printer resolution (100's µm)
Scalable	No	Yes
Prototyping speed	Slow	Fast
Reusable	Yes when clamping	Yes when clamping
Mechanical stability	Low - Channel collapse	High

A comparison between PDMS and the 3D printed plastic is shown in Table 2. A key advantage of PDMS is that the dimensions can be more tightly controlled, as PDMS structures are moulded from lithographically made structures, whereas the resolution

of the 3D printer is limited to 300 μm by 300 μm in the lateral dimension and 25 μm in the vertical dimension. One issue of the lower resolution of the 3D printing is that walls between channels need to be 100s of μm thick, which limits the number of channels that can be placed onto the sensor chip, and thereby the multiplexing capability.

4.3.ii. Sensor chip sealing and mounting

Both a PDMS and 3D printed approach were taken when integrating fluidics with the compact instrument. An in-depth discussion into the development and usage of these two approaches is presented in chapter 6. Being more synonymous with a scalable device the 3D printed approach is briefly described here.

The GMR sensor chip is mounted on a 3D printed base using epoxy adhesive. Mini-magnets are then used for accurately aligning and fixing the sensor chip cartridge onto the instrument, with complementary magnets embedded in the housing. The magnets were glued into place. An exploded rendering of the cartridge is shown in Figure 35.

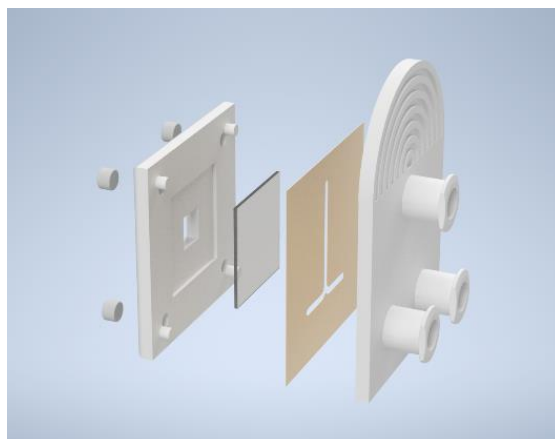


Figure 35: A rendering of the printed fluidic cartridge top and base with the glass chip and orange tape gasket.

4.3.iii. Part compatibility with chemical solutions

A key aspect of the fluidic circuit is its compatibility with the chemicals used for functionalising the sensor chip, as functionalisation ideally is carried out in-situ, i.e. inside the microfluidic channels, which means that the fluidic circuit has to be compatible with a number of solutes. The printed plastics therefore need to be tested for their chemical compatibility. I performed this test by immersing a 3D printed part in the respective chemicals for extended periods of time and measuring the resulting change in mass. The samples were left uncured as this is when the printed material

will be weaker due to less crosslinking between layers and more susceptible to solvents as well as allowing this to inform the worst case scenario.

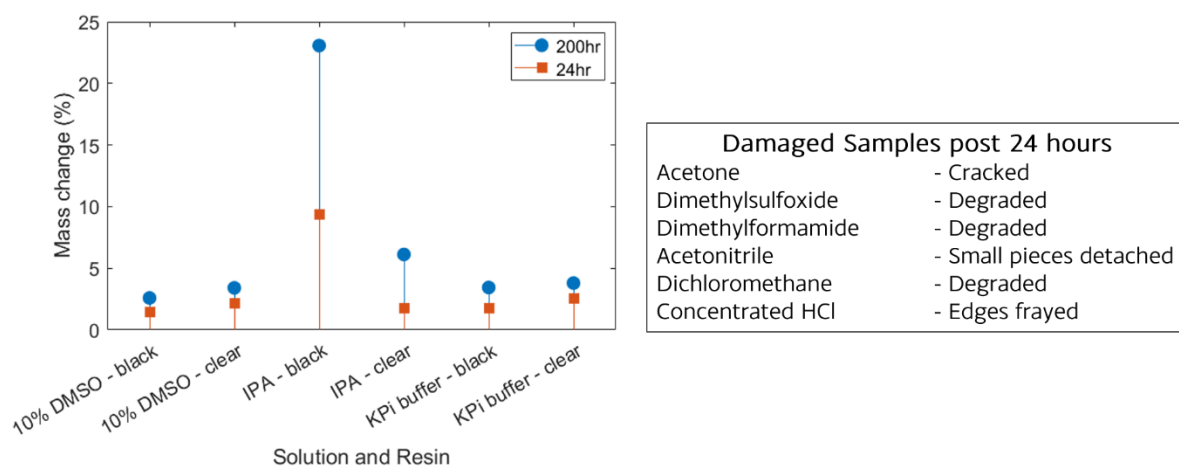


Figure 36: Mass change of 3D printed material using Formlabs® black and clear resins reporting both mass change and visual changes.

From the data shown in Figure 36, some solutions are suitable for use with 3D printed fluidics, specifically the use of a buffer solution when considering it for measurements over the course of hours. One key point is that IPA seems to have a significant effect over 200 hours, especially on the black resin (RS-F2-GPBK-03). This was also notable as the clear resin (RS-F2-GPCL-03) samples generally survived the more aggressive solvents and solutions better than the black resin. The reason for black resin being more susceptible to degradation may be related to the pigment, which may be a weak point allowing the solutions to attack the plastic more easily. For this reason, unless expressly needed, the clear resin was chosen for printed fluidics or any surface that would come into contact with a solution for measurements. Most of the more aggressive solvents and concentrated solutions did degrade or compromise the printed material and so this ruled out the 3D printed cartridges for in-channel functionalisation in cases when solutions required more aggressive solvents for example pure dimethylsulfoxide (DMSO) which degraded even cured prints. As an example, one of the steps used to prepare the surface for antibodies requires a molecule dissolved in DMSO. However the resin even uncured is more than suitable for buffer based measurements and functionalisation steps.

The content of this chapter has showcased the construction of the instrument along with discussing some of the challenges in physically miniaturising the GMR readout. This discussion, however, is lacking the motivation behind the choice of components housed in the instrument. The next chapter justifies the component choices, predominantly based on their effect on the total system noise.

5. Laboratory to point-of-care

Many papers have been published on refractive index sensing, including for clinical applications, yet there is still a clear disconnect between published biosensor research and its translation towards market viability. It is this disconnect that I would like to discuss in this chapter; the majority of the work presented has been published [100] with the consideration that low-cost components will support the development of new technology and avoid the situation where a technology only works with the most expensive instrumentation available. Unsurprisingly, this is an area often overlooked in the literature due to the lack of perceived novelty and while this type of study will never be publishable in Nature or Science, it is arguably more important for making technology practical and commercially viable and make its way to a point of use in the wider world. I have chosen to break down the problem into several parts, including general noise considerations and considerations regarding the choice of resonance Q-factor, to name but a few.

5.1. Point-of-care context

Several papers to date have discussed the fundamental limitations of high Quality (Q) factor resonant sensors [32,101] and thus started to consider the fundamental limitations of these sensors. The main issue with these studies is that they assume a highly stabilised laboratory environment, very narrow linewidth lasers and/or high-resolution spectrometers along with complex and bulky coupling and alignment equipment. Realistically, these conditions cannot be met in a point-of-care or a resource-limited environment. For example, thermal fluctuations introduce wavelength drift both on the sensor response and the light source and they increase the noise of the system more generally. An obvious example is the use of low-cost lasers in handheld devices; these simply do not exhibit the linewidth and stability of laboratory-grade lasers. With this limitation in mind, I undertook a study to understand the limitations of refractive index sensors in a low-cost environment and to identify the best strategy towards making a high-performance, low-cost photonic sensor. The first question was whether to use a resonance with a low or a high Q-factor. It is important to point out that some work has already been done in this direction and a number of point-of-care (POC) devices based on photonic structures have previously been presented [102-108]. Typically, only particular achievements are reported. Here, I

consider the trade-offs and key factors of the entire sensor system in order to evaluate the optimum solution for a low-cost POC device.

The questions to consider include the choice of light source, with a laser and an LED taken as two low-cost and readily available examples. The choice of light source is directly connected to the Q-factor of the photonic resonance. On the receiver side, the choice of sensor/detector was investigated with a particular consideration of the noise produced by the camera sensor. I also considered the choice of manufacturing method of the sensor in the future (electron-beam lithography vs nanoimprint lithography), because electron-beam lithography is not scalable for mass-manufacture.

5.2. Low-Q vs. high-Q resonant systems

The first question to answer was whether to use an optical resonance with a low or a high Q-factor, which ultimately depends on the light source to be used, as the linewidth of the source should be equal to or narrower than that of the resonance. White and Fan [6] and Hu *et al.* [32] both conclude that high-Q resonances result in the highest sensor performance, up to Q-values of $Q \approx 10^5$. High Q-values have the advantage of sharp spectral features that are more easily tracked. The upper limit of $Q \approx 10^5$ determined by these authors typically arises from the intensity and wavelength noise of the high-quality laser source they investigated. Unfortunately, low-cost, non-stabilised lasers tend to exhibit much higher noise values as well as wavelength variations due to drift; none of these were considered in these studies. For example, Figure 37a shows the wavelength noise of a Fabry-Perot laser (Roithner LaserTechnik GmbH - QL85D6SA) which shows mode-hopping and wavelength changes of order $\Delta\lambda = 1\text{-}2$ nm over a period of 60 minutes. This mode hopping is well beyond the small wavelength shifts described by White and Fan [6].

The corresponding intensity noise is shown in Figure 37b, which shows significant relative intensity noise and a drift of $\Delta I \approx 30\%$, even when driven by a very stable power source. In fact, Figure 37c shows a comparison between the driving current generated by a Yokogawa laboratory supply and the supply via a USB computer port, i.e. a battery, used in conjunction with a current smoother (TLV1117CKCS - Texas Instruments). This comparison clearly shows that the power supply is not the reason for the drift observed in Figure 37b, leading to the conclusion that it is instead due to thermal energy from operation since the diode is not actively cooled. Figure 37c also shows that a USB port can be used as a viable power supply. The measurements shown were obtained using a Keithley 2000 Series multimeter connected in series between

the power supply and the laser diode. The traces indicate that the noise most likely arises on the measurement side, corresponding the least significant digit of the multimeter used, due to the traces being so similar.

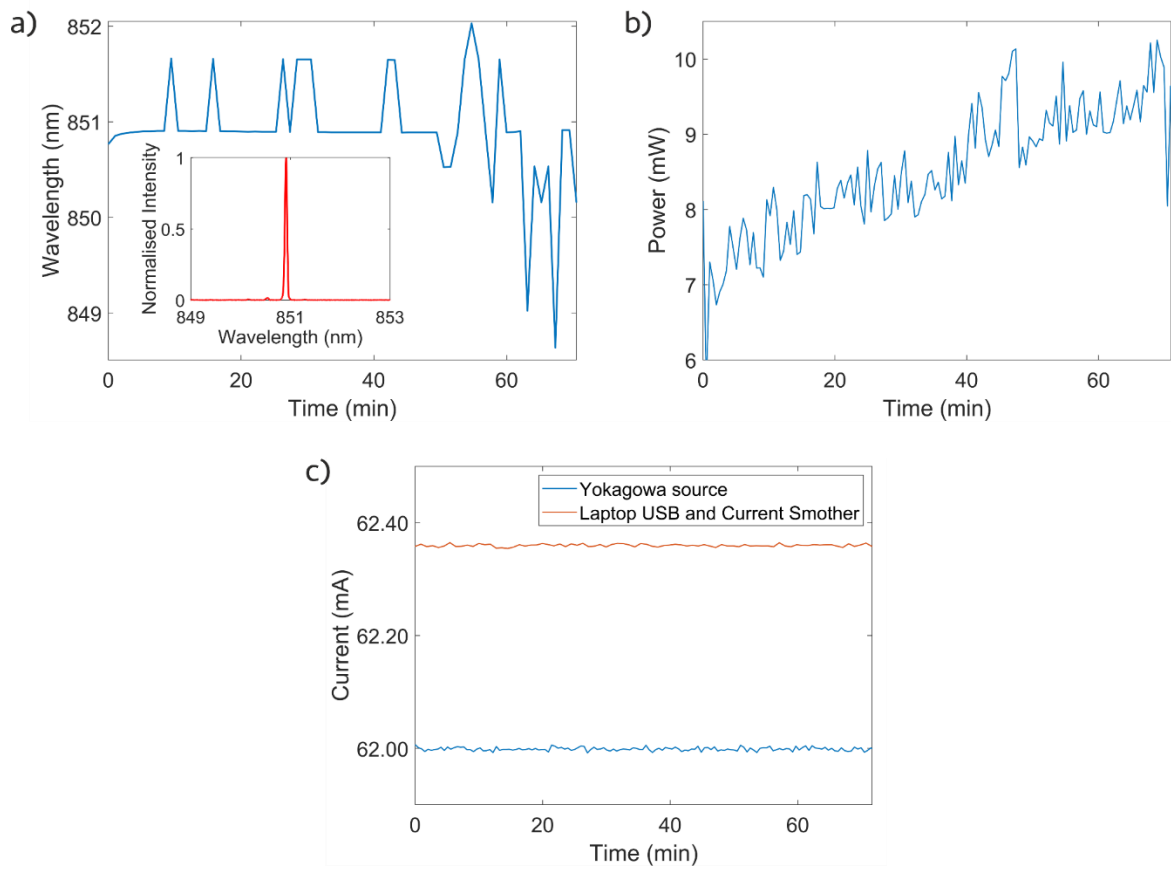


Figure 37: a) Wavelength variation of a low-cost Fabry Perot laser diode (Roithner LaserTechnik GmbH - QL85D6SA) as a function of time, with an example spectrum shown in the inset (FWHM = 55 pm). b) Intensity variation of the laser diode in a). c) A comparison of the laptop battery source and a laboratory current source stabilities. Adapted with permission from [100] © The Optical Society.

As an alternative to Fabry-Perot edge-emitting lasers, vertical cavity surface emitting lasers (VCSELs) typically avoid mode-hopping. However, they are prone to changes in polarisation due to their circular output facet; they also tend to have a broader linewidth (typ. $\Delta\lambda \approx 0.5\text{-}1\text{ nm}$). Example data is provided in Figure 38a, where the wavelength noise of a VCSEL is shown (Thorlabs inc. - L850VH1), with the insert showing a typical spectrum and a full width half maximum (FWHM) of 0.42 nm. From Figure 38a, it is clear that the wavelength stability of the VCSEL is much closer to the values expected by White and Fan [6] and Hu *et al.* [32] as previously discussed. The drawback of the VCSEL is highlighted in Figure 38b, which plots the intensity of the diode as a function of time when measured through a polariser. The general fluctuations of intensity are much lower than for the Fabry-Perot edge-emitting laser in Figure 37,

until the polarisation switches at approximately 30 min. Such jumps in intensity make the use of the VCSEL much less attractive.

Moreover, the mass production of laser diodes means they have an operating wavelength tolerance up to $\Delta\lambda_{tol} \approx 10$ nm, which makes it extremely difficult to match the resonance of the sensor to the wavelength of the laser. Overall, these considerations show that a high-Q system is not suitable for a point-of-care solution operating with low-cost lasers.

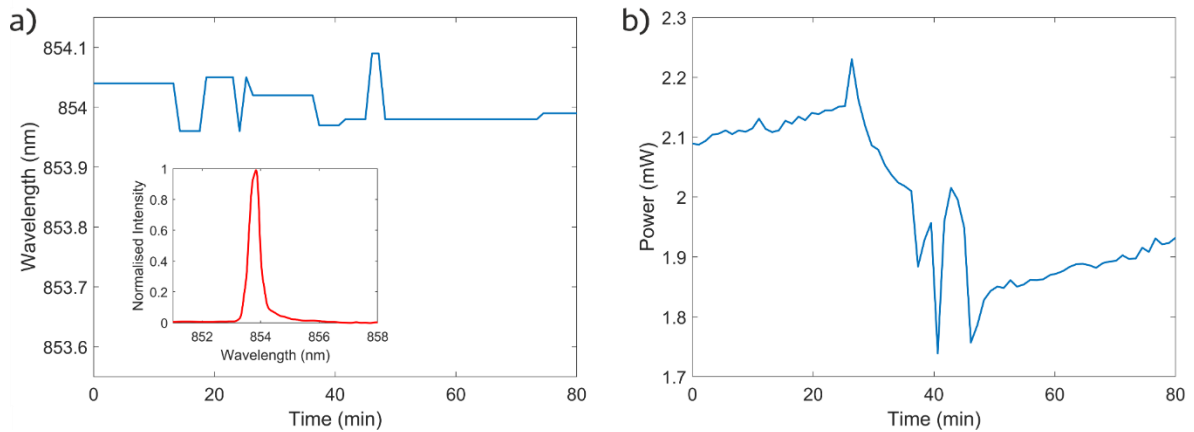


Figure 38: a) Wavelength variation of a vertical-cavity surface-emitting laser (Thorlabs inc. - L850VH1) as a function of time, with an example spectrum shown in the inset. b) Intensity variation of the laser diode in a) taken with a polariser normal to the diode's initial polarisation.

With a laser source ruled out, I considered an LED as the next option. Specifically, I tested a resonant cavity LED (RCLED) in combination with a wavelength filter; an RCLED was chosen as opposed to a conventional LED because of its higher directionality and spectral density [109–111]. RCLEDs consist of an active region being placed between two cavity mirrors, namely Bragg reflectors, to create a Fabry-Pérot cavity resonance. The cavity narrows the LED emission peak giving enhanced spectral density as well as forcing the emission direction to be anisotropic [112]. The cavity Q-factor is purposefully kept low to keep the dominant emission spontaneous rather than stimulated, maintaining the incoherence and broad emission spectrum (FWHM 14.2 ± 0.1 nm). In order to create a suitably narrow spectrum for tracking the sensor's resonance, I introduce narrowband filters, in particular 1 nm and 3 nm filters (Andover Corp. (647FS02), 1 nm and Semrock (LL01-647), 3 nm). Their transmission, together with the original RCLED spectrum, is shown in Figure 39a. The RCLED is from Firecomms Ltd (FB00AKAR). RCLEDs have become more widely available due to their use in short range communications such as those of the plastic fibres in data centres. While the 3 nm linewidth filter provides higher intensity, the narrower line width of 1 nm is more desirable while providing a sufficiently strong signal for the measurements.

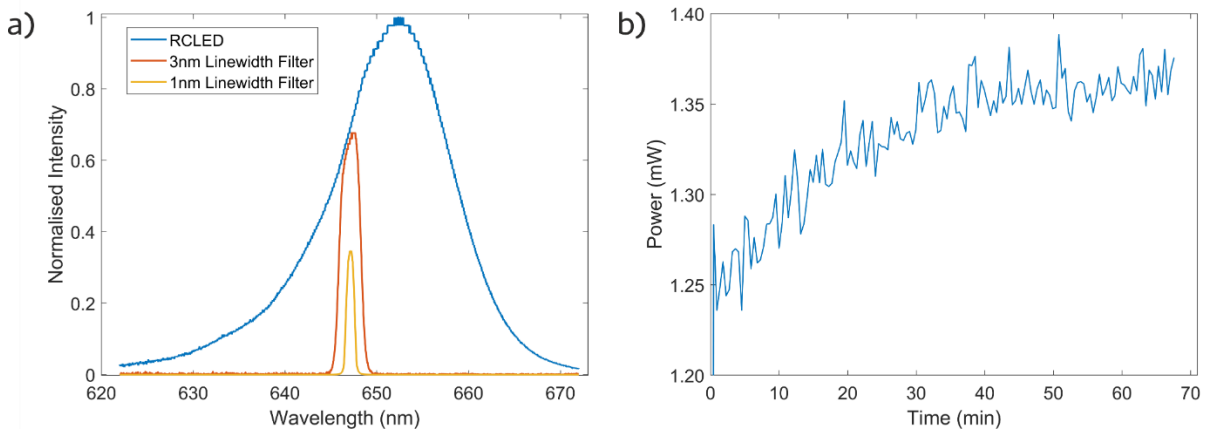


Figure 39: a) Example spectra of a resonant cavity LED (Firecomms LTD. – FB00AKAR) without a filter and with 3 nm and 1 nm linewidth filters. b) Intensity variation of the LED in a).

The need for a filter adds cost, but given its small size, this is only a minor addition. One of the key advantages of the RCLLED filter combination is that the centre wavelength of a filter is much better defined than that of a laser. Furthermore, it is of note that thermal wavelength drift is smaller for the filtered RCLLED than for a laser, which is particularly important for point-of-care applications that operate in a temperature-variable environment and over timescales longer than a few minutes. To quantify this observation, consider the thermal drift for a VCSEL, which is typically $\Delta\lambda/\Delta T \approx 0.06$ nm/K, which arises from the coefficient of thermal expansion of GaAs (which is around 6×10^{-6} °C⁻¹ at room temperature [113,114]). The filter drift (Andover Corp.) is specified as $\Delta\lambda/\Delta T \approx 0.02$ nm/K, so is three times lower than the laser. The intensity noise is also lower for the LED, as we can see by comparing Figure 37b and Figure 39b; the laser has a standard deviation of 0.416 mW and a mean of 8.37 mW giving an SNR of 20.1 (13 dB) while the RCLLED has a standard deviation of 0.027 mW, and a mean of 1.35 mW providing a higher SNR of 50.0 (17 dB). In addition to the lower intensity noise and wavelength noise, the incoherence of the RCLLED also avoids speckle, which is advantageous as discussed in the context of Figure 46 and Figure 44 below.

5.2.i. Lower Q modalities - using guided mode resonance

Having now explored the variability of the light source, we can finally answer the question of the most suitable Q-factor of the resonant sensor. It is clear that the readout of such a resonant system is a convolution of the resonance linewidth and the source linewidth, discussed further in 5.3.iii. Given the wavelength tolerances of 1-3 nm for the low-cost sources that we have now established, high Q ($Q > 1000$, $\Delta\lambda < 1$ nm) modalities such as ring resonators are clearly not suitable for handheld sensor realisations.

Instead, medium-Q ($100 < Q < 1000$) realisations are preferable, which includes the guided-mode resonance (GMR) sensor modality. Typical GMR realisations exhibit a linewidth of a few nanometres (e.g. $Q = 190$ at 650 nm operation wavelength from chapter 3) which is in this range. Hence, the GMR sensor is ideal for the constraints discussed above. Since it is excited with a collimated beam that does not require tight focussing (e.g. to excite a waveguide mode), it is compatible with the RCLED, which is an extended source. In addition the out-of-plane excitation requires much lower alignment precision than e.g. firing a laser into the end of a waveguide or onto a grating coupler.

A further consideration is the thermal noise of the system, beyond that of the source as discussed above, being caused by the drift of the resonance due to thermal fluctuations of the instrument or the analyte. Such fluctuations can be mitigated via a reference channel or by engineering the thermo-optic coefficient of the waveguide/resonant structure [115]; in this context, it has already been recognised [6] that low Q sensors are less susceptible to thermal stability issues. Regarding the use of a reference channel, its ability to compensate temperature fluctuations is limited by the spatial separation between channels [32]. While it is difficult to provide hard numbers for the thermal-fluctuation limited performance of POC sensors, my interpretation of the literature is that the lower bound for the limit of detection in a non-thermally stabilised system is in the $10^{-5} - 10^{-6}$ RIU range [6, 32, 101,115].

A final consideration is the fact that the readout requires imaging of the GMR sensor, which assumes uniform illumination; in fact, when using a laser, the occurrence of speckle and fringes presented a major issue that degraded performance. The RCLED solution addresses this issue as well, as its non-coherent nature avoids any such interference effects. This is discussed further in the context of Figure 46 and the effects are explored in section 5.3.i and Figure 51. The complete system discussed for the rest of this chapter then consists of the sensor chip which is illuminated with the collimated, filtered RCLED and imaged onto the camera, with a beamsplitter combining the two beam paths as described previously in chapter 4.

5.2.ii. Camera choice

There are two options to consider for the camera sensor, i.e. charge-coupled device (CCD) or complementary metal-oxide-semiconductor (CMOS) technology [116,117]. Both types are available at low-cost and a CCD appears the more obvious choice given the technology's maturity. On the other hand, smartphone technology has driven down the price of CMOS sensors and driven up their technological development. Generally, it is considered that CCDs exhibit lower noise than CMOS sensors. Due to

the maturity of CMOS manufacturing and recent developments, especially driven by smartphone camera technology, CMOS cameras are now catching up. Let us consider the differences in operation and what that means for the application considered here.

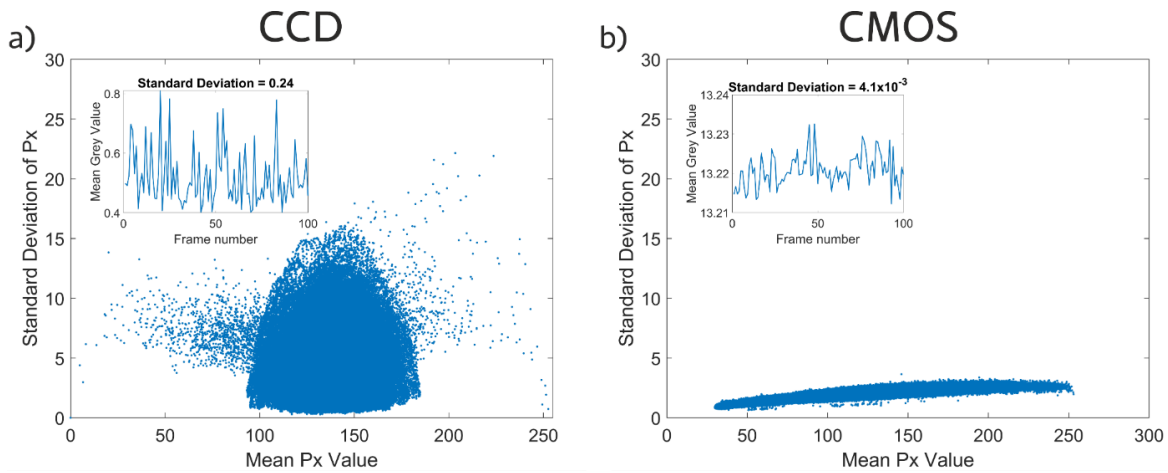


Figure 40: Readout noise of individual pixels taken from 100 frames with uniform illumination. Inserts show the camera bias (average pixel value) with no illumination. a) An example CCD sensor, OV9712 (OmniVision). b) An example CMOS sensor, DMM 72BUC02-ML (The Imaging Source GmbH).

CCDs employ a shift register to move the carriers generated at each pixel and then use a single amplifier per row of pixels. Because charges are shifted repeatedly during readout, CCD sensors experience temporal noise from the reading of each pixel at discrete times as well as the usual noise from the amplifier [118]. Temporal noise is an effect not usually noticed by the human eye, but it is an inherently time-dependent property, so it impacts on the sensor performance and will affect image data analysis more acutely. CCDs can also suffer from smear where excess charge 'bleeds' into adjacent pixels.

CMOS sensors have individual amplifiers per pixel, which means that CMOS sensors do not experience bleeding or temporal noise from pixel to pixel, however each pixel may experience different offsets and sensitivity curves. These variations lead to fixed pattern noise and gain noise; since these are fixed, they can be compensated and most manufacturers design driving circuits accordingly. Another parameter is the dynamic range, which tends to be higher for a CCD than for a CMOS sensor, because of their larger fill-factor (fill-factor is defined here as the ratio of pixel size to pixel spacing). CCDs are able to reach fill-factors near 100%, while most CMOS sensors cannot, due to the manufacturing techniques used in CMOS processing where the wiring is placed on top of the light receiving surface. There are CMOS sensors that are 'Back Illuminated' such as the Prime BSI Scientific CMOS from Teledyne Photometrics, but this technology has not filtered down to low-cost sensors yet and so is only seen in high-end applications such as scientific cameras. The most common solution to the low fill factor

of CMOS cameras is to put micro lenses onto the pixels to capture more light. Altogether, these factors lead to CMOS sensors having higher noise at low light levels, so it is important to work with sufficiently strong light intensities.

Given this wide parameter-space, it is difficult to make the right choice from datasheets alone. I therefore decided to conduct an experimental comparison, following the protocol outlined in [119] described below with results presented in Figure 40.

To ascertain the camera bias:

- 1) Set the camera to a zero millisecond exposure time, which will result in the shortest possible exposure.
- 2) Take 100 frames with no light incident on the sensor (I surrounded the sensor in blackout material).
- 3) Calculate the mean of each frame to track the change in bias in grey value. (Shown in the inserts of Figure 40a and b).

To ascertain individual pixel noise:

- 1) Set the camera to low exposure time (I used a 10 ms exposure time).
- 2) Take 100 frames with uniform illumination incident on the sensor that is not saturating the sensor.
- 3) Calculate the mean and standard deviation of each pixel across the 100 frames and track the sensitivity of each pixel compared to other pixels as well as its variation frame to frame. (Shown in the main body of Figure 40a and b).

A typical result is shown in Figure 40. The inserts show the mean grey values, which is the average grey value across a whole frame with no light incident on the sensor, across 100 frames. From the insert of Figure 40a, the CCD (OV9712 - OmniVision) shows a lower bias but a higher standard deviation. In an experimental setting, the variation in the bias would show as a variation in the intensity frame to frame much like a variation in source intensity noise. The higher bias in the CMOS sensor is needed to overcome the lower quantum efficiency from lower pixel filling fraction. It is interesting to see that for the main figures, taken with uniform illumination across the sensor, the CCD is more grouped in terms of mean pixel value compared with the CMOS sensor (DMM 72BUC02-ML - The Imaging Source GmbH). The reason for this difference is due to the single amplifier while the individual pixels of the CMOS present a much larger spread. However the CMOS again has a lower deviation in pixel value showing its lower noise overall despite the different sensitivities of each pixel. In the

system test in section 5.3.i, I validate that the CMOS camera is superior to the CCD, partly because it can reach smaller pixel sizes which is of great import to this work, but also because of its lower noise floor. However it is possible for a CCD to achieve the same noise level as the CMOS sensors used. It all comes down to parameter space and using what works for the specific implementation. In terms of the final goal of scaling up the technology, the CMOS camera is also given more weight as the technology has been driven by the smartphone sector.

5.2.iii. Visual Q and apparent sensitivity

The huge advantage of the chirped GMR approach is that it translates spectral resolution into spatial resolution; so the sensor information is captured by the pixels of the camera; how best to use the number of available pixels for the maximum performance of the sensor is then an interesting question.

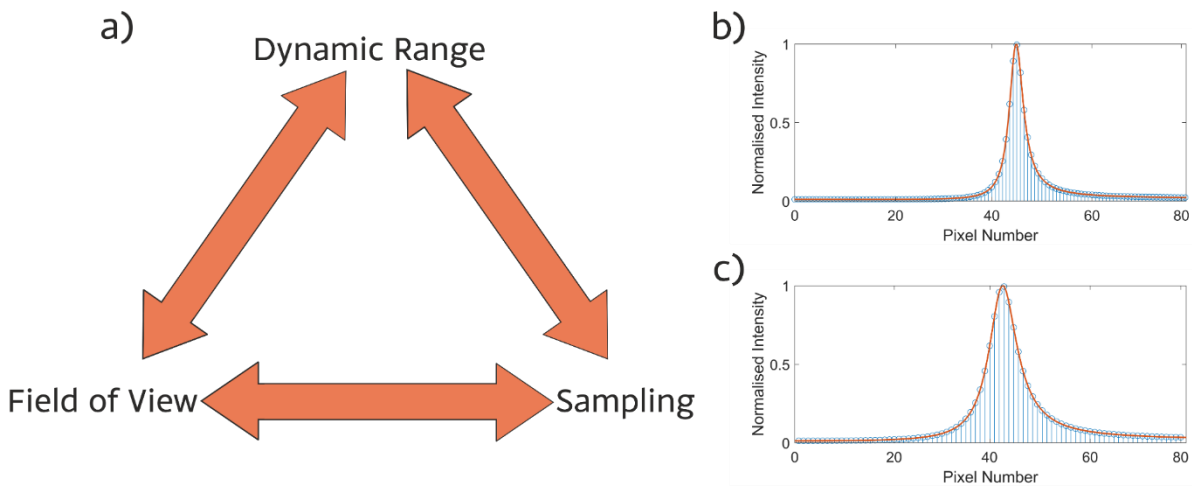


Figure 41: a) The trilemma of the interplay of three major factors for a chirped GMR sensor. b) A resonance representing a large period range chirp. c) A resonance representing a smaller period range chirp than b) which has more sample points across the full width at half maximum.

Having considered the various sources of noise, the pixel size impacts on the sampling of the image and thereby on the achievable accuracy of the curve-fitting. A larger number of pixels provides more information and affords a more accurate fit to the Fano curve (Figure 41b and c). This leads to an interesting trade-off between three parameters; sampling accuracy, field of view and dynamic range. This trade-off is illustrated by the “trilemma” of Figure 41a; better sampling requires more pixels, which can be achieved by increasing the magnification of the optical system, but this will reduce the field of view. A smaller field of view means that fewer measurements can be conducted in parallel, whether just a measurement and reference or a reference with multiplexed measurements (section 6.7). By increasing the magnification, the

resonance curve will also shift across a larger range of pixels for a given refractive index change, so the apparent sensitivity will be higher. This will also decrease the total refractive index range that can be measured, given the limited field of view. As a result the dynamic range of the measurement decreases. For a fixed structure, the dynamic range and field of view are equivalent, reducing our trilemma to a dilemma. When we consider that the chirp of the GMR can be changed over the fixed sensor size this becomes a trilemma.

The limiting factor of this remaining "dilemma", assuming a fixed chirp and sensor size of the GMR, is the pixel size and the total number of pixels, with a smaller pixel size and a higher number of pixels being desirable. Therefore, the CMOS sensor tends to be superior as its resolution is 2592×1944 pixels of 2.2 μm size, compared to the CCD with 1280×720 pixels of 3.2 μm size. Due to the way they are manufactured, CCDs generally have pixel sizes \approx 4 μm . CMOS cameras used in smartphone cameras are able to reach smaller pixel sizes, e.g. the DFM 37UX226-ML (from The Imaging Source GmbH) has a pixel size of 1.85 μm , which has a Sony CMOS STARVIS sensor.

A final point in favour of small pixel size is the optical magnification. For example, if we had two sensors of equal number of pixels, but of different pixel size, the larger sensor would then require a larger optical magnification in order to map the image onto the same number of pixels. This larger optical magnification would reduce the tolerance with respect to placing the sensor accurately into the imaging plane of the optical system. Since a larger tolerance is desirable for a low-cost realisation, lower magnification is advantageous. As a result, the optical magnifications targeted here were between 1:1 and 3:1.

5.2.iv. Fano tracking for time measurements

Throughout this work, the resonance has been tracked against time to measure refractive index changes. The resonance curve is found by converting the image into a line plot, fitting a Fano curve and determining its maximum. The key steps are as follows:

- 1) Select a region of interest from the image (shown in Figure 42a).
- 2) Average the pixel intensity along the resonance to obtain 1D data of intensity against pixel number.
- 3) Fit a fano function to the data (shown in Figure 42b).
- 4) Find the maximum of the Fano fit to use as the resonance position.

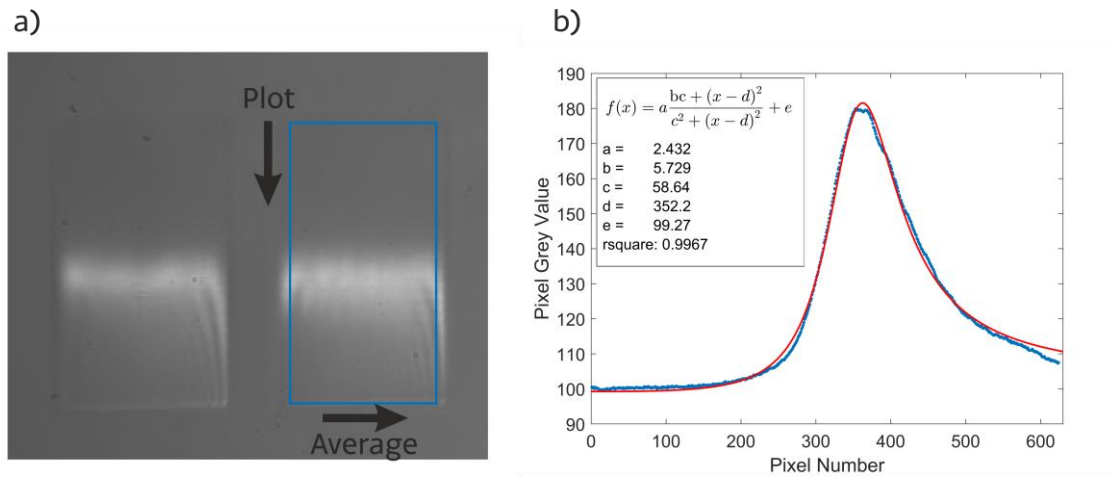


Figure 42: a) Example image of a chirped GMR with a selected region of interest used for fitting. b) Plot of the average pixel values averaged across the width of the region of interest in a) and fitted with a Fano function.

These steps are exemplified by Figure 42, with Figure 42a showing an example of a GMR sensor directly after fabrication; the x-axis of Figure 42b is the pixel number and the y-axis is the grey-value of the sensor. The fitting function shown in the inset of Figure 42b is a Fano lineshape [120] discussed in chapter 2. The coefficients of the Fano function, match up to real physical parameters. For example, "e" represents the minimum intensity of the resonance or background, "d" represents the peak position and "c" describes the width of the resonance. It is worth noting that all parameters are determined by simply mapping the resonance on to pixel values. It is important to note that for the most important parameter, "d", the absolute value is not particularly relevant, whereas its change is very much so, as it describes the shift of the resonance.

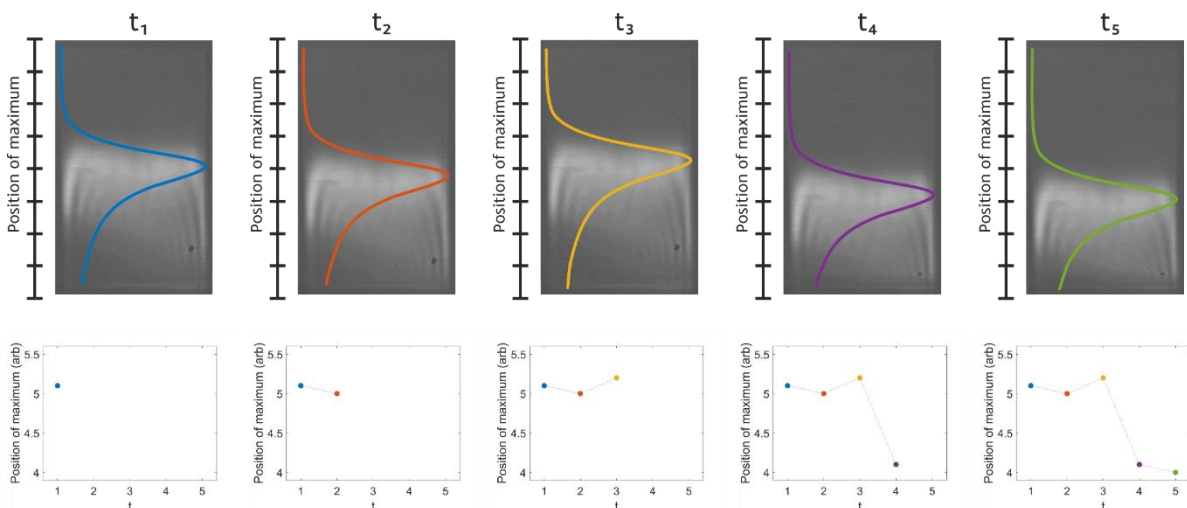


Figure 43: A graphic illustrating how the resonance is tracked by fitting the Fano resonance curve at different time points (for this work time is measured in seconds), also plotted as resonance position against time.

Using this fitting procedure to find the peak position has the advantage of both smoothing and interpolating the pixel values. This reduces the impact of imperfections on the sensor, such as fabrication defects. Using such a fitting approach allows for sub-pixel resolution as discussed in sections 5.3. Tracking the resonance against time is then just a case of repeating these steps, as illustrated in Figure 43. By plotting the change in resonance position against time for a fixed refractive index, a standard deviation of the position can also be obtained. It is understood that three times this standard deviation (3σ) is the accepted method for describing the noise of the system [6]. We found that the key noise source is the camera, as discussed in section 5.3, while drift due to temperature or mechanical drift can be normalised out via a reference channel (5.3.iv). For the remainder of this chapter, the importance of each parameter will therefore be measured by its impact on the 3σ value. It is this 3σ value that leads to the limit of detection (LOD), or smallest detectable change measurable, together with the sensitivity (in nm/RIU, see section 5.3.iv) S :

$$LOD = \frac{3\sigma}{S}$$

5.2.v. Scalability and nano-imprint lithography

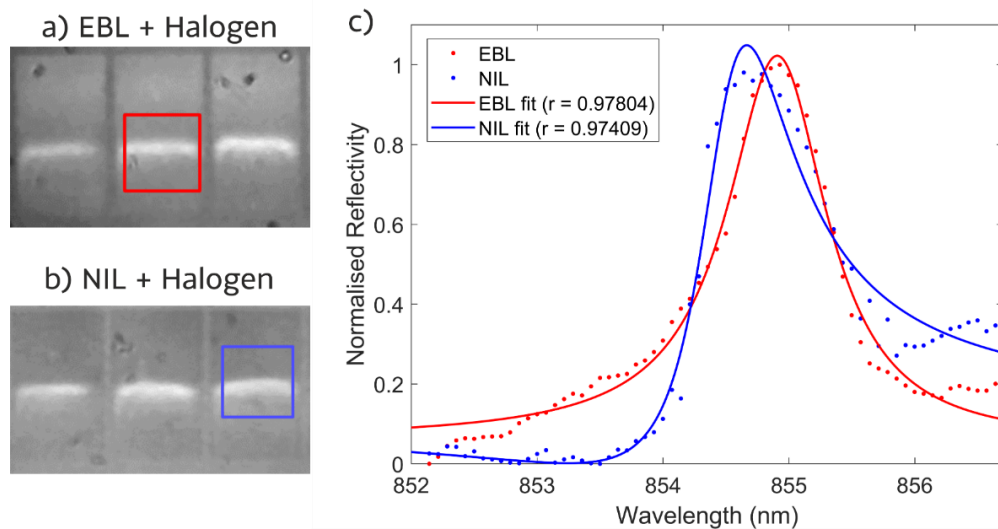


Figure 44: a) Camera image of a chirped GMR sensor produced by electron beam lithography (EBL) and illuminated by a halogen light source. b) Camera image of a chirped GMR sensor produced by nanoimprint lithography (NIL) and illuminated by a halogen source. The halogen source is filtered by a monochromator to achieve single-wavelength resolution. c) Normalised reflectivity of a) and b) demonstrating a very similar FWHM of 0.93 ± 0.01 nm and 1.07 ± 0.01 nm for the EBL and NIL samples, respectively. Reprinted with permission from [100] © The Optical Society.

For the purpose of my research, I used electron-beam lithography to define the sensor chip (cf. section 3.1.iv), which is neither low-cost nor scalable, so does not meet the

end goal of the device developed in the course of my research. I note, however, that the GMR sensor is compatible with CMOS technology, so could be mass-manufactured accordingly.

An alternative, low-cost and scalable method is nanoimprint lithography (NIL), which is briefly discussed here. In fact, nanoimprinted GMR sensor chips have already been demonstrated elsewhere, e.g. by Cunningham *et al.* [96,121,122]. Here, I compare NIL as a method of producing GMRs of the same design as those made by electron-beam lithography. The NIL sample was prepared by my colleague Dr Kezheng Li. The key steps are as follows:

- 1) A Si master is generated using electron-beam lithography.
- 2) Mix UV PDMS KER-4690 A and UV PDMS KER-4690 B in a 1:1 ratio and degas for 20 minutes.
- 3) Cover Si master in silane as a non-stick layer and pour on PDMS mixture. Expose with UV at 2.4 Wcm^{-2} for 14 minutes.
- 4) Spin-coat sample with nanoimprint resist (mr-NIL213FC-200nm_XP from Micro resist Technology GmbH) at 3000 rpm for 60 s.
- 5) Bake resist at $60 \text{ }^\circ\text{C}$ for 3 minutes.
- 6) Stamp resist with PDMS stamp and clamp together.
- 7) Expose with UV at 2.4 Wcm^{-2} for 7 minutes.
- 8) RIE etch samples and clean resist as in section 3.1.v and 3.1.vi.

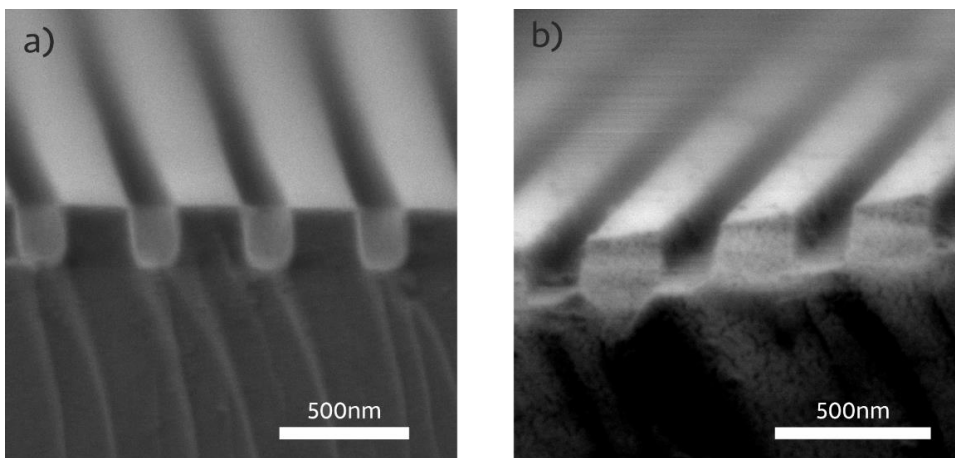
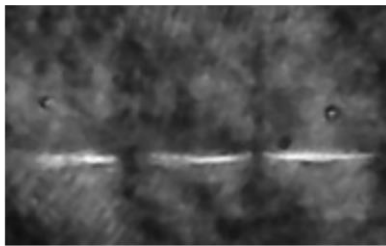


Figure 45: SEM micrograph of the edge face of a chirped GMR produced via a) electron beam lithography and b) nanoimprint lithography highlighting the similarity of the structures produced by the two processes.

Figure 44 shows a comparison and highlights that the linewidth and dynamic range of the resonance curves for both EBL and NIL are very similar. Figure 44c was taken using the regions of interest from the raw images shown in Figure 44a and Figure 44b and fitted with a line plot as described in section 5.2.iv. Twenty samples of nanoimprinted GMRs were tested, all of which show slight variations, with Figure 44 providing a representative example. The NIL sample has a slightly lower r value for the fit. Although this difference is only marginal, it is sufficiently small to highlight that NIL is a viable method. Figure 45 demonstrates the quality of NIL further by showing a cleaved edge of both types of samples. The NIL sample is slightly more trapezoidal in shape which is due to the peeling of the PDMS stamp. However, structural differences such as this one only exhibit a slight variation in GMR performance and only slightly impact on the resonance as seen in Figure 44c.

5.2.vi. Visual clarity: using RCLEDs

a) 850 nm Laser diode



b) 850 nm Halogen

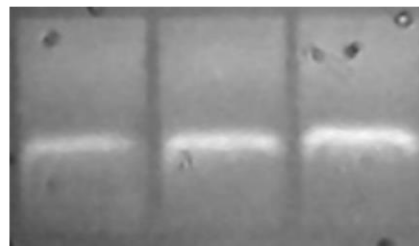


Figure 46: Chirped GMR sensors illuminated by a) a laser diode and b) a halogen source filtered via a monochromator to 850 nm wavelength with a full width half maximum ≈ 0.8 nm. Reprinted with permission from [100] © The Optical Society.

Next, I investigated the impact of the illumination source on the quality of the observed resonance. I compared the structure from Figure 44a by illuminating it with a laser diode and a halogen source filtered through a monochromator, which is the source typically used for laboratory measurements. The halogen source can also be understood as a proxy for the filtered RCLED, which could not be used in this particular comparison because of its 650 nm emission wavelength. The laser diode illuminated sample is shown in Figure 46a, which clearly highlights the narrower linewidth achievable with a narrowband source. The same figure also shows the speckle noise that arises from the coherence of the light source, which provides a significant background noise. By comparison, the halogen source in Figure 46b has a much cleaner image. NB I quantify the impact of speckle noise in section 5.3.i.

The speckle seen in Figure 46a and the wavelength noise of a laser diode (Figure 37a) confirms the use of a resonant cavity LED (RCLED) as a strong contender for the system to achieve a low limit of detection. To further support this choice, I compare a

chirped GMR structure and illuminate it with three different sources (Figure 47), i.e. a halogen source, an RCLED with a 1 nm filter and an RCLED with a 3 nm filter. The halogen was filtered down to a linewidth of 0.8 ± 0.1 nm with a monochromator, error was determined by the precision of the spectrometer used to measure the linewidth. The corresponding chirped GMR resonance curve (Figure 47d) shows a resonance FWHM of $97 \pm 1 \mu\text{m}$. The 1 nm filter closely matches this (FWHM = $110 \pm 1 \mu\text{m}$), with the 3 nm filter ($119 \pm 1 \mu\text{m}$) slightly broader. Here each error was determined by the error of the respective fit. Since the best results achieved by other members of the group have been realised with a filtered halogen similar to Figure 47a, this confirms that the RCLED with a 1 nm filter is a suitable choice for the handheld realisation of a GMR sensor.

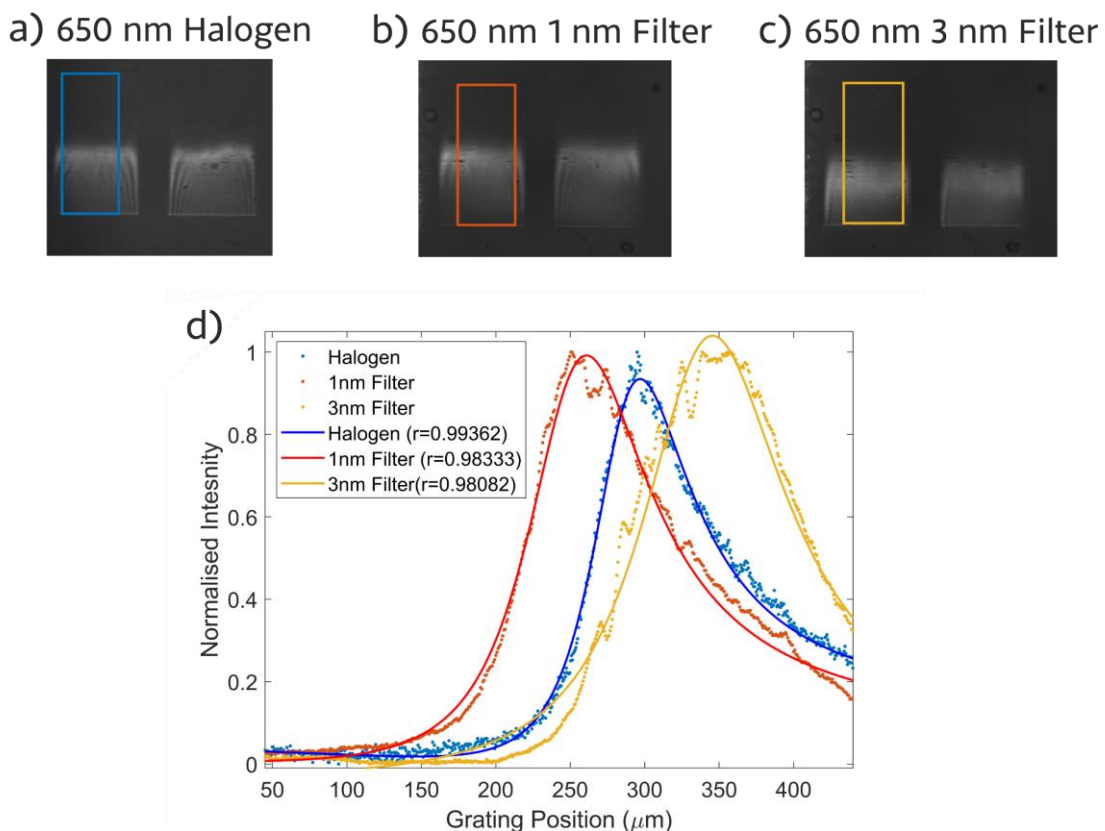


Figure 47: a) Chirped GMR sensors illuminated by a halogen source filtered via a monochromator to 650 nm wavelength with a full width half maximum ≈ 0.8 nm. b) Chirped GMR sensor illuminated by a 650 nm RCLED with a 1 nm linewidth filter. c) Chirped GMR sensor illuminated by a 650 nm RCLED with a 3 nm linewidth filter. d) Normalised reflectivity of a)-c) with FWHM of $97 \pm 1 \mu\text{m}$, $110 \pm 1 \mu\text{m}$ and $119 \pm 1 \mu\text{m}$ for the halogen, 1 nm and 3 nm filter illuminations, respectively.

As a further comparison, I determined the 3σ noise value of the system for a fixed refractive index applied to the surface of the sensor (Figure 48), using the instrument described in chapter 4. The traces show that the narrower linewidth of the 1 nm filter leads to a lower limit of detection than its 3 nm counterpart. It is interesting to note

that the lower intensity of the RCLED filtered down to 1 nm filter (see Figure 39) has little impact, and that the narrower linewidth is the main factor in achieving better noise performance.

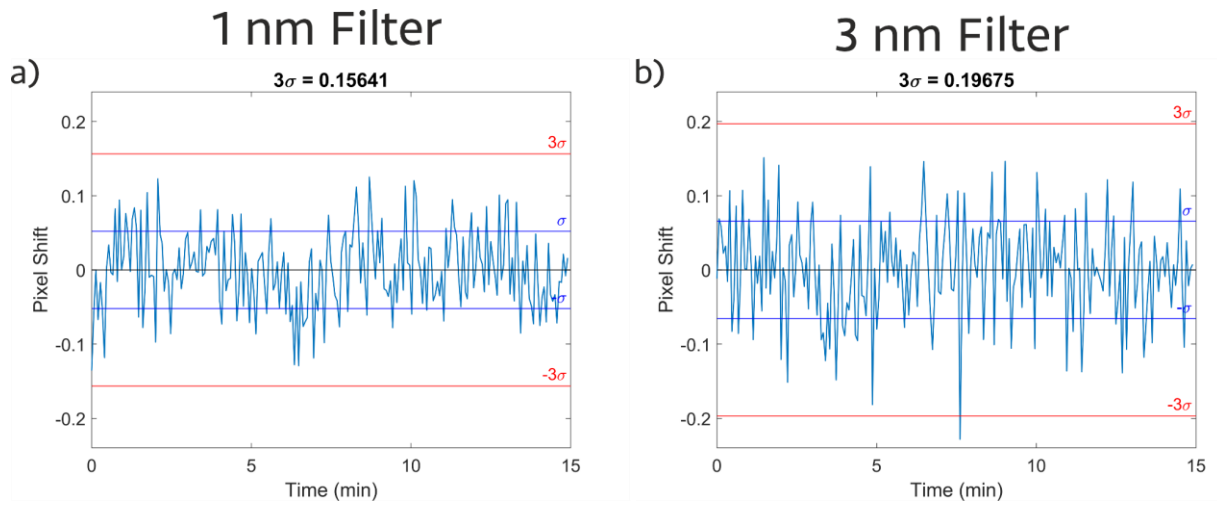


Figure 48: Comparison of the 3σ of a) 1 nm filtered RCLED and b) 3 nm filtered RCLED with fixed cover index of 1.3333.

5.3. Analysis of system performance

5.3.i. Parameters entering the performance comparison

In order to aid in the understanding and identification of the contribution of each noise source towards the overall system noise, I simulated the impact of the various components. The starting point was an ideal Fano resonance curve simulated with rigorous coupled wave analysis (RCWA), using the open source software S4 [56]. Various noise profiles, taken from experimental measurements, such as those shown in Figure 37a and b, were then superimposed onto this ideal Fano curve. The various noise sources were determined as follows:

Camera noise was obtained by measuring the variation of pixel values for constant illumination as described in the camera test protocol [119] and described in section 5.2.ii. The camera noise manifests itself as a white noise distribution across each point in the resonance.

Intensity noise of the illumination sources was obtained from the data shown in Figure 37b and their linewidth was simulated using a Gaussian lineshape. The intensity noise was the most straight forward to implement as the noise is the standard deviation of the Gaussian lineshape. This presents itself as a fluctuation of the

amplitude of the ideal Fano resonance. I note that the intensity noise only had a significant impact when the intensity was very low, yet the fluctuations in the amplitude do affect the fitting quality and so intensity noise was included for completeness.

Pixel size changes were represented by changing the sampling rate of the ideal curve to represent the number of pixels used to image a resonance. For example, by sampling the FWHM of the curve with 10 data points instead of 20, the pixel size is essentially doubled, as also discussed in section 5.2.iii.

Speckle noise was obtained experimentally by illuminating a fixed blank substrate with a laser and measuring the intensity variation of each pixel as described in section 5.2.ii but considering the variation pixel to pixel. Figure 49 shows the distribution of the pixel intensities across one image that has been normalised to remove camera gain differences. While the main peak occurs at similar values, there is a broader distribution for the speckle image. This also highlights the 'patchy' nature of speckle, where some areas are relatively unaffected, while others see a strong background signal as seen by the speckle data reaching extreme values.

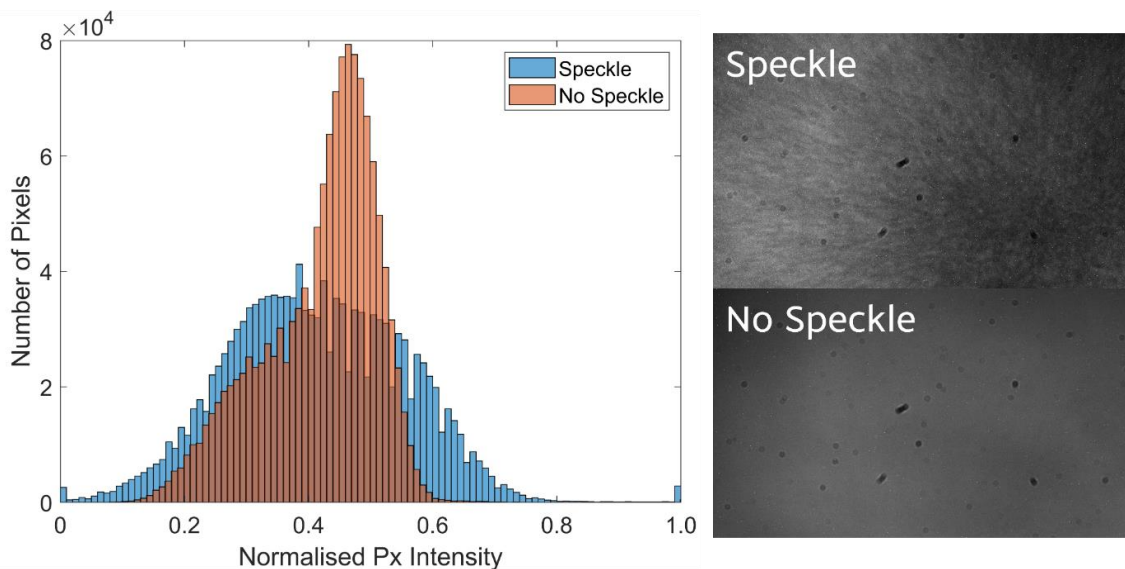


Figure 49: Histogram of pixel intensities across a normalised image when illuminated by a coherent source both with and without the use of a diffuser disk de-speckler with images shown.

Wavelength noise taken from Figure 37a was initially included, but was quickly discounted as it was by far the largest source of noise and overly dominated the study. The wavelength noise produced 3σ values equivalent to several pixels. Without wavelength noise, the highest combination of noise produced 3σ values of less than 2 pixels. This observation reinforces the arguments made in 5.2, i.e. that laser diodes

which are not wavelength stable are not suitable for point-of-care applications and that a filtered RCLED is a superior option.

Other parameters. There are a few more parameters to mention. Due to the minimal difference between GMRs written by EBL and NIL, highlighted in section 5.2.v, a lithography comparison was not included in the model. To assess the impact of the speckle noise from coherent sources alone, I included data that could be achieved with the use of a de-speckler, such as a rotating diffuser disc [123]. For this dataset, I assumed that the speckle-free laser source had the same characteristics as the laser line source without speckle.

5.3.ii. Nature of the model

In order to model this each type of noise was separately superimposed onto the original Fano resonance curve (illustrated in Figure 50). I used the *'normrnd'* function in Matlab® which randomly generates a value r from the normal distribution with expected value mu and standard deviation σ , $'r = normrnd(mu,\sigma)'$. The noisy data was then used to fit a Fano curve as described in section 5.2.iv. Each condition was repeated 200 times to simulate measuring a fixed refractive index and to generate a 3σ value, similar to the data shown in Figure 48, hence each repeat is assigned a time value based on the sampling speed of the real experiment.

Table 3: Noise contributions of the main elements to the system performance expressed as normalised standard deviations used in the noise model then normalised to the relevant pixel area. These numbers confirm the observation that once speckle noise is removed, camera noise dominates over intensity noise.

Noise Component	Standard Deviation (normalized value)	CCD 3.2 μm pixel size (px area affected)	CMOS 2.2 μm pixel size (px area affected)
Pixel Noise CCD	0.018	18×10^{-3} (1 px)	-
Pixel Noise CMOS	0.005	-	5×10^{-3} (1 px)
Laser Diode Intensity	0.393	0.8×10^{-3} (492 px)	0.5×10^{-3} (738 px)
Laser Diode Speckle	0.024	12×10^{-3} (2 px)	8×10^{-3} (3 px)
RCLED Intensity	0.138	0.2×10^{-3} (492 px)	0.1×10^{-3} (738 px)

Normalised standard deviations of each parameter contributing to the overall noise are shown in Table 3 for ease of comparison. The normalisation of the second column (Standard Deviation) in Table 3 are the σ values used in the model to overlay the curve with the steps presented in Figure 50. While the values in the second column of Table 3 serve as inputs to the *normrnd* function, they distort the comparison because they occur over different areas and need to be normalised. Therefore, columns 3 and 4 show the σ divided by the pixel area affected, i.e. by how many adjacent pixels would have the same *mu* value. This is an approximate way of showing which type of noise has the greater effect on the noise floor. The easiest way to explain this is to take the camera read noise on a pixel by pixel basis; therefore, the values in column 2 are the same as those in column 3/4. On the other hand, the intensity noise of the source is the same for all pixels as it affects the entire resonance equally. Therefore, I normalise to the full 492 px sampling area in case of the CCD and 738 px in case of the CMOS camera. If I then compare the σ value of 0.393 for the laser diode divided by the 492 px compared and compare it to the CCD read noise σ of 0.018, I note that the effect of the camera read noise is larger even though its value appears to be smaller. By normalising to the area, it is possible to compare the values in the table to one another. The comparison shows that speckle noise and camera noise of the CCD have the largest effect. In order to minimise system noise, I avoid speckle noise and use the CMOS camera.

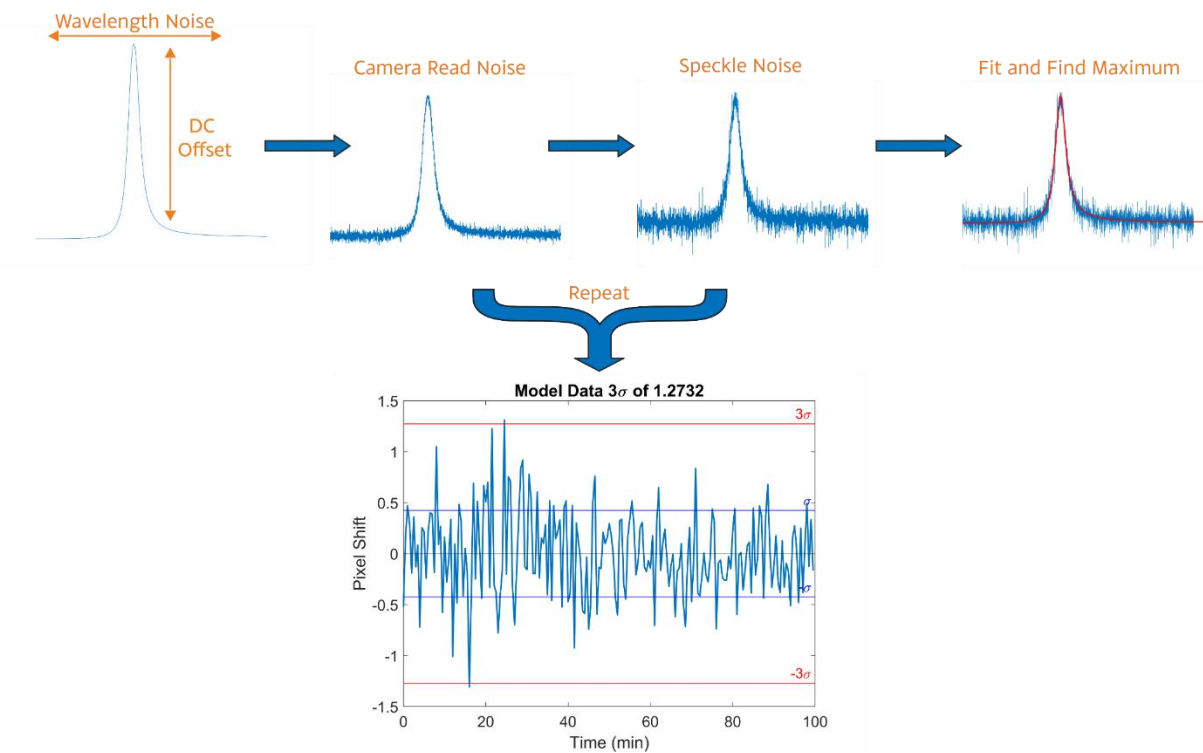


Figure 50: Steps used to apply noise to an S4 simulation to generate a predicted noise for the various components of the instrument considered here.

As noted above, the model tries to emulate the experimental reality as closely as possible. The only variation not accounted for are slowly varying effects such as mechanical or temperature-induced drift. For this reason, a reference channel is important, because it allows removing such slowly-varying effects.

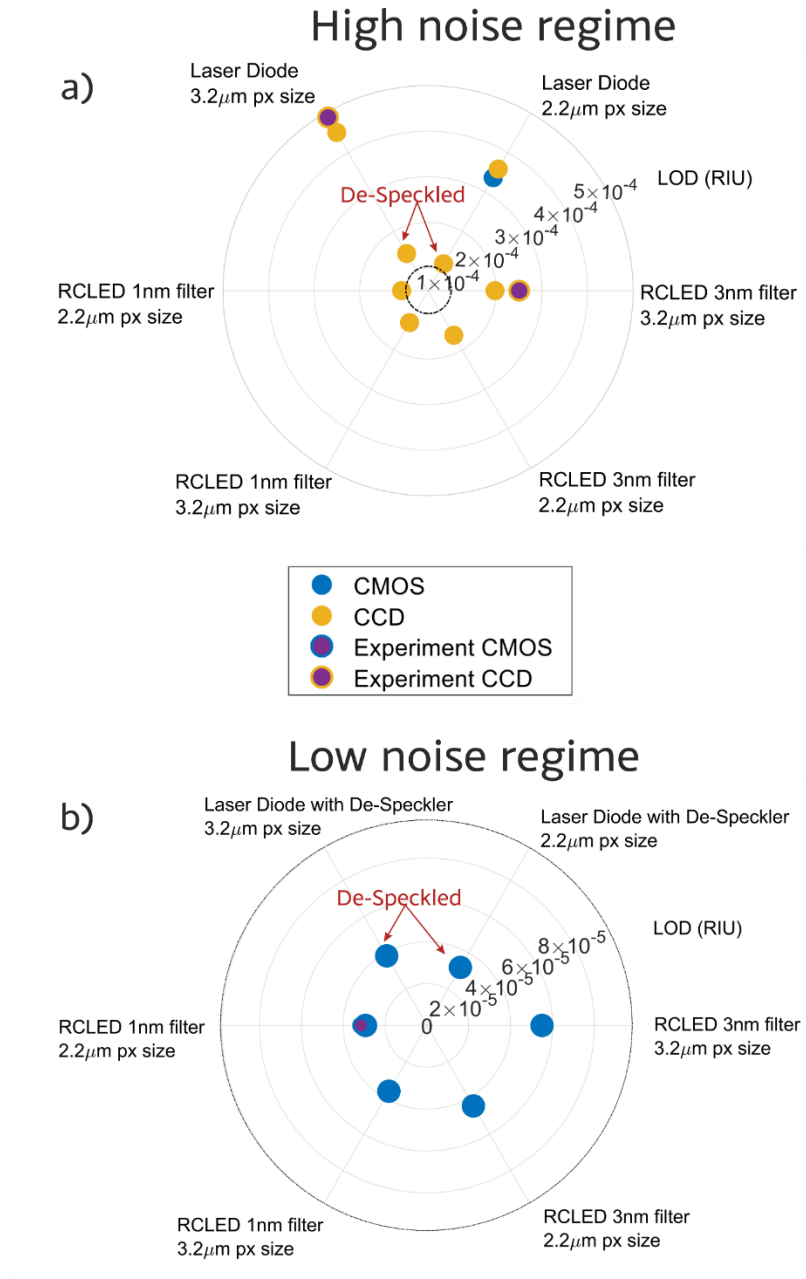


Figure 51: A plot showing the data from a Monte Carlo simulation of noise added to a simulated GMR spectrum compared to experimental values. a) Results greater than 1×10^{-4} RIU. b) Results lower than 1×10^{-4} RIU. The dashed line at 1×10^{-4} RIU in a) shows where b) sits in a). Note that in b), the experimental and theoretical points almost overlap for RCLED 1 nm filter, 2.2 μm px size which gives confidence in the model. Reprinted with permission from [100] © The Optical Society.

Each 3σ value was generated 20 times and averaged to remove the noise arising from the random number generation of the model, which is essentially a Monte-Carlo

simulation. These 3σ results of the model are then combined with the experimentally determined sensitivity (section 5.3.iv), to produce a limit of detection (LOD). The outcome is shown in Figure 51. I split the data into two separate ranges for clarity with Figure 51b sitting inside Figure 51a as indicated by the black dotted line at 1×10^{-4} RIU. In this polar plot, the radius represents the LOD in refractive index units, while each corresponds to a set of source and pixel characteristics. The two cameras (CCD and CMOS) are represented by different colours. Experimental values are indicated by a coloured ring and are discussed in more detail in section 5.3.iv below.

Figure 51 offers several important insights. Beginning with Figure 51, the disadvantage of the speckle noise of a laser diode outweighs its linewidth advantage. This insight is most obvious from the “Laser diode, 3.2 μm pixel size” data point. Once the laser diode has been “de-speckled”, the noise values drop into the low 10^{-4} range.

Regarding linewidth, it is interesting to note that the result achieved with the RCLED and the 1 nm linewidth filter is essentially the same as that achieved with a de-speckled laser of 55 pm linewidth from Figure 37a. This similarity is due to the relatively low Q of the resonance being closely matched to the 1 nm filter and so no advantage is gained from moving to a narrower linewidth source as the resonance linewidth remains dominant.

Another insight is that the noise from the camera had the largest effect for the two types of cameras compared, so the CMOS camera was significantly better than the CCD; this is highlighted by the fact that almost all of the points in the high noise plot of Figure 51a) are yellow and relate to the CCD. In contrast almost all the points in the low noise regime of Figure 51b are blue and have been obtained with the CMOS camera noise.

The pixel size then has a smaller effect, as shown by the fact that different pixel size values typically occur on similar radii, with smaller pixel size being slightly advantageous. Clearly, it is not possible to include experimental points for each parameter combination, but the few experimental values that are available have also been included in these graphs. These were obtained from the instrument configurations described in chapter 4. These instrument configurations were varied to accommodate the different light sources and cameras compared here while keeping the rest of the optics constant such as the imaging and collimating lenses as well as the beam splitter.

I note that the experimental noise values closely match those of the model for the three different experimental values available, which gives confidence in the general conclusions being drawn from the model. The best fit occurs for the RCLED with a 1

nm filter and 2.2 μm pixel size, which almost overlap. Overall, the comparison clearly shows that this model provides a very useful method for evaluating a varied parameter space.

5.3.iii. Impact of source and resonance linewidth on performance

In a related study, I considered the interplay between the linewidth of the source and that of the resonance (Figure 52); it is clear that the response of the system is a convolution of the resonance linewidth and the source linewidth, and the broader of these two linewidths will dominate the system response. While this principle is reasonably obvious and relates directly to the convolution theorem, it is useful to consider it quantitatively. In particular, it is interesting to consider how this convolution impacts on the overall limit of detection, hence I included noise in the study.

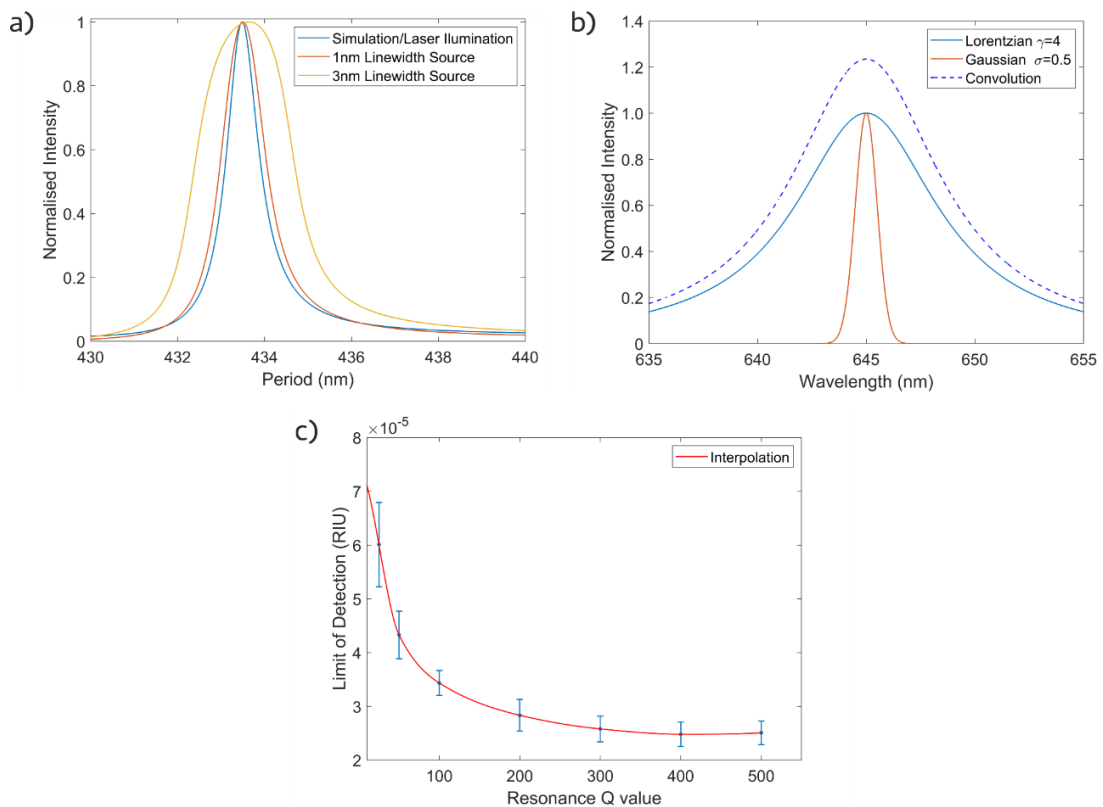


Figure 52: a) Plot of measured resonance linewidth for different source linewidths. b) Example of a convolution of a Gaussian source linewidth with a Lorentzian resonance. c) Limit of detection as a function of resonance Q value convolved with a 1 nm linewidth source.

In the study I considered the source linewidth as a Gaussian function, while the resonance function of the sensor follows a Fano curve, as mentioned in 1.2.ii, which reduces to a Lorentzian line shape when it has no asymmetry. Mathematically, the convolution of a Gaussian and a Lorentzian line shape is known as a Voigt profile [124]. In Figure 52b, I used the parameters for the 1 nm filtered RCLED source read out with

the CMOS camera of 2.2 μm pixel size. I then changed the linewidth of the GMR resonance, expressed as the Q-factor, and convolved it with the source. The results are shown in Figure 52c. Up to Q-values of 200-300, the limit of detection clearly improves, but then asymptotically approaches a value of $2\text{-}3 \times 10^{-5}$ RIU. It is also clear that for Q-values below 100, the limit of detection rises rapidly, so these should be avoided. Overall, this study supports the use of Q-factors between 100-200 that I have used throughout my research (section 3.2.iii). Clearly, the exact optimum depends on the particular parameters of each experiment, but a moderate Q-factor in this range appears to be a good choice for low-cost applications overall further supporting the arguments made in section 5.2.

5.3.iv. Experimental performance

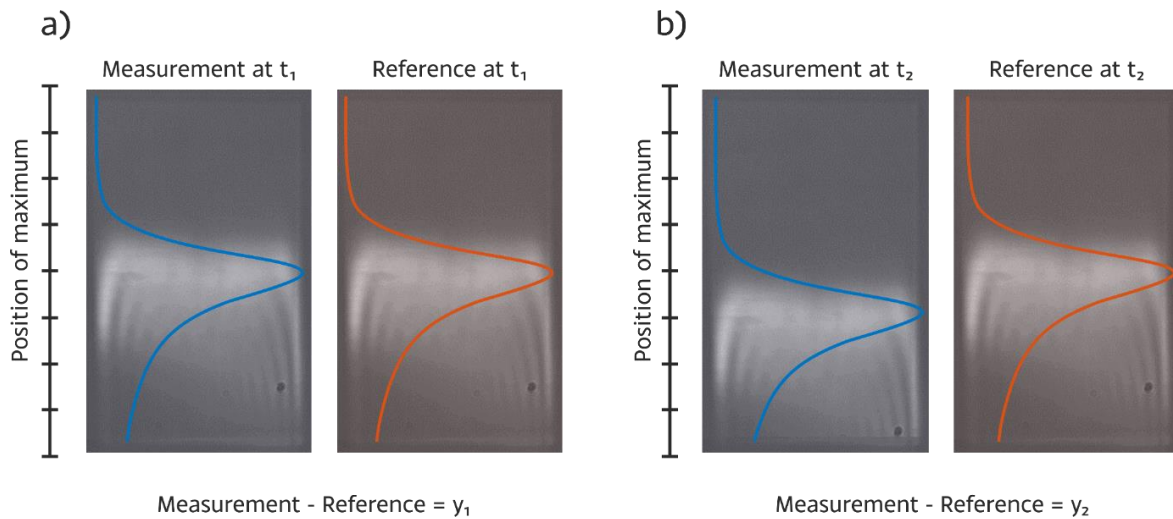


Figure 53: Illustration of the implementation of a reference channel. a) Initial measurement at time t_1 with measurement and reference channels returning the same result. b) At time t_2 , another measurement is taken. The true measurement value is then extracted from the difference in position between measurement and reference channels, thereby compensating for temperature and mechanical drifts.

Having identified the most favourable combination of elements, I conducted a systems test that aims to explore the performance of the best predicted combination in more detail. For this systems test, I used a GMR written by electron-beam lithography, an RCLED driven with 20 mA current with a 1 nm line filter and the CMOS camera (DMM 72BUC02-ML) with 2.2 μm pixel size. To achieve the maximum intensity without saturation of the resonance on the camera, an integration time of 600 ms was used. Given the simplicity and high transmission of the optical path, the spectrally filtered LED provides sufficient signal to produce a high dynamic range image on the CMOS camera. I chose an acquisition rate of 1 image every 4 seconds; this is sufficient to capture the biological events, which happen on a much slower timescale. This relatively

low acquisition rate was also chosen to reduce the amount of data collected and can also be used to create a rolling average, as discussed later in the context of Figure 55d.

With these parameters established, Phosphate Buffered Saline (PBS) at 10 mM, 20 mM, 30 mM and 40 mM concentrations in de-ionised water was used to measure the sensitivity (Figure 54b) and the system noise (Figure 55d); different concentrations of PBS produce different refractive indices. PBS was used instead of the glucose solutions used in the previous work [100] to avoid glucose precipitating on the sensor surface and affecting the measurement. The refractive index values of the different concentrations were verified with a refractometer. The limit of detection is given by dividing the 3σ noise value by the sensitivity as in section 5.2.iv.

Lowering the noise from each component eventually reaches a limit, as there are other sources of noise, such as thermal drift. A reference channel is implemented to account for this type of noise. By using two separate sensors on the same chip, so as to be in the camera's field of view and illuminated by the same source, the shift of one is subtracted from the other. When the measurement sensor is exposed to a refractive index change and the reference solution's refractive index is constant, any shifts due to temperature and other factors are removed. Figure 53 illustrates this principle whereby only one sample shifts due to an analyte. In this configuration, if both the signal and the reference experience a refractive index shift, e.g. due to a temperature change, then the relative shift is zero, leaving only the shift of interest, due to the nature of the analyte. An example for this removal of drift is show in Figure 54. Figure 54a shows the shifts from the measurement and the reference channel, both exhibiting a downward background trend while the measurement channel also records a refractive index shift. By subtracting the two channels, the drift is removed, resulting in Figure 54b, which only shows the resonance shift of interest.

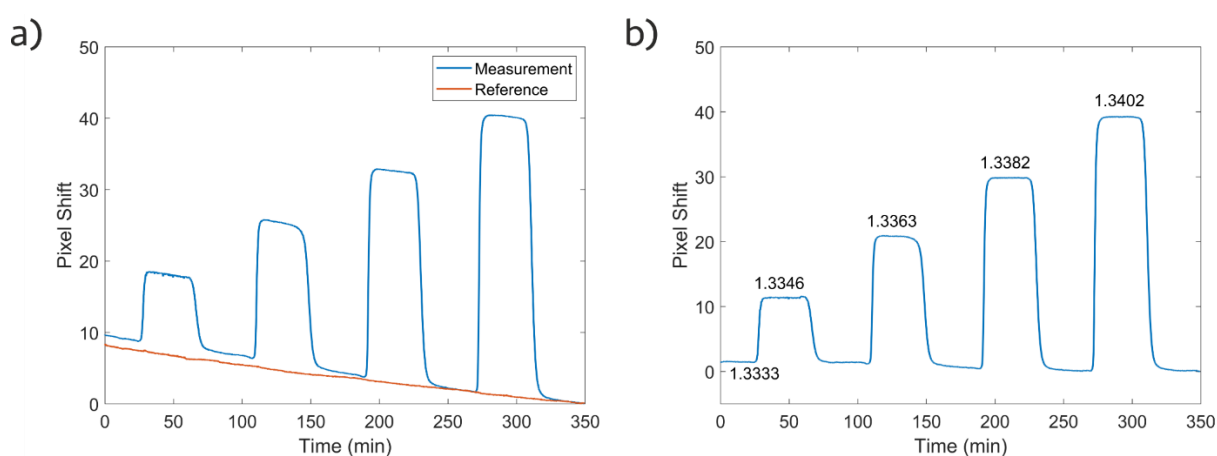


Figure 54: A Bulk refractive index measurements. a) Pixel position of both the measurement and reference channels. b) Difference of the reference and measurement positions in figure a) removing drift from temperature.

While using a reference channel is a powerful tool, it is not without its limitations, such as the field of view requirement for the reference channel. One further problem is that the spatial separation of the two channels can lead to a discrepancy between the temperature drifts seen by each channel, thus the channels should be kept closely together. While there are solutions like covering the reference sensor in a solid material such as glass or using an incubator around all the sensors, these both have issues. In a future device there would be a single flow channel with only specific sensors functionalised. And yet, as the difference in drift happens over the course of 6 hours it is not substantial on the scale of a protein binding assay which roughly a few 10s of minutes (see chapter 6), therefore this configuration should suffice for the intended purposes.

The measurement shown in Figure 54b displays the resonance shift for different concentrations of PBS. By taking the pixel shift divided by the refractive index change the sensitivities of each step can be determined. The values are $8.8 \pm 0.7 \times 10^3$ px/RIU, $6.9 \pm 0.2 \times 10^3$ px/RIU, $6.1 \pm 0.1 \times 10^3$ px/RIU and $5.69 \pm 0.09 \times 10^3$ px/RIU for 10 mM, 20 mM, 30 mM and 40 mM respectively. The errors in the sensitivity values are dominated by the refractometer precision (1×10^{-4} RIU). The drop in sensitivity as refractive index changes stems from the relationship of the resonance shift to cover index shown in chapter 2. For the purposes of calculating limit of detection I use the average sensitivity of $6.8 \pm 1.4 \times 10^3$ px/RIU, with the error being the standard deviation of the four values. This estimation is conservative as it underestimates the sensitivity for small refractive index changes and the expected shift for protein binding occurs at the low end of this range. Furthermore, the refractometer has a precision of 1×10^{-4} RIU, which is also well below the error of this sensitivity approximation. It is worth stating that for each assay, a look-up table is needed to calibrate the response of the sensor; the reason for this is not only to compensate for the non-linear relationship of cover index and resonance wavelength, but also for the non-linearity of surface binding dynamics since each protein having a different conformation and dissociation constant K_d (chapter 6).

Figure 55 shows in more detail how the 3σ value is obtained. Figure 55a highlights the window taken, while Figure 55b and c show the individual 3σ values for the reference channel and measurement channel, having had the thermal drift removed for comparison purposes. It is interesting to note that the reference channel has a higher 3σ value than the measurement despite having a lower R^2 (see inset of Figure 55a). The cause of the 3σ difference is most likely due to the limited field of view and sub-optimal collimation achieved in the instrument. This will lead to each grating having a slightly different resonance width due to varying angular components. Figure 55d then shows the 3σ value for the difference between the two channels with the main trace

in blue producing a 3σ value of 0.215 ± 0.009 px. The error here is given by the standard deviation of the 3σ values from each of the 9 flat sections in Figure 54b. Combining this 3σ value with the sensitivity determined above results in a limit of detection of $3.13 \pm 0.64 \times 10^{-5}$ RIU. The error on this value is mainly due to some of the assumptions made when determining the sensitivity as discussed above, it dominates over the error from variation in the 3σ value between multiple measurements.

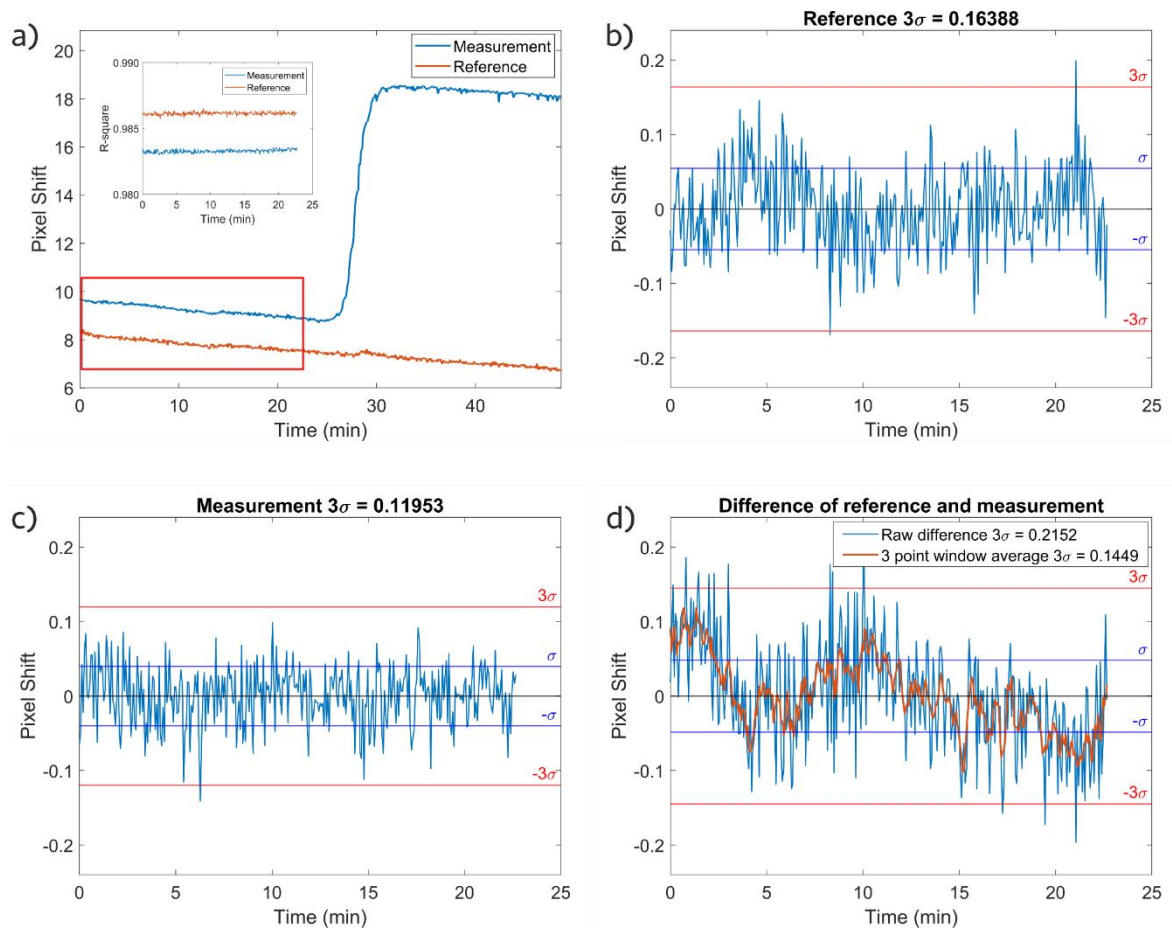


Figure 55: a) section taken from Figure 54 used to calculate the 3σ values of the instrument, insert showing rsquare values for each data point. b) and c) 3σ calculated for the reference and measurement channels respectively for regions shown in a) the drift has been removed for comparison purposes. d) 3σ calculated for the difference of the reference and measurements shown in a) as well as a rolling average to reduce difference noise.

Due to the noise shown in the 3σ graphs being white noise, it will compound when the reference is subtracted from the signal. Conversely combining the measurement and reference 3σ values in quadrature ($\Delta a^2 = \Delta b^2 + \Delta c^2$) yields a slightly lower combined 3σ of 0.203 px. This additional noise from the channel subtraction can be mitigated by taking a rolling average of the trace, essentially applying a low pass filter. For example, the red line plot in Figure 55d is taken by using a window of three points (12 s in real time measurement). By employing this technique, the 3σ drops to 0.1449 px which is

below the value of the original two channels combined in quadrature yielding a small improvement to a LOD of $2.11 \pm 0.43 \times 10^{-5}$ RIU.

Some alternative approaches to reducing the noise increase from channel subtraction are either filtering both channels individually or subtracting the trend of the reference. However, neither of these methods are as efficient for real time measurements as the former requires more calculations and the latter requires the full dataset.

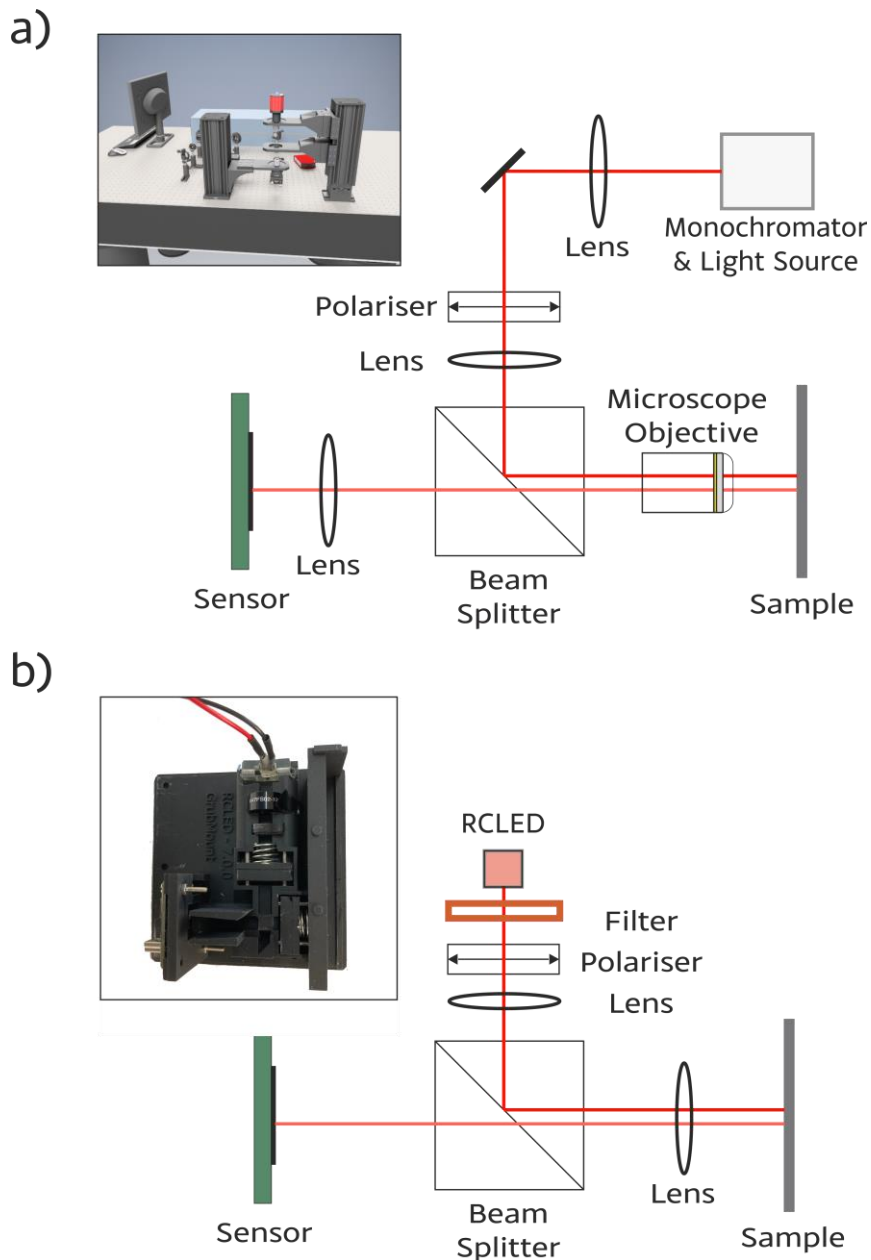


Figure 56: Schematic diagrams of a) the laboratory setup that was the basis for miniaturisation and b) a schematic of my instrument.

Having now considered all sources of noise and optimised the instrument accordingly, it is interesting to consider how it compares to the laboratory setup. For example, Keenan *et al.* were able to measure biological assays down to concentrations of

1 pg/mL [92], using a filtered supercontinuum white light source however our group has more recently moved to filtered halogen sources [30]. Figure 56 shows a comparison of the two setups; the optical magnification of the laboratory setup produces 1.78 px/ μm on the GMR sensor with a 10 \times objective; my instrument has 1.28 px/ μm with a magnification of 2.82 \times .

Figure 57 shows the corresponding 3σ values taken on both setups. As these measurements were made without a reference channel, the thermal drift has been removed by a linear fit to aid in comparison.

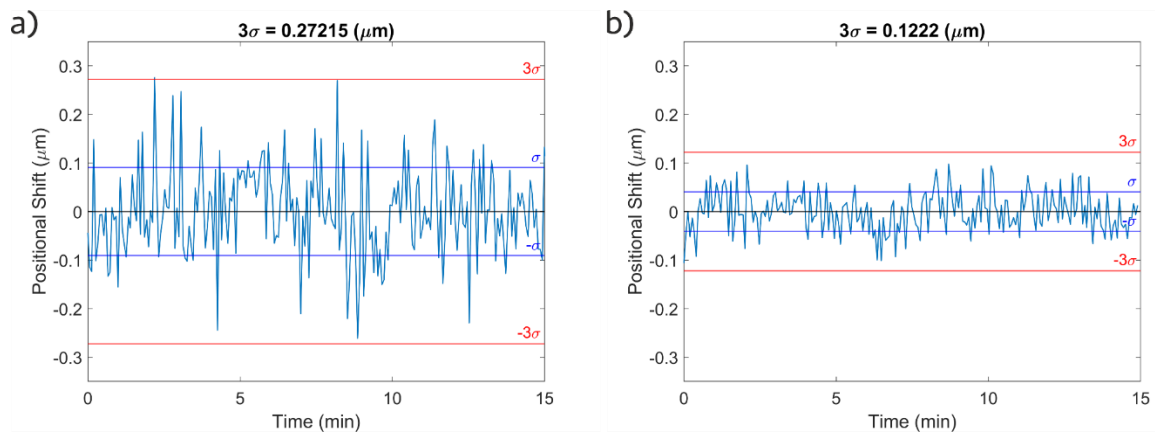


Figure 57: Comparison of the 3σ noise in terms of the spatial shift of the resonance on the GMR sensor chip for ease of comparison for a) the laboratory setup using a halogen light source and monochromator and b) the instrument using a 1 nm filtered RCLED.

The surprising result of the comparison is that the laboratory setup has a 3σ that is $\sim 2\times$ higher than that of my instrument. This difference seems at first counterintuitive, as the full setup achieves a narrower linewidth of 0.82 nm, as discussed in section 5.2.vi, and it uses a much more expensive camera (Photometrics CoolSNAP™ DYNO) with much better noise than the low-cost camera in the instrument. On the other hand, the laboratory setup uses a 100 W halogen source with a spectral density that is much lower than that of the RCLED. The laboratory setup uses many more optical components such as the monochromator, which has less throughput than the fixed filter used for the RCLED. To quantify these observations I used a Thorlabs inc. PM100D power meter. I measured the light incident on the sample to be 17 ± 3 nW for the laboratory setup and 460 ± 20 nW for my instrument. This significant difference is likely to impact on the SNR of the camera sensor. Other contributions to the noise may be spurious reflections from the various optical components. While such reflections are indeed present, both setups use antireflection coated components for the respective wavelengths to minimise these.

In summary, the above measurements make it clear that the simplifications and use of lower cost components in my instrument achieve a similar or better performance than an equivalent laboratory setup. This, in fact, is quite a remarkable conclusion which highlights the potential of the technology to be used in a handheld instrument for real applications.

5.4. Contrast enhancement using polarisation

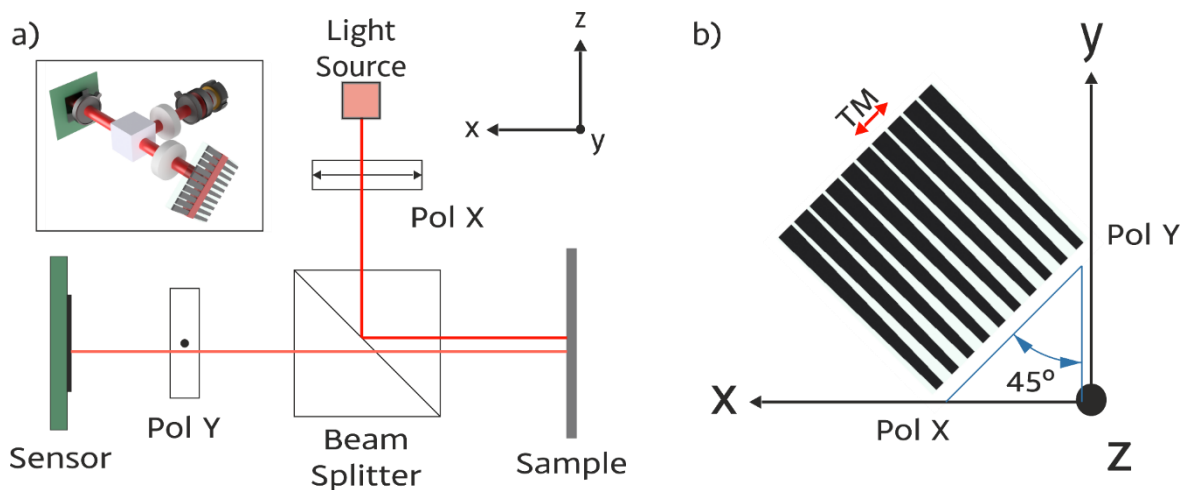


Figure 58: a) Modified setup used to test the benefit of cross-polarisation as a noise reduction technique by inserting two polarisers oriented orthogonally to each other. b) Placement of the chirped GMR sensor at 45 degrees to the orientation of each polariser.

As mentioned above, spurious reflections are minimised by antireflection coating but are still present. As a further attempt at reducing this background and improving contrast, I explored the idea of using polarisation. The principle is based on the resonant scattering method [125] illustrated in Figure 58. The method involves using polarised light incident on the sample with the GMR resonance oriented at 45°. Therefore, the component of the incoming light which is aligned with the resonance can couple to the resonance; on the output side, an analyzer is placed at 45° to the resonance and at 90° to the input polarisation, so it only passes a component of the resonance, yet all the light that has not coupled to the resonance is fully rejected. The key point is that only light coupled to the resonance has its polarisation changed and so is the only light to transmit through the analyser. Any background light and spurious reflections from the substrate or other optical components are filtered out.

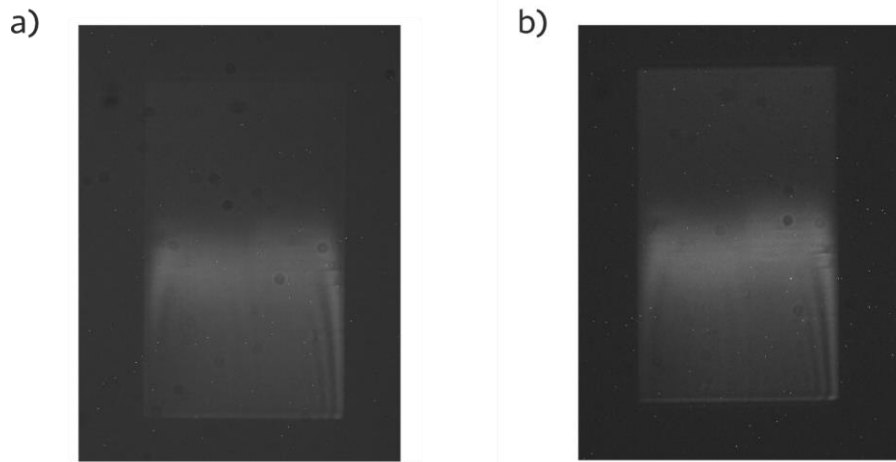


Figure 59: Contrast adjusted images taken at 100 ms exposure with fixed gain. a) GMR TM resonance using a single polariser aligned to the TM resonance. b) TM mode using the polarisation contrast enhancement method.

The result is shown in Figure 59 with a) showing an image taken with a single polariser on the source to only excite the TM mode as described in chapter 4. Figure 59b shows a comparable result taken with the cross-polarisation method. These images have been post-processed to increase the contrast, as some light is lost by the use of the extra polariser. In both cases, the resonance is the only real feature producing contrast. Figure 60 plots the corresponding noise traces and 3σ values of 0.143 px and 0.155 px for contrast enhanced and not enhanced, respectively. The difference is only marginal and may be due to other reasons, such as variations of the sensor chip etc. In conclusion, the gain from this cross-polarisation technique were only marginal and so the technique was not implemented in the instrument.

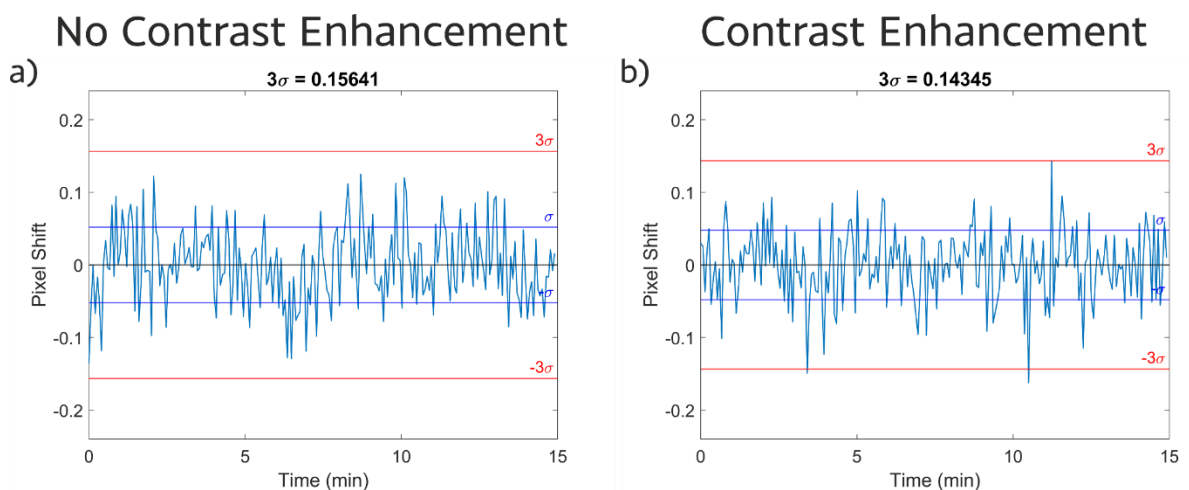


Figure 60: Comparison of the 3σ of a) chirped GMR with no contrast enhancement b) mode using contrast enhancement as shown in Figure 58 with cover index of 1.3333.

It is worth noting, however, that cross-polarisation may be useful if a laser-based system is considered after all, for example to remove some speckle noise. As an

example, I compare a GMR illuminated by a laser source, with and without cross-polarisation in Figure 61; it is clear that polarisation removes much of the speckle noise, although not perfectly so. This yet again shows that the simplest way to deal with speckle noise is to use an incoherent source where possible, such as the filtered RCLED I adopted.

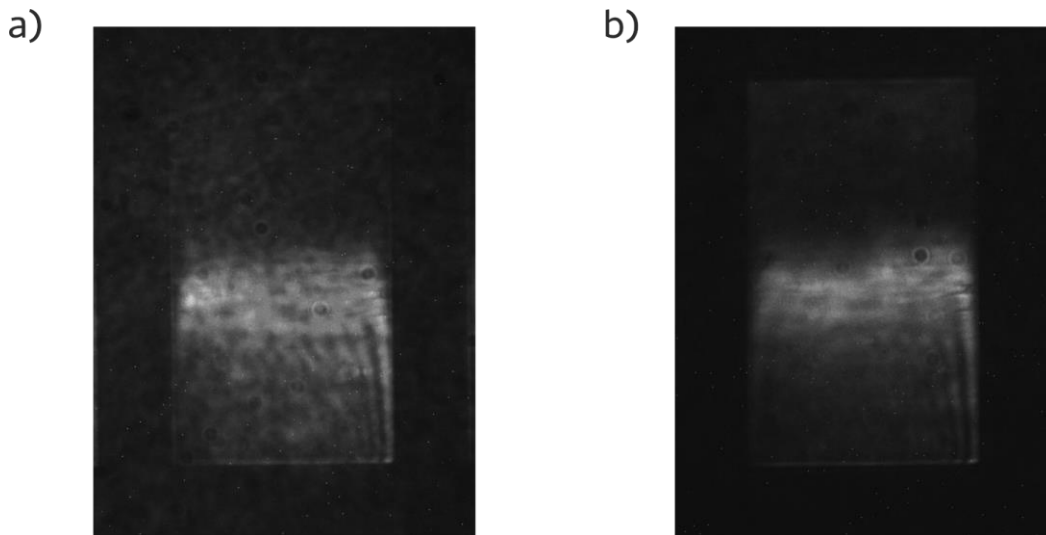


Figure 61: a) TM resonance of a chirped GMR using a coherent source exhibiting speckle. b) TM resonance of the GMR sensor with cross-polarisation applied.

5.5. Comparison with other modalities

The results presented in this chapter have clearly shown that a resonant sensor with a moderate Q-factor together with a filtered RCLED source is a viable approach for realising a handheld biosensor. Naturally, it is worth comparing my results with others presented in the literature (Table 4). When doing so, it is clear that handheld low-cost systems usually use low Q resonances; many also use broadband (LED) sources and camera sensors.

The LOD value for my instrument is in the lower end as compared to the other modalities. This insight is confirmed by a recent review of other refractive index sensors in laboratory setups as discussed by M. Soler *et al.* [126], where the state-of-the-art for photonic crystals is stated as an LOD of 10^{-5} RIU. Devices using single mode waveguides excited with grating couplers tend to achieve an order of magnitude better than this and microrings and nanoplasmonics are another order of magnitude better. This goes to show that the understanding of the noise has successfully addressed many of the limits to accessing low-cost point-of-care devices. On the other hand, I believe that reaching an LOD of $\approx 10^{-5}$ is sufficient for the detection of protein concentrations

in the pg/mL range. This is highlighted in the review by Pitruzello *et al.* [127] and, of course, by the work by colleagues in my own group [30,92] (cf. discussion on Figure 57). I also note that most clinically relevant proteins are present at concentrations in the ng/mL or µg/mL range, so achieving ultimate sensitivity may actually be less important than low-cost and portability.

Table 4: Summary of some photonics modalities used for low-cost approaches to biosensing.

Sensor	Source	Read Out	LOD (RIU)
1D GMR (this work)	RCLED	Camera Sensor	$3.1 \pm 0.6 \times 10^{-5}$
1D GMR Intensity Readout (Gerken group) [128]	LED	Photodetector	1.6×10^{-3}
Mach-Zehnder Interferometer [102] (Antelope system) [129]	superluminescent diode	Camera Sensor (Arrayed Waveguide Grating)	$6 \pm 2 \times 10^{-6}$
1D GMR (Cunningham group) [104]	Tungsten lamp	Smart Phone Camera (Diffraction Grating)	1.1×10^{-3} [130]
Plasmonic NanoHoles (Altug & Lechuga groups colaboration) [107]	LED	Camera Sensor	5.7×10^{-4}

In order to better understand the differences between the modalities shown in Table 4, we can classify these into intensity-based and spectral-based readouts. The intensity-based readout is attractive as it is even simpler by directly measuring an intensity rather than by requiring a spectral fitting process. An example for such an intensity-based readout is the photonic crystal sensor shown by Paulsen *et al.* [128] in the second row, who only use a photodetector. Unfortunately, this modality is also more susceptible to the intensity noise of the source; as a result, they report an LOD in the low 10^3 RIU range. I note that the difference between this intensity-based readout and the spectral readout pursued here and the rest of Table 4 is analogous to AM and FM encoding in communications, with AM being known to be more noisy; the cost of lower noise in FM is a higher bandwidth requirement, which is equivalent to

the need for collecting more data for a spectral readout. My instrument, using a fitting method makes it an 'FM' technique and thus not as susceptible to intensity noise as discussed in section 5.2. Similarly, the solution presented by Martens *et al.* [102] is particularly interesting in this regard and probably represents the most highly performing low-cost sensor we have found. They use a Mach-Zehnder interferometer to provide a highly sensitive response, which is intrinsically an "AM" solution due to an interference signal being a superposition of two amplitudes, but then they feed it through an arrayed waveguide grating, acting as a spectrometer, to create "FM" data which elegantly mitigates the effect of intensity noise, again by fitting to the output mapped spatially onto a camera sensor. With this configuration, they are able to achieve a limit of detection of 6×10^{-6} RIU. On the other hand, theirs is an intrinsically waveguide-based solution, which requires the difficult coupling step from free space into a single-mode waveguide. They overcome this with a superluminescent diode [131], which is very bright, so they manage to couple a sufficient amount of light despite the poor coupling efficiency. The other issue is the fundamental "philosophy" of their approach, which is based on silicon photonics and the associated scalability. While it is true that silicon photonics circuits can be produced at very low-cost, this is only true if they are produced at very high volumes, which, together with the high cost of the superluminescent diode, somewhat weakens the "low-cost" argument for this modality.

5.6. Discussion and conclusions

I have presented some considerations for resonant refractive index sensors with low-cost components and have considered the impact of various noise sources on the overall systems performance. From these studies, it can be concluded that the nature of the light source is a key determining factor for the nature of the sensor; while many previous studies have based their findings on a stabilised light source in a laboratory, the wavelength variations and wavelength noise of available low-cost sources precludes the use of a diode laser. In fact, a filtered LED is a better solution. From this conclusion, the obvious consequence is to use a sensor with a low-to-medium Q-factor. The guided mode resonance (GMR) sensor with a Q-factor of 190 at a wavelength of 650 nm illuminated by a resonant cavity LED (RCLED) through a $\Delta\lambda = 1$ nm filter exemplifies this conclusion. With the wavelength noise minimised by this approach, other noise sources then dominate, with the camera and the readout system making the next most significant contribution to the noise floor.

With regard to cost, I estimate that the original equipment manufacturer (OEM) cost of all the components could be as low as £10 (see section 7.2). This cost is based on assumptions, such as injection moulding of parts that have been 3D printed and using the minimal size for the filter which is one of the more costly components. Beamsplitters tend to be expensive when bought individually, but their use in optical disk drives suggests that they can be procured at very low-cost when bought in volume. On the other hand, a beamsplitter throws away a significant amount of light and also is a source of spurious reflections. Therefore, a setup whereby the GMR sensor is illuminated at an angle with the camera picking up the specular reflection is of interest (c.f section 7.1.i).

In terms of the readout, using a camera is a very cost-effective solution, based on the advances driven by smartphone technology, and it should be noted that the camera readout is the dominant source of noise; this is especially true since the throughput of the optical system is very high such that the camera operates well above its dark noise limit. By comparing a CCD and a CMOS sensor, I found that a CMOS camera gives superior results, both from its experimentally measured noise but also from its smaller pixel size that affords better sampling. However, the parameter space is so large for camera sensors that these experiments have only been able to sample a few data points and do not claim to make a comprehensive assessment. Given that a chirped GMR uses an imaging approach to extract the spectral information, using the filtered LED provides the added bonus of avoiding speckle noise, which has been identified as the dominant source of noise when a coherent light source is used.

In summary the insights gained in this study have helped me to develop a low-cost, high performance refractive index sensor based on the guided mode resonance (GMR) modality. The GMR has achieved a refractive index limit of detection of $3.13 \pm 0.64 \times 10^{-5}$ RIU. The limit of detection presented here is comparable to other, laboratory based systems that have measured biomarkers at clinically relevant concentrations, so it can be expected to also be able to detect proteins in the low ng/mL or pg/mL range. For example, Cetin *et al.* [132] have shown in laboratory measurements that plasmonic nanohole arrays with a refractive index limit of detection of 2×10^{-5} RIU can detect 700 pg/mL of IgG; the same configuration later achieved 145 pg/mL of vascular endothelial growth factor [29]. Luan *et al.* [133] have shown that with a limit of detection of 3.3×10^{-4} RIU, they can reach detection limits of 5.5 ng/mL for biotin. Kenaan *et al.* [92] have demonstrated the detection of 10 pg/mL for CRP with a stated LOD of 5.8×10^{-5} RIU for a GMR system in the laboratory. Using my system to conduct biomolecular measurements is the subject the next chapter.

6. Biological measurements

6.1. Relevance of biological assays

The desired application for the sensors described in this thesis is their use as an immunosensor, i.e. to detect protein biomarkers via antibody-antigen binding [134–137]. In order to facilitate this application, the sensor is functionalised with a capture molecule (antibody) and when a solution containing the proteins of interest (antigen) is flowed over it, they will selectively bind to the surface. There are many different protein biomarkers in the human body, each of which are indicative of certain health conditions. Here I focus on C-reactive protein (CRP) and Immunoglobulin G (IgG), as both molecules are commercially available and have clinical relevance. CRP is a marker for inflammation in humans [138] and IgG forms part of the body's general immune response [139]. In humans, the nominal level for CRP is $< 10 \mu\text{g/mL}$ with general levels varying based on age, gender and ethnicity and of course health [140]. IgG is a molecule of $\approx 150 \text{ kDa}$ weight while CRP is a tetramer of five repeating units non-covalently bonded to form a molecule of $\approx 115 \text{ kDa}$ weight. Images of the relevant protein structures from the Protein Data Bank (PDB) [141,142] are shown in Figure 62.

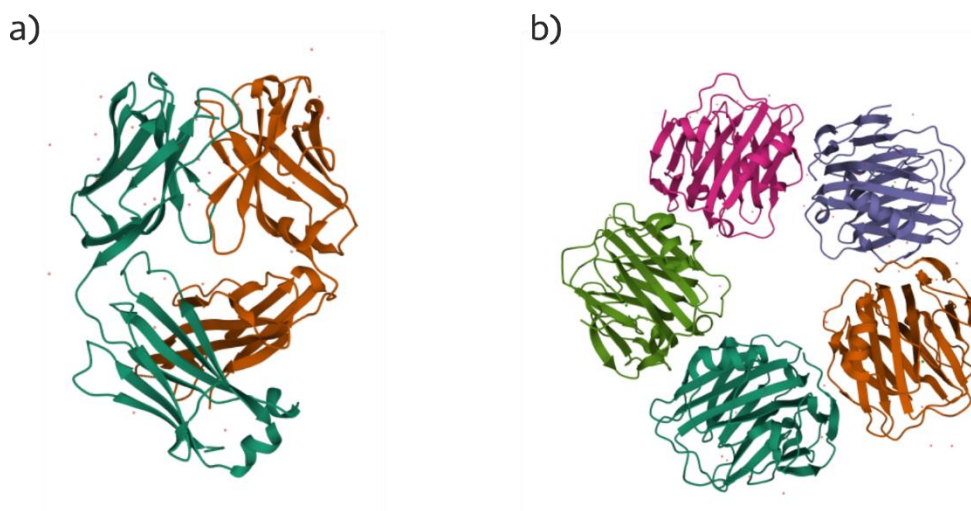


Figure 62: a) IgG1 protein structure (protein data bank code PDB ID: 3FZU) [141,143] b) CRP protein structure (protein data bank code PDB ID: 3PVO) [142].

When it comes to protein assays, the absolute detected concentration is only partially relevant. For example, elevated CRP will only inform that the patient has some inflammation. The power of protein sensing is to provide the relative level of a multitude of proteins, which is why multiplexing is a desirable feature in a biosensor [144] (cf. section 6.7). The information contained in this chapter aims to

develop the optimised instrument, which has so far only been discussed in terms of refractive index sensing, towards providing real capabilities for bio-sensing.

6.1.i. Functionalisation protocol

To measure a protein concentration, the sensor surface needs to be prepared to selectively capture the desired protein. As a first step, a glycol-based molecule is used as a linker between the sensor surface and the antibody. The use of glycol-based molecules was introduced to the research group by Dr L. Miller and optimised by Dr A. Kenaan [92] and Dr B. Coulson. The general steps used for surface functionalisation used throughout this work are presented in Figure 63 and expanded on below.

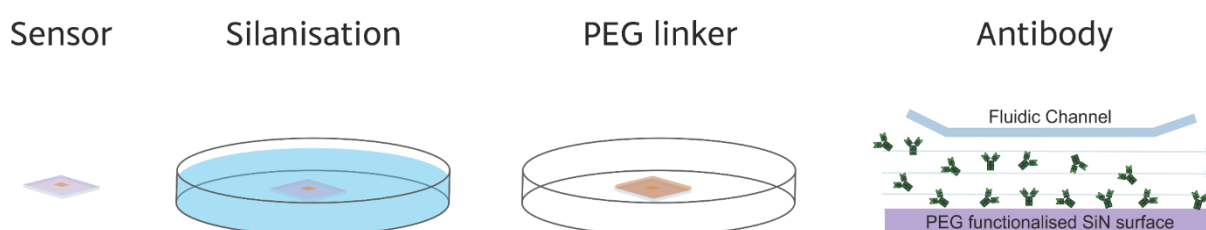


Figure 63: The practical process of functionalising a GMR sensor for protein assays, starting from a clean sensor and finishing with antibodies added in flow.

Clean Sensor: This step is accomplished in the final cleaning process of the fabrication process (section 3.1). The main objective is not only to remove contaminants but also to create hydroxyl (Si-OH) groups on the surface. Hydroxyl groups can also be created via an ozone cleaning process, which consists of 10 min ozone treatment followed by soaking in a stirred Hellmanex® III surfactant solution and two stirred de-ionised water soaks, each for 10 min. This is followed by a final 30 min ozone treatment and a soak in ethanol.

Surface silanisation: This step involves forming a layer that is ready for functionalisation. Here I use (3-mercaptopropyl) trimethoxysilane (MPTES), shown in Figure 64, which has a saline group that reacts with the silicon in the silicon nitride that have hydroxyl groups attached on the surface. The sensor is submerged in a solution of 4% MPTES in IPA (silanisation Figure 63 and Figure 65). It is important to avoid water as this can cause unwanted polymerisation. While this step is usually done overnight, it can also be done in 6 hours. Once complete, the sensor is rinsed in IPA and blown dry with nitrogen. The result is a surface with available thiol groups (R-SH) that can be bonded to.

Polyethylene glycol (PEG) linker: We use a PEG molecule consisting of a maleimide-PEG6-succinimidyl ester, which is a 6-chain long molecule with an ester functional group (left side of the molecule in Figure 64) and a maleimide (right side of the

molecule in Figure 64). The maleimide has a double carbon bond that will bond with the R-SH (thiol) group of the MPTES and thus bind the PEG to the silanised surface.

The PEG is purchased from Sigma-Aldrich and is prepared to 1 mM concentration (molecular weight 601.60 g/mol) in dimethyl sulfoxide (DMSO) to a volume of 200 μ L. This volume is then pipetted directly on to the sensor chip (15 mm²) as shown in the third image of Figure 63 and left overnight. When finished, the sensor is rinsed in DMSO and blown dry with nitrogen. As the DMSO is not as volatile as IPA, it is harder to dry the sample, but it is imperative to make sure that all DMSO is removed as leftover traces can denature antibodies. It is important to avoid hydrolysing the ester, as this results in losing the nitrogen functional group, which is key for binding the antibodies.

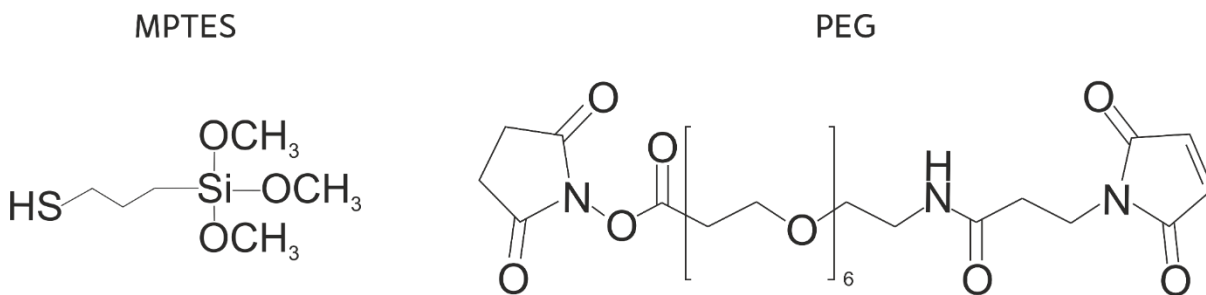
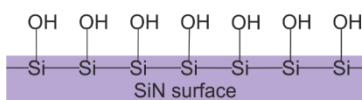


Figure 64: The (3-mercaptopropyl) trimethoxysilane (MPTES) and maleimide-PEG6-succinimidyl ester (PEG) molecules used for surface functionalisation.

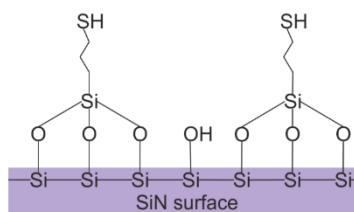
Antibody binding: All previous steps are completed in sealed containers but the antibodies need to be in solution in order to avoid being denatured. To this end, the sensor is first encapsulated in the microfluidic channels and the proteins are aliquoted to a concentration of 50 μ g/mL in 10 mM phosphate buffered saline (PBS) at a pH of 7.4. The antibodies are then flown over the sensor inside the channels to bind to the PEG molecule on the surface. The reaction occurs via an amine group in the antibody to the ester of the PEG, resulting in a peptide bond, as shown in the final step of Figure 63 and Figure 65. The antibodies need to be injected relatively quickly, as the water in the PBS will start hydrolysing the ester of the PEG. Timing is critical in this process, as hydrolysis with water happens on a similar timescale as the antibody binding.

After the surface is covered in antibodies, there may be unreacted PEG molecules and other areas on the surface that other proteins could non-specifically bind to. To mitigate the impact of non-specific binding on the desired result, a blocking buffer is employed and introduced in flow. I used Casein Blocking Buffer from Sigma-Aldrich (B6429) at a 10% concentration in PBS to act as such a blocker.

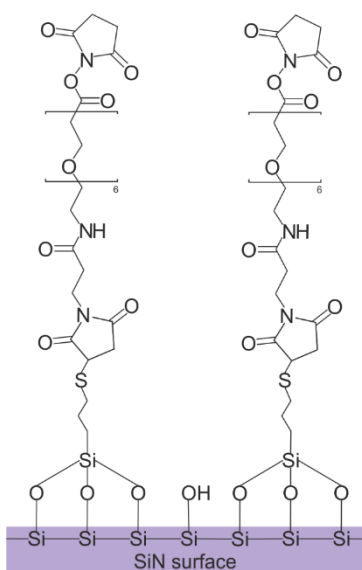
1. Sensor



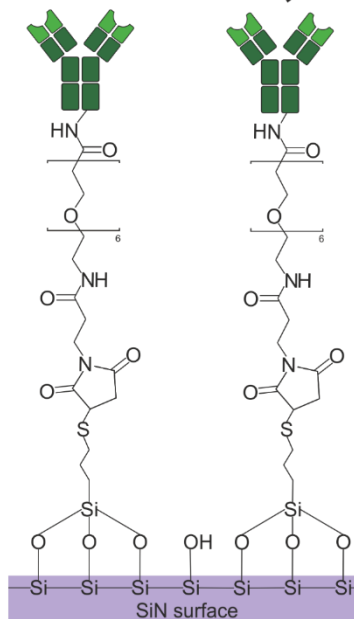
2. Silanisation



3. PEG linker



4. Antibody



*Antibodies not to scale

Figure 65: Functionalisation steps and the chemical structures that bind to the surface in the process illustrated in Figure 63.

While the process described here works well for the research phase, any final use of the cartridge and instrument would require pre-functionalisation of the antibodies and the blocking protein on the sensor. The functionalised sensor can then be protected for storage by an agent such as the StabilCoat® Immunoassay Stabilizer from Sigma-Aldrich (S0950), which is essentially a sugar coating that "Effectively preserves the conformation and activity of dried proteins in immunoassays". For this reason, the results described here are assumed to be generally applicable for future uses, however some optimisation will be required to reach the end use goal and to move away from flow-based functionalisation.

One of the main issues with this functionalisation protocol is that proteins used as capture molecules have many amine groups on their surface. For this reason, proteins do not sit uniformly oriented on the surface. While one cannot selectively choose which particular amine group binds, the flexibility of the PEG linker should aid in keeping the binding sites more accessible for antigen binding.

6.1.ii. Diffusion boundary layer impact on assays

Antibody-antigen binding is a dynamic process, so there is an on-rate K_a and an off-rate K_d [145,146], respectively, the association and dissociation constants. For example, for IgG/anti-IgG and CRP/anti-CRP, these constants are shown in Table 5 [147]. The units for dissociation (K_d) are relatively straight forward as it is just the rate for surface bound concentration to decrease, analogous to the half-life of a radioactive nucleus. The units for association (K_a) are similar but there is a dependence on concentration (or molarity) in the solution hence the units being $M^{-1}s^{-1}$, where higher concentrations will bind more quickly due to more molecules being present.

Table 5: Association and dissociation constants for antibody-antigen binding for CRP and IgG, taken from [147].

Antibody-antigen	Antigen Mass (kDa)	K_a ($M^{-1}s^{-1}$)	K_d (s^{-1})
IgG and anti-IgG	150	2.5×10^5	3.0×10^{-4}
CRP and anti-CRP	115	1.0×10^7	2.6×10^{-2}

The constants in Table 5 come with some assumptions, as the values are based on equilibrium conditions obtained in solution, not on a surface. Therefore, when using a functionalised surface, there are many factors to contend with. While the detailed principles and mechanisms behind surface functionalisation are beyond the scope of this work, there are some considerations to take forward. Most of this discussion is informed by the work by Yang *et al.* [147] who simulated a sensor surface in a microchannel using COMSOL to observe the effect of different parameters on surface binding, specifically with respect to the diffusion boundary layer.

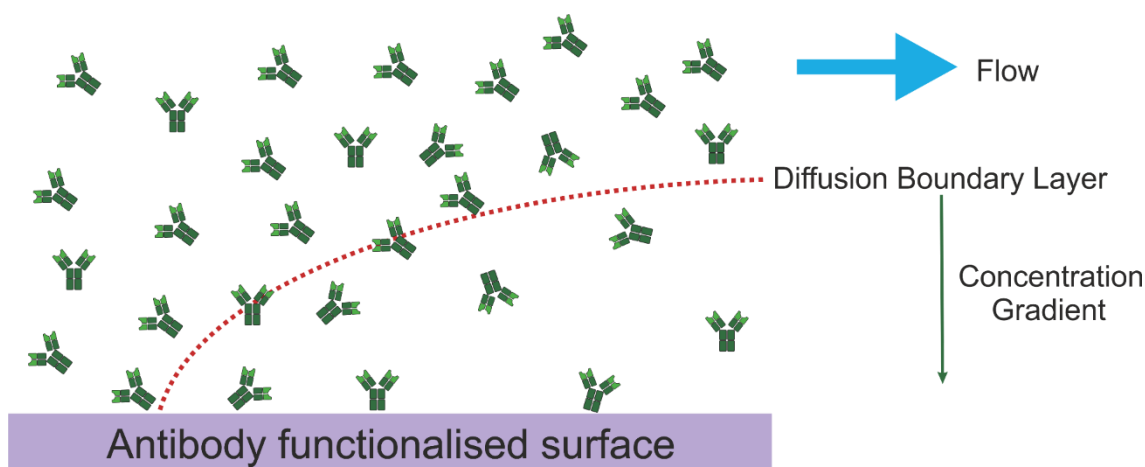


Figure 66: As proteins bind to a surface, a concentration gradient forms which creates a diffusion boundary layer acting as a barrier between the bulk solution and the surface.

The diffusion boundary layer forms when a protein in solution binds to the surface effectively reducing the concentration of proteins in solution close to the surface as illustrated in Figure 66. While other proteins can and will diffuse, driven by the concentration gradient, the boundary layer certainly limits binding. Yang *et al.* [147] show that the best way to overcome the diffusion boundary layer is to use a higher concentration of protein. Higher concentrations increase the gradient so allowing more protein to reach the surface. This approach does not work in a diagnostic setting because determining the concentration of protein is the very purpose of the exercise and cannot be controlled in this setting. Other factors that will affect the diffusion boundary layer are discussed in 6.2.iii with the key parameters being flow rate and channel size.

6.2. Assay viability and parameter considerations

6.2.i. QCM-D as an assay development tool

A common tool for optimising a functionalisation protocol is a Quartz Crystal Microbalance with Dissipation monitoring (QCM-D). The operating principle is based on the resonant frequency of a piezoelectric sensor that has an alternating voltage applied to it. When there is a mass change on the sensor, for example the binding of proteins (Figure 67a), the resonant frequency of the system will shift downwards (Figure 67b). This operating principle is somewhat analogous to the resonance shift of a GMR sensor, in that the resonance frequency shifts downward due to mass attaching to the sensor surface. As we tend to report wavelength rather than frequency in Photonics, the change due to binding is upwards for the GMR while it is downward for the QCM-D. For my QCM-D measurements, I used a Qsense instrument from Bolin Scientific.

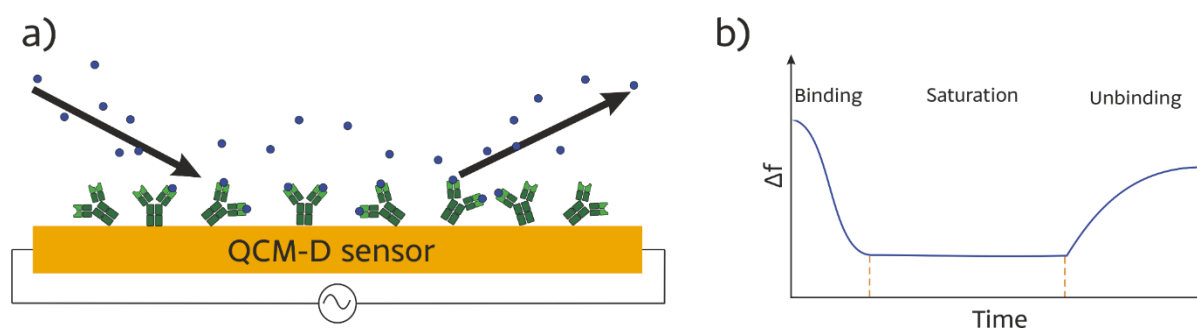


Figure 67: a) Schematic of a QCM-D sensor functionalised with antibodies with an antigen binding and unbinding. b) Expected response of the resonant frequency from a QCM-D sensor for binding and unbinding.

The dissipation aspect of the QCM-D sensor is related to the energy lost from the resonance when not driven by an external force, i.e. the alternating voltage. Depending on how damped the system is, the larger the dissipation will be. The dissipation can be affected by various factors, but the most common one is the flexibility of the surface-bound molecules. For example, a very rigid molecule will not dampen the system very much, while a flexible molecule will dampen the response much more. While this aspect of QCM-D is not critical to my use of the technique, the results from dissipation are nevertheless interesting to consider.

When using QCM-D, the shift is measured as a frequency shift (Δf). An additional advantage is that the frequency shift is directly linked to the mass through the Sauerbrey equation [148]:

$$\Delta m = -C \times \frac{\Delta f}{n}$$

where the change in mass Δm is related to the frequency shift by the mass sensitivity constant C , which has a value of 17.7 ng/cm²Hz for a 5 MHz crystal, while n represents the number of the harmonic of the resonance. This equation is not very accurate as it assumes a rigid structure on the surface and doesn't take into account the effect of the solution on the resonance [148]. Nevertheless, a QCM-D is a very useful tool for indicating the feasibility of an assay and checking its parameter space. It should also be noted that a certain magnitude of physical mass change may not translate directly to an equivalent magnitude of shift on a GMR based on where the proteins are placed in the evanescent tail.

6.2.ii. CRP and IgG assay testing

While the surface chemistry has been developed by colleagues [92,149], I performed basic controls to ensure that the protocol works as expected, and that I, as a physicist, am capable of handling the chemistry/biology aspects of my project correctly. As an example, Figure 68 presents anti-IgG being bound to the surface of four QCM-D sensors as presented in section 6.1.i, followed by flowing IgG at high concentration (10 µg/mL) over the surface to measure the binding. The anti-IgG used was polyclonal Rabbit IgG produced in Goat from Sigma-Aldrich (R2004). As this work is proof-of-principle, it does not matter that we are using polyclonal anti-IgG rather than the monoclonal version. The complementary Rabbit IgG used as the target molecule was also sourced from Sigma-Aldrich (I5006).

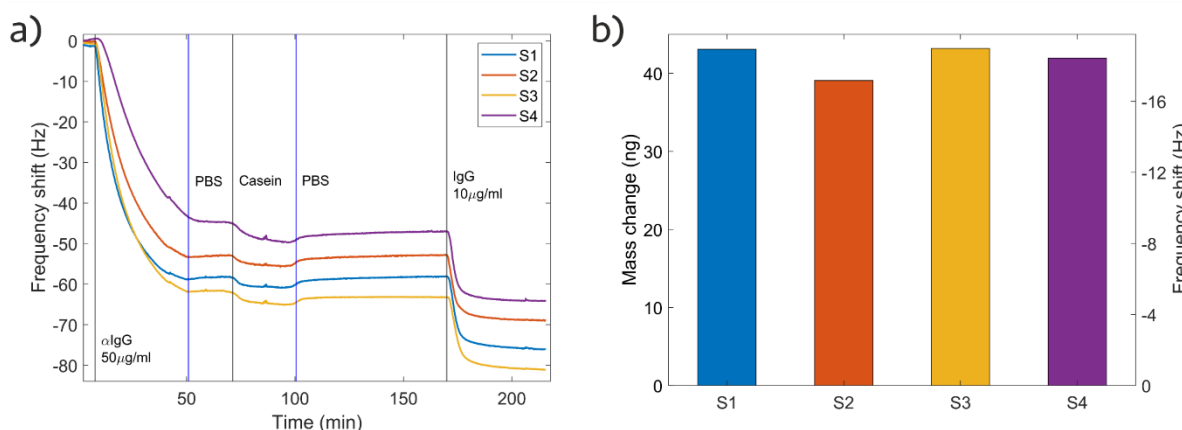


Figure 68: a) QCM-D resonant frequency plot of a four IgG assay. b) Mass change for the 10 µg/mL IgG step with a standard deviation of 1.9 ng across the 4 sensors.

Figure 68a shows the traces for the 7th frequency mode; the 7th mode was used for all QCM-D measurements. The 7th mode is conventionally chosen, as it offers a good trade-off between sensitivity to external vibration and sensitivity to the changes on the surface. From Figure 68a, it is clear that each sensor shifts by a different amount. This difference between the measured curves could be due to factors in the functionalisation, such as different densities of the PEG layer on the surface, leading to different anti-body binding. The most likely cause is a difference in response of each sensor, as they were not able to settle before the antibodies are introduced. This conclusion is supported by the results of mass binding shown in Figure 68b calculated using the Sauerbrey equation. Taking the standard deviation of the masses bound gives a $\sigma = 1.9$ ng across the four sensors (S1-S4) and this is only 4.5% of the mean binding from the four sensors. This is a relatively small percentage, especially considering the assumptions made in the Sauerbrey equation discussed in 6.2.i. This shows that all four sensors present very similar shifts upon antigen binding, which suggests that the variations seen in the antibody binding are of little consequence.

Similar to Figure 68, Figure 69 shows data comparing the binding of CRP and anti-CRP compared to the IgG/anti-IgG assay. The anti-CRP used was polyclonal anti-Human CRP produced in Goat (Bethyl Laboratories, Inc A80-125A) paired with the Human CRP expressed in *E. coli* (BioVision, Inc. 4864). Figure 69a shows the frequency trace for the 7th mode and while the modes are spread out, sensor 2 seems to read much lower than all the other sensors. Sensor 2's difference is further highlighted as the dissipation traces for IgG in Figure 69 show similar results, but the CRP traces in Figure 69 have a marked difference. The main conclusion that can be drawn from these differences, is that sensor 2 is less sensitive than its counterparts, which could be due to it not being seated properly.

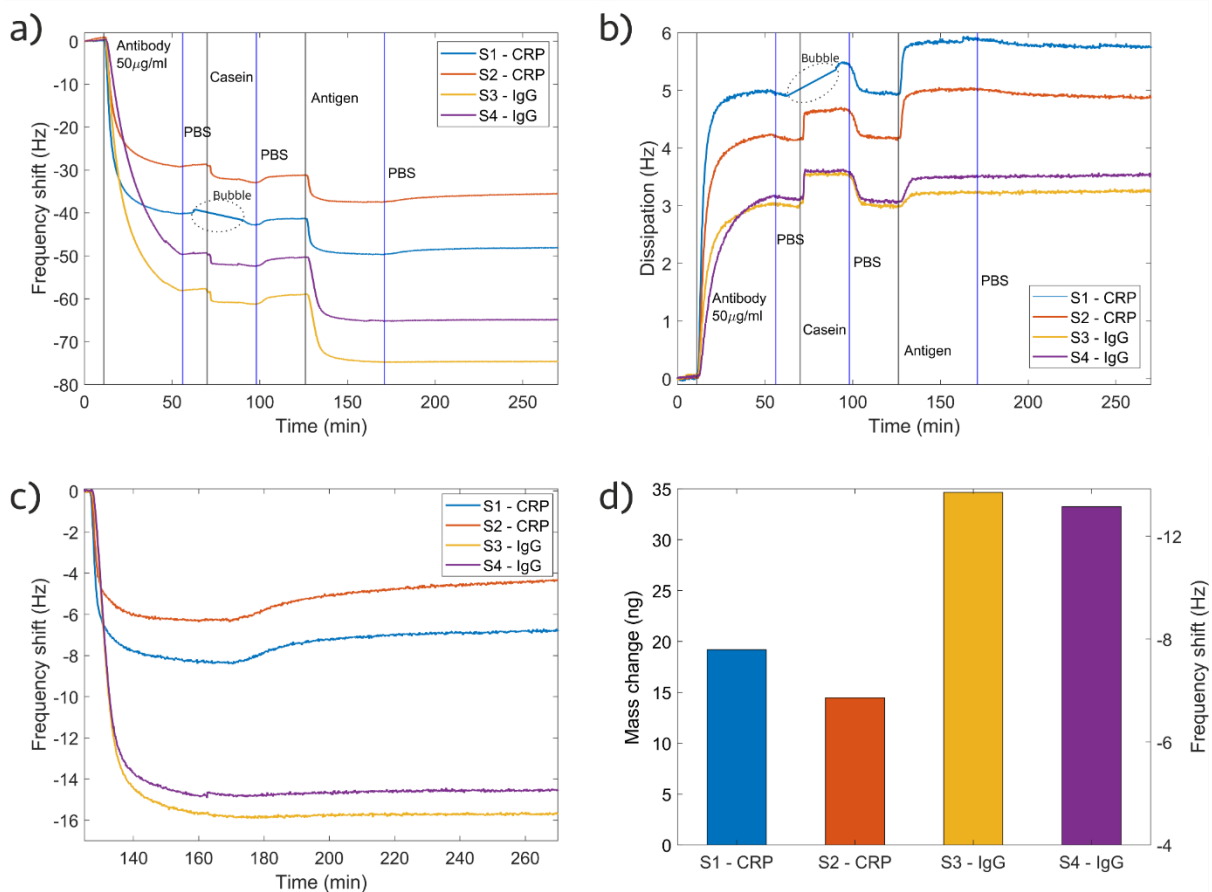


Figure 69: QCM-D data comparing IgG and CRP Assays. a) All four frequency shift traces. b) The dissipation change for each sensor. c) Antigen binding events for all four sensors with the initial trace set to zero. d) Mass change for each sensor for visual comparison.

Nevertheless, Figure 69 provides some interesting insights. Firstly, Figure 69b for CRP binding generates a larger shift in dissipation than for IgG. While the structural biology is beyond the scope of this thesis, it is interesting that the CRP tetramer is less rigid than the IgG protein (shown in Figure 62). Secondly, the mass deposited on the surface is higher for IgG than for CRP as conveyed in Figure 69c, where the shifts have been zeroed and Figure 69d where the mass change is plotted. IgG is ≈ 150 kDa which is 1.2 \times larger than CRP which is ≈ 115 kDa. Furthermore, the difference between the mass on the surface is $\approx 2\times$ if we use the average mass from sensor 1 and 2 (CRP) compared to 3 and 4 (IgG). However, if we assume sensor 2 is somewhat anomalous and so compare sensor 1 and 3 which have mass changes of 19.2 ng and 34.6 ng respectively, the difference is $\approx 1.8\times$. The difference of mass deposited on the surface for IgG is still greater than the mass difference of the proteins. To explain this difference, we must look to the K_d and K_a values shown in Table 5. Here the ratio of un-binding to binding is higher for CRP which means that even if the concentration flown over the surface is the same, there will be a lower saturation point in the CRP assay. This conclusion, however, is not the definitive answer as there are many parameters in play such as

diffusion rate across the diffusion boundary layer. Furthermore there could also be differences in the packing density of the IgG and CRP antibodies which can also lead to difference of binding sites being accessible to the antigens.

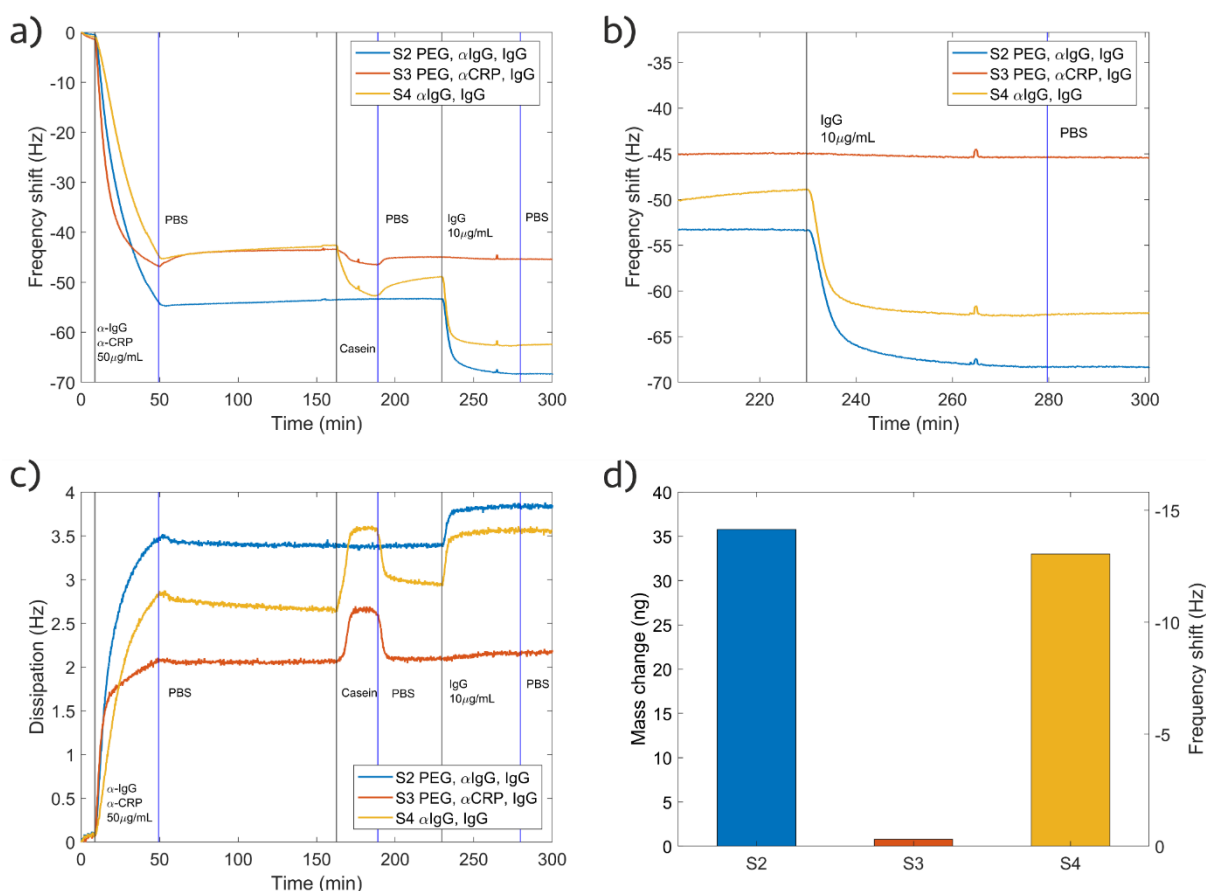


Figure 70: Three separate control measurements of the IgG assay using different parameters. a) Frequency shift of the sensors with b) zoomed in on the IgG binding. c) Dissipation change across the sensors. d) Mass change calculated from a).

With the insights gained from Figure 69, it is worth considering controls. Such controls are presented in Figure 70. They were undertaken by measuring the IgG antigen but with different functionalisation chemistries. First was the standard IgG assay without the use of the casein blocking buffer (S2 in Figure 70) with the aim of measuring the non-specific binding in the presence of the correct antibody. The aim is to observe if not blocking with casein results in a significantly larger shift for antigen binding compared to previous results. Second is measuring the non-specific binding by functionalising the surface with anti-CRP and measuring against IgG (sensor 3 in Figure 70). Finally is measuring the binding of the IgG assay, however the surface is only prepared with MPTES and not with PEG (sensor 4 in Figure 70).

Interestingly, sensor 2 does not have significantly more binding than the counterparts in Figure 69 indicating minimal non-specific binding and a good surface coverage of

anti-IgG. Although not the intent of the measurement it also indicates that the Casein does not significantly block the binding sites of the anti-IgG. In fact, the small steps pre and post casein blocking in Figure 69a (60-120 minutes) already indicate the validity of blocking, especially for the PEG-functionalised protocol. Backing up this conclusion is the minimal binding observed with sensor 3, which represents a traditional control. Finally the results from sensor 4 are the least enlightening but do show the benefits of the PEG as while the antigens that stick to the surface are more rigid (apparent from the dissipation, Figure 70c) compared to PEG bound antibodies, the casein step is much larger than for all other measurements.

6.2.iii. Probing the diffusion boundary layer

For the photonic experiments conducted in the instrument, I am more concerned with the total binding than with the kinetics of the binding. The parameters that I am concerned with are the flow rate and channel height, as these affect the diffusion boundary layer [147]. The reason that these parameters affect the diffusion boundary layer is that a higher velocity replenishes the depleted proteins, which have bound to the surface, more rapidly. The velocity can be increased either by increasing the flow rate or by reducing the channel size, so the two parameters are connected. Decreasing the channel size reduces the volume of the channel hence the flow velocity increases if the flow rate is kept constant. An added benefit of smaller channels is that the proteins at the top of the channel have a smaller distance to diffuse to the surface, thereby reducing the amount of analyte that will never 'see' the sensor surface because the channel is higher than the diffusion length.

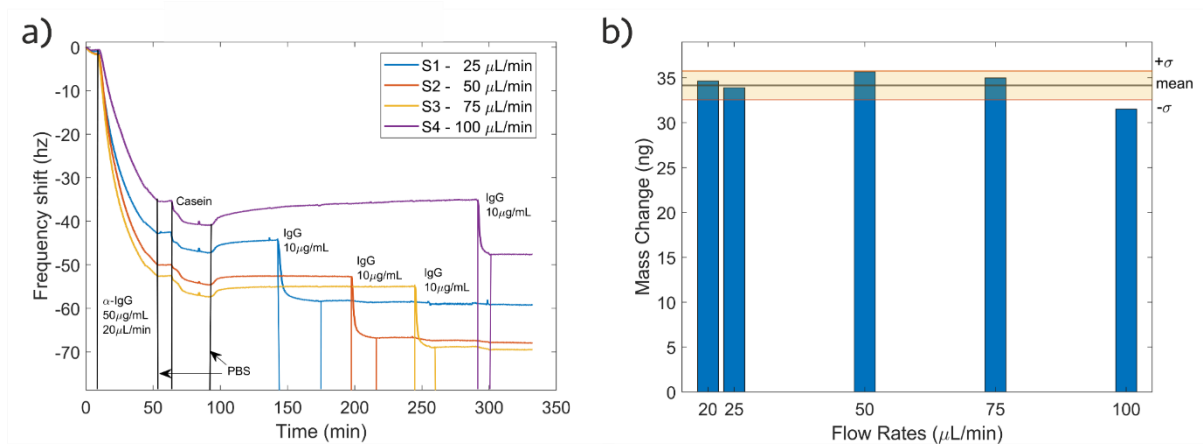


Figure 71: a) QCMD data of an IgG assay done at different flow rates, legend denotes which flow rate 10 μg/mL IgG is first injected. b) Mass deposited at each flow rate with data for 20 μL/min taken from Figure 69 sensor 3, marked with the mean and standard deviations of all values.

The height of the channels used throughout this project is typically on the scale of hundreds of micrometres for the photonics experiments, while the channel height of the QCM-D is fixed to $\sim 400 \mu\text{m}$. Conventionally, $20 \mu\text{L}/\text{min}$ is used as this gives approximately an hour flow time for 1 mL of sample. I compared the flow rates of $20 \mu\text{L}/\text{min}$ used in Figure 68-Figure 70 to $25 - 100 \mu\text{L}/\text{min}$ flow rates with the QCM-D traces in Figure 71a. The experiment shown in Figure 71a was conducted by setting the flow rate and letting the sensor stabilise, as much as was practical, then introducing the IgG to one of the sensors at one flow rate. Figure 71b presents the mass change on the surface as extracted from the frequency shifts in Figure 71a as well as including data for sensor 2 in Figure 69. The key point about Figure 71b is that the flow rate has no significant change on the mass that binds to the sensor. The variation of sensor 4 is most likely linked to the drift seen before antigen binding so should be considered an outlier in terms of mass on the surface.

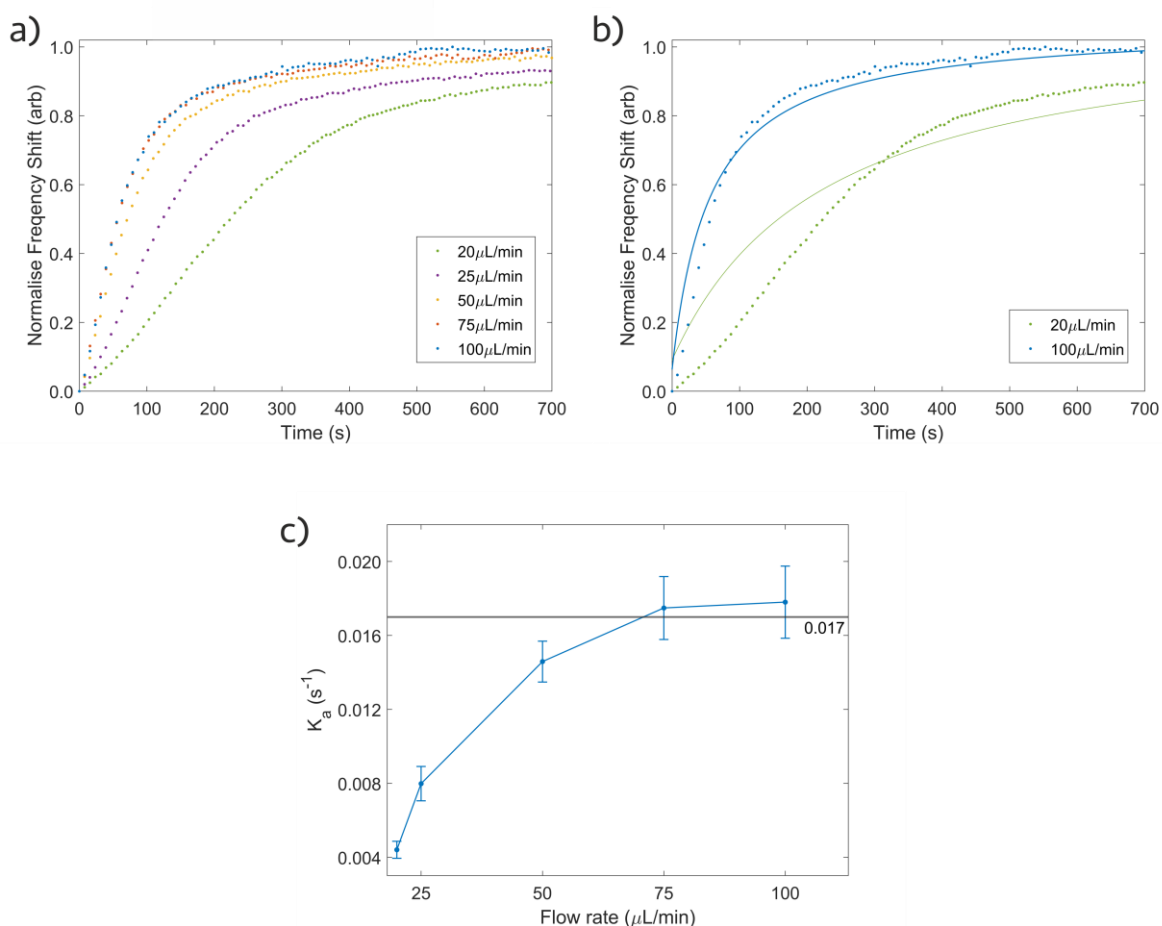


Figure 72: a) Binding events of $10 \mu\text{g}/\text{mL}$ IgG at different flow rates. b) $20 \mu\text{L}/\text{min}$ and $100 \mu\text{L}/\text{min}$ binding rates with Langmuir fit. c) Plot of parameter k from the fits against flow rate with the expected K_a [147] marked. Data is from Figure 71 and Figure 69.

Figure 72a shows the binding curves, normalised to the maximum frequency shift to remove the frequency magnitude differences, for each flow rate for IgG binding. Each

flow rate was fitted with a Langmuir isotherm function (20 and 100 $\mu\text{L}/\text{min}$ examples in Figure 72b) as it is a simple model used for approximating binding interactions [150,151] and is of the form:

$$\frac{Kx}{1 + Kx} + e$$

Interestingly, the K value, in units of s^{-1} , should represent the association constant (K_a) of the antibody. For biological binding x is the time but for gas absorption, which the Langmuir model was originally conceived, x represents the partial pressure of the gas. The measured values of each fit, collated in Figure 72c, include a combination of association kinetics from the antigen binding, as well as from diffusion. The consequence of this, is that the binding rate will not match the true association constant when the system is diffusion limited. A visible sign of a result being diffusion limited, is how the fit and the data matches poorly at the lower flow rates, with the fastest and slowest flow rates represented in Figure 72b. Conversely higher flow rates match much better.

Figure 72c conveys the relationship between the flow rate and the K_a value obtained from each fit, with the error bars obtained from the confidence interval of the value. The line in Figure 72c represents the expected association constant for IgG binding to anti-IgG where $K_a = 2.5 \times 10^5 \text{ M}^{-1}\text{s}^{-1}$ [147]. While K_a here is given in $\text{M}^{-1}\text{s}^{-1}$, I used a fixed concentration of $10 \mu\text{g}/\text{mL}$ of IgG, which with its weight of 150 kDa yields 67 nM , so for this fixed concentration the expected $K_a = 0.017 \text{ s}^{-1}$, which my results approach at higher flow rates, as higher flow rate overcomes the diffusion boundary layer.

The value of K_a increases with flow rate, as flow rate reduces the size of the diffusion boundary layer [147]. By $100 \mu\text{L}/\text{min}$ it has saturated and the values for $75 \mu\text{L}/\text{min}$ and $100 \mu\text{L}/\text{min}$ are slightly above the calculated line, although still within the confidence interval. Other reasons why the measured values are higher than expected could stem from the difference between binding rates in solution and any surface kinetics as well as any uncertainty in the fit. These differences could also arise from the assumptions of the Langmuir isotherm [151]:

- Homogeneous adsorption sites
- Each adsorption site binds an individual solute molecule
- Dynamic reversible equilibrium established in the timeframe of the experiment
- No interaction between solutes on the surface to alter their adsorption behaviour.

Each of these assumptions are likely not to hold in the real system. For example, the diffusion boundary layer discussed above implies that the binding sites will not be perfectly homogeneous, if the antibody binding step is diffusion limited. Furthermore, the access of the antigen to binding sites being inhomogeneous is also diffusion limited.

The results presented here are useful to show the effect of flow rate, and by extension channel height, on binding rates. However, these results are specific to the details of the QCM-D used for these experiments. The main result I am concerned with, is that the saturation of a sensor is barely affected by flow rate (Figure 71b). In short, flow rate impacts on the time needed to reach saturation, but not on the magnitude of the observed frequency shift. A further consideration for flow rate is that higher flow rates mean higher pressures which increases the risk of leakage. For this reason, I used a flow rate between 20-50 $\mu\text{L}/\text{min}$ in most of my experiments as this gives a flow time of 25 - 50 minutes for 1 mL samples.

6.3. Fluidic delivery of samples

As discussed in section 4.3, PDMS is commonly used to build the fluidic delivery system for research purposes [152]. PDMS has the advantages of being easy to implement and to prototype in research situations, as well as being very versatile in the shape and resolutions that can be realised. For these reasons, PDMS fluidics were the starting point for the work I conducted.

6.3.i. PDMS channel fabrication

The fabrication of PDMS channels starts by creating a mould for the channel tracks.
Channel master fabrication process:

1. The Si wafer is cleaned using the same process as laid out in the first step in section 3.1.ii.
2. Spin with SU8 2050 from Kayaku Advanced Materials Inc. using a three-step spin process for an SU8 thickness around 150 μm :
 - 500 rpm for 10 seconds
 - 750 rpm for 10 seconds
 - 1200 rpm 60 seconds

3. Pre-exposure bake:
 - 65 °C for 2 minutes
 - 95 °C for 10 minutes
 - 65 °C for 2 minutes
4. The sample is then exposed using the Kloe DILASE 650 system using parameters that achieve a 10 μm spot size. Using a speed of 1.3 mms^{-1} and 65% power in conjunction with a filter of optical density of 1.3 doses the sample with approximately 240 mJ/cm^2 .
5. Post-exposure bake:
 - 65 °C for 2 minutes
 - 95 °C for 10 minutes
 - 65 °C for 2 minutes
6. Develop for 8 minutes in EC Solvent and rinse in IPA and blow dry with nitrogen.
7. Hard bake overnight at 180 °C

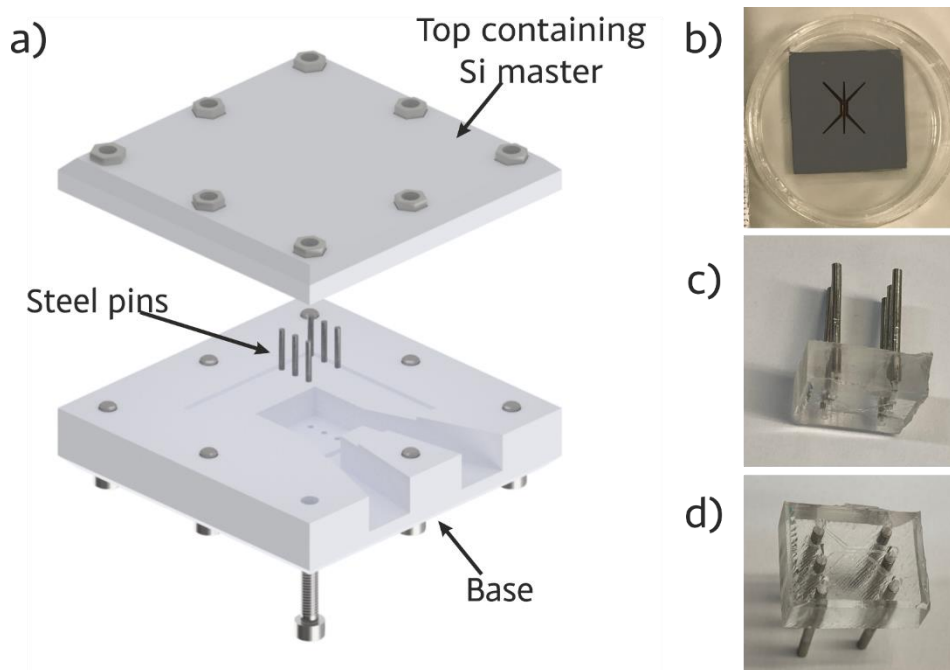


Figure 73: a) Schematic of the 3D printed mould for PDMS channels. b) The silicon and SU8 master that sits in the top of a). c-d) Side and bottom view of PDMS channels with metal tubing inserts.

The channel master is then encapsulated in an ABS plastic mould printed using FDM printing with the design shown in Figure 73a with the channel master in Figure 73b. The final channels with tubing inserts are presented in Figure 73c and d. The different type of plastic is required as the photo-initiators of SLA resins inhibit the curing of

PDMS [153,154]. As the resolution of the channels is determined by the channel master, the printer resolution is not a limiting factor making FDM printing (which has lower resolution than SLA) suitable for PDMS moulds. Steel pins are used to create holes where tubing can later be inserted to connect the channels to external tubing and luer connectors.

6.3.ii. PDMS implementation

Our group originally oxygen-bonded channels directly to sensors, which achieves good fluidic seals. However, this method, necessitates the functionalisation protocol to be performed inside the channel, which turns the entire substrate and the channel walls into an active surface - thereby extracting antigens from the analyte before they reach the sensor. A better method is to clamp the PDMS channel onto the sensor. Once moulded, I pressure-fit 1.6 mm outer diameter steel tubing into the PDMS inlet and outlet holes, which can then be attached to flexible fluidic Tygon™ tubing (0.8 mm inner diameter and 2.4 mm outer diameter). The tubing is fitted with luer connectors to enable the connection to syringe pumps. To hold the sensor and the PDMS channels in connection, a 3D-printed clamp is used. The clamp (shown in Figure 74) is held together with six screws in a hexagonal pattern to allow a uniform distribution of pressure. A silicone gasket is placed under the sensor to provide a flexible compressible underlayer, which balances the strain and helps to avoid cracking of the sensors.

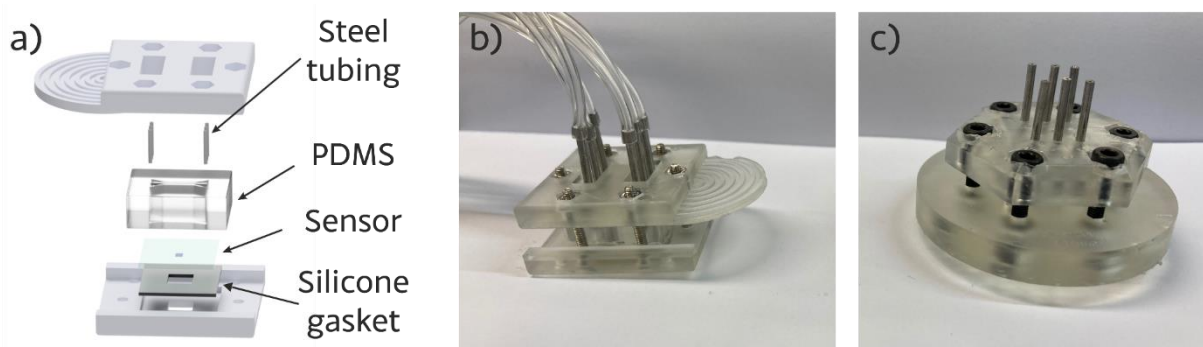


Figure 74: a) Exploded view of the clamp that holds the PDMS channels and 15 mm² sensor together using M2 screws. b) An operational device clamped together. c) Clamp used for optical bench setups shown for comparison.

6.3.iii. Fluidic pumping and sample injection

I used a Legato® 101 syringe pump from KD Scientific Inc. to drive the analyte through the channels. When flowing solutions, there is the option to withdraw or infuse (“pull” or “push”), which both have their advantages and disadvantages. When withdrawing, the inlet is placed directly into the sample vial and the withdrawing syringe will pull it

through. By pulling, a sufficiently strong negative pressure may build up that can cause PDMS channels to collapse. This same pressure can also cause the solution to degas should a blockage occur. Withdrawing is how the QCM-D system used in 6.2 operates, which is driven by a peristaltic pump. Since the QCM-D does not employ “soft” PDMS channels, there is no danger of collapsing.

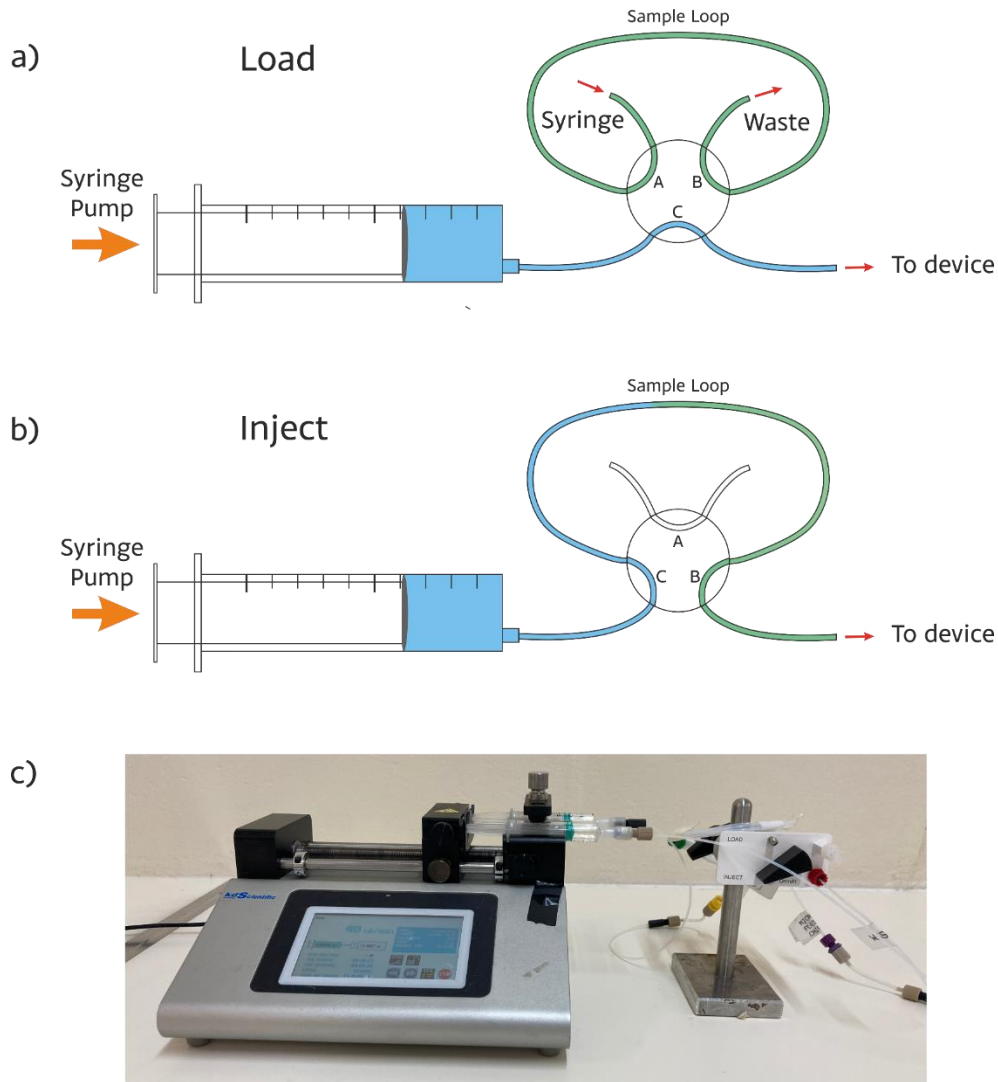


Figure 75: Schematic diagram with syringe pumping and a sample loop, sample fluid in green, buffer solution in blue. a) Sample loop in the load configuration. b) Sample loop in the inject configuration. Switching between load and inject is achieved by rotating the valve to switch connections A, B and C. c) Kd Scientific inc. Legato® 101 syringe pump and Diba Omnifit® Sample loop.

The alternative is to infuse, which requires the use of a sample loop, such as the Diba Omnifit® Sample loop, and a syringe acting as a reservoir (visualised in Figure 75). By pushing the solution through the channel, channel collapse and degassing are avoided. Furthermore, if the channels are not properly sealed, air will not be sucked in. Using a sample loop also enables continuous flow as the analyte is loaded and then injected into the stream by switching the valve. When infusing, there is a risk of bubbles should

the sample storage loop (tube with green sample Figure 75a) not be fully filled with solution. A strong advantage of the sample loop is that once the sample is fully infused, the flow will immediately revert back to the buffer as they are flowing in succession powered by the reservoir.

6.3.iv. Fluidic integration using printed channels

While PDMS channels have great use in academic research, they lack the desired scalability required to translate a technology into a commercial system; their softness also leads to the danger of collapse as described above. As an alternative, I explored the use of 3D printing to make the channels, originally proposed in the group by Dr Simmons; 3D printed channels are “hard” and therefore not prone to collapse; furthermore, 3D printing achieves spatial resolutions of 300 μm , which is comparable to injection moulding [155], so is a good proxy for a scalable technology. Printing individual channels would require wall thicknesses of 300-500 μm due to the resolution of the 3D printer and to achieve the necessary structural strength. For this reason, separate enclosed channels were ruled out as these would take up too much of the field of view, limiting space for multiple sensors (cf. section 6.7). Instead, I implemented a solution exploiting laminar flow [156] which utilises multiple streams of solution to flow in parallel without turbulent mixing (Figure 76a). Turbulent and laminar flow are commonly seen in nature as exhibited in Figure 76b and c respectively.

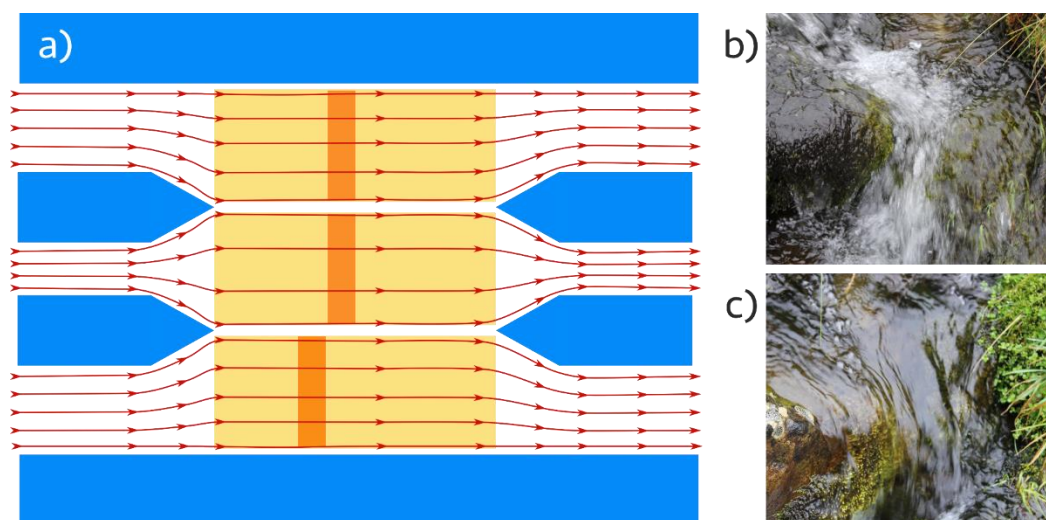


Figure 76: a) Laminar flow concept for delivering different samples to adjacent GMR sensors 300 μm wide with the resonance depicted by the darker orange bars. b) Turbulent flow in nature. c) Laminar flow in nature.

Whether a fluid flow is laminar is determined by the Reynolds number (Re) [157]. Generally speaking, when $Re < 100$ the flow is laminar and when $Re > 1000$, it is

turbulent. The values in-between these limits are considered transitional and so could lead to either type of flow. The Reynolds number Re is given by:

$$Re = \frac{\rho V D}{\mu}$$

where ρ is the density of the liquid, here taken as that of water at standard temperature and pressure 1000 kgm^{-3} . V is the velocity of the flow, which can be approximated from the flow rate and cross-sectional area. For example, by taking the width as 1 mm (Figure 77c) and the height as $500 \mu\text{m}$, then for a flow rate of $20 \mu\text{L}/\text{min}$ the velocity is $V = 1.5 \times 10^{-3} \text{ ms}^{-1}$. D is the characteristic dimension where we can just take the width of 1 mm, and finally, μ is the dynamic viscosity of the liquid, i.e. its resistance to flow, which for water $\mu \approx 1 \times 10^{-3} \text{ Pa}\cdot\text{s}$. For this example, we obtain a value of $Re = 1.5$, which is well below the limit for laminar flow. Since the dependency of the Reynolds number on each of the terms is linear, any of these values could vary by a small factor, yet the overall system would still safely operate in the laminar flow regime.

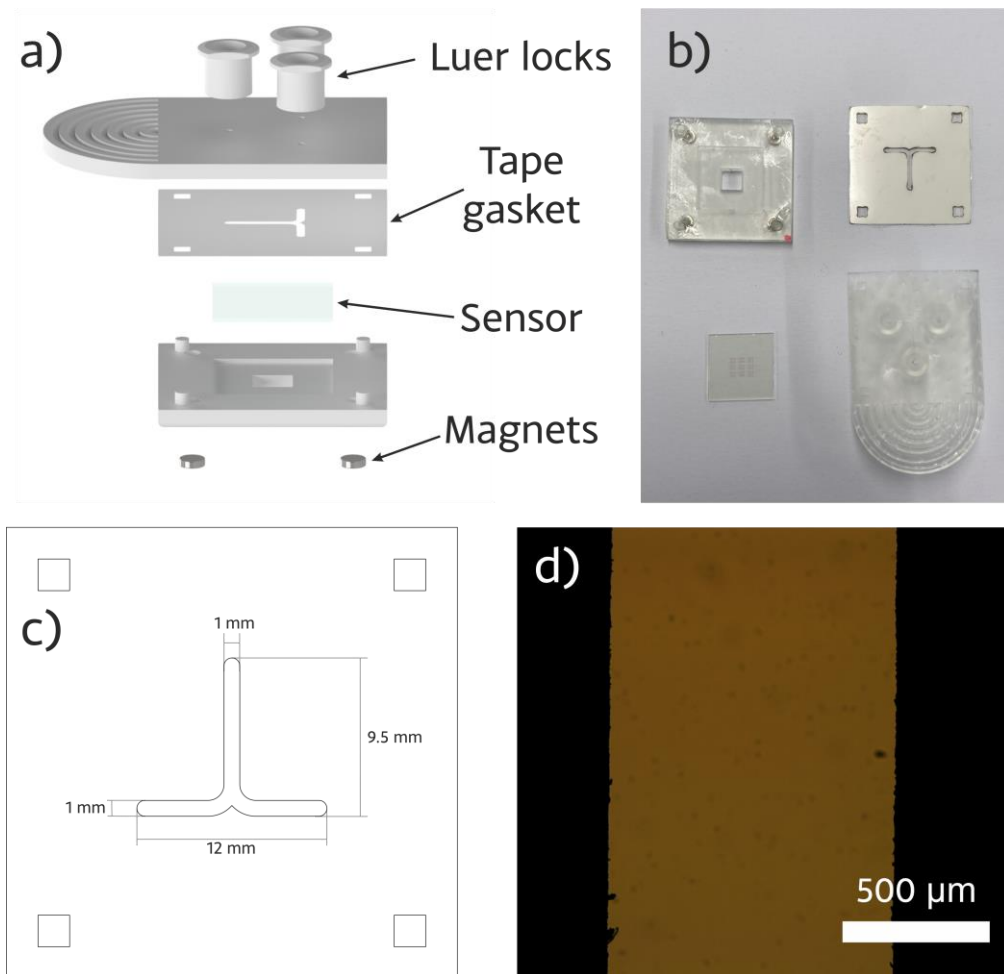


Figure 77: a) Computer aided designs of printed fluidic circuit elements. b) Separated components printed with a laser cut tape gasket. c) Channel schematic with dimensions labelled. d) Microscope image of the laser cut tape showing side roughness.

The designs for the sensor cartridge were based on practical limitations. Such limitations included allowing for sufficient space above the imaging optics, for the base thickness, as well as balancing the separation between luer connectors but making sure the channels sat only on the substrate. The design is presented in Figure 77a with the 3D printed realisation shown in Figure 77b. A schematic of the full dimensions is shown in Figure 77c with the edges of laser cut tape gasket exhibited in Figure 77d. 3M™ Microfluidic Diagnostic Tape 9965 was used for the gasket. The tape is 90 µm total thickness and the adhesive is hydrophobic, adding to the efficacy of the seal provided by the tape between the layers. Due to the printer resolution, the channel height printed was designed as 300 µm. The sensors, pre-functionalised up to the PEG step, were epoxy-bonded into the cartridge base for 30 min. Then the top is mounted using the tape gasket and the sides are epoxy-bonded and left clamped together overnight. To minimise PEG hydrolysis with water, the sealed cartridges were placed in a container with desiccant. The reason for applying epoxy to the edges is to reduce leakage by reinforcing the tape adhesion at any weak points that may be caused by print roughness.

The channel operates in the laminar flow regime, but we also need to consider the diffusion between flow channels. The diffusion time for a given molecule is determined by the diffusion distance w and the molecule's diffusion coefficient D , hence diffusion time (t_d) is given by:

$$t_d = \frac{w^2}{2D}$$

This formula provides a good indication of feasibility but I also conducted some modelling using COMSOL to illustrate the effect. I used COMSOL 3.5a and generally followed the application guide for a Controlled Diffusion Micromixer [158], using my geometry for the channels and key parameters relevant to my study as summarised in Table 6.

Table 6: Parameters used in COMSOL fluidic simulation [158].

Parameter	Value
Flow Rate	20 µL/min
IgG concentration	4 nmol/L
Diffusion coefficient (IgG)	3.89×10^{-7} cm ² /s
Channel height	300 µm

In order to understand the limiting case, I used a concentration of 5 µg/mL which is much higher than the target for the LOD. The main results are presented in Figure 78

showing the concentration across the channel (Figure 78a), pressure (Figure 78b) and velocity (Figure 78c). The channel shape was imported from the CAD file used in printing. Tape thickness was discounted, as it would only have a minimal additional effect on the results, as diffusion in the lateral dimension dominates. Figure 78a is the key result and it does show some diffusion between the two channels, which suggests that it is important to leave a gap between the sensors in order to account for this. The model in Figure 78a represents a flow rate of 20 $\mu\text{L}/\text{min}$, hence if diffusion did become an issue, the flow rate could be increased. For comparison over a 3.5 mm length (the furthest a sensor will be from where the channels meet) the COMSOL model predicts a diffusion length of $\sim 100 \mu\text{m}$. In contrast, when using the diffusion equation with a time of 1 s (the time to travel the 3.5 mm) and using the diffusion coefficient in Table 6, produces a diffusion distance of $9 \mu\text{m}$, which is an order of magnitude smaller. The discrepancy most likely arises from the fact that the diffusion time does not account for concentration or temperature. It could also be the case that COMSOL is predicting some mixing, separate from whether the fluid is laminar, induced by the structure (ripple where channels meet of Figure 78a). In any case, whether the distance is $9 \mu\text{m}$ or $100 \mu\text{m}$ does not make a difference in practise, as both sizes can be accommodated by the channel and sensor size.

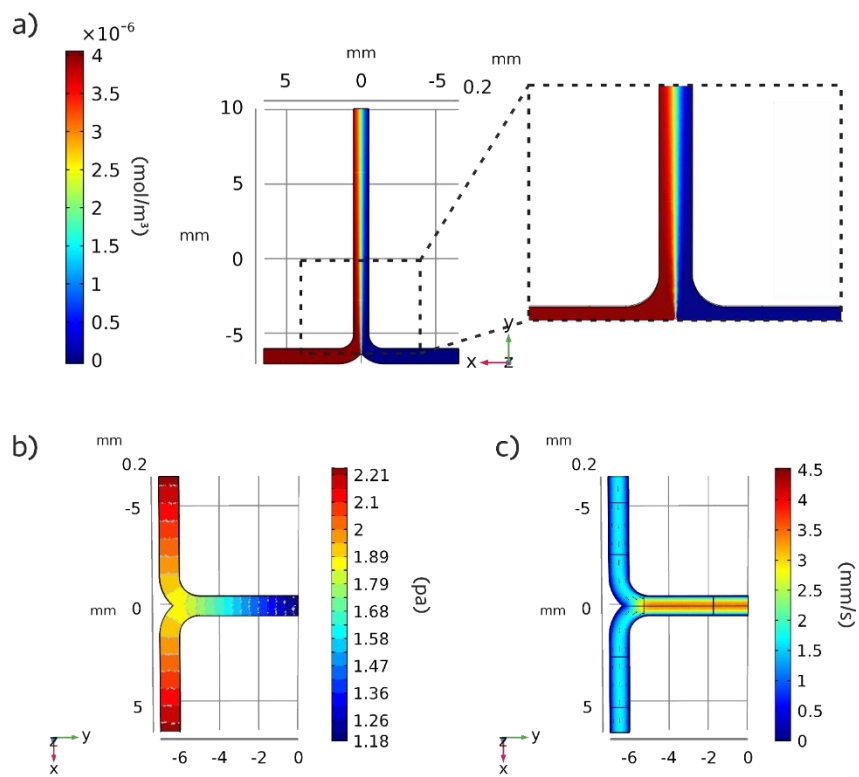


Figure 78: COMSOL 3.5a simulations of 3D printed laminar flow channels with a 20 $\mu\text{L}/\text{min}$ flow rate. a) Concentration of analyte in left and right channel depicting diffusion for 5 $\mu\text{g}/\text{mL}$ concentration of IgG. b) Pressure distribution on the walls of the channel. c) Flow rate of solutions in channels at channel junction.

The 3D printed fluidic circuit is shown in Figure 79a. To demonstrate the laminar working for protein binding, a composite image is shown in Figure 79b. The composite image is generated by overlaying two images separated in time (pre and post antibody binding). Areas of intensity overlap (no change) appear grey while areas of difference appear as either magenta or green, depending which image has the higher pixel value. From Figure 79b several things can be observed:

- A clear boundary can be seen between the two GMR sensors (second from left) where half of the channel has shifted and the other half has not.
- The boundary appears smaller than is predicted by the model of Figure 78.
- The tape on the left side shows movement highlighting the need to seal the edges of the printed cartridge with epoxy.

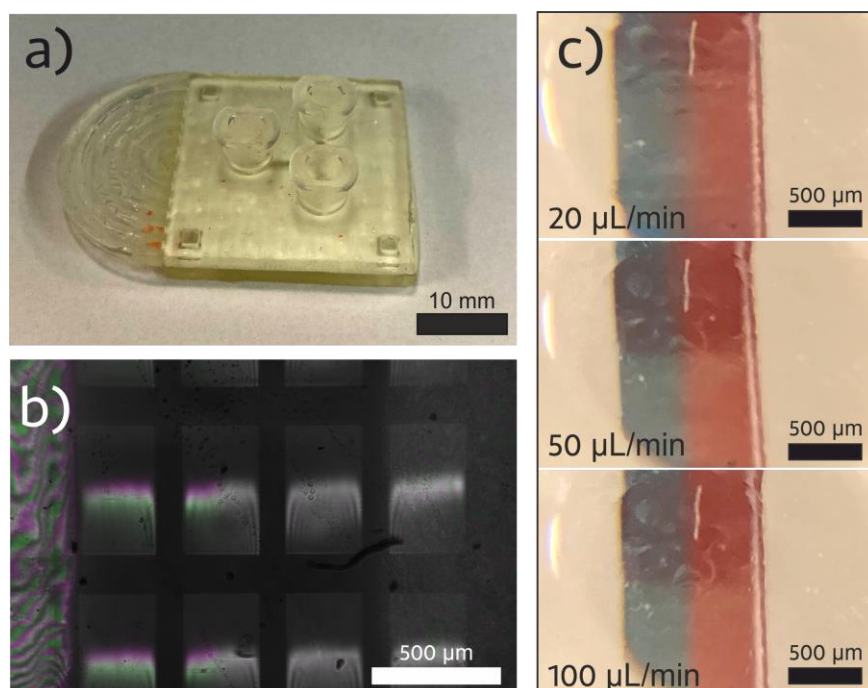


Figure 79: a) 100 mm wide printed fluidics sealed with 3M™ 9965 Tape and epoxy. b) Two images separated in time and superimposed, using different colours; areas of similarity are in greyscale while differences are highlighted by green and magenta colouring, respectively. c) Dye flown through both channels at different flow rates to study diffusion, using food dye.

As the proteins being used are too small to be directly observed, two dyes were used to visually inspect the laminar flow at different flow rates (Figure 79c). The molecules of the dye are smaller and have a much higher diffusion rate (typical rate $\approx 10^{-6} \text{ cm}^2\text{s}^{-1}$ for glucose sized molecules [159]) than the proteins of interest and so provide an upper limit for this coarse test. At the faster flow rates, the boundary is more sharply defined, which is expected, as the transition time is shorter, so diffusion plays a relatively smaller role. Some blurring is observed at the lower flow rates, indicating diffusion, yet the separate channels can be clearly distinguished indicating the viability of this

approach. The blurring indicates that there is some turbulence as predicted by the model of Figure 78 indicating that a boundary of $\sim 100\ \mu\text{m}$ is to be expected in practice.

One notable factor of the printed fluidic circuits is that they have a yield of about 80%, which is lower than the PDMS clamping method; PDMS clamping is much more reliable and only fails when overtightened, thus cracking the sensor substrate which happens rarely once practised. The sources of failure generally come from issues with sealing and result in the following problems:

Problem: One issue is that the printed parts are often not flat - despite being designed as such - due to their thin size causing warping in the finishing process.

Solution: By warming the prints to $40\ ^\circ\text{C}$, they can be clamped together to self-reference and mate more tightly.

Problem: A further issue comes from the alignment, which is done by hand, often meaning the tape does not align perfectly to the printed channel and its inlets and outlets. The result is a potential for turbulence from voids or worse, a place where the fluid pressure can peel the tape from the substrate or top fluidic section.

Solution: This problem was solved by optimising for tighter tolerances and adding in alignment pillars to reduce reliance of hand alignment. Most of the issues with the fluidic circuits can be reduced further by moving to manufacturing techniques that are not human dependent i.e. using machinery to assemble parts will have higher positional accuracy than achieved by hand.

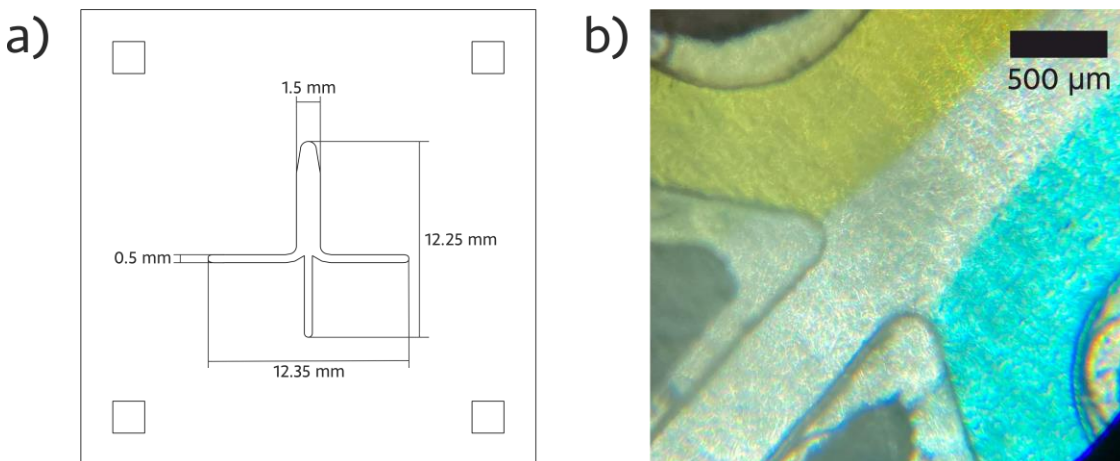


Figure 80: a) Three channel schematic with x and y dimensions for both the print and laser cut. b) Image of channels with three fluids with a flow rate of $20\ \mu\text{L}/\text{min}$ at point of contact. Area of middle channel expansion highlighted.

So far, the printed channels have only been demonstrated with two flow channels and a higher degree of multiplexing is yet to be demonstrated. For the PDMS channels, it is straightforward to add more channels, with four channels having already been

demonstrated [92] and the only limiting factor is the field of view. In principle, the laminar flow approach allows for an infinite number of parallel channels to flow adjacent to one another, although it is important to ensure that the pressure in every channel is similar to avoid unequal stream sizes and flow rates between adjacent streams [160].

With these considerations in mind, Figure 80a presents a three-channel design with three inlets feeding into a single outlet. Figure 80b shows the channels in operation using dye solutions. The three streams flow successfully without mixing.

6.3.v. Summary

In conclusion, the 3D printed fluidic channels were designed with the following parameters and properties based on the studies above:

Channel width: Each flow stream width was 500 μm as this accommodates a 300 μm wide GMR sensor and allows separation of sensors to account for the small amount of mixing across streams.

Channel height: The channel height is $\approx 390 \mu\text{m}$ determined by the resolution of the printer and the thickness of the sealing tape.

Flow rate: A flow rate of 20 $\mu\text{L}/\text{min}$ can be used in the channels. While this does not produce the sharpest laminar flow boundary, it is sufficient for creating distinct flow streams. Higher flow rates would improve the laminar flow, but channel leakage may become an issue due to increased pressure.

GMR Placement: GMR sensors are to be positioned no further than 3 mm away from the meeting of the channels. As the sensors are 500 μm in the longest dimension and the field of view is $\sim 1.5 \text{ mm}$, this constraint is not an issue.

6.4. Antibody functionalisation

Having discussed the principles of functionalisation in section 6.2, I now turn to GMR measurements with functionalised sensors. The functionalisation data consists of data sets for both anti-IgG and anti-CRP. While these antibodies are of similar size and should therefore exhibit similar resonance shifts upon binding, the QCM-D data of Figure 69 indicates that the anti-IgG should produce a larger change. My starting assumption is that the mass change seen on the QCM-D translates directly to a shift of the GMR resonance. Where possible, the data has also been taken for the shift of

the casein blocking buffer that followed as demonstrated in Figure 81 to aid in further comparisons. The example data in Figure 81 shows a difference in shift magnitude for anti-IgG and anti-CRP which is expected as a difference is observed in the data in section 6.2.ii, although it is explored further here. The data in this section is presented in microns, because it reports the resonance shift on a chirped GMR sensor.

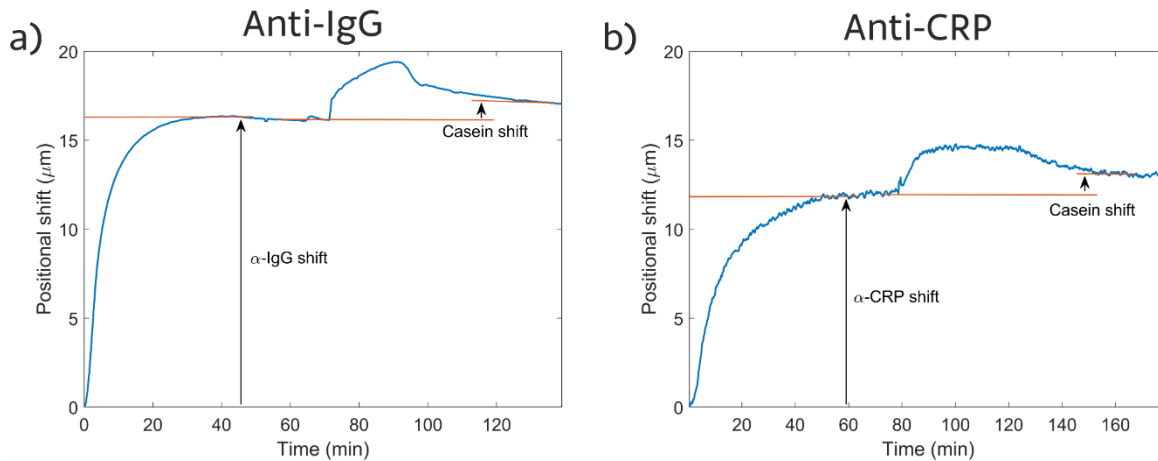


Figure 81: Example antibody binding data and blocking steps for a) anti-IgG and b) anti-CRP exhibiting the steps taken for antibody binding and casein binding.

6.4.i. Comparison of fluidic parameters

The main parameters that are discussed next are flow rate, channel size and concentration. I varied the flow rate between 20 $\mu\text{L}/\text{min}$ and 50 $\mu\text{L}/\text{min}$, the channel size was varied between 150 μm (represented by the PDMS channels) and 390 μm (represented by the printed channels) and the concentration between 25 $\mu\text{g}/\text{mL}$ and 50 $\mu\text{g}/\text{mL}$.

The results shown in Figure 82 represent the average shift from a given combination of parameters with the error given as the standard deviation between repeats. Where there is only a single experiment, no error is given and so the data point should be considered with some caution. When first looking at Figure 82, it is clear that no combination of parameters results in the same shift. The first source of variation might be a difference in sensitivity between separate chirped GMR sensors. It is true that fabrication will result in some variability, however fabrication tolerances alone would not produce such a wide variation in results. For this reason, fabrication is largely discounted as the source of disparity.

Since the antibody-PEG binding forms a covalent bond, there is no unbinding of antibodies from the surface. Considering this, the variation seen in Figure 82 indicates that the antibody binding is diffusion limited, as it does not reach a consistent saturation point. One cause will be the area of the chip functionalised with PEG that is

not active and that will remove antibodies from the solution intensifying the diffusion boundary before the sensor for diffusion limited systems i.e. low concentrations and flow rates.

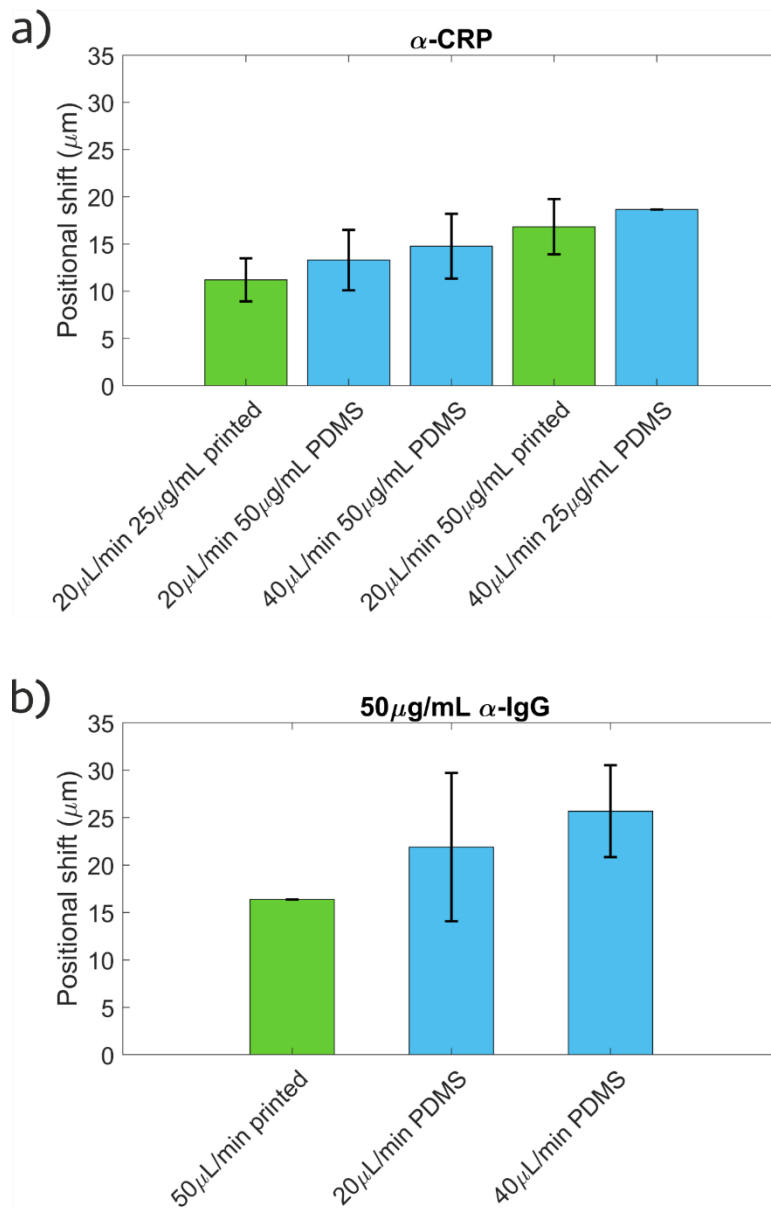


Figure 82: Average shifts observed on GMR sensors for a variety of flow rates and concentrations compared for a) anti-CRP and b) anti-IgG. The error bars are two times the standard deviation between measurements.

I can derive the following insights from the data in Figure 82.

- The faster flow rate does increase the magnitude of the shift, as expected, since faster flow helps to minimise the impact of the diffusion boundary layer.
- PDMS channels outperform the 3D printed channels even at a lower flow rate.

The second point is to be expected, as the PDMS channels are smaller in terms of channel height, so they lead to a higher channel velocity and to a shorter diffusion

distance for the target proteins to the sensor surface. While these trends make sense, there are some data points that do not match. For example, in Figure 82a the largest shift is observed for a 25 $\mu\text{g}/\text{mL}$ CRP concentration at 40 $\mu\text{L}/\text{min}$, even though there is another data point for the same flow with twice the concentration (50 $\mu\text{g}/\text{mL}$). To consider this apparent discrepancy further, the data from Figure 82 has been separated into individual points and is plotted in Figure 83.

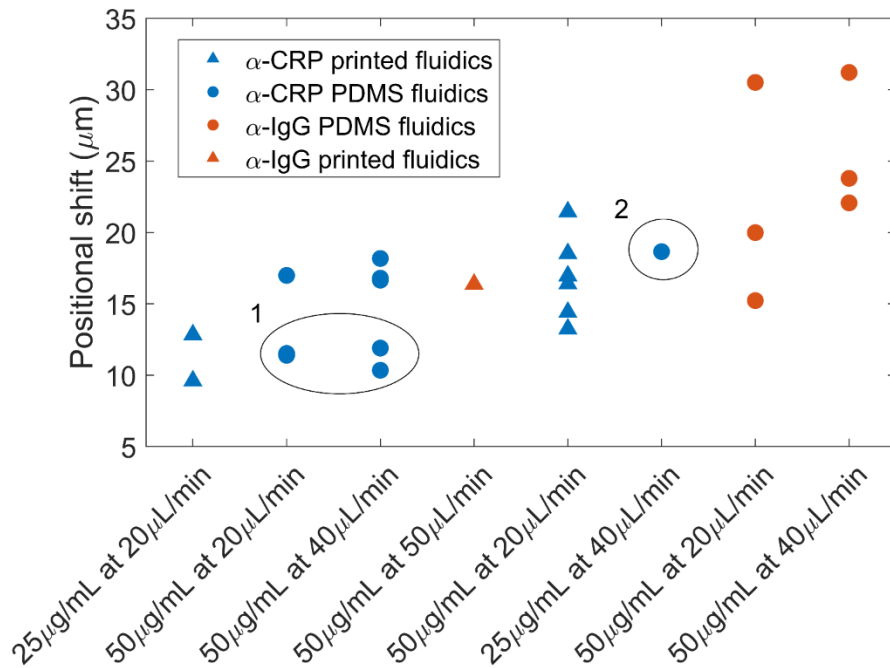


Figure 83: Plot of the antibody shifts for each parameter combination as shown in Figure 82. Anomalous results highlighted in 1 and 2.

Figure 83 helps to recognise a few other points. The key is the variability within each parameter space. The 20 $\mu\text{L}/\text{min}$ for CRP data has the most data points as well as the data being relatively tightly packed compared to others. However, it is clear that the data still has a large variability. Part of this variability will be due to settling of the sensor as the experiment needs to be started relatively quickly when a solution hits the GMR as the PEG will hydrolyse with water. If we accept that the chemistry is variable, then the results circled in Figure 83 can be considered as potential anomalies where the PEG layer on samples in circle 1 may possibly have undesirably hydrolysed, thus reducing the average shift. Separately, point 2 is not a true representation as it consists of only one data point. By removing the circled data points, the trend starts to look more like what I expected:

- Anti-IgG produces a larger shift than anti-CRP as already discussed in section 6.2.ii.
- A faster flow rate or a higher concentration lead to a larger shift as they minimise the impact of the diffusion boundary layer.

One aspect to note is that the PDMS channels were a lot less susceptible to leaking due to pressure and so could withstand faster flow rates. The advantage of faster flow rate addresses the diffusion boundary layer issue which is a large part of the issue here.

6.4.ii. Functionalisation variation

Another parameter that might be responsible for the variations in surface chemistry is the casein blocking step. If fewer antibodies bind to the PEG layer, then more casein will occupy the remaining binding sites. Figure 84 shows the corresponding relationship between antibody shift and casein shift, which appears somewhat random. This random correlation may indicate that non-specific binding is not linked to antibody concentration, which is possible due to the PEG layer both acting as a blocker to non-specific binding as well as spacing the antibodies from the surface. The data in Figure 84 further highlights the variability of the surface functionalisation, which has been the main issue with the biological assays I have studied.

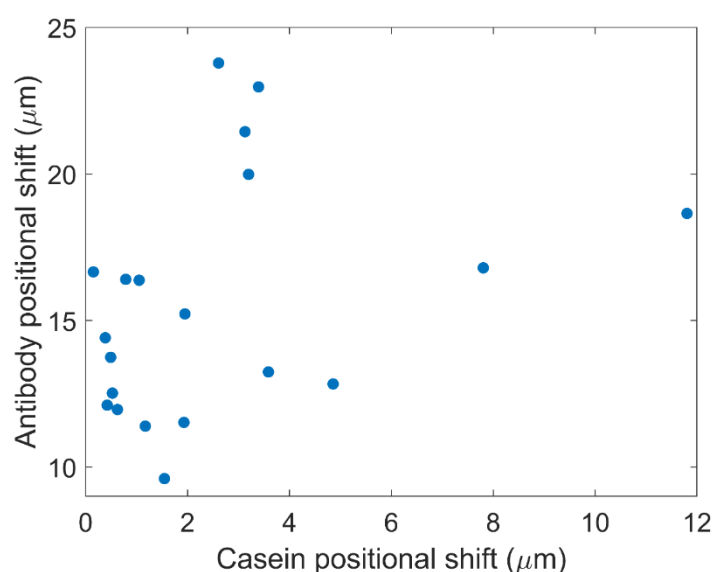


Figure 84: A plot of antibody shift against casein blocking shift on a chirped GMR sensor.

6.5. Biological measurements on the integrated device

Having achieved a relatively good LOD of $3.1 \pm 0.6 \times 10^{-5}$ RIU for refractive index sensing with my instrument, I had hoped that I could achieve the same pg/mL biological performance as reported by other group members by following the same surface chemistry protocol.

Unfortunately, this proved not to be the case as I describe in the next section.

6.5.i. Performance of protein assay

Figure 85 presents the data taken for a CRP assay that used the laminar flow channels described in section 6.3.iv and was measured using my handheld instrument. I used a flow rate of 20 $\mu\text{L}/\text{min}$ and a concentration of 25 $\mu\text{g}/\text{mL}$ for the antibody functionalisation.

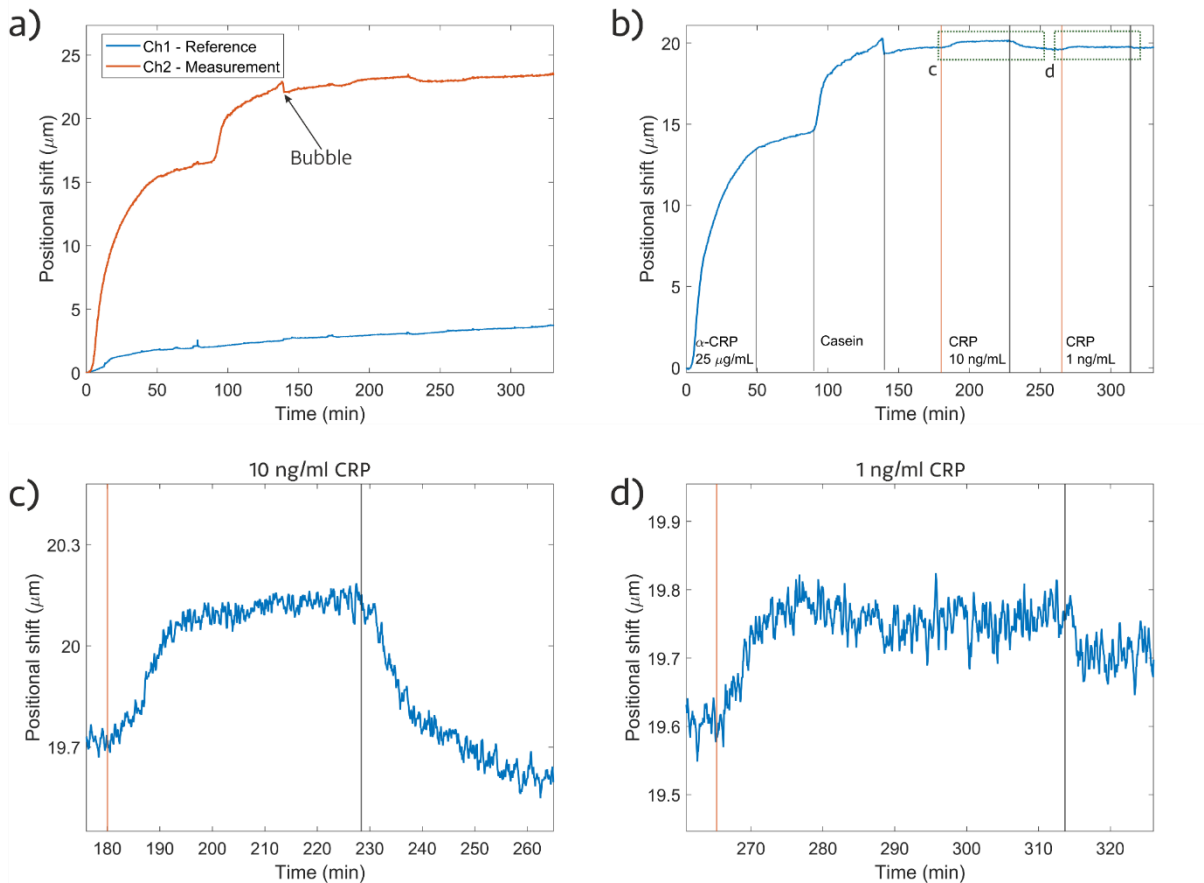


Figure 85: a) Measurement and reference channels for a CRP assay. A bubble at the transition of casein to PBS is marked. b) Difference between signal and reference channels of a) plotted with solution injections marked by red lines. c) Focus on the section where 10 ng/mL CRP was injected. d) Focus on the section where 1 ng/mL CRP was injected.

The data presented in Figure 85c) and d) describe the 10 ng/mL and 1 ng/mL binding steps, respectively. These are promising results that both show the characteristic binding curve and also show unbinding as soon as the buffer is introduced. The pixel shifts are 0.50 px (0.39 μm) for the 10 ng/mL and 0.17 px (0.14 μm) for the 1 ng/mL. The lower concentration is just above the 3σ value from chapter 5 of 0.14 px when processed with a low pass filter.

I also attempted to measure the kinetics of the binding, similar to the Biacore system [161]. By measuring the binding in terms of its kinetics, the certainty of the measurement can be improved. One analysis method that shows promise has been

developed by Li *et al.* [162], to which I am a co-author and contributed with my understanding of the noise sources. The method utilises the Langmuir isotherm function in combination with a predictive filter to reduce the readout noise and improve the limit of detection. Unfortunately, I was not able to fit a binding curve to the data of Figure 85. The reasons for this relate to how diffusion-limited the fluidic configuration is. However, despite this limitation, achieving a 1 ng/mL result is a promising milestone in the development of this handheld instrument.

6.5.ii. Protein assay troubleshooting

Even though the observation of binding for a 1 ng/ml concentration on my instrument was exciting, I conducted further studies to understand the discrepancy to the pg/mL results achieved by my colleagues on the laboratory setup. Multiple aspects were checked for the discrepancy including:

- The type of protein (CRP and IgG were both tried, the IgG being identical to that used by my colleagues)
- The assay viability (QCM-D data of section 6.2.ii)
- The fluidics and the limitations they may impose (section 6.4)

These studies have not been able to identify the source of the discrepancy and so I delved further to try and identify possible causes.

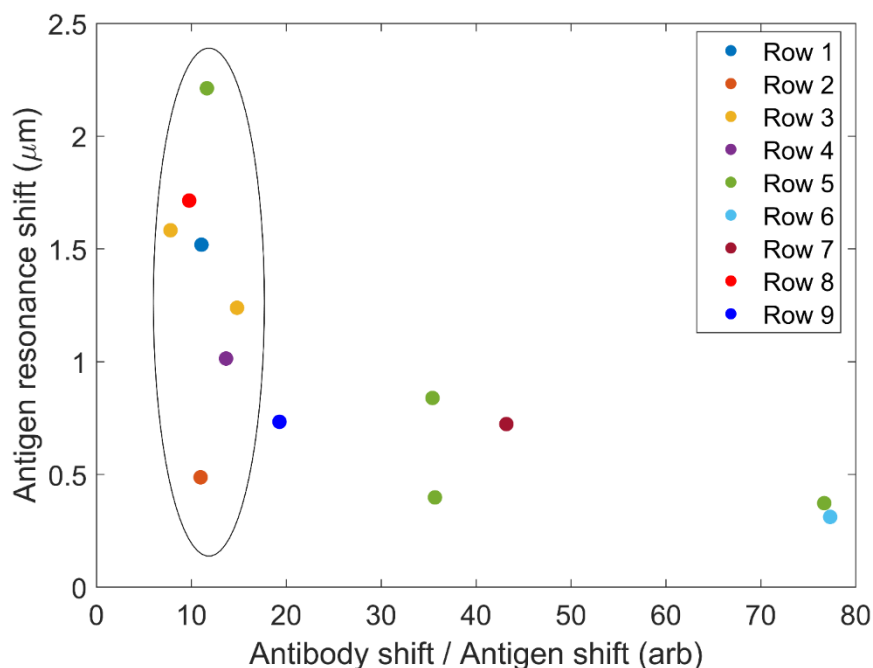


Figure 86: Resonance shifts observed upon antigen binding for a variety of configurations described in Table 7. Resonance shifts are reported in μm as data was taken across different setups.

I used the results in Figure 85 as a starting point for the exploration of the various parameters. I used an antigen concentration of 1 µg/ml or higher to ensure that large shifts were observed that could be easily compared. PDMS fluidics were used because they resulted in larger shifts as shown in Figure 83. The relationship between the shift due to the antibody on the sensor surface and the shift due to antigen binding is important as they should be directly related. The antigen shift is plotted against the antibody shift in Figure 86. As the PEG layer has been determined as a possible source of variability, the antibody shift is normalised to its antigen shift. The aim of the normalisation is to highlight any data that may vary from the expected trend of antigen shift being proportional to antibody shift. As the data is taken from a range of experimental parameters, Table 7 lists these parameters.

Table 7: Values of antibody and antigen shifts pertaining to the data sets in Figure 86. The antibody concentration is 50 µg/mL and antigen concentration is 1 µg/mL.

Data	Assay	Flow rate (µL/min)	Antibody Shift (µm)	Antigen Shift (µm)	Notes
●	CRP	40	16.80	1.52	α-CRP 25 µg/mL
●	CRP	20	5.35	0.49	CRP 10 µg/mL
●	CRP	40	1) 18.35 2) 12.34	1) 1.24 2) 1.58	
●	CRP	40	13.84	1.01	No Blocker
●	IgG	20	1) 25.74 2) 14.20 3) 28.57 4) 29.71	1) 2.21 2) 0.40 3) 0.37 4) 0.84	
●	IgG	40	24.10	0.31	
●	IgG	40	31.24	0.72	No Blocker
●	CRP	20	16.75	1.71	Printed Fluidics, CRP 10 µg/mL
●	IgG	40	14.14	0.73	O2Bond Nano-hole array [30] on instrument

There are some interesting details that may be hard to see at first glance:

A zone of consistency: I highlight a zone of a consistent ratio between antibody shift and antigen binding in Figure 86 with an oval. Apart from the green dot, these are all

for the CRP assay. This is encouraging, as despite the variability of the antibody shift, the antibody/antigen shift ratio is reasonably constant.

Protein batch is not an issue: One variable considered was the age or batch of the stock as the polyclonal nature and age of the stock solution could contribute to the variation of the results seen in my measurements. However, the data presented in section 6.2.ii and 6.2.iii use different stock solutions and were taken more recently than most of the data of this section. Also considering the internal consistency of most of the data here, which is from multiple stocks, rules out age or batch as a significant factor.

Shift Magnitude: The magnitudes show a reasonable amount of internal consistency (despite the outliers). The results do not point to an obvious reason for the discrepancy to the pg/mL results achieved by my colleagues on the laboratory setup. It is not down to the diffusion limited nature of the set up otherwise the PDMS fluidics would have outperformed the printed fluids in section 6.4.i.

6.5.iii. Channel placement effect on surface chemistry

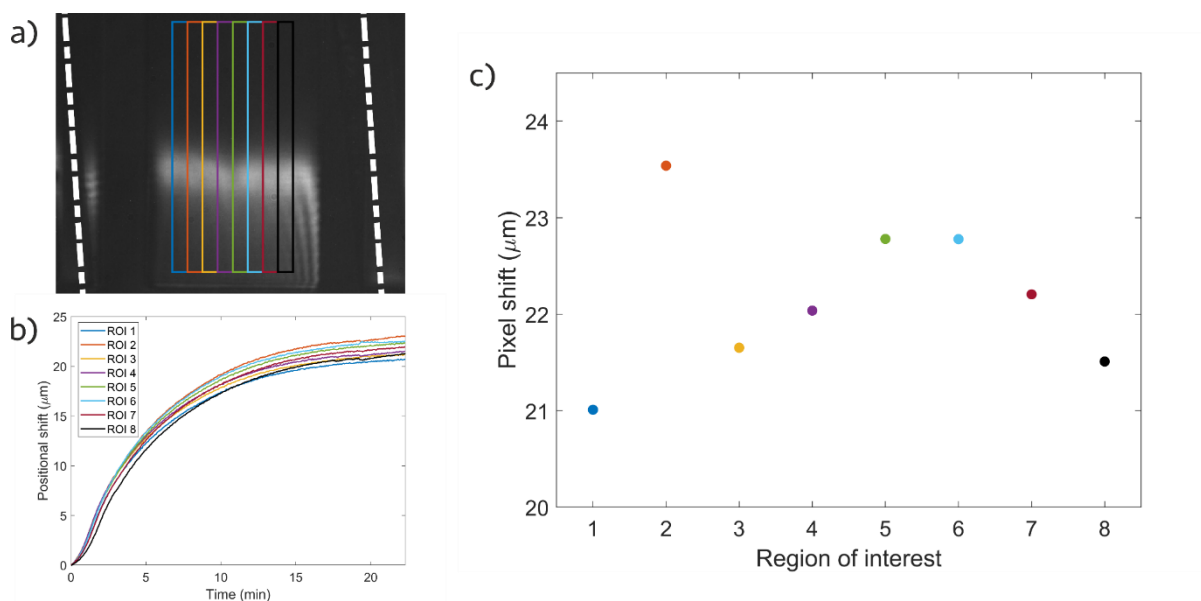


Figure 87: a) Regions of interest analysed of a GMR in a channel, channel walls marked in white. b) Shifts measured for 50 $\mu\text{g/mL}$ anti-IgG at 40 $\mu\text{L/min}$ across the width of the GMR. c) positional shifts between $t = 0$ and $t = 23$. Note: the colours in b) and c) refer to the corresponding ROIs in a).

Another issue could be the placement of the GMR nanostructure with respect to the channel boundaries; it is well understood that the fluid flows more slowly near a boundary than in the centre of the channel [145] (Figure 78c). To explore this parameter, I compared multiple adjacent regions of interest (ROI) (Figure 87). The data confirms that there is a slight difference of antibody binding across the channel. Taking

the mean shift of all the ROIs produces a shift of $22.2 \pm 0.8 \mu\text{m}$. The variation may have a component linked to the velocity profile but the variation is small enough not to be a concern, especially as this will be reduced further by taking a larger ROI across the width of the resonance.

6.5.iv. Further factors – operating wavelength and source.

The variation in the chemistry appears to be the largest barrier to pushing the results from my instrument to the levels reported by others using GMR modalities. The work by Conteduca *et al.* [30] uses a nano-hole array at 650 nm and so is sufficiently different in terms of modality to explain the difference in biological limit of detection. The work by Kenaan *et al.* [92] however uses a 1D chirped GMR and so begs the question of why my instrument does not reach the low pg/mL regime.

An initial consideration could be that the move from 850 nm wavelength to a 650 nm resonance has affected the sensitivity in some way, although it should work in my favour, as shorter wavelength should result in higher surface sensitivity. Another consideration is that Kenaan *et al.* used a supercontinuum source in their set up. The use of this source could be benefiting from the coherence that it exhibits compared to the RCLED I have used - however this does not seem like a strong argument. Having considered many factors, I also asked my colleague Dr Conteduca to run some direct comparison measurements to try and isolate the variables due to human factors, but these studies indicate human error is not likely to be a factor because results taken by Dr Conteduca are consistent with those in section 6.5.ii. A final consideration was that of the hydrophobicity of the channel material, as proteins will tend to preferentially adhere to hydrophobic surfaces. A preliminary result done in collaboration with Dr Kunstmann-Olsen where PDMS channels were passivated to be hydrophilic indicates hydrophobic channels to be the cause of issue, however, further testing is required.

6.6. Comparison with other handheld devices

As discussed in chapter 5, a few other handheld photonic biosensors have already been reported in the literature. While my instrument compared well to them in terms of refractive index LOD, it is also worth considering the biological limit of detection. Table 8 is a replica of the one presented in section 5.5, with the addition of the final column, which reports the limit of detection for proteins.

Looking at the LOD in RIU the highest performer is the Mach-Zehnder implementation by Martens *et al.* [102] (which became the Antelope System) and this is also one of the highest performing assays in biological terms with 19.5 ng/mL

Table 8: Summary of photonic modalities used for low-cost approaches to biosensing with refractive index LOD and protein assay LOD.

Sensor	Source	Read Out	LOD (RIU)	Assay LOD
1D GMR (this work)	RCLED	Camera Sensor	$3.1 \pm 0.6 \times 10^{-5}$	1 ng/mL CRP
1D GMR Intensity Readout (Gerken group) [128]	LED	Photodetector	1.6×10^{-3}	24 ng/mL CD40 ligand antibody (150 kDa) ^a
Mach-Zehnder Interferometer [102] (Antelope system) [129]	Super-luminescent diode	Camera Sensor (Arrayed Waveguide Grating)	$6 \pm 2 \times 10^{-6}$	19.5 ng/mL CRP
1D GMR (Cunningham group) [104]	Tungsten lamp	Smart Phone Camera (Diffraction Grating)	1.1×10^{-3} [130]	637.5 ng/mL IgG
Plasmonic NanoHoles (Altug & Lechuga groups colaboration) [107]	LED	Camera Sensor	5.7×10^{-4}	18 μ g/mL CRP (36 pg/mL CRP Altug ^b [163])

^a Value published based on SNR

^b Labelled implementation

The work by Paulsen *et al.* is based on an intensity readout for a GMR and claims a limit of detection for a molecule of a similar size to CRP of 24 ng/mL [128], although this value was extrapolated and not actually demonstrated, so should be taken as aspirational.

The final configuration considered here is the plasmonic nanohole array in the last row of Table 8 (Fabri-Faja *et al.* [107]) which has an average bulk LOD compared to the other modalities in Table 8. For the biological measurement, they report an LOD of 18 μ g/mL, which appears somewhat high. The reason for this could be due to the

operation being in transmission thus resulting in a low signal intensity when binding occurs. Confirmation of this assumption can be found in further work by the same group [163] where they use a similar setup but reduce the LOD to 36 pg/mL by using gold nanoparticle labelling. While using labels is an obvious route to reducing the LOD, it is not conducive to making a low-cost POC sensor that is the goal of this work.

When comparing the results in Table 8 to my work, the result of 1 ng/mL compares rather well, despite the caveats and need for further improvement described above. With further work, these results could be optimised further, thereby lowering the detection limit and increasing reproducibility.

6.7. Multiplexing capabilities

Most assays in clinical practise require more than a single biomarker to inform the exact nature or the status of a disease, or to exclude patient-to-patient variations. For example, the National Institute for Health and Care Excellence (NICE) recommends taking a ratio of albumin to creatinine to assess kidney disease, rather than measuring proteinuria as a single marker [164]. For this reason, it is important to demonstrate the multiplexing capability of my instrument.

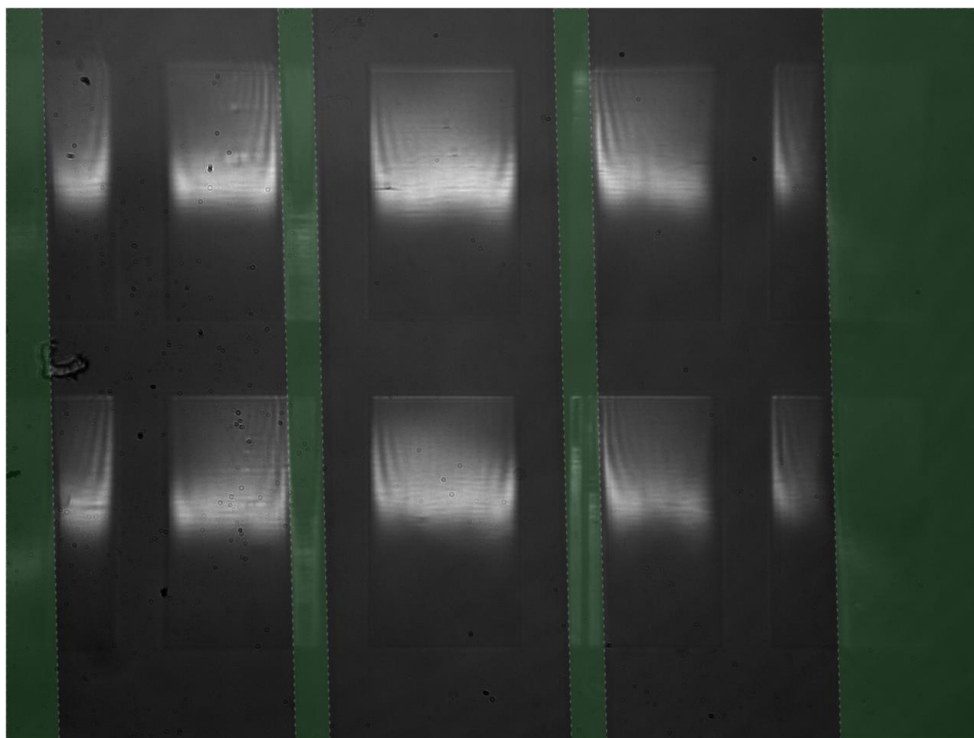


Figure 88: Example measurement using three channels. Green highlighted areas show where PDMS is in contact with sensor surface.

My instrument is capable of basic multiplexing, for example using two measurement channels and a reference, as it can operate with three parallel fluidic channels as shown in Figure 88. The number of channels here is limited by the size of the fluidic channels and the fact that the GMR sensor is aligned to these channels by hand; further improvements, including automation, could clearly increase the number of channels available for multiplexing.

A further way to increase channel count would be to use the lateral flow approach described above, which removes the fluidic limitation, and to functionalise the sensors using spotting technology; spotters can deposit antibodies using ink-jet technology and dispense droplets small enough to form 100 - 200 μm size pads on the sensor. Using spotting technology, one can easily see the potential for depositing 10 or more different antibodies within the available field of view.

7. Outlook

7.1. Measuring success and potential improvements

Is the instrumentation I have developed ready for commercialisation? I believe it is getting there, but it is not quite there yet. Does the progress made imply the work presented here was unsuccessful? Definitely not. People have created companies based around less, an extreme case being the “diagnostic company” Theranos. The progress made therefore is valid since it has produced a useful discussion on low-cost biosensors that was scrutinised by peers [100], as well as being open about the trials of development. It is worth then, considering the metrics with which to judge the adequacy of a given technology. The most obvious one is performance but in order to fully discuss viability performance should be judged alongside the potential production cost of the instrument, as well as its size and complexity to run.

In terms of performance, the instrument has achieved a bulk limit of detection of $3.1 \pm 0.6 \times 10^{-5}$ RIU which is very competitive compared to other biosensors. The biological limit of detection has been shown for CRP, where 1 ng/mL in buffer has been achieved. Regarding size, I have already demonstrated handheld operation, and some considerations for improvements are laid out in section 7.1.i below.

Considerations regarding the cost and manufacture are briefly discussed in section 7.2. The complexity of operation is something that has only been considered briefly, with potential improvements to fluidic handling discussed in section 7.3.ii. The biosensor is capable of being run by a reasonably low specification computing device, such as a smart phone app. The main computational requirements are the image handling and the calculations needed for peak tracking. A full exploration of these aspects has not been covered here due to the presumed simplicity of implementation at a future stage.

7.1.i. Potential improvements

Beam splitter: While work has been conducted to increase GMRs tolerance to angle [165,166] the angular dependence can be used to remove the need for a beam splitter cube. As briefly mentioned in section 2.2.v the resonance can also be excited at non-zero angles, i.e. incident at $+\theta$ and collected at $-\theta$, so a system realisation relying on angular incidence, without a beamsplitter, can clearly be considered.

Lenses: If the size of the instrument is to be further compacted, the number of lenses could be reduced. At least one lens is required to collimate any light source used, hence it would be ideal to have a single imaging and collimating lens. However, by using

meta-lenses and flat optics [167,168] the instrument could be redesigned in a much smaller form factor i.e. long and thin. The only argument against tackling these types of engineering challenges is if the instrument does not benefit from becoming any smaller.

Surface Chemistry: The final major issue to address is the limit of detection. The instrument has demonstrated an LOD for CRP well below the clinical range, but developing the reliability of the assays is key, so many repeat measurements would need to be conducted. A key question remains: does the LOD need to be lower? This would certainly be the case if samples were going to be diluted in the process of testing. The bigger question will be how to tune the surface chemistry to achieve an appropriate dynamic range, so that the response of each analyte is matched to its clinically relevant range. There is a fundamental limit to the highest protein concentration that can bind to the surface. While detecting low concentrations is important, it is equally important to be able to measure high concentrations as well, as many diseases result in elevated levels of proteins that are important to capture.

Sample Cartridge: The fluidic channels are currently not conducive to a low-cost setting, due to the need for syringe pumps and the complexity of the fluidic arrangement. Improving and simplifying the fluidics requires significant development of the instrument to achieve a commercial device. The changes required to achieve this may need a complete redevelopment, some preliminary work is presented in section 7.2.

Improving LOD: The instrument is capable of incorporating the higher Q modality of dielectric nanoholes by Conteduca *et al.* [30] with no change to the instrument. The use of the dielectric nanoholes is somewhat of an incremental improvement, sensitivity can be increased significantly by incorporating a phase-based approach which is explored in 7.3.i.

7.2. Economic considerations for commercialisation

7.2.i. Manufacturing techniques

One aspect that has been considered throughout the development of this work is the potential manufacturing process. The photonic sensor, which will be mounted on a cartridge, is arguably the most important aspect of the entire system. As discussed in chapter 5 the use of processes such as electron beam lithography used to create the sensor chip are not scalable, yet more scalable processes are applicable to the

manufacture of these photonic structures, such as nano-imprint lithography. The feature size required and material used (silicon nitride) for the sensor is compatible with CMOS manufacturing. To estimate what the cost per chip could be let's make some assumptions:

- Average cost of fabricating one wafer \approx \$650 [169]. This number includes all the costs of running and maintaining a CMOS foundry.
- Cost per 152 mm wafer \approx \$150, based on our group's cost per wafer and so the actual cost could be lower.
- The size of the chip will be reduced to a side length \leq 5 mm.
- The process yield is 90% [169].

With these assumptions approximately 650 individual chips can be made from one 152 mm wafer with a cost of \sim \$1.22 per chip. As some of these assumptions are over estimations, such as cost per wafer since it is based on small batch costs, I predict that the sensors could be manufactured for $<$ \$1 a chip.

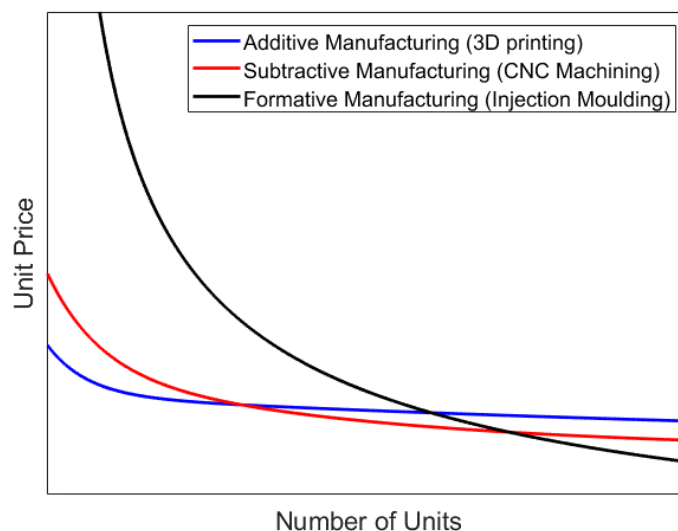


Figure 89: Economics of scale of the three key types of manufacturing techniques. [155,170]

Regarding the instrument housing, which has been realised using 3D printing, the issue is the feature resolution in order to ensure that the cartridge can be inserted accurately and that the optical elements are positioned precisely. I have already discussed that 3D printing has a feature resolution similar to that of injection moulding [64]. Additive manufacturing such as 3D printing, however, is not a suitable solution for large scale volumes. Figure 89 illustrates the economics of scaling-up three manufacturing processes. Additive manufacturing is the cheapest in terms of the initial cost of equipment, but when moving to higher volumes, this cost barely comes down with volume due to the relatively high raw material cost and the slow speed of the process.

Subtractive manufacturing is similarly limited by processing time and has an even higher initial equipment cost, which makes it look similar economically.

Formative manufacturing such as injection moulding, is the process of choice for large-scale manufacturing. While the initial cost of equipment for production is high, the raw materials are significantly cheaper than those of the other methods, and the speed of production is significantly higher. Since the main cost is the manufacture of the mould, injection moulding should only be used once the design has been firmly locked down, so it ideally complements the flexibility advantage of 3D printing. The crossover between these methods in Figure 89 will happen at production quantities in the 1000s – 10,000s range [155], clearly large scale production volumes.

7.2.ii. Component cost

For scale-up, the components such as the optical elements and the camera, if purchased directly from an Original Equipment Manufacturer (OEM) would reduce cost significantly. Currently, the components (cf. chapter 5) were purchased from retail companies that may also be Value-Added Resellers (VAR). Essentially, this means that the cost to build one instrument is not representative of the cost of the future final product.

For example, the camera purchased from The Imaging Source cost around £138.00. However, The Imaging Source will have purchased the CMOS sensor from an OEM and added functionality which may not be needed here. The bare Aptina MT9V024 sensor is available on its own for ~10% the cost (Mouser Electronics, Inc). Other 5 MP sensors are available for £5-£6, however, using an unintegrated sensor requires your own software and hardware integration. A further example is the beamsplitter, purchased from Thorlabs, which cost £140 at the time of writing. Should this component still be required in a final device, the cost could be reduced drastically as beamsplitters are commonly utilised in CD and DVD drives, where the entire drive may cost less than £10.

Components such as the filter which is required for the LED source will benefit greatly from mass manufacture. Costing £200 (at time of purchase) from QuantumDesign UK and Ireland Ltd, for a 12.5 mm diameter size. The filter is much larger than required as the beam size is < 5 mm in diameter. In future, larger wafers could be produced and diced to size. Considering the implications of manufacturing techniques discussed in 7.2.i, I estimate that the OEM cost of the instrument could be ~£50 and potentially much less (~£10) should the scale of manufacture be sufficiently large.

7.3. Preliminary work for further development

I now discuss preliminary results of other ideas that may be useful for improving the sensor technology in the future.

7.3.i. Interferometry in an autonomous device

Despite the chirped GMR only supporting a low Q resonance, it has performed incredibly well in the low-cost instrumentation I have developed. While the performance is suitable for large proteins and molecules, more sensitivity is required to measure small proteins (such as procalcitonin ≈ 13 kDa) at low concentration. As discussed in chapter 5, using a higher Q resonance to increase performance is not compatible with low-cost light sources. Alternatively, a GMR-based solution which shows promise has been developed by Barth *et al.* [171]. Barth *et al.*'s approach uses interferometry to detect refractive index changes, which is intrinsically more sensitive than the resonance-only method employed here; as the analyte binds to the surface, the resonance exhibits a phase change which can be detected accurately. Using this method requires a coherent source and the two signals need to be spatially overlapped, e.g. by using a Wollaston prism, for two polarisation modes. The reason to use two polarisation modes is that they both have different phase responses across the resonance as shown in Figure 90.

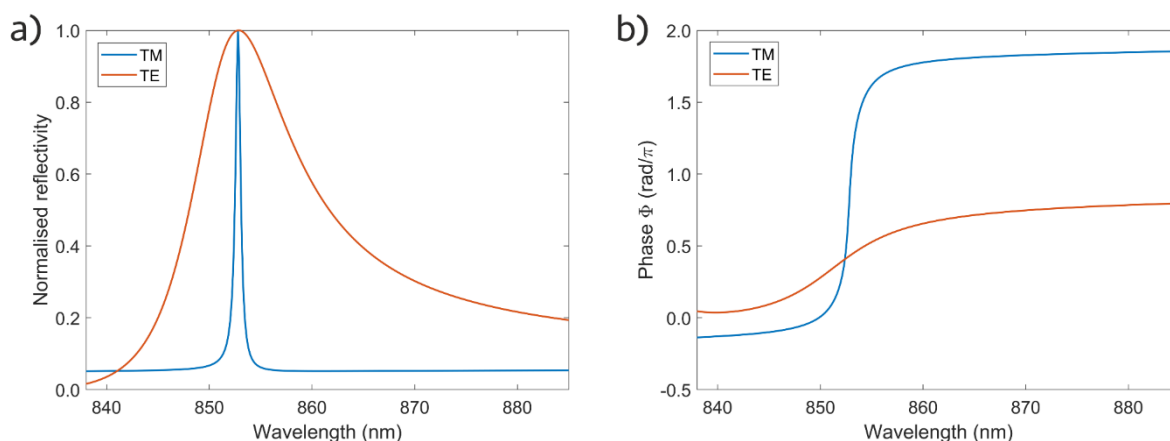


Figure 90: a) wavelength and b) phase response for grating structure parameters $a = 570$ nm, $t = 150$ nm, $n_{inc} = 1.45$, $n_g = 2$, $n_{cover} = 1.33$ and $FF = 0.74$ for TE and TM polarisation. Both signals can interfere once passing through a 45° polariser, with the TE being used as the reference and the TM as the signal.

Working in conjunction with Ms. Barth, we developed a prototype instrument that worked on a compact scale which could be made using low-cost components (Figure 91). In the initial realisation, Ms. Barth used a Wollaston prism to enable the interference effect; such a prism is a relatively expensive component that is unlikely to

follow the economics of scale. We therefore came up with an alternative, which is to use a double-slit configuration that uses diffraction to create the interferogram (Figure 91a). In this case, the reflections of the two gratings that are being interfered are aligned to different slits, and so, when a phase change occurs at input, the resulting interferogram will shift accordingly. An interferogram from this approach not only benefits from the sensitivity of using phase, it also has a well-defined output pattern that can be very easily filtered.

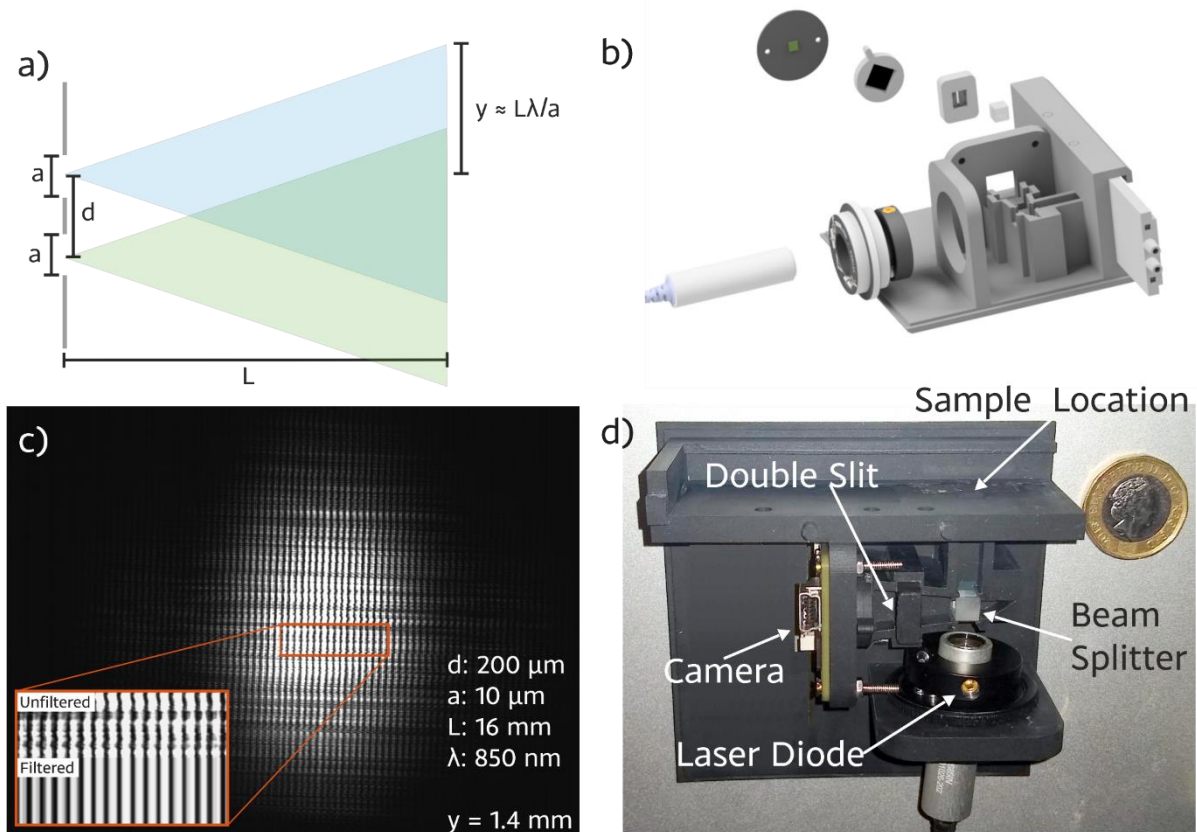


Figure 91: a) Schematic of the double slit interference method employed for compact phase interferometry. b) A rendering of the housing for the instrument. c) Raw image of an interferogram taken on the instrument with dimensions of the double slit. Insert presents a comparison between spatially filtered and unfiltered pattern. d) 3D printed housing with components labelled.

A 3D printed housing was designed (Figure 91b) and manufactured (Figure 91d) to contain all the components required for operation. This work so far is only at the proof-of-principle stage and is yet to be tested for refractive index sensing. The fringe spacing of the interferogram is determined by $w = L\lambda/d$. So for the double slits used to generate Figure 91c the fringe spacing is $\approx 68 \mu\text{m}$, which with the same DMM 72BUC02-ML camera ($2.2 \mu\text{m}$ pixels) as in chapter 5 provides ~ 30 pixels per fringe which should be sufficient to allow accurate sampling, especially as there are multiple fringes to track. Examples of the fringes are demonstrated in the insert of Figure 91c, showing the power of spatial filtering.

7.3.ii. Integrated fluidics for clinical samples

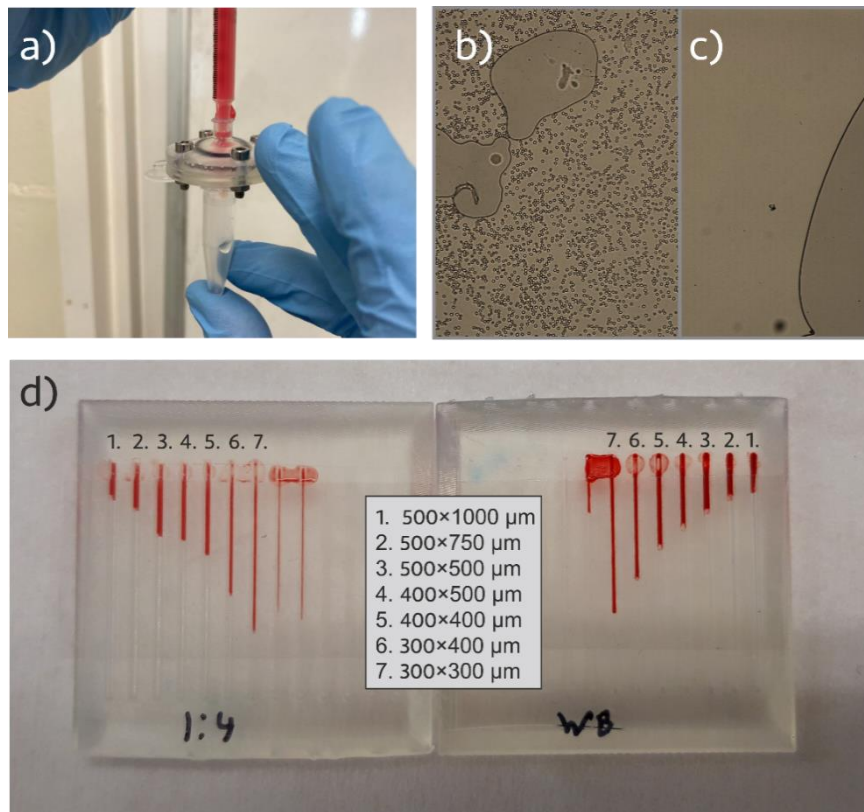


Figure 92: a) Filtered whole blood using the Vivid™ Plasma Separation Membrane. b) Microscope image of whole blood pre- filtering. c) Microscope image of blood plasma post-filtering. d) Capillary channels of various cross-sectional areas (labelled) showing travel of 10 μL of whole blood and 1:4 whole blood to buffer.

One of the key remaining aspects requiring further work is the fluidics. While the fluidic channels I developed have been useful for sample delivery in my experiments, the use of a syringe pump and sample loop are not practical in a point-of-care or resource-limited environment. To this end, a cartridge that works passively to manipulate and deliver sample to the sensor surface is required. I have done some initial tests in conjunction with Dr Kunstmann-Olsen using blood at finger prick volumes ($<20 \mu\text{L}$). Blood is an easy sample to obtain in a point-of-care setting for use in protein assays and contains high concentrations of clinically relevant targets. The first task was to remove the blood cells and to measure the plasma with the remaining proteins. To achieve the separation of the blood into plasma without centrifugation I employed the Vivid™ Plasma Separation Membrane from Pall Corporation. Figure 92a presents the filtration using positive pressure from a syringe with relevant micrographs presented in Figure 92b and c. With the ability to successfully separate the plasma demonstrated, the method for moving the blood around the device by capillary forces alone was then considered.

We started by replicating the work of Kokalj *et al.* [172] and Dosso *et al.* [173]. The technique they used involves sealed channels and a working fluid adsorbed into a pad to pressurise the air to pump sample liquids. In testing, this proved difficult to seal reliably despite appearing straightforward to replicate, even though the lack of mechanical components is a huge benefit of this approach. We then came up with an alternative approach to simply use capillary channels [174]. These channels were created by 3D printing as we have the capability to print down to 300 μm features. Using whole blood as well as a 1:4 blood to buffer ratio, capillaries of various sizes were tested, shown in Figure 92d. The longest capillary that can be seen to have worked successfully with whole blood has a channel cross-section of 300 μm x 300 μm and a travel length of 13.3 mm. The top of the channel is sealed with ELISA SealPlate® film. With the capillaries proven to work sufficiently with the more viscous whole blood, a cartridge was designed that incorporated the filter paper and a GMR as shown in Figure 93.

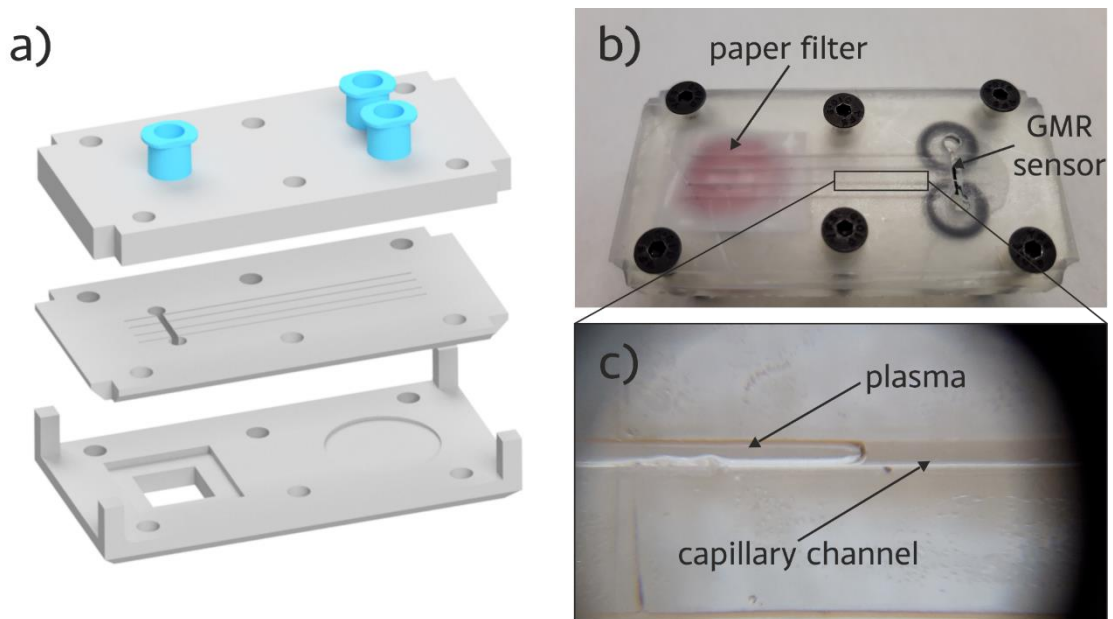


Figure 93: a) Rendering of a capillary flow cartridge with Luer inlets and outlets. b) Assembled cartridge with blood filtering and plasma flow to the GMR sensor. c) Enlarged image of the capillary channel with plasma flowing through.

A key issue with this approach is that the filter paper wicks very slowly and the plasma only drips through at a slow speed, such that the entire process takes 10s of mins. Another issue is that there is no wash step, so it may be difficult to identify specific binding of proteins from non-specific physical adsorption.

7.3.iii. Antibiotic susceptibility assay

The work presented so far describes an assay based upon antibody-antigen binding, which is used to detect protein biomarkers. However, protein assays are not the only test of use in healthcare. An area of great importance is antimicrobial susceptibility testing as bacterial infections are becoming increasingly resistant to treatment [175]. Current testing relies on methods such as culturing bacteria on agar plates, which can take several days to produce results. In this context, Miller and Silver *et al.* [149] have tethered a cephalexin drug molecule to a PEG linker allowing it to be surface bound using the MPTES functionalisation method used in chapter 6. The advantage of immobilising drug molecules is that they can then be probed with surface based sensors such as the GMR instrument I have developed. Cephalexin is a β -lactam based drug, similar to penicillin and a common form of antibiotic resistance is β -lactam resistance. β -lactam drugs bind to the penicillin binding protein that are critical to the cell wall cohesion of the bacterium. The resistance mechanism employed by the bacteria involves releasing an enzyme that breaks down the active β -lactam ring in the drugs structure [149]. By applying a patient's sample such as urine, from a patient with a urinary tract infection (UTI), the change of the surface-bound antibiotics can be monitored thus deducing if the infection is resistant to the antibiotic.

The actual change in the β -lactam ring is too small to be measured by a GMR but the assay developed by Miller *et al.* relies on flowing isolated, penicillin binding protein (PBP3) over the surface post exposure to the sample that binds to any unaffected drug. The assay involves the following steps:

- Flow sample over measurement surface, here tested with a blend of recombinant β -lactamase proteins purchased from Sigma-Aldrich (L7920) containing 40–70 IU β -lactamase I and 6–10 IU β -lactamase II. This stock was diluted 1:6 in 50 mM potassium phosphate buffer (KPi) [149].
- Wash measurement surface with sodium dodecyl sulphate (SDS) to remove any remaining enzyme.
- Flow PBP3 over measurement and control (t_4 of Figure 94)
- Wash measurement and control with SDS to remove non-covalently bonded PBP3 (this step is missing from the experiment in Figure 94)

A negative result occurs when the PBP3 remains covalently bound to the unaffected drug layer even when washed with SDS; in contrast, if the drug is broken down by enzymes present in the sample, then the PBP3 will be washed off by the SDS and leave the surface, thus resulting in a resonance shift.

The assay was conducted in conjunction with my colleague Mr. Callum Silver using my instrument. Figure 94a presents the resulting resonance shift, with each stage marked and labelled in the table in Figure 94b. Both channels here are referenced to a third channel that only had KPi flown through.

Unfortunately this experiment did not have the final SDS wash step required to remove any non-covalently bound PBP3 from the measurement channel. Therefore it is inconclusive if any PBP3 would have remained bound to the sensor surface in either channel and so is unclear whether the β -lactamase broke down the drug surface. One thing that can be seen in Figure 94 is that there is a binding curve for the β -lactamase at t_1 and also PBP3 seen on the surface at t_4 . While the results of the assay may be inconclusive, it is clear that the resonance shifts measured are more than sufficient to indicate that the instrument is sensitive enough as demonstrated by the magnitudes seen. This assay therefore could be implemented in this device in the future.

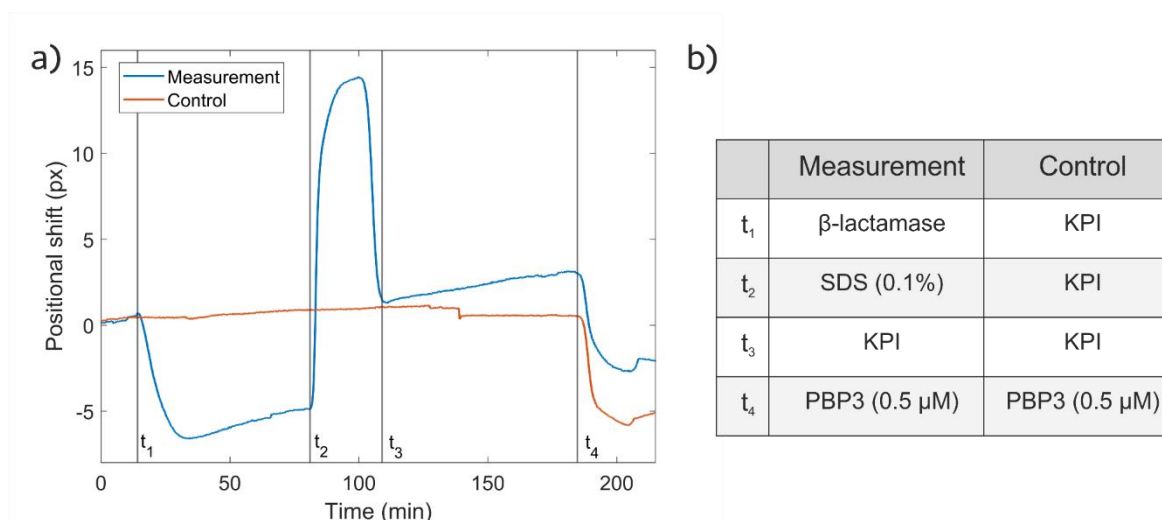


Figure 94: a) Resonance shift plot for a beta lactam drug assay. b) Solutions injected at the marked time stamps.

7.3.iv. Dopamine-based surface chemistry

It is clear from the results in chapter 6 that there is variability in the surface chemistry I used. One possible cause is the hydrolysis of the PEG linker used to connect antibodies to the surface. One way to circumvent this risk of hydrolysis is to use a different surface functionalisation protocol. My colleague Ms. Bakshi identified a poly-dopamine protocol [176], which is based on the chemistry used by mussels to attach to rocks [177]. Dopamine itself is a hormone in the human body, however, when polymerised, it becomes a layer that will adhere to almost any kind of surface [178] and thus will allow to stick antibodies to a sensor surface. Using a dopamine polymerisation layer results in a thicker tethering layer in the 10s of nm range [178]. Compared to the

PEG layer used previously, the key aspect is that poly-dopamine does not react with water, hence there is no risk of hydrolysis, which removes the time constraint of flowing antibodies over the sensor before the surface layer reacts.

The process of functionalisation proceeds as follows:

- Place a GMR sensor vertically (to avoid aggregates on the surface) in a solution of 2 mg/mL dopamine hydrochloride (sigma Aldrich H8502) in 10 mM Tris Buffer for 2 hours.
- Rinse in DI water and blow dry with nitrogen.
- Seal sensor in channel and run from antibody step as described in chapter 6.

Not only is there no reactivity with water, but there are also fewer functionalisation steps and the entire process can be completed in a single day, as opposed to three days for the PEG based process. As an early example to illustrate the viability of this protocol, I conducted an IgG binding assay. The results are shown in Figure 95 using the same experimental setup as in section 6.1.i.

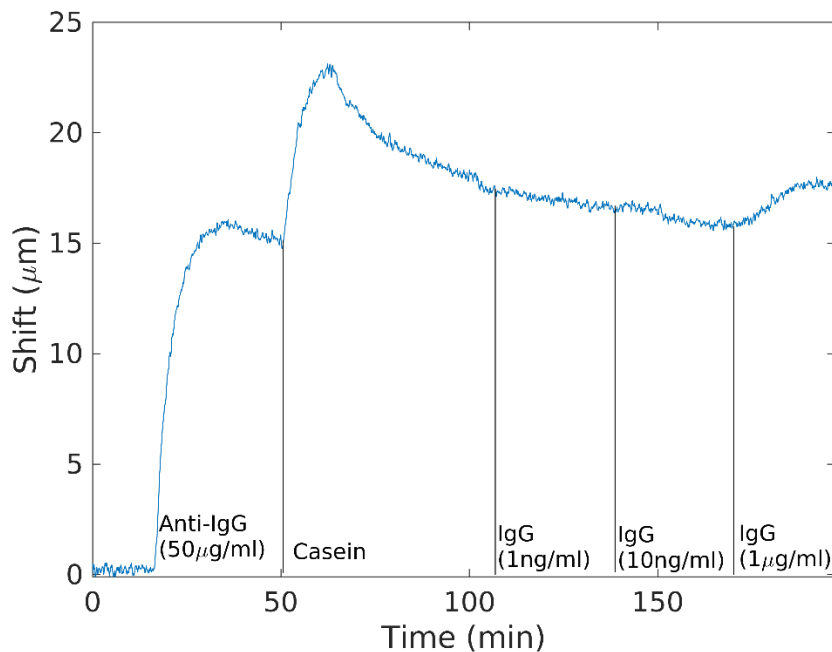


Figure 95: IgG protein assay using poly-dopamine surface chemistry. The antibody shift is 15.44 μm the casein shift is 2.77 μm and the 1 μg/mL antigen 1.33 μm.

Starting with the introduction of the anti-IgG antibody at $t = 15$ min, I note that the antibody binding achieves a 15.4 μm shift, which is less but comparable to the 25 μm shift observed for a similar concentration (50 μg/mL) using the PEG process. For the actual assay, with 1 μg/mL concentration, we observe a shift of 1.33 μm. This shift again matches the results presented earlier in chapter 6 as this antibody-antigen ratio is 11.6

which is consistent with the findings for PEG. The internally consistent ratio indicates that the poly-dopamine binding has similar surface orientation characteristics to PEG. While the results are similar to those presented in chapter 6 it is on the lower end of the scale for antibody binding. The main reason for this will be that the poly-dopamine approach is not as optimised as that for PEG. The result of the slightly lower antibody shift is that the lower antigen shifts are lost to the noise, this is in conjunction with the reasons discussed in chapter 6 about measuring low concentrations.

8. Conclusion

To summarise, a photonic biosensor has been presented based upon the guided mode resonance modality. Made in silicon nitride for an operational wavelength of 647.1 nm, the resonance has a typical Q-factor of around $Q = 190$. The sensors are chirped to translate the spectral response into a spatial response that can be easily read out with a camera. The instrument was constructed with low-cost considerations in mind. As such the housing was prototyped using additive manufacturing and off-the-shelf components were chosen for the construction.

A study into the performance of these components was conducted to understand the sources of noise, the interplay of the different parameters and the link to the quality factor of the sensor. The results showed that for use in uncontrolled environments, moderate to low Q values are desirable. Interestingly, it was also found that low-cost laser sources were unsuitable due to wavelength tolerances and, when using a camera as a sensor, the speckle noise from the source's coherence. The optimal source was determined to be an RCLED with a laser line filter which provided suitable spectral density with tolerable noise values. Other than speckle noise, the highest source of noise in the system was the camera, leading to the choice of a CMOS camera which also offered the smallest pixel size (useful to increase sampling). Each of these components were combined into a microscope-style configuration using two lenses and a beam splitter cube to image the GMR sensor, which was illuminated with collimated light. After optimising the instrument, it achieved a bulk LOD = $3.1 \pm 0.6 \times 10^{-5}$ RIU for refractive index sensing, which is remarkably low for a handheld instrument and comparable with laboratory-based modalities.

With such a low bulk detection limit achieved, the device was tested with two different antibody-antigen assays. IgG and CRP were chosen due to their clinical relevance in the human immune response. The lowest concentration measured was 1 ng/mL of CRP in a buffer solution using laminar flow channels as a sample delivery system. While further testing is required to optimise this detection for a clinical matrix, such as serum, the result indicates the feasibility of the device for clinical diagnostics. Further work is also needed to integrate fluidic handling to remove the need for external syringe pumps to make this a truly autonomous device.

Upon completion of this work it is clear that understanding a system is an important step in research. Too often ideas are tried once and if they work they are taken forward and if they fail they are forgotten. The converse is also true where the perceived best solution is repeatedly tried without considering that there may be a better one. An example from my work is the use of the RCLED, which wasn't tried until almost two

years into my PhD. I had assumed that lasers were the best source and all the drawbacks could be engineered to not be a problem.

In a similar way my approach could have been more focused for the biological measurements. Had I not just assumed the assay would work for me as it had for colleagues I may not have spent so long repeating the same measurements expecting a different outcome. As such, if I had started the work with the QCM-D sooner and gained that understanding of biological assays I may have been able to explain the difference between my work and my associates, which will remain my biggest disappointment from this work. Furthermore writing this thesis has helped me understand that even when I considered myself to be taking a holistic view, one's view can always be broader and the skill is identifying when to focus in. Nevertheless these factors should not detract from the progress I have made in approaching a problem. The fact the work presented here has resulted in publication shows merit in the findings which have discussed new aspects not considered in the literature before. So while there can always be improvements to the path taken, it's as they say "hindsight is 20/20", I am extremely proud of what I have achieved.

Bibliography

- [1] P. Ball, 'The lightning-fast quest for COVID vaccines - and what it means for other diseases', *Nature*, vol. 589, no. 7840, pp. 16-18, Jan. 2021.
- [2] G. George, K. R. Lakhani, and P. Puranam, 'What has changed? The Impact of Covid Pandemic on the Technology and Innovation Management Research Agenda', *Journal of Management Studies*, vol. 57, no. 8. Blackwell Publishing Ltd, pp. 1754-1758, Dec. 01, 2020.
- [3] B. Merriman, I. Torrent, and J. M. Rothberg, 'Progress in Ion Torrent semiconductor chip based sequencing', *Electrophoresis*, vol. 33, no. 23. Wiley-VCH Verlag, pp. 3397-3417, Dec. 01, 2012.
- [4] Allied Market Research, 'Biophotonics Market by End User and Application - Global Opportunity Analysis and Industry Forecast', 2017.
- [5] D. A. Armbruster and T. Pry, 'Limit of blank, limit of detection and limit of quantitation.', *Clin. Biochem. Rev.*, vol. 29 Suppl 1, no. Suppl 1, pp. S49-52, 2008.
- [6] I. M. White and X. Fan, 'On the performance quantification of resonant refractive index sensors', *Opt. Express*, vol. 16, no. 2, pp. 1020-1028, 2008.
- [7] W. Zhou and S. Fan, *Photonic Crystal Metasurface Optoelectronics*. Academic Press, 2019.
- [8] A. Drayton, I. Barth, and T. F. Krauss, 'Guided mode resonances and photonic crystals for biosensing and imaging', in *Semiconductors and Semimetals 100, Photonic Crystal Metasurface Optoelectronics*, 2019, pp. 115-148.
- [9] A. Yariv, *Optical electronics*. Saunders College Publ., 1991.
- [10] I. D. Block, N. Ganesh, M. Lu, and B. T. Cunningham, 'A Sensitivity Model for Predicting Photonic Crystal Biosensor Performance', *IEEE Sens. J.*, vol. 8, no. 3, pp. 274-280, 2008.
- [11] Y. H. Tan, M. Liu, B. Nolting, J. G. Go, J. Gervay-Hague, and G. Y. Liu, 'A nanoengineering approach for investigation and regulation of protein immobilization', *ACS Nano*, vol. 2, no. 11, pp. 2374-2384, Nov. 2008.
- [12] R. W. Wood, 'XLII. On a remarkable case of uneven distribution of light in a diffraction grating spectrum', *Philos. Mag. Ser. 6*, vol. 4, no. 21, pp. 396-402, 1902.
- [13] Lord Rayleigh, 'III. Note on the remarkable case of diffraction spectra described by Prof. Wood', *London, Edinburgh, Dublin Philos. Mag. J. Sci.*, vol. 14, no. 79, pp. 60-65, 1907.
- [14] S. S. Wang, M. G. Moharam, R. Magnusson, and J. S. Bagby, 'Guided-mode resonances in planar dielectric-layer diffraction gratings', *J. Opt. Soc. Am. A*, vol. 7, no. 8, p. 1470, 1990.

- [15] R. Magnusson and S. S. Wang, 'Transmission bandpass guided-mode resonance filters', *Appl. Opt.*, vol. 34, no. 35, p. 8106, 1995.
- [16] R. Magnusson, 'The guided-mode resonance biosensor: Principles, models, and applications', in *2020 IEEE Photonics Conference, IPC 2020 - Proceedings, 2020*, pp. 1-2.
- [17] R. Magnusson, D. Wawro, S. Zimmerman, and Y. Ding, 'Resonant photonic biosensors with polarization-based multiparametric discrimination in each channel', *Sensors*, vol. 11, no. 2, pp. 1476-1488, 2011.
- [18] B. T. Cunningham, P. Li, S. Schulz, B. Lin, C. Baird, J. Gerstenmaier, C. Genick, F. Wang, E. Fine, and L. Laing, 'Label-free assays on the BIND system', *J. Biomol. Screen.*, vol. 9, no. 6, pp. 481-490, 2004.
- [19] B. Liedberg, C. Nylander, and I. Lunström, 'Surface plasmon resonance for gas detection and biosensing', *Sensors and Actuators*, vol. 4, pp. 299-304, 1983.
- [20] Z. Yu and S. Fan, 'Extraordinarily high spectral sensitivity in refractive index sensors using multiple optical modes', *Opt. Express*, vol. 19, no. 11, pp. 10029-10040, 2011.
- [21] P. Pfeifer, U. Aldinger, G. Schwotzer, S. Diekmann, and P. Steinrücke, 'Real time sensing of specific molecular binding using surface plasmon resonance spectroscopy', *Sensors Actuators, B Chem.*, vol. 54, no. 1, pp. 166-175, 1999.
- [22] Z. Altintas, Y. Uludag, Y. Gurbuz, and I. E. Tothill, 'Surface plasmon resonance based immunosensor for the detection of the cancer biomarker carcinoembryonic antigen', *Talanta*, vol. 86, pp. 377-383, Oct. 2011.
- [23] J. Homola, 'Surface plasmon resonance sensors for detection of chemical and biological species', *Chem. Rev.*, vol. 108, no. 2, pp. 462-493, 2008.
- [24] C. Genet and T. W. Ebbesen, 'Light in tiny holes', *Nature*, vol. 445, no. 7123, pp. 39-46, 2007.
- [25] L. Martín-Moreno, F. J. García-Vidal, H. J. Lezec, K. M. Pellerin, T. Thio, J. B. Pendry, and T. W. Ebbesen, 'Theory of extraordinary optical transmission through subwavelength hole arrays', *Phys. Rev. Lett.*, vol. 86, no. 6, pp. 1114-1117, 2001.
- [26] H. Liu and P. Lalanne, 'Microscopic theory of the extraordinary optical transmission', *Nature*, vol. 452, no. 7188, pp. 728-731, 2008.
- [27] A. E. Cetin and S. N. Topkaya, 'Photonic crystal and plasmonic nanohole based label-free biodetection', *Biosens. Bioelectron.*, vol. 132, pp. 196-202, May 2019.
- [28] A. A. Yanik, A. E. Cetin, M. Huang, A. Artar, S. Hossein Mousavi, A. Khanikaev, J. H. Connor, G. Shvets, and H. Altug, 'Seeing protein monolayers with naked eye through plasmonic Fano resonances', *Proc. Natl. Acad. Sci.*, vol. 108, no. 29, pp. 11784-11789, 2011.
- [29] X. Li, M. Soler, C. I. Özdemir, A. Belushkin, F. Yesilköy, and H. Altug, 'Plasmonic nanohole array biosensor for label-free and real-time analysis of live cell secretion', *Lab Chip*, vol. 17, no. 13, pp. 2208-2217, 2017.

- [30] D. Conteduca, I. Barth, G. Pitruzzello, C. P. Reardon, E. R. Martins, and T. F. Krauss, 'Dielectric Nanohole Array Metasurface For High-Resolution Near-Field Sensing and Imaging', *Nat. Commun.*, vol. 12, no. 1, p. 3293, Dec. 2021.
- [31] D. K. Armani, T. J. Kippenberg, S. M. Spillane, and K. J. Vahala, 'Ultra-high-Q toroid microcavity on a chip', *Nature*, vol. 421, no. 6926, pp. 925–928, 2003.
- [32] J. Hu, X. Sun, A. Agarwal, and L. C. Kimerling, 'Design guidelines for optical resonator biochemical sensors', *J. Opt. Soc. Am. B*, vol. 26, no. 5, pp. 1032–1041, 2009.
- [33] J. Juan-Colás, T. F. Krauss, and S. D. Johnson, 'Real-Time Analysis of Molecular Conformation Using Silicon Electrophotonic Biosensors', *ACS Photonics*, vol. 4, no. 9, pp. 2320–2326, 2017.
- [34] W. Bogaerts, P. de Heyn, T. van Vaerenbergh, K. de Vos, S. Kumar Selvaraja, T. Claes, P. Dumon, P. Bienstman, D. van Thourhout, and R. Baets, 'Silicon microring resonators', *Laser Photonics Rev.*, vol. 6, no. 1, pp. 47–73, 2012.
- [35] S. Dante, D. Duval, D. Fariña, A. B. González-Guerrero, and L. M. Lechuga, 'Linear readout of integrated interferometric biosensors using a periodic wavelength modulation', *Laser Photonics Rev.*, vol. 9, no. 2, pp. 248–255, 2015.
- [36] S. Herranz, A. F. Gavela, and L. M. Lechuga, 'Label-free biosensors based on bimodal waveguide (BiMW) interferometers', in *Methods in Molecular Biology*, vol. 1571, Springer, 2017, pp. 161–185.
- [37] A. B. González-Guerrero, J. Maldonado, S. Dante, D. Grajales, and L. M. Lechuga, 'Direct and label-free detection of the human growth hormone in urine by an ultrasensitive bimodal waveguide biosensor', *J. Biophotonics*, vol. 10, no. 1, pp. 61–67, 2017.
- [38] M. Huang, A. A. Yanik, T.-Y. Chang, and H. Altug, 'Sub-wavelength nanofluidics in photonic crystal sensors', *Opt. Express*, vol. 17, no. 26, p. 24224, 2009.
- [39] B. Cunningham, P. Li, B. Lin, and J. Pepper, 'Colorimetric resonant reflection as a direct biochemical assay technique', *Sensors Actuators, B Chem.*, vol. 81, no. 2–3, pp. 316–328, 2002.
- [40] A. L. Washburn, L. C. Gunn, and R. C. Bailey, 'Label-free quantitation of a cancer biomarker in complex media using silicon photonic microring resonators', *Anal. Chem.*, vol. 81, no. 22, pp. 9499–9506, 2009.
- [41] E. Valera, W. W. Shia, and R. C. Bailey, 'Development and validation of an immunosensor for monocyte chemotactic protein 1 using a silicon photonic microring resonator biosensing platform', *Clin. Biochem.*, vol. 49, no. 1, pp. 121–126, 2016.
- [42] F. Liang, N. Clarke, P. Patel, M. Loncar, and Q. Quan, 'Scalable photonic crystal chips for high sensitivity protein detection', *Opt. Express*, vol. 21, no. 26, pp. 32306–32312, 2013.
- [43] House of Commons Science and Technology Committee, *Bridging the valley of death: improving the commercialisation of research*, no. March. London, 2013.

- [44] S. H. Barr, T. Baker, S. K. Markham, and A. I. Kingon, 'Bridging the Valley of Death: Lessons Learned From 14 Years of Commercialization of Technology Education', *Acad. Manag. Learn. Educ.*, vol. 8, no. 3, pp. 370–388, Sep. 2017.
- [45] T. J. Foxon, 'Technological and institutional "lock-in" as a barrier to sustainable innovation', 2002.
- [46] C. M. Christensen, *The Innovator's Dilemma When New Technologies Cause Great Firms to Fail How Can Great Firms Fail? Insights from the Hard Disk Drive Industry*. Harvard Business Review Press, 2013.
- [47] C. J. Kelly and A. J. Young, 'Promoting innovation in healthcare', *Futur. Healthc. J.*, vol. 4, no. 2, pp. 121–125, Jun. 2017.
- [48] G. V. Angelov, D. P. Nikolakov, I. N. Ruskova, E. E. Gieva, and M. L. Spasova, 'Healthcare sensing and monitoring', in *Lecture Notes in Computer Science (including subseries Lecture Notes in Artificial Intelligence and Lecture Notes in Bioinformatics)*, vol. 11369 LNCS, Springer Verlag, 2019, pp. 226–262.
- [49] N. Florio, 'British In Vitro Diagnostic Association: Near Patient Testing the Value story', London, 2021.
- [50] M. F. Drummond, B. O'Brien, G. L. Stoddart, and G. W. Torrance, *Methods for the Economic Evaluation of Health Care Programmes*, Fourth Edi. Oxford University Press, 2015.
- [51] J. D. Joannopoulos, S. G. Johnson, J. N. Winn, and R. D. Meade, *Photonic crystals: Molding the flow of light*. 2011.
- [52] Feynman, *The Feynman Lectures on Physics, Vol. II: Mainly Electromagnetism and Matter*, The New Mi. Basic Books, 2013.
- [53] D. J. Griffiths, *Introduction to Electrodynamics*, 3rd ed. Prentice Hall, 1999.
- [54] Kittel C, *Introduction to Solid State Physics*, 8th ed. New York: John Wiley & Sons, Ltd, 1996.
- [55] M. G. Moharam and T. K. Gaylord, 'Rigorous coupled-wave analysis of metallic surface-relief gratings', *J. Opt. Soc. Am. A*, 1986.
- [56] V. Liu and S. Fan, 'S4: A free electromagnetic solver for layered periodic structures', *Comput. Phys. Commun.*, vol. 183, no. 10, pp. 2233–2244, 2012.
- [57] H. Kogelnik, 'Theory of Optical Waveguides', in *Guided-Wave Optoelectronics*, 1998, pp. 7–88.
- [58] S. S. Wang and R. Magnusson, 'Theory and applications of guided-mode resonance filters', *Appl. Opt.*, vol. 32, no. 14, pp. 2606–2613, 1993.
- [59] G. J. Triggs, M. Fischer, D. Stellinga, M. G. Scullion, G. J. O. Evans, and T. F. Krauss, 'Spatial resolution and refractive index contrast of resonant photonic crystal surfaces for biosensing', *IEEE Photonics J.*, vol. 7, no. 3, 2015.
- [60] I. D. Block, L. L. Chan, and B. T. Cunningham, 'Photonic crystal optical biosensor incorporating structured low-index porous dielectric', *Sensors Actuators B Chem.*, vol. 120, no. 1, pp. 187–193, 2006.

- [61] S. Fan and J. D. Joannopoulos, 'Analysis of guided resonances in photonic crystal slabs', *Phys. Rev. B - Condens. Matter Mater. Phys.*, vol. 65, no. 23, pp. 1-8, 2002.
- [62] E. Diaz and M. Knobl, 'Optical Components Prototyping illumination systems with stock optical components', 2012.
- [63] G. J. Triggs, Y. Wang, C. P. Reardon, M. Fischer, G. J. O. Evans, and T. F. Krauss, 'Chirped guided-mode resonance biosensor', *Optica*, vol. 4, no. 2, pp. 229-234, 2017.
- [64] D. V. Rosato, D. V. Rosato, and M. G. Rosato, 'Fundamentals of Product Design', in *Injection Molding Handbook*, 3rd ed., Springer US, 2000, pp. 415-478.
- [65] Formlabs, 'Guide to SLA 3D Printing for Education and Research [White Paper]', 2016.
- [66] Y. Wang, C. P. Reardon, N. Read, G. J. Triggs, and T. F. Krauss, 'Guided mode resonance imaging-a novel sensing technique to study bacterial biofilm antibiotic resistance', in *Optics InfoBase Conference Papers*, 2017.
- [67] M. Elwenspoek, R. Wiegerink, and R. Wiegerink, *Mechanical microsensors*. Springer Science & Business Media, 2001.
- [68] B. Sonny Bal and M. Rahman, *Advances in Ceramics - Electric and Magnetic Ceramics, Bioceramics, Ceramics and Environment*. InTech, 2012.
- [69] M. Das, K. Bhimani, and V. K. Balla, 'In vitro tribological and biocompatibility evaluation of sintered silicon nitride', *Mater. Lett.*, vol. 212, pp. 130-133, 2018.
- [70] P. M. George, A. W. Lyckman, D. A. LaVan, A. Hegde, Y. Leung, R. Avasare, C. Testa, P. M. Alexander, R. Langer, and M. Sur, 'Fabrication and biocompatibility of polypyrrole implants suitable for neural prosthetics', *Biomaterials*, vol. 26, no. 17, pp. 3511-3519, Jun. 2005.
- [71] K. Luke, Y. Okawachi, M. R. E. Lamont, A. L. Gaeta, and M. Lipson, 'Broadband mid-infrared frequency comb generation in a Si₃N₄ microresonator', *Opt. Lett.*, vol. 40, no. 21, pp. 1-4, 2015.
- [72] J. S. Male, 'Thermally Enhanced Paper Microfluidics for Photonic Crystal Biosensors in Amorphous Silicon', University of York, 2019.
- [73] ALLRESIST AR-P 6200 (CSAR 62). <http://www.allresist.com/csar-62-ar-p-6200/>. [Accessed: 30 Apr. 2020].
- [74] ALLRESISTAR-PC 5090. <http://www.allresist.com/ar-pc-5090-5091-electra-92/>. [Accessed: 30 Apr. 2020].
- [75] S. Prakash and J. Yeom, *Nanofluidics and Microfluidics: Systems and Applications*. William Andrew, 2014.
- [76] J. I. Goldstein, D. E. Newbury, J. R. Michael, N. W. M. Ritchie, J. H. J. Scott, and D. C. Joy, *Scanning electron microscopy and X-ray microanalysis*. Springer, 2017.

- [77] T. H. P. Chang, 'Proximity effect in electron-beam lithography.', in *J Vac Sci Technol*, 1975, vol. 12, no. 6, pp. 1271-1275.
- [78] G. P. Watson, 'Dose modification proximity effect correction scheme with inherent forward scattering corrections', *J. Vac. Sci. Technol. B Microelectron. Nanom. Struct.*, vol. 15, no. 6, pp. 2309-2312, 1997.
- [79] M. Rooks, N. Belic, E. Kratschmer, and R. Viswanathan, 'Experimental optimization of the electron-beam proximity effect forward scattering parameter', *J. Vac. Sci. Technol. B Microelectron. Nanom. Struct.*, vol. 23, no. 6, pp. 2769-2774, 2005.
- [80] R. D. Mansano, P. Verdonck, and H. S. Maciel, 'Mechanisms of surface roughness induced in silicon by fluorine containing plasmas', *Vacuum*, vol. 48, no. 7-9, pp. 677-679, Sep. 1997.
- [81] B. E. E. Kastenmeier, P. J. Matsuo, G. S. Oehrlein, R. E. Ellefson, and L. C. Frees, 'Surface etching mechanism of silicon nitride in fluorine and nitric oxide containing plasmas', *J. Vac. Sci. Technol. A Vacuum, Surfaces, Film.*, vol. 19, no. 1, pp. 25-30, 2001.
- [82] R. Legtenberg, H. Jansen, M. De Boer, and M. Elwenspoek, 'Anisotropic reactive ion etching of silicon using SF₆/O₂/CHF₃ gas mixtures', *J. Electrochem. Soc.*, vol. 142, no. 6, p. 2020, 1995.
- [83] V. Bhalla, S. Carrara, C. Stagni, and B. Samorì, 'Chip cleaning and regeneration for electrochemical sensor arrays', *Thin Solid Films*, vol. 518, no. 12, pp. 3360-3366, 2010.
- [84] L. Sirghi, O. Kylián, D. Gilliland, G. Ceccone, and F. Rossi, 'Cleaning and hydrophilization of atomic force microscopy silicon probes', *J. Phys. Chem. B*, vol. 110, no. 51, pp. 25975-25981, 2006.
- [85] T. F. Krauss, R. M. De La Rue, and S. Brand, 'Two-dimensional photonic-bandgap structures operating at near-infrared wavelengths', *Nature*, vol. 383, no. 6602, pp. 699-702, 1996.
- [86] Formlabs, 'FDM vs. SLA Compare the Two Most Popular Types of 3D Printers For Education [White Paper]', 2019.
- [87] T. Duda and L. V. Raghavan, '3D Metal Printing Technology', *IFAC-PapersOnLine*, vol. 49, no. 29, pp. 103-110, 2016.
- [88] V. Hahn, F. Mayer, M. Thiel, and M. Wegener, '3-D Laser Nanoprinting', *Opt. Photonics News*, 2019.
- [89] R. Barakat, 'Application of Apodization to Increase Two-Point Resolution by the Sparrow Criterion I Coherent Illumination', *J. Opt. Soc. Am.*, vol. 52, no. 3, p. 276, 1962.
- [90] R. Barakat and E. Levin, 'Application of Apodization to Increase Two-Point Resolution by the Sparrow Criterion II Incoherent Illumination', *J. Opt. Soc. Am.*, vol. 53, no. 2, p. 274, 1963.

- [91] Y. Wang, C. P. Reardon, N. Read, S. Thorpe, A. Evans, N. Todd, M. Van Der Woude, and T. F. Krauss, 'Attachment and antibiotic response of early-stage biofilms studied using resonant hyperspectral imaging', *npj Biofilms Microbiomes*, vol. 6, no. 57, 2020.
- [92] A. Kenaan, K. Li, I. Barth, S. Johnson, J. Song, and T. F. Krauss, 'Guided mode resonance sensor for the parallel detection of multiple protein biomarkers in human urine with high sensitivity', *Biosens. Bioelectron.*, vol. 153, p. 112047, 2020.
- [93] J. Juan-Colás, I. S. Hitchcock, M. Coles, S. Johnson, and T. F. Krauss, 'Quantifying single-cell secretion in real time using resonant hyperspectral imaging', *Proc. Natl. Acad. Sci. U. S. A.*, vol. 115, no. 52, pp. 13204–13209, 2018.
- [94] The Imaging Source Europe GmbH, *USB 2.0 monochrome Board cameras*. <https://www.theimagingsource.com/products/board-cameras/usb-2.0-monochrome/>. [Accessed: 30 Apr. 2021].
- [95] Ø. I. Helle, F. T. Dullo, M. Lahrberg, J. C. Tinguely, O. G. Hellesø, and B. S. Ahluwalia, 'Structured illumination microscopy using a photonic chip', *Nat. Photonics*, vol. 14, no. 7, pp. 431–438, May 2020.
- [96] W. Chen, K. D. Long, H. Yu, Y. Tan, J. S. Choi, B. A. Harley, and B. T. Cunningham, 'Enhanced live cell imaging via photonic crystal enhanced fluorescence microscopy', *Analyst*, vol. 139, no. 22, pp. 5954–5963, Oct. 2014.
- [97] C. Szydzik, A. F. Gavela, S. Herranz, J. Roccisano, M. Knoerzer, P. Thurgood, K. Khoshmanesh, A. Mitchell, and L. M. Lechuga, 'An automated optofluidic biosensor platform combining interferometric sensors and injection moulded microfluidics', *Lab Chip*, vol. 17, no. 16, pp. 2793–2804, 2017.
- [98] J. Quinchia, D. Echeverri, A. F. Cruz-Pacheco, M. E. Maldonado, and J. Orozco, 'Electrochemical Biosensors for Determination of Colorectal Tumor Biomarkers', *Micromachines*, vol. 11, no. 4, p. 411, Apr. 2020.
- [99] R. Mukhopadhyay, 'When PDMS isn't the best', *Anal. Chem. (Washington, DC)*, vol. 79, no. 9, pp. 3248–3253, 2007.
- [100] A. Drayton, K. Li, M. Simmons, C. Reardon, and T. F. Krauss, 'Performance limitations of resonant refractive index sensors with low-cost components', *Opt. Express*, vol. 28, no. 22, p. 32239, Oct. 2020.
- [101] K. Saurav and N. Le Thomas, 'Probing the fundamental detection limit of photonic crystal cavities: erratum', *Optica*, vol. 4, no. 10, pp. 1305–1305, 2017.
- [102] D. Martens et al., 'A low-cost integrated biosensing platform based on SiN nanophotonics for biomarker detection in urine', *Anal. Methods*, vol. 10, no. 25, pp. 3066–3073, Jul. 2018.
- [103] S. Jahns, M. Bräu, B.-O. Meyer, T. Karrock, S. B. Gutekunst, L. Blohm, C. Selhuber-Unkel, R. Buhmann, Y. Nazirizadeh, and M. Gerken, 'Handheld imaging photonic crystal biosensor for multiplexed, label-free protein detection', *Biomed. Opt. Express*, vol. 6, no. 10, pp. 3724–3736, 2015.

- [104] D. Gallegos, K. D. Long, H. Yu, P. P. Clark, Y. Lin, S. George, P. Nath, and B. T. Cunningham, 'Label-free biodetection using a smartphone', *Lab Chip*, vol. 13, no. 11, p. 2124, 2013.
- [105] A. B. González-Guerrero, J. Maldonado, S. Dante, D. Grajales, and L. M. Lechuga, 'Direct and label-free detection of the human growth hormone in urine by an ultrasensitive bimodal waveguide biosensor', *J. Biophotonics*, vol. 10, no. 1, pp. 61-67, 2017.
- [106] F. Yesilkoy, R. A. Terborg, J. Pello, A. A. Belushkin, Y. Jahani, V. Pruneri, and H. Altug, 'Phase-sensitive plasmonic biosensor using a portable and large field-of-view interferometric microarray imager', *Light Sci. Appl.*, vol. 7, no. 2, p. 17152, Feb. 2018.
- [107] N. Fabri-Faja, O. Calvo-Lozano, P. Dey, R. A. Terborg, M. C. Estevez, A. Belushkin, F. Yesilköy, L. Duempelmann, H. Altug, V. Pruneri, and L. M. Lechuga, 'Early sepsis diagnosis via protein and miRNA biomarkers using a novel point-of-care photonic biosensor', *Anal. Chim. Acta*, vol. 1077, pp. 232-242, 2019.
- [108] R. A. Terborg et al., 'Lens-free interferometric microscope for point-of-care label-free detection of sepsis biomarkers', in *Frontiers in Optics - Proceedings Frontiers in Optics + Laser Science APS/DLS*, 2019, p. FM3F.6.
- [109] R. G. Baets, D. Delbeke, R. Bockstaele, and P. Bienstman, 'Resonant-Cavity Light-Emitting Diodes: a review', in *Light-Emitting Diodes: Research, Manufacturing, and Applications VII*, 2003, vol. 4996, pp. 74-86.
- [110] X. Buet, E. Daran, D. Belharet, F. Lozes-Dupuy, A. Monmayrant, and O. Gauthier-Lafaye, 'High angular tolerance and reflectivity with narrow bandwidth cavity-resonator-integrated guided-mode resonance filter', *Opt. Express*, vol. 20, no. 8, p. 9322, Apr. 2012.
- [111] H. Neve, J. Blondelle, R. Baets, P. Demeester, P. Daele, and G. Borghs, 'Resonant Cavity LED's', in *Microcavities and Photonic Bandgaps: Physics and Applications*, Dordrecht: Springer, 1996, pp. 333-342.
- [112] R. Wirth, C. Karnutsch, S. Kugler, and K. Streubel, 'High-efficiency resonant-cavity LEDs emitting at 650 nm', *IEEE Photonics Technol. Lett.*, vol. 13, no. 5, pp. 421-423, 2001.
- [113] R. Feder and T. Light, 'Precision thermal expansion measurements of semi-insulating GaAs', *J. Appl. Phys.*, vol. 39, no. 10, pp. 4870-4871, 1968.
- [114] E. D. Pierron, D. L. Parker, and J. B. McNeely, 'Coefficient of expansion of GaAs, GaP, and Ga(As, P) compounds from -62° to 200°C', *J. Appl. Phys.*, vol. 38, no. 12, pp. 4669-4671, 1967.
- [115] X. Fan, I. M. White, S. I. Shopova, H. Zhu, J. D. Suter, and Y. Sun, 'Sensitive optical biosensors for unlabeled targets: A review', *Anal. Chim. Acta*, vol. 620, no. 1-2, pp. 8-26, Jul. 2008.

- [116] M. Bigas, E. Cabruja, J. Forest, and J. Salvi, 'Review of CMOS image sensors', *Microelectronics J.*, vol. 37, no. 5, pp. 433–451, May 2006.
- [117] B. Kisacanin, S. S. Bhattacharyya, and S. Chai, *Embedded Computer Vision*. Springer Science & Business Media, 2009.
- [118] H. Tian, B. Fowler, and A. El Gamal, 'Analysis of temporal noise in CMOS photodiode active pixel sensor', *IEEE J. Solid-State Circuits*, vol. 36, no. 1, pp. 92–101, 2001.
- [119] Teledyne Photometrics, *Technical Note: Camera Test Protocol [White Paper]*. <https://www.photometrics.com/learn/white-papers>.
- [120] M. F. Limonov, M. V. Rybin, A. N. Poddubny, and Y. S. Kivshar, 'Fano resonances in photonics', *Nat. Photonics*, vol. 11, no. 9, pp. 543–554, 2017.
- [121] M. Lu, S. J. Park, B. T. Cunningham, and J. G. Eden, 'Microcavity plasma devices and arrays fabricated by plastic-based replica molding', *J. Microelectromechanical Syst.*, vol. 16, no. 6, pp. 1397–1402, Dec. 2007.
- [122] C. J. Choi, I. D. Block, B. Bole, D. Dralle, and B. T. Cunningham, 'Label-free photonic crystal biosensor integrated microfluidic chip for determination of kinetic reaction rate constants', *IEEE Sens. J.*, vol. 9, no. 12, pp. 1697–1704, Dec. 2009.
- [123] T. Stangner, H. Zhang, T. Dahlberg, K. Wiklund, and M. Andersson, 'Step-by-step guide to reduce spatial coherence of laser light using a rotating ground glass diffuser', *Appl. Opt.*, vol. 58, no. 19, pp. 5427–5435, 2017.
- [124] A. B. McLean, C. E. J. Mitchell, and D. M. Swanston, 'Implementation of an efficient analytical approximation to the Voigt function for photoemission lineshape analysis', *J. Electron Spectros. Relat. Phenomena*, vol. 69, no. 2, pp. 125–132, Sep. 1994.
- [125] M. Galli, S. L. Portalupi, M. Belotti, L. C. Andreani, L. O'Faolain, and T. F. Krauss, 'Light scattering and Fano resonances in high-Q photonic crystal nanocavities', *Appl. Phys. Lett.*, vol. 94, no. 7, 2009.
- [126] M. Soler, O. Calvo-Lozano, M.-C. Estevez, and L. M. Lechuga, 'Nanophotonic Biosensors: Driving Personalized Medicine', *Opt. Photonics News*, vol. 31, no. 4, pp. 24–31, 2020.
- [127] G. Pitruzzello and T. F. Krauss, 'Photonic crystal resonances for sensing and imaging', *J. Opt.*, vol. 20, no. 7, p. 73004, 2018.
- [128] M. Paulsen, S. Jahns, and M. Gerken, 'Intensity-based readout of resonant-waveguide grating biosensors: Systems and nanostructures', *Photonics Nanostructures - Fundam. Appl.*, vol. 26, pp. 69–79, 2017.
- [129] *Antelope DX*. <https://www.antelope-dx.com/>. [Accessed: 28 Apr. 2020].
- [130] C. J. Choi and B. T. Cunningham, 'Single-step fabrication and characterization of photonic crystal biosensors with polymer microfluidic channels', *Lab Chip*, vol. 6, no. 10, pp. 1373–1380, Sep. 2006.

- [131] D. Martens, A. Stassen, W. Van Roy, and P. Bienstman, 'Novelty low-cost integrated photonic biosensor using broadband source and on-chip spectral filter', in *Proceedings Symposium IEEE Photonics Society Benelux*, 2015, pp. 173-176.
- [132] A. E. Cetin, D. Etezadi, B. C. Galarreta, M. P. Busson, Y. Eksioglu, and H. Altug, 'Plasmonic Nanohole Arrays on a Robust Hybrid Substrate for Highly Sensitive Label-Free Biosensing', *ACS Photonics*, vol. 2, no. 8, pp. 1167-1174, 2015.
- [133] E. Luan, H. Yun, M. Ma, D. M. Ratner, K. C. Cheung, and L. Chrostowski, 'Label-free biosensing with a multi-box sub-wavelength phase-shifted Bragg grating waveguide', *Biomed. Opt. Express*, vol. 10, no. 9, pp. 4825-4838, Sep. 2019.
- [134] R. M. T. De Wildt, C. R. Mundy, B. D. Gorick, and I. M. Tomlinson, 'Antibody arrays for high-throughput screening of antibody-antigen interactions', *Nat. Biotechnol.*, vol. 18, no. 9, pp. 989-994, 2000.
- [135] J. Qin, X. Li, L. Cao, S. Du, W. Wang, and S. Q. Yao, 'Competition-Based Universal Photonic Crystal Biosensors by Using Antibody-Antigen Interaction', *J. Am. Chem. Soc.*, vol. 142, no. 1, pp. 417-423, Jan. 2020.
- [136] M. E. Goldberg and L. Djavadi-Ohanian, 'Methods for measurement of antibody/antigen affinity based on ELISA and RIA', *Curr. Opin. Immunol.*, vol. 5, no. 2, pp. 278-281, Jan. 1993.
- [137] B. T. Cunningham, M. Zhang, Y. Zhuo, L. Kwon, and C. Race, 'Recent Advances in Biosensing with Photonic Crystal Surfaces: A Review', *IEEE Sens. J.*, vol. 16, no. 10, pp. 3349-3366, 2016.
- [138] S. Black, I. Kushner, and D. Samols, 'C-reactive protein', *J. Biol. Chem.*, vol. 279, no. 47, pp. 48487-48490, Nov. 2004.
- [139] M. Biburger, A. Lux, and F. Nimmerjahn, 'How immunoglobulin G antibodies kill target cells: Revisiting an old paradigm', in *Advances in Immunology*, vol. 124, Academic Press Inc., 2014, pp. 67-94.
- [140] A. Khera, D. K. McGuire, S. A. Murphy, H. G. Stanek, S. R. Das, W. Vongpatanasin, F. H. Wians, S. M. Grundy, and J. A. De Lemos, 'Race and gender differences in C-reactive protein levels', *J. Am. Coll. Cardiol.*, vol. 46, no. 3, pp. 464-469, Aug. 2005.
- [141] J. Arndt, D. Houde, W. Domeier, S. Berkowitz, and J. R. Engen, *IgG1 Fab characterized by H/D exchange*. <http://dx.doi.org/10.2210/pdb3fzu/pdb>.
- [142] C. Guillon, U. Mavoungou Bigouagou, P. Jeannin, Y. Delneste, and P. Gouet, *Monoclinic form of Human C-Reactive Protein*. <http://dx.doi.org/10.2210/pdb3pvo/pdb>.
- [143] D. Houde, J. Arndt, W. Domeier, S. Berkowitz, and J. R. Engen, 'Characterization of IgG1 Conformation and conformational dynamics by hydrogen/deuterium exchange mass spectrometry', *Anal. Chem.*, vol. 81, no. 7, pp. 2644-2651, Apr. 2009.

- [144] P. Yager, T. Edwards, E. Fu, K. Helton, K. Nelson, M. R. Tam, and B. H. Weigl, 'Microfluidic diagnostic technologies for global public health', *Nature*, vol. 442, no. 7101, pp. 412-418, Jul. 2006.
- [145] P. Schuck and H. Zhao, 'The role of mass transport limitation and surface heterogeneity in the biophysical characterization of macromolecular binding processes by SPR biosensing.', *Methods Mol. Biol.*, vol. 627, pp. 15-54, 2010.
- [146] N. G. Welch, J. A. Scoble, B. W. Muir, and P. J. Pigram, 'Orientation and characterization of immobilized antibodies for improved immunoassays (Review)', *Biointerphases*, vol. 12, no. 2, Jun. 2017.
- [147] C. K. Yang, J. S. Chang, S. D. Chao, and K. C. Wu, 'Effects of diffusion boundary layer on reaction kinetics of immunoassay in a biosensor', *J. Appl. Phys.*, vol. 103, no. 8, 2008.
- [148] J. Kankare, 'Sauerbrey equation of quartz crystal microbalance in liquid medium', *Langmuir*, vol. 18, no. 18, pp. 7092-7094, Sep. 2002.
- [149] L. M. Miller, C. D. Silver, R. Herman, A. K. Duhme-Klair, G. H. Thomas, T. F. Krauss, and S. D. Johnson, 'Surface-Bound Antibiotic for the Detection of β -Lactamases', *ACS Appl. Mater. Interfaces*, vol. 11, no. 36, pp. 32599-32604, Aug. 2019.
- [150] I. Langmuir, 'The constitution and fundamental properties of solids and liquids. Part I. Solids', *J. Am. Chem. Soc.*, vol. 38, no. 11, 1916.
- [151] R. A. Latour, 'The Langmuir isotherm: A commonly applied but misleading approach for the analysis of protein adsorption behavior', *J. Biomed. Mater. Res. - Part A*, vol. 103, no. 3, pp. 949-958, Mar. 2015.
- [152] K. Raj M and S. Chakraborty, 'PDMS microfluidics: A mini review', *J. Appl. Polym. Sci.*, vol. 137, no. 27, p. 48958, Jul. 2020.
- [153] Venzac, Bastien, S. le Gac, C. Otto, and A. T. Lenferink, 'PDMS curing inhibition by 3D-printed templates. Why? And how to avoid it.', in *NanoBioTech-Montreux 2019*, 2019.
- [154] M. A. M. M. Ferraz, J. B. Nagashima, B. Venzac, S. Le Gac, and N. Songsasen, '3D printed mold leachates in PDMS microfluidic devices', *Sci. Rep.*, vol. 10, no. 1, pp. 1-9, Dec. 2020.
- [155] N. Hopkinson and P. Dickens, 'Rapid prototyping for direct manufacture', *Rapid Prototyp. J.*, vol. 7, no. 4, pp. 197-202, 2001.
- [156] G. M. Whitesides, 'The origins and the future of microfluidics', *Nature*, vol. 442, no. 7101, pp. 368-373, Jul. 2006.
- [157] N. W. Ryan and M. M. Johnson, 'Transition from laminar to turbulent flow in pipes', *AIChE J.*, vol. 5, no. 4, pp. 433-435, 1959.
- [158] *Comsol: Controlled Diffusion Micromixer*.
<https://www.comsol.com/model/controlled-diffusion-micromixer-12641>.
 [Accessed: 25 Jan. 2021].

- [159] A. N. Bashkatov, E. A. Genina, Y. P. Sinichkin, V. I. Kochubey, N. A. Lakodina, and V. V. Tuchin, 'Glucose and Mannitol Diffusion in Human Dura Mater', *Biophys. J.*, vol. 85, no. 5, pp. 3310–3318, 2003.
- [160] C. Kunstmann-Olsen, J. D. Hoyland, and H. G. Rubahn, 'Influence of geometry on hydrodynamic focusing and long-range fluid behavior in PDMS microfluidic chips', *Microfluid. Nanofluidics*, vol. 12, no. 5, pp. 795–803, Mar. 2012.
- [161] P. Säfsten, S. L. Klakamp, A. W. Drake, R. Karlsson, and D. G. Myszka, 'Screening antibody-antigen interactions in parallel using Biacore A100', *Anal. Biochem.*, vol. 353, no. 2, pp. 181–190, Jun. 2006.
- [162] K. Li, R. Gupta, A. Drayton, I. Barth, D. Conteduca, C. Reardon, K. Dholakia, and T. F. Krauss, 'Extended Kalman Filtering Projection Method to Reduce the 3σ Noise Value of Optical Biosensors', *ACS Sensors*, vol. 5, no. 11, pp. 3474–3482, Oct. 2020.
- [163] A. Belushkin, F. Yesilkoy, J. J. González-López, J. C. Ruiz-Rodríguez, R. Ferrer, A. Fàbrega, and H. Altug, 'Rapid and Digital Detection of Inflammatory Biomarkers Enabled by a Novel Portable Nanoplasmonic Imager', *Small*, vol. 16, no. 3, p. 1906108, Jan. 2020.
- [164] *Assessment and monitoring of chronic kidney disease - NICE Pathways*. <https://pathways.nice.org.uk/pathways/chronic-kidney-disease/assessment-and-monitoring-of-chronic-kidney-disease#content=view-node%3Anodes-testing-for-proteinuria>. [Accessed: 11 May 2021].
- [165] F. Lemarchand, A. Sentenac, E. Cambriil, and H. Giovannini, 'Study of the resonant behaviour of waveguide gratings: Increasing the angular tolerance of guided-mode filters', *J. Opt. A Pure Appl. Opt.*, vol. 1, no. 4, pp. 545–551, Jul. 1999.
- [166] B. Xu, D. Zhang, Y. Huang, Q. Wang, B. Li, and D. Zhang, 'Real-time angular sensitivity compensation of guided-mode resonance filter', *IEEE Photonics Technol. Lett.*, vol. 26, no. 3, pp. 231–234, Feb. 2014.
- [167] Z. Zhou, J. Li, R. Su, B. Yao, H. Fang, K. Li, L. Zhou, J. Liu, D. Stellinga, C. P. Reardon, T. F. Krauss, and X. Wang, 'Efficient Silicon Metasurfaces for Visible Light', *ACS Photonics*, vol. 4, no. 3, pp. 544–551, Mar. 2017.
- [168] A. Martins, K. Li, J. Li, H. Liang, D. CONTEДУCA, B.-H. V. Borges, T. F. Krauss, and E. R. Martins, 'On metalenses with arbitrarily wide field of view', *ACS Photonics*, p. acsphotronics.0c00479, Jun. 2020.
- [169] D. Gajera, 'Process costing of microchip', West Virginia University, 2006.
- [170] D. L. Bourell, 'Perspectives on Additive Manufacturing', *Annu. Rev. Mater. Res.*, vol. 46, pp. 1–18, 2016.
- [171] I. Barth, D. Conteduca, C. Reardon, S. Johnson, and T. F. Krauss, 'Common-path interferometric label-free protein sensing with resonant dielectric nanostructures', *Light Sci. Appl.*, vol. 9, no. 1, pp. 1–9, Dec. 2020.

- [172] T. Kokalj, Y. Park, M. Vencelj, M. Jenko, and L. P. Lee, 'Self-powered imbibing microfluidic pump by liquid encapsulation: SIMPLE', *Lab Chip*, vol. 14, no. 22, pp. 4329–4333, Nov. 2014.
- [173] F. Dal Dosso, T. Kokalj, J. Belotserkovsky, D. Spasic, and J. Lammertyn, 'Self-powered infusion microfluidic pump for ex vivo drug delivery', *Biomed. Microdevices*, vol. 20, no. 2, Jun. 2018.
- [174] D. D. Cunningham, 'Fluidics and sample handling in clinical chemical analysis', *Anal. Chim. Acta*, vol. 429, no. 1, pp. 1–18, Feb. 2001.
- [175] I. Sultan, S. Rahman, A. T. Jan, M. T. Siddiqui, A. H. Mondal, and Q. M. R. Haq, 'Antibiotics, resistome and resistance mechanisms: A bacterial perspective', *Front. Microbiol.*, vol. 9, no. SEP, p. 2066, Sep. 2018.
- [176] Z. Wang, H. C. Yang, F. He, S. Peng, Y. Li, L. Shao, and S. B. Darling, 'Mussel-Inspired Surface Engineering for Water-Remediation Materials', *Matter*, vol. 1, no. 1, pp. 115–155, Jul. 2019.
- [177] Q. Wei, K. Achazi, H. Liebe, A. Schulz, P. L. M. Noeske, I. Grunwald, and R. Haag, 'Mussel-Inspired Dendritic Polymers as Universal Multifunctional Coatings', *Angew. Chemie - Int. Ed.*, vol. 53, no. 43, pp. 11650–11655, Oct. 2014.
- [178] H. Lee, S. M. Dellatore, W. M. Miller, and P. B. Messersmith, 'Mussel-inspired surface chemistry for multifunctional coatings', *Science (80-.)*, vol. 318, no. 5849, pp. 426–430, 2007.